Early detection of the process of vascular calcification with novel bone seeking radiopharmaceuticals using SPECT-CT and P ET-CT

Bordoloi, Jayanta Kumar

Awarding institution:
King's College London

Early detection of the process of vascular calcification with novel bone seeking radiopharmaceuticals using SPECT-CT and PET-CT.

Jayanta Kumar Bordoloi

0974106

Thesis submitted for the degree of Doctor of Philosophy 2015

Supervised by

Prof. Catherine M. Shanahan and

Prof. Philip J. Blower

Abstract

Positron emission tomography (PET) and single photon emission computed tomography (SPECT) are clinically established sensitive molecular imaging modalities. However, their use in clinical cardiology remains limited. Early or intermediate stages of vascular calcification are thought to enhance plaque vulnerability. Computed tomography (CT), the “gold standard” for clinical imaging of calcification, fails to detect the early stages of calcification. PET and SPECT imaging may be used to detect the early stages of calcification *in vivo*.

The aim of the project was to evaluate novel and clinically established bone seeking SPECT and PET agents for imaging vascular calcification using experimental animal models. Technetium-99m labelled methylene diphosphonate (^{99m}Tc-MDP), fluorine-18 sodium fluoride (^{18}F-NaF) and the novel bone seeking agents technetium-99m labelled dipicolylamine alendronate (^{99m}Tc-DPA Ale) and nitrido bis(dithiocarbamatebisphospho nate) (^{99m}Tc-N (DTCBP)$_2$) were tested *in vitro* and for imaging *in vivo* using rat models of medial vascular calcification.

In the initial *in vitro* studies the bone seeking radiotracers described here demonstrated their potential for avid binding with different minerals, both of biological and synthetic origin, with ^{99m}Tc-DPA-Ale and ^{18}F-NaF binding most efficient. Rat models for vascular calcification were established by diet modification and sub-cutaneous injections. For optimising the *in vivo* imaging protocol, a robust rat model with extensive calcification was established by feeding a special warfarin diet and sub-cutaneous administration of vitamin D_3. Another model, with slow and progressive calcification, was achieved by feeding rats with warfarin diet only, and was found to be an ideal candidate for the longitudinal imaging study. *In vivo* imaging with animal models for vascular calcification

revealed that the radiotracers can detect vascular calcification earlier than computed tomography. Longitudinal studies with the calcified rat model showed that the radiotracers can also play a role in monitoring disease progression.

However, the study also revealed several unexpected findings. SPECT and PET images showed radiotracer uptake in the abdominal aorta and mesenteric artery. Histological evidence of calcification was seen in the thoracic aorta which was not detected on SPECT and PET imaging. Histological sections also revealed that the calcified regions in the abdominal aorta are in proximity to the lumen whereas in the thoracic aorta they are deep seated, close to the adventitia which may account for the differential in uptake. The longitudinal imaging study showed that uptake of the radiotracers also reduced with maturity in calcification. These findings raise some intriguing questions, and answering them would help in a better understanding of the process of vascular calcification and developing strategies for *in vivo* imaging with SPECT-CT and PET-CT.

In conclusion, bone seeking radiopharmaceuticals have the potential to be used as agents for early diagnosis of vascular calcification and further study needs to be done to address the interesting questions raised in this thesis.

Declaration

I declare that the work under taken in this thesis is my own original work, except where acknowledgement has been made.

Jayanta Kumar Bordoloi

Acknowledgements

Firstly, I want to express my sincere thanks to my supervisors Professor Cathy Shanahan and Professor Phil Blower, for believing in me and giving me the opportunity to work with them. I am fortunate to have both of you as my mentors. Your support and encouragement and belief in me have always motivated me. Without your valuable advice and comments this thesis would not have been possible.

Besides my supervisors I would like to thank Dr. Rafael de Rosales for his insightful comments, encouragement and much needed guidance in radiolabeling and quality control of novel compounds. I am also grateful to Dr. Kavitha Sunassee and Steven Clark for guiding and helping me in every step of the *in vivo* imaging studies. This study was carried out in the BHF Centre of Excellence, Cardiovascular Division James Black Centre, and the Division of Imaging Sciences & Biomedical Engineering, King's College London. I would like to thank the lab managers Division of Imaging Sciences & Biomedical Engineering David Thakor and Barry Crook whose relentless support made working in the laboratory smooth and easy. Furthermore, I would like to thank my colleagues and seniors in the James Black Centre for their help and support. Special thanks to Dr. Alex Kapustin and Gosia Furmanik for assisting and training me in the tissue culture work. I would also like to thank Robert Hayward for all the help in the laboratory as well as in the BSU.

I would like to thank all my friends, especially Can Can, Jo, Rosie, Chin Yee, Yiwen, Ally, Anne, Julia, Zaitul and Krisanat for putting up with me. It is not easy to be friends with someone who always has something to say, in other words a chatter box. Thanks for

listening to me and for being kind and helpful. I owe my deepest gratitude to my parents for their support, both emotional and financial.

Last but not the least I would like to thank the British Heart Foundation, for providing us with the much needed funding for the research.

Table of Contents

List of figures

Chapter 5

Chapter 6

List of tables

List of publication

1. Bordoloi JK, Berry D, Khan IU, et al. Technetium-99m and rhenium-188 complexes with one and two pendant bisphosphonate groups for imaging arterial calcification. *Dalton Trans.* 2015(44): 4963–4975

Abbreviations

^{18}F-NaF	Fluorine-18 sodium fluoride
^{99m}Tc-MDP	Technetium-99m methylene diphosphonate
^{99m}Tc-DPA Ale	Technetium-99m dipicolylamine alendronate
^{99m}Tc-N (DTCBP)$_2$	Technetium-99m nitrido bis(dithiocarbamatebisphosphonate)
AB	Apoptotic bodies
CT	Computed Tomography
DPA	Dipicolylamine
DTC	Dithiocarbamate
EBCT	Electron Beam Computed Tomography
MDP	MDP-Methylene diphosphonate
MRI	Magnetic Resonance Imaging
MV	MV-Matric Vesicles
PET	Positron Emission Tomography
SD	Sprague-Dawley
SPECT	Single Photon Emission Computed Tomography
VSMC	Vascular Smooth Muscle Cells
CKD	Chronic kidney disease
CVD	Cardiovascular diseases
DALY	Disability-adjusted life year
SSNMR	Solid-state nuclear magnetic resonance
LDL	Low density lipoprotein
LVH	Left ventricular hypertrophy

NIDDM	Noninsulin-dependent diabetes mellitus
NMR	Nuclear magnetic resonance
BMP	Bone morphogenetic proteins
CVC	Calcifying vascular cells
OPN	Osteopontin
ALP	Alkaline phosphatase
MGP	MGP-Matrix Gla protein
Ahsg	α2-Heremans-Schmid glycoprotein
PPi	Pyrophosphate
ATP	Adenosine triphosphate
EXOs	Exosomes
PWV	Pulse wave velocity

Chapter 1: Pathobiology of vascular calcification.

Vascular calcification is a complex process of biomineralisation in which bioapatite is deposited ectopically in the blood vessels.[1] It is a common finding in patients with atherosclerosis, diabetes mellitus type II, hypertension, hyperparathyroidism and chronic kidney disease (CKD).[2] Bioapatite is a form of calcium phosphate which closely resembles hydroxyapatite and is a major constituent of bone.

The presence of arterial calcification is a clinically significant predictor of cardiovascular events such as ischemic heart disease, myocardial infarction and cardiac arrest. Clinically it can be detected and quantified using computed tomography (CT).[3-7] Cardiovascular diseases (CVD's) are the leading cause of deaths worldwide claiming 17 million lives in 2008. Almost 3 million of these deaths were of individuals under the age of 60. CVD's include diseases of the heart, vascular diseases of the brain and diseases of the blood vessels. The overall disease burden is measured in "disability-adjusted life year" (DALY), which is an expression of the number of years lost due to ill-health, disability or premature death. It has been observed that the percentage of premature deaths due to CVD's is 4% in high-income countries and 42% in low-income countries.[8, 9] Studies show that patients with CKD have a several fold higher susceptibility to vascular calcification in comparison to normal individuals and often die due to cardiovascular complications.[10, 11]

A recent study of the minerals found in calcified plaques by solid-state nuclear magnetic resonance (SSNMR) technique revealed that the constituents are similar to those of bone.[12] Based on the layer of vessel wall where hydroxyapatite crystal is accumulated, vascular calcification can be classified into two categories i.e. intimal and medial calcification.

1.1 Atherosclerotic intimal calcification

Atherosclerosis is one of the underlying causes of cardiovascular disease and arises due to immune-inflammatory response to endothelial injury and endothelial dysfunctions caused by various risk factors.[13, 14] The risk factors include elevated and modified low density lipoprotein (LDL); free radicals caused by cigarette smoking, hypertension and diabetes mellitus; genetic alterations; elevated plasma homocysteine concentrations; and combinations of these or other factors.[14] The process of atherosclerosis is complex (Figure 1.1) involving a sequence of events. The lesions of atherosclerosis occur principally in large and medium-sized elastic and muscular arteries.

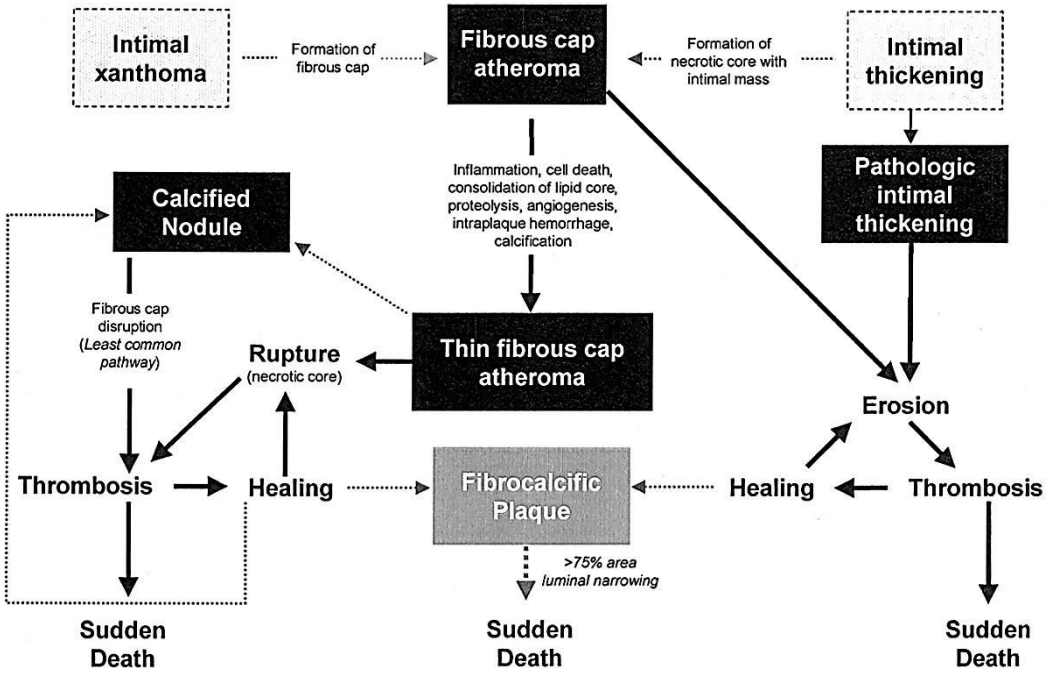

Figure 1.1: A simplified illustration of the processes leading to development of atherosclerotic lesions, their classification based on American Heart Association (AHA) and possible clinical outcome. Adapted from Virmani et al. Arterioscler. Thromb. Vasc. Biol. 2000;20:1262-1275,

Atherosclerotic plaque may develop at an early age and continue progressing with age. The rate of progression may vary from individual to individual.[15] The probability of a

person with atherosclerosis having a cardiac event is dependent on the number of plaques present and their vulnerability to rupture. Intimal calcifications in the arteries are a result of cellular necrosis, inflammation and lipid dysfunction, which is a distinctive feature of atherosclerotic plaques. The calcifications observed in such plaques are patchy and discontinuous (Figure 1.2 A&C).[16, 17] Cholesterylic lipids and carbonates are found to be embedded in the hydroxyapatite mineral present in intimal calcified plaques.[18]

1.2 Medial Artery Calcification/ Mönckeberg's sclerosis

Medial calcification is morphologically as well as chemically distinct from intimal calcification.[19] It is a common finding in patients with CKD, diabetes and aging. Unlike atherosclerotic calcification, medial calcification is characterised by uniform deposition of amorphous minerals around the medial layer of the blood vessel.[20] This causes stiffening of the arteries which results in systolic hypertension and left ventricular hypertrophy (LVH).[19] Medial arterial calcification is considered to be a strong predictor of cardiovascular events in patients with noninsulin-dependent diabetes mellitus (NIDDM).[21] It has also emerged as a significant predictor of foot amputation in patient with diabetes mellitus type 2.[22] Although hydroxyapatite is present in both intimal and medial plaques, solid state ^{13}C NMR studies have confirmed that there are distinct differences in the spectrum of the mineral from the intimal calcification which shows signals from cholesterol-related compounds, fatty acids, and carbonate substituted into the hydroxyapatite matrix. On the other hand the spectrum obtained from the medial calcification shows signals from fatty acids only.[18]

The process of vascular calcification was previously considered as an irreversible, passive process developed as a result of ageing, but with the advances in various fields of science like electron microscopy, physiology, molecular biology etc. the perception has now changed. Even though the process is not completely understood the process of

calcification is now considered to be a regulated and progressive process with similarities to bone formation.[23-26] It has been established that in uremic conditions vascular smooth muscle cells (VSMC) actively take up calcium and phosphate to form bioapatite.[27]

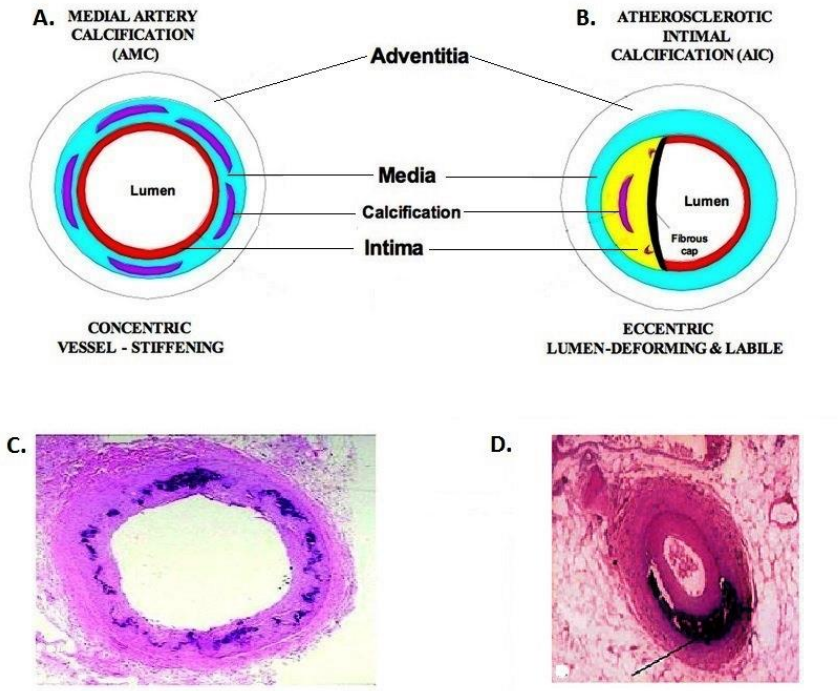

Figure 1.2 A&B: Diagrammatic representation of medial artery calcification and atherosclerotic intimal calcification; **C:** Von-Kossa staining of a peripheral artery with medial calcification. **D:** Von Kossa staining of a section of aorta with atherosclerotic intimal calcification. Towler. IBMS BoneKEy. 2008; 5(2):41-58

1.3 Theories of vascular calcification

Several theories have been put forward to explain the molecular process that leads to vascular calcification. These are outlined in the following sections.

1.3.1 Induction of bone formation/osteogenesis

This hypothesis was advocated by Demer *et al*. According to them the formation of calcification is initiated by osteoblast-type cells. The process is complex and involves the participation of many molecular and cellular signalling processes underlying normal bone

formation.[28, 29] The origin of the osteoblast cells is unclear but studies suggests that stimuli caused by factors such as oxidative stress, bone morphogenetic proteins (BMP) or changes in pyrophosphate levels induce VSMC to undergo phenotypic changes to form osteoblast cells. Demer *et al*. coined the term “calcifying vascular cells” (CVC’s) for an isolated population of smooth muscle cells that spontaneously express genes normally associated with osteoblast differentiation, form nodules and mineralise under long-term *in vitro* culture. During the phenotypic transition the VSMC loses its specific markers such as SM α-actin and SM22α, and gains osteogenic markers like osteopontin (OPN), Cbfa-1/Runx2, alkaline phosphatase (ALP), and osteocalcin.[28-30] *In vitro* studies confirm that an increase in extracellular levels of Ca and P accelerates the process of calcification of VSMCs and the process is mediated by vesicle release.[31] Pericytes, also called Rouget cells after their discoverer, Charles Rouget, are cells associated with capillaries, precapillary arterioles and post-capillary venules. Studies suggest that pericytes present in the vessel wall contribute to vascular calcification. Pericytes share several phenotypic resemblances with CVC’s, including α-SM-actin. *In vitro* studies demonstrate that pericytes form large multicellular nodules containing a mineralised matrix after ≈8 weeks in culture.[32-34] The nodules strongly resemble the matrix found in calcified vessels and express bone-specific markers like osteopontin, matrix Gla protein and osteocalcin. In addition, the presence of hydroxyapatite crystals has also been reported within the nodules. [35, 36]

1.3.2 Loss of inhibition

Most body fluids and organs contain inhibitors of calcium phosphate deposition, which prevent spontaneous mineralisation (Table 1.1). Several such calcification-inhibiting molecules have been identified using mouse mutational analyses. According to this

hypothesis an imbalance or inactivation of these calcification inhibitors would eventually lead to ectopic calcification.

Matrix Gla protein (MGP) belongs to the family of N-terminal γ-carboxylated mineral binding proteins. It is a 10.6 kDa, vitamin K-dependent protein that binds calcium via its glutamic acid (Gla) residues. It acts as a chelator for calcium and inhibits the deposition of calcium phosphate.[37, 38] MGP also regulates bone morphogenetic protein-2 (BMP-2) and helps mediate the clearance of calcium phosphate from the circulation.[39] Studies suggest that MGP is also expressed in lipid-rich layers of human atherosclerotic plaques.[40] Spontaneous calcification of the aorta and cartilage is reported in MGP-null mice.[41] Price *et al.* demonstrated that by administration of warfarin, a vitamin-K antagonist, the γ-carboxylation of MGP can be inhibited. This leads to extensive calcification *in vivo* specific to the media in rats.[42] Fetuin-A, also known as α2-Heremans-Schmid Glycoprotein (Ahsg) is an important circulating inhibitor of calcification. It inhibits the formation of new hydroxyapatite but has no effect on previously formed crystals. Fetuin-A is primarily produced in the liver of adult individuals. It is believed that fetuin-A inhibits vascular calcification in different junctures: (i) It disrupts the death-signalling pathways, and inhibits VSMC apoptosis; (ii) VSMC loads fetuin-A into intracellular vesicles, and prevents nucleation of calcium and phosphate; (iii) It improves the clearance of apoptotic bodies (ABs) from the extracellular matrix by enhancing the binding of ABs to adjacent viable cells. This in turn reduces the amount of free ABs to bind and nucleate calcium and phosphate in the extracellular matrix.[43] Osteopontin (OPN) is an acidic RGD-containing phosphoprotein found only in mineralised tissues such as bones and teeth. OPN is absent in normal arteries, however it has been reported that OPN is abundant at sites of calcification in human atherosclerotic plaques and in calcified aortic valves.[44, 45] OPN regulates calcification by two distinct mechanisms: (i) it

acts as a potent inhibitor of hydroxyapatite crystal formation; (ii) it protects endothelial cells by binding with α5γ3 thereby inhibiting apoptosis.[46-48] Studies show that inactivation of OPN gene in MGP-null mice accelerates the process of calcification.[47, 49]

Inorganic pyrophosphate (PPi) comprises of two phosphate Pi molecules bound by a high energy anhydride bond. Alkaline phosphatase (ALP), a hydrolase enzyme, dephosphorylates PPi to yield inorganic (Pi). The latter is one of the key constituent in hydroxyapatite formation. On the other hand, PPi acts as an inhibitor for vascular calcification because it is a small molecule that binds to nascent hydroxyapatite crystals and prevents further incorporation of inorganic phosphate (Pi) ions into these crystals.[50] It has been demonstrated that exogenous pyrophosphate inhibits aortic calcification in rats that are given large doses of vitamin D_3.[51] Furthermore, deficiency of pyrophosphate generator, ecto-nucleotide pyrophosphatase/ phosphodiesterase-1 (Enpp1) and the pyrophosphate transporter, ankylosis protein (Ank), results in reduced plasma

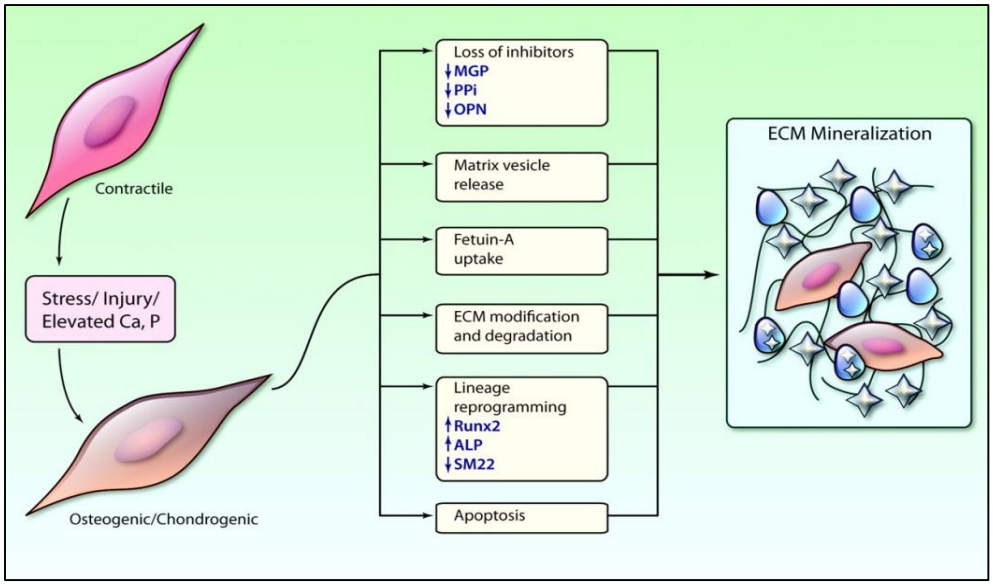

Figure 1.3: VSMC mediated vascular calcification. Diagrammatic representation of various factors involved in the conversion of a VSMC into an osteogenic phenotype, thereby resulting in the deposition of bioapatite in the extracellular matrix. Shanahan et al. Circ Res. 2011;109:697-711

pyrophosphate levels, which leads to extensive arterial calcification in humans[52] and in mice[53].

PPi also prevents VSMC's from undergoing phenotypic changes to osteoblast cells.[54] Lately the role of nucleoside-associated polyphosphates and the purinergic system in the inhibition of vascular calcification has been elucidated. It has been demonstrated that adenosine triphosphate (ATP), the substrate for the aforementioned Enpp1, can inhibit calcium phosphate deposition in two ways: firstly it acts as a source of PPi and secondly as a direct inhibitor when present in the extracellular matrix. [55, 56] The direct inhibition by ATP is elegantly illustrated by the use of a nonhydrolysable ATP species that also manages to completely inhibit calcium and phosphate deposition at the same concentration as hydrolysable ATP.

Table 1.1: Inhibitors of vascular calcification, and their roles in inhibiting biomineralisation.

Inhibitors	Role of the inhibitor
OPN	Stimulates resorption of calcium phosphate crystals. Anchors osteoclasts to minerals and regulates the pH around the ectopic mineralisation sites.
MGP	Binds to calcium and phosphate through the vitamin-K dependent reaction. Binds to BMP-2.
OPG	Functions as a decoy receptor that neutralises the cell-bound and soluble forms of RANKL.
BMP-7	Prevents CKD induced vascular calcifications. Preserves SMC phenotype and reverse the progression towards the osteoblastic phenotype in VSMCs.
Fetuin-A	Solubilises basic calcium phosphate as a colloid and forms calciprotein particles. Antagonises TGFs and BMPs.
Pyrophosphate	Directly blocks hydroxyapatite formation.
Multiple-pass transmembrane protein (ANK)	Acts as a transmembrane transporter that shuttles pyrophosphate between intracellular and extracellular compartments.

Smad proteins are intracellular mediators of signalling initiated by Tgf-βs, activins and BMP. Structurally, Smad6 is different from the other Smad proteins. It inhibits the phosphorylation of Smad1 that is induced by BMP binding to its receptor.[57, 58] Smad6-

null (Madh6$^{-/-}$) mice spontaneously develop calcification in the vessel wall demonstrating that it is an important calcification inhibitor.[59]

1.3.3 Cell death/Apoptosis

Apoptosis is a process of systematic and controlled cell death which is initiated by the activation of endogenous proteases.[60] Cell death is considered to be the primary mechanism of calcification especially in atherosclerotic plaques with large areas of necrotic tissue. During apoptosis, the cell actively disassembles itself and reduces cell size by the formation of phosphatidylserine-containing vesicles, "apoptotic bodies" (ABs).[61] ABs are released into the extracellular matrix in response to cell death. These are the structures that form the nidus for calcification in the vessel wall.[26] It has also been observed that increased rate of apoptosis of VSMCs is one of the mechanisms of vascular calcification as dying cells become highly permeable to calcium and phosphate.[62]

In addition to the ABs matrix vesicles (MVs) are implicated in the pathogenesis of vascular calcification. Traditionally, based on their size and presumed biogenetic pathways, extracellular vesicles (EVs) are broadly classified into: (a) ABs, 800–5,000 nm diameter and released by cells undergoing programmed cell death; (b) MVs, also referred to as shedding MVs, are membranous vesicles (50–1,000 nm diameter) that are produced by budding from the plasma membrane; and (c) exosomes (EXOs), 40–100 nm diameter vesicles considered to be of endocytic origin.[63]

The conventional definition of MVs is that they are small (20-200 nm) lipid bound spherical bodies, which have their origin in plasma membrane of chondrocytes and osteoblasts. Additionally they are associated with hydroxyapatite crystals and act as nucleation sites.[63,64,31] To expound this mechanism further: MVs were found selectively located at sites of initial calcification in cartilage, bone, and predentin. The first crystals

of apatitic bone mineral are formed within MVs close to the inner surfaces of their investing membranes. In the osteogenic literature, matrix vesicle biogenesis occurs by polarised budding and pinching-off of vesicles from specific regions of the outer plasma membranes of differentiating growth plate chondrocytes, osteoblasts, and odontoblasts. Polarised release of MVs into specific zones of developing matrix determines the precise and planned distribution of calcification. Initiation of the first mineral crystals within MVs (phase 1) is facilitated by the activity of MV phosphatases (e.g. alkaline phosphatase, adenosine triphosphatase and pyrophosphatase) and this is augmented by calcium-binding molecules (e.g. annexin I and phosphatidyl serine), all associated with the MV membrane. Phase 2 of biologic mineralisation begins with crystal release through the MV membrane, exposing preformed hydroxyapatite crystals to the extracellular fluid. The extracellular fluid is conducive to the crystal expansion, having sufficient Ca^{2+} and $(PO_4)^{3-}$, with preformed crystals serving as the foundation for the formation of new crystals by a process of homologous nucleation. The precipitation of calcium-phosphate crystals, occur in the extracellular matrix of the vasculature (Figure 1.3).

This knowledge from the field of osteology was translated and explored in the vascular paradigm. MVs released by VSMCs under quotidian conditions do not calcify, being armed with inhibitors like MGP and Fetuin A. On the other hand, MVs released under uremic stress behave akin to their counterparts discharged by bone and cartilage sources.[31] Recent studies have questioned the origin of MVs as being the plasma membrane. The exosomal pathway with multivesicular bodies being intermediaries may more likely play a role in the formation, packaging and release of MVs.[64]

1.4 Clinical importance of vascular calcification

Diabetes is one of the leading causes of chronic kidney disease (CKD) and patients suffering from CKD have a high risk of fatal cardiovascular complications resulting from

vascular calcification.[65, 66] In comparison with the general population, patients with CKD are at a 40 fold higher risk of death due to cardiovascular disease.[67] Atherosclerotic plaques are a common finding in patients with CKD, diabetes and hypertension. They block the myocardial coronary artery reducing the blood supply to the myocardium and causing ischemic heart disease. Rupture of vulnerable atherosclerotic plaque causes fatal cardiac and cerebral infarction and thrombosis. The common cause of plaque rupture is an increase in biomechanical stress and disruption in the fibrous cap.[68] Although there is a correlation between the amount of calcification and the stage and extent of atherosclerosis, its role in plaque rupture is unclear and the views are divided.[29, 69] A study done by Ehara *et al*. using intravascular ultrasound (IVUS) in a population of 178 patients (61 with acute myocardial infarction, 70 with unstable angina, and 47 with stable angina) concluded that presence of "spotty calcification" increases the probability of plaque rupture and plaque erosion.[70] According to some studies, stress induced by microcalcification in thin fibrous cap promotes plaque rupture,[68] whereas other studies show that calcification of atherosclerotic plaques has no impact on biomechanical stress, hence does not play any role in plaque rupture. It is rather believed that calcification provides structural stability to the plaque, thus they are less prone to rupture. [68, 71, 72]

Medial arterial calcification does not cause any obstruction in the blood circulation; however it affects the haemodynamics differently. It is a common finding in patients with diabetes mellitus, albuminuria and hypertension.[73, 74] Often it is considered as an inconsequential finding but studies show that it is a predictive marker for cardiovascular events.[22] Medial arterial calcification results in vascular stiffness. The speed of propagation of arterial pressure waves through the arterial tree is termed pulse wave velocity (PWV). Pulse wave analysis using Doppler US and MRI is used to measure aortic stiffness.[75] This increased pulse wave velocity results in decreased diastolic blood-

pressure and increased systolic blood pressure.[76] These changes lead to left ventricular hypertrophy,[47] which is highly associated with mortality in patients with cardiovascular disease. Medial arterial calcification also leads to cutaneous necrosis caused by calcific uremic arteriolopathy (calciphylaxis).

Over the last decade the perspective that calcification is a passive process has evolved and now scientific community is in an agreement that it is an active and regulated process. Vascular calcification is a multifaceted disease which involves various tightly regulated processes contributing to the pathology.

References

1. Abedin M, Tintut Y, Demer LL. Vascular calcification - Mechanisms and clinical ramifications. *Arterioscler Thromb Vasc Biol.* 2004;24(7):1161-1170.

2. Kapustin AN, Davies JD, Reynolds JL, et al. Calcium Regulates Key Components of Vascular Smooth Muscle Cell-Derived Matrix Vesicles to Enhance Mineralization. *Circ Res.* 2011;109(1):E1-U41.

3. Rennenberg RJ, Kessels AG, Schurgers LJ, et al. Vascular calcifications as a marker of increased cardiovascular risk: a meta-analysis. *Vasc Health Risk Manag.* 2009;5(1):185-197.

4. Iribarren C, Sidney S, Sternfeld B, et al. Calcification of the aortic arch: Risk factors and association with coronary heart disease, stroke, and peripheral vascular disease. *JAMA.* 2000;283(21):2810-2815.

5. Shaw LJ, Raggi P, Schisterman E, et al. Prognostic Value of Cardiac Risk Factors and Coronary Artery Calcium Screening for All-Cause Mortality. *Radiology.* 2003;228(3):826-833.

6. Kondos GT, Hoff JA, Sevrukov A, et al. Electron-Beam Tomography Coronary Artery Calcium and Cardiac Events: A 37-Month Follow-Up of 5635 Initially Asymptomatic Low- to Intermediate-Risk Adults. *Circulation.* 2003;107(20):2571-2576.

7. Raggi P. The use of electron-beam computed tomography as a tool for primary prevention. *Am. J. Cardiol.* 2001;88(7B):28J-32J.

8. Mendis S, Puska P, Norrving B, World Health Organization., World Heart Federation., World Stroke Organization. *Global atlas on cardiovascular disease prevention and control*. Geneva: World Health Organization in collaboration with the World Heart Federation and the World Stroke Organization; 2011.

9. World Health Organization. *Global health risks : mortality and burden of disease attributable to selected major risks*. Geneva, Switzerland: World Health Organization; 2009.

10. Tamashiro M, Iseki K, Sunagawa O, et al. Significant association between the progression of coronary artery calcification and dyslipidemia in patients on chronic hemodialysis. *Am J Kidney Dis.* 2001;38(1):64-69.

11. Moe SM, Chen NX. Pathophysiology of vascular calcification in chronic kidney disease. *Circ Res.* 2004;95(6):560-567.

12. Duer MJ, Friscic T, Proudfoot D, et al. Mineral Surface in Calcified Plaque Is Like That of Bone Further Evidence for Regulated Mineralization. *Arterioscl Throm Vas.* 2008;28(11):2030-2208.

13. Ledley RS, Park CM, Ray RD. Application of the ACTA-scanner to visualization of the spine. *Comput Tomogr.* 1979;3(1):57-69.

14. Ross R. Atherosclerosis is an inflammatory disease. *Am Heart J.* 1999;138(5 Pt 2):S419-420.

15. Mackay J, Mensah GA, Mendis S, et al. World Health Organization. *The atlas of heart disease and stroke*. Geneva: World Health Organization; 2004.

16. Schoppet M, Shroff RC, Hofbauer LC, et al. Exploring the biology of vascular calcification in chronic kidney disease: What's circulating? *Kidney Int.* 2008;73(4):384-390.

17. Towler DA. Vascular calcification: a perspective on an imminent disease epidemic. *IBMS BoneKEy.* 2008;5(2):41-58.

18. Reid DG, Shanahan CM, Duer MJ, et al. Lipids in biocalcification: contrasts and similarities between intimal and medial vascular calcification and bone by NMR. *J Lipid Res.* 2012;53(8):1569-1575.

19. Amann K. Media calcification and intima calcification are distinct entities in chronic kidney disease. *Clin J Am Soc Nephrol.* 2008;3(6):1599-1605.

20. Nakamura S, Ishibashi-Ueda H, Niizuma S, et al. Coronary calcification in patients with chronic kidney disease and coronary artery disease. *Clin J Am. Soc Nephrol.* 2009;4(12):1892-1900.

21. Niskanen L, Siitonen O, Suhonen M, et al. Medial Artery Calcification Predicts Cardiovascular Mortality in Patients With NIDDM. *Diabetes Care.* 1994;17(11):1252-1256.

22. Lehto S, Niskanen L, Suhonen M, et al. Medial Artery Calcification: A Neglected Harbinger of Cardiovascular Complications in Non–Insulin-Dependent Diabetes Mellitus. *Arterioscler Thromb Vasc Biol.* 1996;16(8):978-983.

23. Tyson KL, Reynolds JL, McNair R, et al. Osteo/chondrocytic transcription factors and their target genes exhibit distinct patterns of expression in human arterial calcification. *Arterioscler Thromb Vasc Biol.* 2003;23(3):489-494.

24. O'Brien KD, Kuusisto J, Reichenbach DD, et al. Osteopontin is expressed in human aortic valvular lesions. *Circulation.* 1995;92(8):2163-2168.

25. Shanahan CM, Cary NR, Salisbury JR, et al. Medial localization of mineralization-regulating proteins in association with Monckeberg's sclerosis: evidence for smooth muscle cell-mediated vascular calcification. *Circulation.* 1999;100(21):2168-2176.

26. Proudfoot D, Skepper JN, Hegyi L, et al. Apoptosis regulates human vascular calcification in vitro: evidence for initiation of vascular calcification by apoptotic bodies. *Circ Res.* 2000;87(11):1055-1062.

27. Floege J, Ketteler M. Vascular calcification in patients with end-stage renal disease. *Nephrol Dial Transplant.* 2004;19 (5):V59-66.

28. Demer LL. A skeleton in the atherosclerosis closet. *Circulation.* 1995;92(8):2029-2032.

29. Bostrom K, Watson KE, Horn S, et al. Bone morphogenetic protein expression in human atherosclerotic lesions. *J Clin Invest.* 1993;91(4):1800-1809.

30. Hruska KA, Mathew S, Saab G. Bone morphogenetic proteins in vascular calcification. *Circ Res.* 2005;97(2):105-114.

31. Reynolds JL, Joannides AJ, Skepper JN, et al. Human vascular smooth muscle cells undergo vesicle-mediated calcification in response to changes in extracellular calcium and phosphate concentrations: a potential mechanism for accelerated vascular calcification in ESRD. *J Am Soc Nephrol* 2004;15(11):2857-2867.

32. Doherty MJ, Ashton BA, Walsh S, et al. Vascular Pericytes Express Osteogenic Potential In Vitro and In Vivo. *J Bone Miner. Res.* 1998;13(5):828-838.

33. Schor AM, Allen TD, Canfield AE, et al. Pericytes derived from the retinal microvasculature undergo calcification in vitro. *J Cell Sci.* 1990 1990;97(3):449-461.

34. Brighton CT, Lorich DG, Kupcha R, et al. The pericyte as a possible osteoblast progenitor cell. *Clin Orthop Relat Res.* 1992(275):287-299.

35. Tilton RG. Capillary pericytes: perspectives and future trends. *J Electron Microsc Tech.* 1991;19(3):327-344.

36. Johnson RC, Leopold JA, Loscalzo J. Vascular calcification: pathobiological mechanisms and clinical implications. *Circ Res.* 2006;99(10):1044-1059.

37. Luo GB, Ducy P, McKee MD, et al. Spontaneous calcification of arteries and cartilage in mice lacking matrix GLA protein. *Nature.* 1997;386(6620):78-81.

38. Rezg R, Barreto FC, Barreto DV, et al. Inhibitors of vascular calcification as potential therapeutic targets. *J Nephrol.* 2011;24(4):416-427.

39. Zebboudj AF, Shin V, Bostrom K. Matrix GLA protein and BMP-2 regulate osteoinduction in calcifying vascular cells. *J Cell Biochem.* 2003;90(4):756-765.

40. Shanahan CM, Cary NR, Metcalfe JC, et al. High expression of genes for calcification-regulating proteins in human atherosclerotic plaques. *J Clin Invest.* 1994;93(6):2393-2402.

41. Luo G, Ducy P, McKee MD, et al. Spontaneous calcification of arteries and cartilage in mice lacking matrix GLA protein. *Nature.* 1997;386(6620):78-81.

42. Price PA, Faus SA, Williamson MK. Warfarin-induced artery calcification is accelerated by growth and vitamin D. *Arterioscler Thromb Vasc Biol.* 2000;20(2):317-327.

43. Reynolds JL, Skepper JN, McNair R, et al. Multifunctional roles for serum protein fetuin-a in inhibition of human vascular smooth muscle cell calcification. *J Am Soc Nephrol.* 2005;16(10):2920-2930.

44. O'Brien ER, Garvin MR, Stewart DK, et al. Osteopontin is synthesized by macrophage, smooth muscle, and endothelial cells in primary and restenotic human coronary atherosclerotic plaques. *A Arterioscler Thromb Vasc Biol.* 1994;14(10):1648-1656.

45. O'Brien KD, Kuusisto J, Reichenbach DD, et al. Osteopontin Is Expressed in Human Aortic Valvular Lesions. *Circulation.* 1995 1995;92(8):2163-2168.

46. Lomashvili KA, Cobbs S, Hennigar RA, et al. Phosphate-induced vascular calcification: role of pyrophosphate and osteopontin. *J Am Soc Nephrol.* 2004;15(6):1392-1401.

47. Giachelli CM, Speer MY, Li X, et al. Regulation of Vascular Calcification: Roles of Phosphate and Osteopontin. *Circulation Research.* 2005;96(7):717-722.

48. Scatena M, Almeida M, Chaisson ML, et al. NF-kappaB mediates alphavbeta3 integrin-induced endothelial cell survival. *J Cell Biol.* 1998;141(4):1083-1093.

49. Speer MY, McKee MD, Guldberg RE, et al. Inactivation of the osteopontin gene enhances vascular calcification of matrix Gla protein-deficient mice: evidence for

osteopontin as an inducible inhibitor of vascular calcification in vivo. *J Exp Med.* 2002;196(8):1047-1055.

50. Meyer JL. Can biological calcification occur in the presence of pyrophosphate? *Arch Biochem Biophys.* 1984;231(1):1-8.

51. Schibler D, Russell RG, Fleisch H. Inhibition by pyrophosphate and polyphosphate of aortic calcification induced by vitamin D3 in rats. *Clin Sci.* 1968;35(2):363-372.

52. Rutsch F, Vaingankar S, Johnson K, et al. PC-1 nucleoside triphosphate pyrophosphohydrolase deficiency in idiopathic infantile arterial calcification. *Am J Pathol* 2001;158(2):543-554.

53. Ho AM, Johnson MD, Kingsley DM. Role of the mouse ank gene in control of tissue calcification and arthritis. *Science.* 2000;289(5477):265-270.

54. Fleisch H, Russel RGG, Strauman.F. Effect of Pyrophosphate on Hydroxyapatite and Its Implications in Calcium Homeostasis. *Nature.* 1966;212(5065):901-903.

55. Villa-Bellosta R, Sorribas V. Prevention of Vascular Calcification by Polyphosphates and Nucleotides. *Circ J.* 2013 ;77(8):2145-51.

56. Fish RS, Klootwijk E, Tam FW, et al. ATP and arterial calcification. *Eur J Clin. Invest.* 2013;43(4):405-412.

57. Hata A, Lagna G, Massague J, et al. Smad6 inhibits BMP/Smad1 signaling by specifically competing with the Smad4 tumor suppressor. *Genes Dev.* 1998;12(2):186-197.

58. Imamura T, Takase M, Nishihara A, et al. Smad6 inhibits signalling by the TGF-[beta] superfamily. *Nature.* 1997;389(6651):622-626.

59. Galvin KM, Donovan MJ, Lynch CA, et al. A role for smad6 in development and homeostasis of the cardiovascular system. *Nature Genet.* 2000;24(2):171-174.

60. Thompson CB. Apoptosis in the pathogenesis and treatment of disease. *Science.* 1995;267(5203):1456-1462.

61. Henson PM, Bratton DL, Fadok VA. Apoptotic cell removal. *Curr Biol.* 2001;11(19):R795-805.

62. Clarke MC, Littlewood TD, Figg N, et al. Chronic apoptosis of vascular smooth muscle cells accelerates atherosclerosis and promotes calcification and medial degeneration. *Circ Res.* 2008;102(12):1529-1538.

63. Kalra H, Simpson RJ, Ji H, et al. Vesiclepedia: a compendium for extracellular vesicles with continuous community annotation. *PLoS Biol.* 2012;10(12):e1001450.

64. Kapustin AN, Chatrou ML, Drozdov I, et al. Vascular Smooth Muscle Cell Calcification is Mediated by Regulated Exosome Secretion. *Circ Res.* Feb 23 2015.

65. Virgolini I, Angelberger P, Li SR, et al. Indium-111-labeled low-density lipoprotein binds with higher affinity to the human liver as compared to iodine-123-low-density-labeled lipoprotein. *J Nucl Med.* 1991;32(11):2132-2138.

66. Foley RN, Parfrey PS, Sarnak MJ. Clinical epidemiology of cardiovascular disease in chronic renal disease. *Am J Kidney Dis.* 1998;32(5 Suppl 3):S112-119.

67. Sarnak MJ, Levey AS. Cardiovascular disease and chronic renal disease: a new paradigm. *Am J Kidney Dis.* 2000;35(4 Suppl 1):S117-131.

68. Huang H, Virmani R, Younis H, et al. The impact of calcification on the biomechanical stability of atherosclerotic plaques. *Circulation.* 2001;103(8):1051-1056.

69. Wexler L, Brundage B, Crouse J, et al. Coronary artery calcification: pathophysiology, epidemiology, imaging methods, and clinical implications. A statement for health professionals from the American Heart Association. Writing Group. *Circulation.* 1996;94(5):1175-1192.

70. Ehara S, Kobayashi Y, Yoshiyama M, et al. Spotty calcification typifies the culprit plaque in patients with acute myocardial infarction: an intravascular ultrasound study. *Circulation.* 2004;110(22):3424-3429.

71. Nandalur KR, Baskurt E, Hagspiel KD, et al. Calcified Carotid Atherosclerotic Plaque Is Associated Less with Ischemic Symptoms Than Is Noncalcified Plaque on MDCT. *AJR Am J Roentgenol.* 2005;184(1):295-298.

72. Otsuka F, Finn AV, Virmani R. Do vulnerable and ruptured plaques hide in heavily calcified arteries? *Atherosclerosis.* 2013;229(1):34-37.

73. Psyrogiannis A, Kyriazopoulou V, Vagenakis AG. Medial arterial calcification is frequently found in patients with microalbuminuria. *Angiology.* 1999;50(12):971-975.

74. Abou Hassan N, D'Orsi ET, D'Orsi CJ, et al. The Risk for Medial Arterial Calcification in CKD. *J Am Soc Nephrol.* 2011;7(2):275-279.

75. Stoner L, Young J.M, and Fryer S. Assessments of Arterial Stiffness and Endothelial Function Using Pulse Wave Analysis. *Intl J Vasc Med.* 2012; 2012:903107.

76. Dao HH, Essalihi R, Bouvet C, et al. Evolution and modulation of age-related medial elastocalcinosis: impact on large artery stiffness and isolated systolic hypertension. *Cardiovas Res.* 2005;66(2):307-317.

Chapter 2: Application of medical imaging in detection of vascular calcification: a review.

2.1 Introduction

Medical imaging plays a crucial role in screening of patients and determining the type and extent of any disease. It is extremely important for patient management, observing disease progression and the outcome of treatment. Diagnostic clinical imaging provides physicians with the facility of evidence based treatment for diseases which in turn is helpful in improving the prognosis. Medical imaging modalities have also become an indispensable tool in drug research.[1, 2]

The discovery of x-rays by W.C. Röntgen in 1895 gave birth to the field of *in vivo* medical imaging. However, the major developments in the field of medical imaging have taken place in the last 50 years with the invention of various imaging modalities including radionuclide imaging, ultrasonography, CT, MRI, digital radiography etc.

2.2 Conventional X-ray imaging and fluoroscopy

Plain X-ray imaging is the oldest and most widely available medical imaging tool. It is a transmission-based imaging technique wherein X-rays from a source are allowed to pass through a patient on to a film or a detector to create an image. Based on the density and attenuation of different organs, a 2-dimensional (2D) image of different intensities is obtained on a photographic film. It is a relatively inexpensive and simple procedure hence used in various clinical studies. Plain radiographs provide a qualitative assessment of vascular calcification. Plain X-ray has been successfully used to detect vascular calcification *in vivo*. (See Table- 2.1). Kauppila et al. assessed the severity, location and progression of lumbar aortic calcification in a baseline X-ray image of 617 cardiac patients, with follow up after 25 years, to develop a severity score. They proposed a

grade for severity which was scaled from 0-24 depending on the number of foci and extent of calcification. They concluded that the score could successfully identify patients vulnerable to fatal cardiovascular events.[3] Using the same severity scoring system Wilson et al. conducted a study on the lateral lumbar radiograms of a larger cohort of patients (1049 males and 1466 females; mean age 61 years). They concluded that X-rays detect the presence of calcification in the abdominal aorta and are an independent predictor of vascular morbidity and mortality.[4] In yet another study London et al. used radiograms of the pelvis and thighs of 202 end stage renal disease (ESRD) patients who had been on dialysis for more than a year to confirm the presence of medial and intimal calcification.[5] A simple vascular calcification scoring system (SVCS) to predict the probability of cardiovascular event in patients with ESRD was devised by Adragão et al.[6] Using the same scoring system complimented with a Doppler device to measure pulse wave velocity (PWV), pulse pressure (PP) and ankle brachial index (ABI) Adragão et al. demonstrated that SVCS and ABI are associated with vascular calcification and mortality in ESRD patients undergoing haemodialysis. However, plain X-ray radiography does not provide a 3D view of organs, hence offers a restricted view of the affected organs.

Fluoroscopic cardiac angiography is widely used for the diagnosis of obstructive coronary artery disease. It uses continuous X-rays which are passed through the patient into a fluorescent screen to obtain real time dynamic images of the heart. Based on how the x-ray images are obtained, there are two types of fluoroscopy machines currently in use:

2.1.1 Image intensifier: This was designed and developed in the 1950's. X-rays pass through the patient and fall onto a fluorescent screen coupled to a television system which enables real time imaging of dynamic processes.

Table 2.1: Studies published by various research groups demonstrating the successful use of X-ray imaging in detecting vascular calcification.

Study and year	No. of patients	Radiograms used
Niskanen et al.1990[7]	277 [133 diabetic (70M and 63F) + 144 non-diabetic individuals (62M and 82F).]	Chest, abdomen and legs
Kauppila et al. 1997[3]	617 (217M and 400F) Framingham Heart Study participants.	Lumbar
Wilson et al. 2001[4]	2515 (1049M and 1466F) Framingham Heart Study participants.	Lumbar
London et al. 2003[5]	202 ESRD patients on haemodialysis (HD) for at least 1 year.	Pelvis and thigh
Adragão et al. 2004[6]	123 (75M and 48F) HD patients.	Pelvis and hands
Adragão et al. 2009[8]	101 (71 M and 30F) HD patients	Pelvis and hands
Adragão et al. 2011[9]	219 HD patients	Abdomen, pelvis and hands

An image intensifier consists of a large vacuum tube with an input phosphor layer followed by a photocathode layer, an array of focusing electrodes and an output phosphor layer. In the past 6 decades image intensifiers have gone through several technological modifications, including increase in the field of view, replaced camera tubes with charged coupled devices (CCD's) and replacing television systems with liquid crystal display (LCD) monitors. Despite many improvements being incorporated it still has disadvantages which include its bulk and requirement for a high vacuum and voltage sensitivity.[10]

2.1.2 Flat-panel-detector (FPD): FPD is a recent development and is currently favoured equipment in the cardiac catheterisation laboratory. In FPD machines the vacuum tube is replaced by an indirect solid state system which uses thallium (Tl) activated caesium iodide (CsI) crystals as detectors. It also lacks the requirement of a television camera to produce images on the monitor. Hence this equipment is much smaller and more compact compared to an image intensifier device providing it with flexibility in positioning

while imaging patients. The main drawback is the high cost, restricting its use for general purposes.[10]

Several experimental studies have been conducted comparing the sensitivity and specificity of fluoroscopy in detecting coronary artery calcification. The method of calculating the sensitivity and specificity of a clinical study has been illustrated in Table 2.2 and 2.3. Table 2.4 represents the findings by various groups, which suggest that fluoroscopy is sensitive in detecting coronary artery calcification.

Table 2.2: Possible outcomes of a clinical study.

		Diseased subject	**Non Diseased (Normal)**	**Test Total**
Test Result	**Positive (Number)**	True positive (A)	False positive (B)	Test positive (A+B)
	Negative (Number)	False negative (C)	True negative (D)	Test negative (C+D)
	Total	Total Diseased (A+C)	Total Normal (B+D)	

Table 2.3: Formula used to calculate the sensitivity, specificity, positive and negative predictive values using the outcomes of a study. (As mentioned in Table 2.2) [11-13]

Parameter	**Formula**
Sensitivity: the ability of a test to correctly diagnose an individual as diseased.	$\frac{A}{A+C} \times 100$
Specificity: The ability of the test to correctly identify those patients without the disease.	$\frac{D}{B+D} \times 100$
Positive predictive value: It is the % measure to determine how many of the test positives are true positives.	$\frac{A}{A+B} \times 100$
Negative predictive value: Is the converse of positive predictive value.	$\frac{D}{C+D} \times 100$

Agatston et al. reported a study conducting ultrafast CT on 584 subjects out of which 50 patients with previous history of CAD underwent fluoroscopy too. They concluded that angiography demonstrated that only 52% of calcific deposits were detected by

fluoroscopy whereas the sensitivity of ultrafast CT was found to be 90%.[14] Heussel et al. compared the findings from 40 patients that underwent coronary angiography, spiral CT and fluoroscopy. They concluded that spiral CT had a positive predictive value of 83% in detecting coronary artery calcification, whereas the positive predictive value of fluoroscopy was only 50%.[15]

Table 2.4: Sensitivity and specificity of coronary angiography in detecting calcification as published by various groups.

Reference	Patients (n)	Sensitivity (%)	Specificity (%)
Bartel et al. [16]	360	56	95
Hamby et al. [17]	500	76	78
Bierner et al. [18]	436	57	92
Aldrich et al. [19]	181	66	52
Margolis et al. [20]	800	40	93
Hung et al. [21]	92	79	83
Detrano et al. [22]	301	67	81
Uretsky et al. [23]	600	65	85

Fluoroscopic coronary angiography has several disadvantages, firstly it is user dependent and relies on the skill and experience of the operator, and secondly it cannot be used for quantification. Coronary angiography is an invasive procedure requiring contrast media to be injected into the coronary artery via a long catheter. The catheters are usually inserted through the right femoral artery. Occasionally brachial or radial arteries may be used as the site of insertion. There are several serious risks associated with the procedure of catheterisation and also from the dyes used. The minor ones include the risks of bleeding, infection, and pain at the site of catheter insertion. Although rare, serious and life threatening complications like allergic reaction from the dye, renal failure, embolism, stroke and serious injury to vasculature have also been reported.[24, 25]

2.3 Computed tomography (CT)

CT is a commonly performed imaging modality. In the past three decades the use of CT in medical diagnostics has grown exponentially, with more than 70 million scans performed in the year 2007 in United States only. CT scans of the chest contribute to a majority of the CT scans performed as it has become a routine practice for the management of patients with cardiac diseases and pulmonary embolism.[26] It is considered as the gold standard for non-invasive imaging and quantification of vascular calcifications.[27] It is also used in assessing disease progression as well as monitoring response to therapy.

The first CT machine, also known as the EMI (named after the company British EMI Corp.) device was invented by Godfrey Hounsfield in the early 1970's. It was a dedicated head scanner, which used a water-filled box to rest the patient's head and was presented at a British Radiological Society meeting in 1972.[28] In 1974, the second generation CT machine with whole body scanning capability was developed and installed by Ledley et al. at Georgetown University.[29] Rapid developments took place and by 1976 the third and fourth generations of CT were invented which had better scanning properties.[28] Hounsfield along with mathematician Allan Cormack won the Nobel Prize in 1979 for their pioneering work. The advantage of CT is that it provides high resolution images obtained as slices (tomography) which resolves the problem of superimposition of organs that is often encountered in other planar projection-based imaging modalities.

2.3.1 Conventional CT or single slice computed tomography (SSCT):

Computed tomography has significant advantages over fluoroscopy in imaging coronary artery calcification. It is a non-invasive imaging modality that is comparatively easy to perform and has no life-threatening risks associated with it. CT scans of the chest and coronary angiograms of 27 patients evaluated by Timins et al. showed that the sensitivity

of CT in detecting coronary artery calcification in patients with significant coronary artery disease (CAD) was 78%, 63% and 16% for the left anterior descending (LAD), left circumflex (LCX), and the right coronary artery (RCA) respectively. The specificities were 78%, 80%, and 100%, and positive predictive values were 88%, 83%, and 100%.[30] In another study 161 patients (135 male and 26 female) diagnosed with CAD by coronary angiography underwent CT scanning. Coronary calcium on CT was detected in 108 patients out of which 90% had clinically significant coronary stenosis (>75%) on angiography. Out of 205 stenotic arteries, CT detected calcification in 133 vessels with an overall sensitivity of CT in detecting coronary calcium was 65%.[13] Heussel et al. compared the sensitivity and specificity of spiral CT and fluoroscopy in detecting coronary artery calcification in a cohort of 40 patients (33 male and 7 female) out of which 19 patients were suffering from a stenosis ≥75 %. The patients underwent spiral CT, coronary angiography, and fluoroscopy. They concluded that spiral CT was superior to fluoroscopy in detecting coronary calcium with a sensitivity of 100% and specificity of 33%.[15] Although conventional CT is more sensitive than fluoroscopy in detecting coronary artery calcification, it has serious limitations of slow scan time and motion artefacts.

2.3.2 Electron beam computed tomography (EBCT):

To image the heart with conventional CT is a challenge as it requires ultrafast scan time in order to overcome motion artefacts. EBCT was developed in the 1984 to overcome the drawbacks of conventional CT. Unlike a conventional CT machine that uses a rotating X-ray tube the EBCT has no moving parts. Instead it allows an electron beam to bombard a stationary tungsten target placed at 210° in the gantry to produce a rotating fan of X-rays. It permits a very rapid scan time and serial transaxial images with a thickness of 3-6 mm are obtained in 100 ms.[31] To image the whole heart, 40-50 slices of images are

acquired with patient holding breath for 30-40 seconds. Originally known as cine or ultrafast CT, the term EBCT is now used to distinguish it from conventional CT scans because modern multi-detector scanners are also capable of ultrafast scanning. EBCT systems are equipped with quantitative software that enables the quantification of calcified regions.

The first study that reported the use of EBCT in detecting coronary artery calcification was published by Tanenbaum et al. A cohort of 54 patients (36 male and 18 female) was used, out of which 43 patients were diagnosed with significant CAD by coronary angiography. They determined that the sensitivities for 1-, 2-, 3-vessel disease and left main artery disease were 82%, 89%, 92% and 100% respectively.[32] In 1994, Agatston et al. formulated the first quantification system for coronary calcium using EBCT. A total of 584 patients (out of which 409 were male and 175 female) were used in the study. [109] patients had CAD established either by coronary angiography (>50% luminal narrowing) or a history of myocardial infarction and the remaining 475 test subjects had no history of CAD. They derived a calcium scoring system based on Hounsfield units (HU) and area of a calcific lesion. Hounsfield units are a unit measure that represents the different density levels of tissues.[28] Calcium score of 1 was designated to any lesion with ≥1mm2 in size and HU of 130-199 and similarly 2 = 200-299, 3 = 300-399 and 4 = 400-499. The sensitivity, specificity and predictive values for clinical CAD were calculated for calcium scores in each decade. A sensitivity of 71% and 74% and a specificity of 91% and 70%, respectively, were obtained in subjects of age groups 40 to 49 and 50 to 59 years, and total calcium score of 50. They also compared the findings of EBCT with fluoroscopy and concluded that EBCT was superior in detecting coronary calcium.[14] A correlative study was conducted on 38 dissected coronary arteries by Rumberger et al. They concluded that the histologic findings had a strong correlation with calcium scoring.[33] Similar

conclusions were reached by Denzel et al. from a study in which they compared calcium score generated by CT in comparison to sonography and histology in 92 carotid artery endarterectomy specimens.[34]

2.3.3 Multi-slice computed tomography (MSCT) or Multi-detector computed tomography (MDCT):

Although EBCT has proved to be a successful non-invasive imaging modality, it does have some limitations. EBCT is expensive equipment dedicated for cardiac imaging, hence found only in selected hospitals. MDCT employs an x-ray tube and a detector assembly which revolves around the patient to obtain images. One advantage of modern MDCT over conventional CT is scan speed. With a modern MDCT scanner up to 320 simultaneous sections with a thickness of 1.5 – 0.6 mm can be obtained in every rotation, hence reducing the time of the procedure.[35, 36] Due to its ability to obtain high resolution images in a relatively short time it has, has replaced EBCT and is currently *in vivo* imaging of vascular calcification. It is now considered as the gold standard for evaluating the degree of arterial stenosis and has a very high (95-100%) negative predictive value for CAD.[36, 37] Oto et al. performed a comparative study between multi detector computed tomography (MDCT) and digital angiography for the assessment of lower extremity arterial occlusive disease. They concluded that the sensitivity, specificity and accuracy of MDCT in detecting mild calcifications are more than 99%.[38] Coronary computed tomographic angiography (CCTA) using a 16-MDCT scanner can detect CAD in patients with high sensitivity and specificity without pharmacologic manipulation of patient heart rates.[39] In comparison to 16 slice CCTA, 64-slice CCTA provides improved temporal resolution and spatial resolution which allows optimal three-dimensional visualisation of the variable and complex anatomy of coronary arteries.[40]

In a cohort of 230 individuals without CAD, Budoff et al. assessed the diagnostic accuracy of electrocardiographically-gated 64-multidetector row coronary computed tomographic angiography (CCTA). They concluded that the sensitivity, specificity, and positive and negative predictive values of 64 slice CT to detect ≥50% stenosis were 95%, 83%, 64%, and 99%, respectively.[41] The use of 128 slice CT for CCTA instead of 64 slice CT reduces the acquisition time and radiation dose significantly.[42, 43] More recently, 256 and 320 slice CT has been introduced and has been successfully used as a non-invasive diagnostic tool for CAD. The advantages of these machines over their predecessors are faster acquisition time, improved planar as well as 3-D image quality and more importantly significant reduction in radiation dose.[44, 45]

2.4 Intravascular ultrasonography (IVUS)

With the advances in catheter technology and ultrasound imaging, a new modality of imaging IVUS has been developed. IVUS utilises transducers mounted on the tips of catheters to obtain cross-sectional images of the coronary arteries during cardiac catheterization. It provides information about the lumen of the artery and the thickness and tissue characteristics of the arterial wall. There are two types of IVUS imaging catheter systems: (i) rotational and (ii) phased array. Rotational IVUS catheters are armed with a single transducer rotated at 1800 rotations per minute (RPM) operating at up to 9-45 MHz. Phased array catheters on the other hand have no mechanical parts, instead they have an electronically-scanned 64 element array transducer operating in the 20 MHz range.[46]

The earliest studies to detect coronary artery calcification were published by Mintz et al. IVUS and fluoroscopy was performed on 110 patients (84 male, 26 female) undergoing transcatheter therapy for symptomatic CAD. They concluded that calcification was detected only in 48% of the patients whereas IVUS could detect calcification in 76% of

the test subjects.[47] In another study by the same group, they investigated 1155 lesion in 1117 test subjects with IVUS as well as angiography. Out of the 1155 lesions IVUS detected calcium in 841 (P<0.0001 versus angiography) as compared to 440 detected by angiography.[48] Similar finding was reported by Tuzcu et al. who concluded that IVUS is more sensitive in detecting coronary artery calcification than angiography. Studies also show that IVUS can be used to identify fibrofatty plaque and positive remodelling.[49] A recent development in this field has been the combination (IVUS) and intravascular photoacoustic (IVPA) imaging, which facilitates the assessment of plaque morphology and composition.[50] As opposed to other imaging modalities like CT and MRI, IVUS finds a limited use in clinical practice because of its disadvantages. It is expensive and it visualises only a limited portion of the coronary tree and is an invasive modality performed only in conjunction with coronary angiography.

Table 2.5: Advantages and drawbacks of various anatomic imaging tools.

Imaging modality	**Advantages**	**Drawbacks**
X-ray	Inexpensive and easily available modality	Does not provide 3D images Quantification is not possible Poor sensitivity Use of ionising radiation Does not provide molecular information
Fluoroscopy	Gold standard for diagnosing obstructive CAD	Invasive Use of ionising radiation Does not provide molecular information
CT	Gold standard for *in vivo* quantification of calcification Allows high resolution 3D imaging of organ system	Fails to detect micro-calcifications Does not provide molecular information
IVUS	Real time high resolution imaging Allows assessment of total vessel lumen	Invasive Restricted FOV User dependent Risk of infection and plaque rupture

2.5 Molecular imaging

Molecular imaging is an emerging field which utilises a multidisciplinary approach to visually depict and quantify biological/biochemical processes. The above mentioned imaging techniques CT, X-ray and ultra-sonography are modalities that screen the anatomical changes in an organ and do not provide any information of changes at the molecular, cellular and sub-cellular level. Anatomical changes are late manifestations of the molecular processes that truly underlie diseases. These changes are often irreversible damages occurred due to the progression of disease. The modern approach is to target the molecular processes that cause a disease to diagnose the disease early thereby greatly improving the prognosis.

A range of molecular imaging probes that target cellular processes or markers of specific disease have been developed over the years. Most biomolecules present in tissues are in very low concentrations (in the picomolar [10^{-9} M] to nanomolar [10^{-12} M] range). This makes detecting them using molecular imaging agents extremely challenging. Hence, molecular imaging probes must be extremely sensitive in their interactions, home to their targets and be retained in adequate quantities for a suitable period for it to be detected. The probe should also bind specifically to the intended target and not elsewhere in order to get a high target to background ratio for better detectability. Therefore, an ideal molecular probe should have a high sensitivity and specificity (not to be confused with sensitivity and specificity of a clinical study).

Utilising the advances in cell and molecular biology, molecular probes have been also developed for imaging modalities like radionuclide imaging and optical imaging. Molecular imaging can be considered as an extension of nuclear medicine where patients are imaged by injecting specific radioactive pharmaceuticals.[51] Out of all molecular

imaging tools currently available, radionuclide imaging is the most well established and routinely used modality in clinical practice.

2.6 Optical Imaging

Optical imaging is an extension of well-established *in vitro* technique of fluorescence microscopy and bench top luminometry into an *in vivo* imaging modality.[51] The advantage of optical imaging is that it is very sensitive imaging modality and does not use harmful ionising radiation.[52] Zaheer et al. developed a fluorescent derivative (Pam78) to target the hydroxyapatite present in the calcified regions in transgenic mouse model (homozygous deletion of GLA protein $Mgp^{-/-}$). Pam78 is a conjugate of a bisphosphonate, pamidronate, and a NIR fluorophore, IR Dye 78 (Figure 2.1).[53, 54] The conjugation reaction was carried out in an aqueous solution with a yield of 18-21%.

A study by Kozoloff et al. demonstrated that a fluorescent bisphosphonate analogue, far-red fluorescent pamidronate (FRFP), is an accurate biomarker of bisphosphonate deposition and retention *in vivo*.[55] Aikawa et al. used a derivative of Pam78 (OsteoSense750/OS750, VisEn Medical Inc, Woburn, Mass) for *in vivo* imaging of ApoE deficient mouse fed with atherogenic diet. She concluded that NIRF imaging agent binds to nanocrystals of hydroxyapatite elaborated by vascular smooth muscle cells that undergo vesicle-mediated calcification.[56] Macru et al. used Time-Resolved Laser Induced Fluorescence Spectroscopy (TR-LIFS) to detect macrophages, thin fibrous cap and other markers of vulnerable plaque.[57] New optical imaging techniques like multiphoton laser scanning microscopy, optical coherence tomography (OCT) and photoacuostic imaging (PAI) are under development which may help to provide new insights in vascular calcification and atherosclerosis.

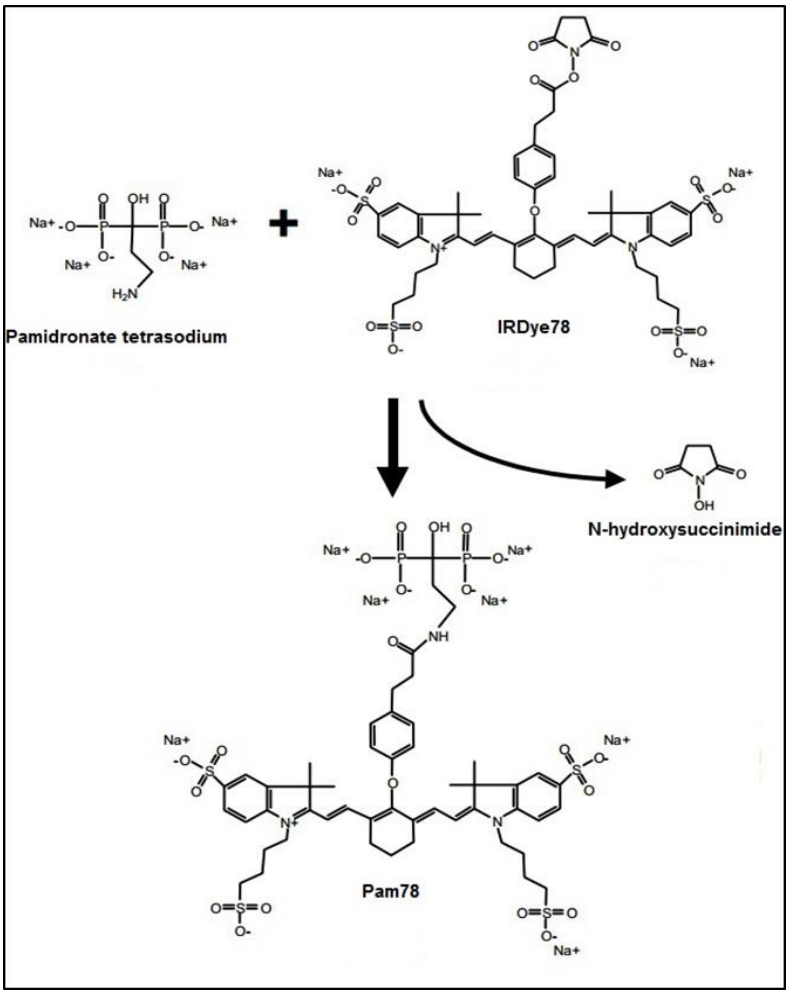

Figure 2.1: Synthesis of Pam78 by conjugating the primary amine of pamidronate tetrasodium with the sodium salt of the N-hydroxysuccinimide (NHS) ester of IRDye78. Zaheer et al. Nat Biotechnol. Dec 2001;19(12):1148-1154

.

2.7 Radionuclide Imaging

Radionuclide imaging is a quantitative molecular imaging tool that provides scans with high sensitivity (10^{-10}-10^{-12} mol/L) and specificity with information on processes at molecular and cellular level. Unlike optical imaging, radionuclide imaging do not have the problem of penetration as it uses γ-radiation for the detection of the probe. Advances in understanding the molecular and cellular mechanisms of atherogenesis have been exploited in developing new radiopharmaceuticals for both PET and conventional gamma imaging. Although numerous radiopharmaceuticals are being investigated for their potential in cardiovascular imaging especially in detecting atherosclerotic plaque and vascular calcification, clinical use in the field of cardiology is limited to perfusion studies with SPECT (^{201}Tl, and ^{99m}Tc-labelled sestamibi & tetrofosmin) and PET (^{18}F-FDG, ^{15}N-NH^{4+} and ^{82}Rb)[58, 59]

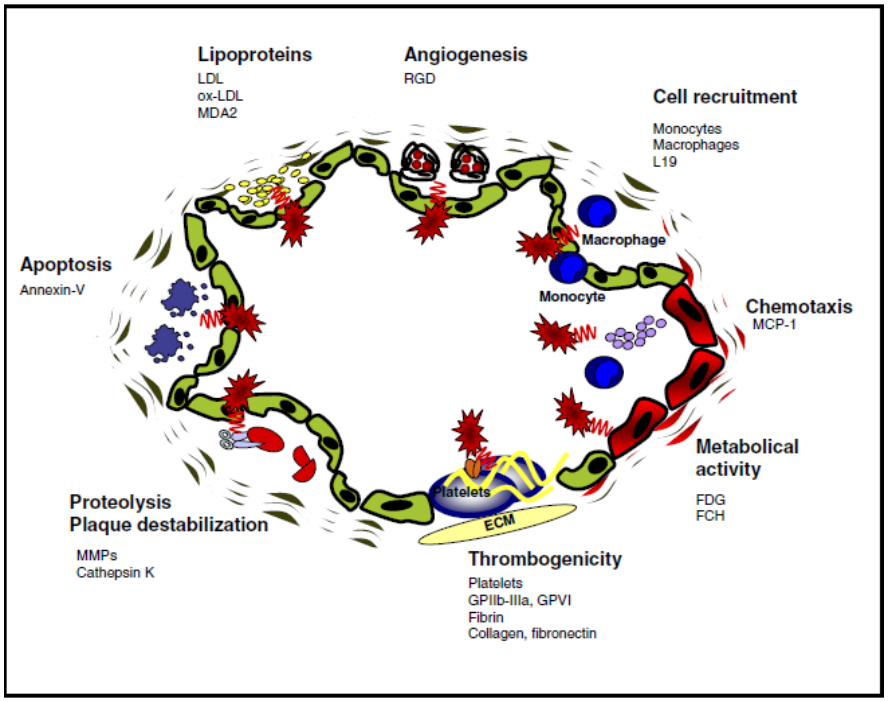

Figure 2.2: Different biological targets exploited for radionuclide imaging of atherosclerosis.

Langer et al. Journal of the American College of Cardiology.2008; 52:1 – 12

2.7.1 Metabolic Factors:

Atherosclerosis involves an ongoing inflammatory response and plays a crucial role from the initiation to progression of the lesion.[60] Macrophages and other inflammatory cells present in the atherosclerotic plaques have a high metabolic activity.^{18}F-FDG (fluorodeoxyglucose) is a FDA approved diagnostic pharmaceutical used for the evaluation of cases related to oncology, neurology and cardiology.[61] It is a glucose analogue and is retained by cells in proportion to their metabolic activity. The transportation of ^{18}F-FDG into the cells is mediated by glucose transporters where it is phosphorylated by hexokinase to ^{18}F-FDG-6- phosphate. ^{18}F-FDG-6- phosphate is retained in the cells as it cannot be metabolised further in the glycolytic pathway. ^{18}F-FDG has been successfully used for *in vivo* imaging of atherosclerosis.[62-64] Figure 2.2 shows some of the high priority imaging targets exploited and the radiopharmaceuticals developed for imaging atherosclerosis.[65]

2.7.2 Angiogenesis:

Angiogenesis is defined as the process of de novo formation of microvessels from pre-existing precursor cells.[66] Angiogenesis predominantly occurs in response to biological stimuli like ischemia, hypoxia, inflammation, shear stress, and traumatic injury.[67] It is a common finding in wound healing, inflammation and various cancers. Angiogenesis is a complex, multistep process involving a variety of cells, along with both stimulatory and inhibitory factors.[68] Vascular endothelial growth factor (VEGF) is a key stimulator that regulates the process of angiogenesis. VEGF ligands have four known isoforms, binding to specific VEGF receptors (VEGFR-1, VEGFR-2, and VEGFR-3).[68] Gambhir et al. successfully radiolabeled VEGF-121 with ^{64}Cu (^{64}Cu-6DOTA-VEGF121) and used it for PET imaging of VEGFR-2 in a murine model of hind limb ischemia-induced angiogenesis.[69] VEGF121 labelled with ^{111}In has also been developed as a targeting

ligand for SPECT and was successfully used to image peripheral angiogenesis in a rabbit model of hind limb ischemia.[70] Atherosclerotic lesions express high levels of the αVβ3 integrin hence they can be used as molecular targets for imaging angiogenesis.

It is a heterodimeric transmembrane glycoprotein that binds avidly with RGD (arginine-glycine-aspartic acid)-containing components of the interstitial matrix such as vitronectin and fibronectin. ^{18}F-galacto-RGD is taken up by αVβ3 in cancer cells. However, it demonstrates high non-specific uptake in the liver and intestine.[71] Laitinen et al. used ^{18}F-galacto-RGD and ^{68}Ga-DOTA-RGD to image vascular inflammation in hypercholesterolemic LDLR$^{-/-}$ApoB$^{100/100}$ mice. They demonstrated specific uptake of the radiopharmaceutical in atherosclerotic lesions of mouse aorta.[72, 73] Recently, Beer et al. evaluated the feasibility of the use of ^{18}F-galacto-RGD in imaging in human carotid plaque. The study was conducted on a cohort of 10 patients with high-grade carotid artery stenosis scheduled for carotid endarterectomy. They concluded that ^{18}F-galacto-RGD had significantly higher uptake in the stenotic areas as compared with non-stenotic areas.[74] 99mTc-NC100692 (maraciclatide), a tracer that binds with αVβ3 & αVβ5, has been developed by GE Healthcare, in a kit based formulation which has been successfully used to image angiogenic endothelium in animal models.[75, 76]

Table 2.6: Different radiopharmaceuticals developed to image atherosclerotic plaques and the underlying biology.

Research group and year	Underlying Plaque Biology	Radionuclide Tracer	Experimental Setting
Lees at al. 1988 [77]	Inflammation	^{99m}Tc-LDL	Human carotid/ ileofemoral artery
Virgolini et al. 1991 [78]	Lipoprotein accumulation	^{123}I-LDL	Human carotid artery
Virgolini et al. 1991 [79]		^{125}I-LDL	Rabbit aorta
Tsimikas et al. 1999 [80]		^{123}I-MDA2 (Ab to ox-LDL epitope)	Rabbit arteries
Shaw et al. 2001 [81]		^{125}I-IK17 (Ab to ox-LDL epitope)	Mouse aorta
Hardoff et al.1993 [82]		^{123}I-SP4 (apoliprotein B fragment)	Rabbit aorta
Lu et al. 1996 [83]		^{125}I-SP4	Rabbit aorta
Ohtsuki et al. 2001 [84]	Chemotaxis	^{125}I-MCP-1 (chemotactic molecule)	Rabbit aorta
Lee et al. 2005 [85]	Angiogenesis	^{125}I-c(RGD(I)yV) (peptide binding $_{v3}$)	Murine ischemic hind limbs/HUVECs
Hua et al. 2005 [86]		^{99m}Tc-(NC100692) (peptide binding $_{v3}$)	Murine ischemic hind limbs
Virgolini et al. 1990 [87]	Monocyte recruitment/ activity	^{111}In-monocytes	Human arteries
Lederman et al. 2001[88]		^{18}F-FDG (metabolic activity)	Rabbit iliac artery
Rudd et al. 2002 [62]		^{18}F-FDG	Human carotid artery
Haim et al. 2004 [89]		^{18}F-FDG	Human arteries
Matter et al. 2006 [90]		^{18}F-FDG in comparison with ^{18}F-FCH	Mouse aorta
Kelly et al. 2005 [91]		VHSPNKK-modified magnetofluorescent nanoparticle	Mouse carotid artery
Kolodgie et al. 2003 [92]	Apoptosis	^{99m}Tc-annexin V	Rabbit aorta
Kietselaer et al. 2004 [93]		^{99m}Tc-annexin V	Human carotid artery
Johnson et al. 2005 [94]		^{99m}Tc-annexin V	Swine coronary artery
Isobe et al. 2006 [95]		^{99m}Tc-annexin V	Mouse aorta
Schäfers et al. 2004 [96]	Proteolysis	^{123}I-HO-CGS27023 A (MMP inhibitor)	Mouse carotid artery
Jaffer et al. 2007 [56]		GHPGGPQKC-NH_2(cathepsin K substrate) - NIRFprobe.	Mouse aortae and human carotid arteries
Minar et al. 1989 [97]	Thrombogenicity and cell recruitment	^{111}In-platelets	Human carotid artery
Moriwaki et al. 1995 [98]		^{111}In-platelets	Human carotid artery
Gawaz et al. 2005 [98, 99]		^{125}I-GPVI/^{123}I-GPVI (platelet collagen receptor)	Mouse carotid artery
Mitchel et al. 2000 [100]		^{99m}Tc-DMP-444 (GPIIb-IIIa inhibitor)	Canine coronary artery
Cerqueira et al. 1992 [101]		^{99m}Tc-T2G1s Fab (fibrinogen binding)	Canine femoral/carotid artery
Matter et al. 2004 [90, 102]		^{125}I-L19 (fibronectin binding)	Mouse aorta

2.7.3 Apoptosis:

Apoptosis is a distinctive feature of atherosclerotic plaques that can be imaged using radiolabeled annexin V. Annexin V is a natural human phosphatidylserine-binding protein which is exposed to the extracellular membrane during apoptosis. ^{99m}Tc-annexin has been widely used and studied to image apoptosis both in atherosclerotic plaque and tumours. Human annexin V is obtained by recombinant DNA technique, conjugated with hydrazinonicotinamide (HYNIC) and labelled with ^{99m}Tc.

For PET imaging of apoptosis, annexin V has been radiolabeled with ^{18}F using N-succinimidyl-4-^{18}F-fluorobenzoic acid (^{18}F-SFB) chemistry to ^{18}F-fluoroannexin (^{18}F-FAN).[103] This method of labelling annexin V relies on nonspecific reaction of the prosthetic group (^{18}F-SFB) with any available amine groups in this protein. Another method of radiolabeling involves targeting the free thiol groups that are present only in cysteine residues. In this approach a thiol-reactive reagent N-[4-[(4-^{18}F fluorobenzylidene)aminooxy]butyl]maleimide (^{18}F-FBABM) is allowed to react with annexin V-128, an engineered form of annexin V containing one cysteine.[104]

Synaptotagmin 1 is a membrane protein present in all synaptic vesicles and regulated secretory vesicles of neural and neuroendocrine cells. Synaptotagmin 1 is characterised by an intravesicular domain, a single transmembrane domain, and a large cytoplasmic region containing two C2 domains (C2A and C2B). The first C2 (C2A) domain of synaptotagmin 1 binds negatively charged phospholipids including phosphatidylserine.[105] Zhao et al. successfully radiolabeled the C2A domain of the Synaptotagmin 1 with ^{99m}Tc with using a fusion protein glutathione S-transferase (^{99m}Tc-C2A-GST). *In vivo* SPECT imaging of acute myocardial infarction (AMI) mouse models showed increased uptake of the radiopharmaceutical in areas with ischemic injury.[106] Tavare et al. designed and

synthesised a new ^{99m}Tc-labelled bioconjugate for apoptosis imaging, based on C2A, the phosphatidylserine (PS)-binding domain of rat synaptotagmin I.[107]

2.7.4 Proteolysis:

Proteases contribute to the progression of atherosclerotic lesions through degradation of the extracellular matrix. Strategies to image proteolytic activity include the use of radiolabeled matrix metalloproteinase (MMP) inhibitors, substrates of MMP and cathepsins. CGS 27023A derivative (R)-2-(N-((6-fluoropyridin-3-yl)methyl)-4-methoxyphenyl-sulphonamido)-N-hydroxy-3methylbutan amide is an inhibitor of MMP 2, -8, -9 and -13. A broad spectrum of MMP inhibitors has been conjugated with ^{123}I to develop the radioligand ^{123}I-HOCGS27023A for *in vivo* imaging of MMP activity.[96] ^{18}F-labelled derivative of the MMP inhibitor CGS 27023A has also been developed for PET studies. Giersing et al. reported the synthesis of DTPA-N-TIMP-2 and its radiolabeling with ^{111}In.[108]

2.7.5 Thrombogenicity and cell recruitment:

Thrombogenicity is one of the prime features of vulnerable plaques and the strategy to image the process was by radiolabeling cells involved in thrombus formation. Radiolabeled (^{111}In) platelets were successfully used to image atherosclerosis.[97]

Monocytes play a key role in all phases of atherogenesis. The early stage of atherogenesis is marked by the recruitment of monocytes into the intima. In the intima monocytes take up oxidised LDL and differentiate into foam cells to form “fatty streaks”.[109, 110] The dynamics of monocyte recruitment to developing plaques can be clinically exploited as a viable imaging tool. Radiopharmaceuticals that have been developed to image atherosclerosis include ^{111}In-oxine labelled monocytes for targeting cells specific to atherosclerosis.[87, 111]

Table 2.7: Recent studies that demonstrate the successful use of ^{18}F-sodium fluoride in imaging

Research group and year	No. of patients	Radiopharmaceutical used	Target
Derlin et al. 2010[112]	75	^{18}F-Fluoride	Arteries
Li et al. 2012 [113]	61	^{18}F-Fluoride	Calcified atherosclerotic plaque.
Derlin et al. 2011 [114]	269	^{18}F-Fluoride	Common carotid arteries.
Dweck et al. 2012 [115]	119	^{18}F-FDG & ^{18}F-Fluoride	Coronary arteries.
Quirce et al. 2013 [115, 116]	15	^{18}F-Fluoride	Carotid arteries.
Joshi et al. 2014 [117]	40	^{18}F-Fluoride/^{18}F-FDG	Carotid arteries.

2.7.6 Use of bone seeking agents:

Vascular calcification is one of the common phenomena involved with atherosclerosis, an avenue that was not explored in nuclear medicine until recently. The use of ^{18}F as a bone imaging agent was presented by Blau et al. in 1962, but its use remained restricted due to the unavailability of dedicated PET scanning equipment.[118] The availability of modern PET scanners has renewed the interest in ^{18}F-fluoride and its use in PET scanning of bones. By the process of chemisorption ^{18}F-fluoride ions binds onto hydroxyapatite, then it replaces the hydroxyl (OH-) group of the hydroxyapatite matrix [$Ca_{10}(PO_4)_6(OH)_2$] to form fluoroapatite [$Ca_{10}(PO_4)_6F_2$].[119] Recently, ^{18}F-fluoride has been studied for its possibility to be used in imaging atherosclerosis. Table 2.7 illustrates the recent studies published by various groups who reported the use of ^{18}F-NaF for *in vivo* imaging to detect arterial calcification. One of the earliest works was published by Derlin et al. The study was conducted on 75 patients with a history of atherosclerosis and vasculitis. The patients were undergoing whole body PET-CT scan with ^{18}F-NaF to evaluate bone metastases. They concluded that out of 1930 sites of calcification (on CT), increased radiotracer accumulation was observed in only 254 sites (12%).[112] Joshi et al.

recently demonstrated the successful use of ^{18}F-NaF in detecting and localising vulnerable calcified plaques in a cohort of 40 patients with carotid artery calcification.[117]

2.8 Multimodality imaging

Every imaging modality has its advantages and disadvantages and none can provide information on all aspects of structure and function, hence an approach to get greater information is to integrate the imaging modalities. Integrating two modalities enables us to utilise the advantages of both the modalities while negating their drawbacks.[120] Multimodality imaging has seen vast development in the recent past but the concept is decades old. The first prototype SPECT-CT system was developed in 1966 by Kuhl et al.[121] However, it took 30 years for SPECT and PET systems fused with CT scanners to gain popularity. The CT scans are used as anatomical references for the 3D images obtained in a SPECT or PET systems for physicians to locate the diseased area accurately. The CT scans are also used for attenuation correction of SPECT and PET images.[121-123] SPECT-CT and PET-CT imaging is now a routinely performed medical imaging modality in different branches of medicine. PET-CT has become an indispensable part of oncology and has been used for radiotherapy treatment planning.[124] The advantage of using a PET- or SPECT-CT system is that it integrates the sensitivity and molecular information of PET imaging coupled with a high resolution CT image. On the other hand the use of ionising radiation by both modalities is a major limitation as it increases the radiation burden on the patients.

Although a challenging task, efforts were made to integrate MRI with nuclear imaging (PET and SPECT). A prototype of a preclinical simultaneous PET-MRI was developed in the late 1990's by Marsden et al. at King's College London in collaboration with Shao et al. of University of California, Los Angeles.[125] PET-MRI enables the integration of the sensitivity of radionuclide imaging with high resolution and better soft tissue contrast of

MRI. It has three important advantages over PET- and SPECT-CT: (1) Simultaneous imaging is possible with PET-MRI whereas the images obtained from PET and SPECT-CT are sequential; (2) In comparison with CT, MRI provides a better soft tissue contrast. (3) The radiation burden delivered to the patient is also significantly reduced as MR does not involve the use of ionising radiation.[126] Recently, the US Food and Drug Administration (FDA) has approved the PET-MRI systems developed by Royal Philips Electronics and Siemens Healthcare. This has opened the door for research and development for developing agents to be used in these scanners.

There have been efforts to develop agents for simultaneous PET-MR imaging. Choi et al. demonstrated the use of ^{124}I conjugated with serum albumin (SA)-coated manganese doped magnetism engineered iron oxide (SA-MnMEIO) as a multimodal agent for imaging sentinel nodes in mice.[127] Nahrendorf et al. used a trireporter nanoparticle (^{64}Cu-TNP) to target macrophage activity and image atherosclerotic plaques in ApOE mice. The agent was developed by derivatising magnetic nanoparticle base material with DTPA for the nuclear tracer ^{64}Cu and a near-infrared fluorochrome, yielding a trimodality reporter for PET, MRI, and fluorescence imaging.[128] Hwang et al. developed a quadruple imaging agent using cobalt–ferrite nanoparticle surrounded by rhodamine (MF) that was conjugated with luciferase (MFB) and p-SCN-bn-NOTA (2-(4-isothiocyanatobenzyl)-1,4,7-triazacyclonane-1,4,7-triacetic acid) followed by ^{68}GaCl3 (magnetic-fluorescent bioluminescent-radioisotopic particle, MFBR) capable of fluorescence, bioluminescence, bioluminescence resonance energy transfer (BRET), positron emission tomography (PET) and magnetic resonance (MR) imaging of tumour vasculature *in vivo*.[129] A 99mTc-bisphosphonate (dipicolylamine alendronate)-iron oxide nanoparticle conjugate was developed by Torres et al. for simultaneous SPECT-MRI.[130] Blower et al. have described

an array of aluminium hydroxide stabilised $MnFe_2O_4$ and Fe_3O_4 nanoparticles that have potential to be used as a dual modality PET/MRI agent.[131]

Another notable multimodality imaging approach is the integration of optical imaging with radiological imaging modalities such as PET, SPECT, CT and MRI. Cai et al. developed a dual modality agent based on ^{64}Cu-RGD-peptide and fluorescent quantum dots (QD) for PET and NIRF imaging. They conjugated 1,4,7,10-tetraazacyclododecane-N,N',N'',N'''-tetraacetic acid (DOTA) on the surface of QD for ^{64}Cu chelation.[132] Although radiolabeled RGD has been primarily used for imaging neovascularisation in tumours, it has the potential to be used in atherosclerotic plaque imaging also.

2.9 Summary

In the quest to establish a convenient and cost effective imaging modality that will successfully identify the early stages of vascular calcification, several avenues have been explored. A range of technologies have been evaluated from the simple x-ray to complex multimodality imaging. CT is considered as the 'gold standard' for the *in vivo* diagnosis of vascular calcification. Recent findings suggest that CT fails to detect microcalcifications, which might play a crucial role in plaque rupture. The need to detect these pathological changes at the molecular level *in vivo* has been the driving force behind developing novel labelling techniques. Several molecular probes have been developed for the detection of atherosclerosis, but imaging the multifaceted vascular calcification paradigm remains unchartered.

2.10 Aims and outline of the thesis

The main objective of the project is to study novel and clinically-established bone seeking radiopharmaceuticals for imaging vascular calcification. After a thorough *in vitro* evaluation the radiopharmaceuticals were subsequently used to investigate vascular

calcification in vivo using small animal SPECT-CT and PET-CT. The rationale for choosing the radiopharmaceuticals are discussed below.

2.10.1 ^{99m}Tc-labelled bisphosphonates as an agent for imaging vascular calcification

Bisphosphonates (BPs) are analogues of pyrophosphate where the central oxygen of the pyrophosphate (P-O-P) is replaced by a carbon (P-C-P) (Figure 2.3). The replacement with carbon provides stability and makes the compound resistant to biological degradation including enzymatic hydrolysis.[133] Pyrophosphates exist naturally in the body and act as inhibitors of biomineralisation.[134] BPs have been widely used as an antiresorptive agent to treat metabolic bone disorders like Paget's disease and osteoporosis. They have also been used in management of patients with metastatic bone disease and multiple myeloma. Bisphosphonates bind avidly with hydroxyapatite (HA), which is one of the major constituents of the inorganic matrix of the bone. The processes of calcification and normal bone formation are indistinguishable and use similar signalling pathways.

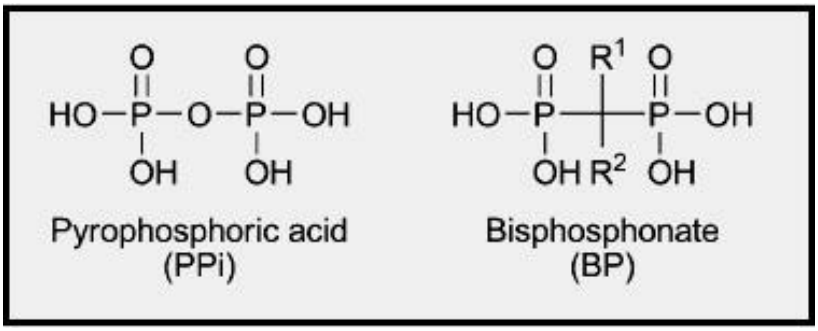

Figure 2.3: Basic structure of pyrophosphate and bisphosphonate.

The affinity of bisphosphonates to bind with hydroxyapatite can be capitalised in imaging vascular calcification. Optical imaging using a bisphosphonate conjugate has been successful in detecting microcalcifications. Radiolabeled bisphosphonates might provide a solution for the problem posed in optical imaging.

(A): ^{99m}Tc-MDP

^{99m}Tc-MDP is the clinically established bone seeking SPECT agent used in our study.[135, 136] There have been reports of extra-osseous uptake of ^{99m}Tc-MDP linked to atherosclerosis and vascular calcification. DeLong et al. reported the visualisation of calcified femoral arteries in patients undergoing bone scans. After a study conducted on 237 patients, Lantto et al. concluded that radiolabeled bisphosphonates might have a role in imaging atherosclerosis.[137, 139] Despite published case studies of radiolabeled bisphosphonates being visualised in calcified arteries, the prospect of using them as a tool for detection of vascular calcification remains untapped.

(B) ^{99m}Tc-labelled novel bisphosphonates: ^{99m}Tc-N(DTCBP)$_2$ and ^{99m}Tc-DPA Ale

In order to overcome the drawbacks of ^{99m}Tc-MDP, including the unknown nature of its structure, composition and compromised stability *in vivo*, two novel bisphosphonates were explored (see Figure 2.4). These compounds have enhanced binding affinity and *in vivo* stability. This is achieved by separating the bisphosphonate from the radiometal chelator rendering the chemical bifunctional.

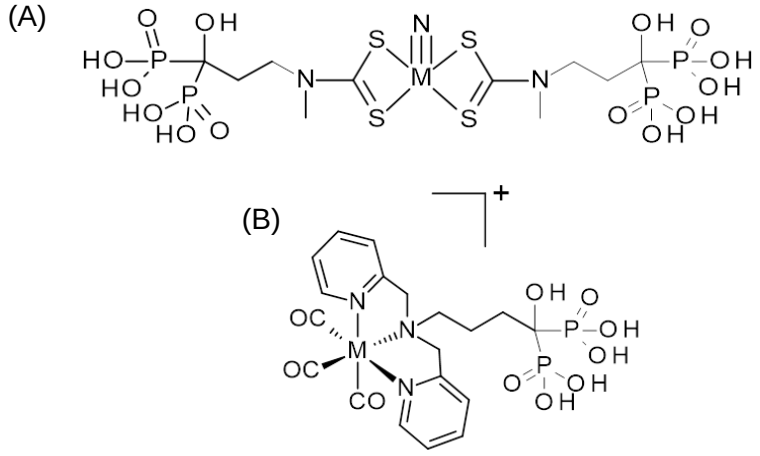

Figure 2.4: Novel radiolabeled bisphosphonate used in the study (M=^{99m}Tc). (A) ^{99m}Tc-N(DTCBP)$_2$ and (B) ^{99m}Tc-DPA Ale

2.10.2 ^{18}F-NaF PET for imaging vascular calcification

^{18}F-NaF has been in the forefront of PET imaging of VC recently. Several clinical studies have shown promising results with ^{18}F-NaF for the detections of microcalcifications. However, there is a distinct lack of published pre-clinical animal models of calcification using ^{18}F-NaF. To complement our bisphosphonate studies, both *in vivo* and *in vitro* ^{18}F-NaF was used.

The thesis is divided into seven chapters. A brief outline of the thesis is described below:

Chapter 3 describes the initial investigation and characterisation of the radiopharmaceuticals. *In vitro* binding assays with minerals of synthetic (hydroxyapatite) and biological origin (isolated from human intimal and medial plaque). *In vitro* and *in situ* binding assays were also performed with ABs from calcifying and control VSMCs. ABs and MVs form the first nidus nidus for biomineralisation in the vasculature.

Chapter 4 addresses the development of animal models of vascular calcification. We attempted to replicate a previously published murine model of medial arterial calcification. In conjunction, modifications were made to an established rat models of vascular calcification to reduce pain threshold as well as to comply with the Home Office requirement.

Chapter 5 describes the findings of the pilot cum optimization study conducted to determine whether the bone seeking radiopharmaceuticals binds with regions of vascular calcification. SPECT-CT and PET-CT studies were performed with the radiotracers ^{99m}Tc-MDP, ^{99m}Tc-N(DTCBP)$_2$, ^{99m}Tc-DPA Ale and ^{18}F-NaF.

Chapter 6 illustrates longitudinal SPECT-CT and PET-CT imaging with the radiopharmaceuticals ^{99m}Tc-MDP, ^{99m}Tc-DPA Ale and ^{18}F-NaF. The purpose of the study

was demonstrate the feasibility of early detection of vascular calcification with bone seeking agents and monitor the disease progression.

Chapter 7 provides the summary of our findings and some future perspectives.

References

1. Katz J. Pharmaceutical discovery and development: nuclear and molecular imaging technologies recognized. *J Nucl Med.* 1999;40(7):22N-23N, 26N.

2. Pellecchia M, Bertini I, Cowburn D, et al. Perspectives on NMR in drug discovery: a technique comes of age. *Nat Rev Drug Discov.* 2008;7(9):738-745.

3. Kauppila LI, Polak JF, Cupples LA, et al. New indices to classify location, severity and progression of calcific lesions in the abdominal aorta: a 25-year follow-up study. *Atherosclerosis.* 1997;132(2):245-250.

4. Wilson PW, Kauppila LI, O'Donnell CJ, et al. Abdominal aortic calcific deposits are an important predictor of vascular morbidity and mortality. *Circulation.* 2001;103(11):1529-1534.

5. London GM, Guerin AP, Marchais SJ, et al. Arterial media calcification in end-stage renal disease: impact on all-cause and cardiovascular mortality. *Nephrol Dial Transpl.* 2003;18(9):1731-1740.

6. Adragao T, Pires A, Lucas C, et al. A simple vascular calcification score predicts cardiovascular risk in haemodialysis patients. *Nephrol Dial Transpl.* 2004;19(6):1480-1488.

7. Niskanen LK, Suhonen M, Siitonen O, et al. Aortic and lower limb artery calcification in type 2 (non-insulin-dependent) diabetic patients and non-diabetic control subjects. A five year follow-up study. *Atherosclerosis.* 1990;84(1):61-71.

8. Adragao T, Pires A, Birne R, et al. A plain X-ray vascular calcification score is associated with arterial stiffness and mortality in dialysis patients. *Nephrol Dial Transpl.* 2009;24(3):997-1002.

9. Adragao T, Pires A, Branco P, et al. Ankle--brachial index, vascular calcifications and mortality in dialysis patients. *Nephrol Dial Transpl.* 2012;27(1):318-325.

10. Nickoloff EL. AAPM/RSNA physics tutorial for residents: physics of flat-panel fluoroscopy systems: Survey of modern fluoroscopy imaging: flat-panel detectors versus image intensifiers and more. *Radiographics.* 2011;31(2):591-602.

11. Lalkhen AG, McCluskey A. Clinical tests: sensitivity and specificity. *Continuing Education in Anaesthesia, Critical Care & Pain.* 2008;8(6):221-223.

12. Parikh R, Mathai A, Parikh S, et al. Understanding and using sensitivity, specificity and predictive values. *Indian J Ophthalmol.*2008;56(1):45-50.

13. Masuda Y, Naito S, Aoyagi Y, et al. Coronary artery calcification detected by CT: clinical significance and angiographic correlates. *Angiology.* 1990;41(12):1037-1047.

14. Agatston AS, Janowitz WR, Hildner FJ, et al. Quantification of coronary artery calcium using ultrafast computed tomography. *J Am Coll Cardiol.* 1990;15(4):827-832.

15. Heussel CP, Voigtlaender T, Kauczor H, et al. Detection of coronary artery calcifications predicting coronary heart disease: comparison of fluoroscopy and spiral CT. *Eur Radiol.* 1998;8(6):1016-1024.

16. Bartel AG, Chen JT, Peter RH, et al. The significance of coronary calcification detected by fluoroscopy. A report of 360 patients. *Circulation.* 1974;49(6):1247-1253.

17. Hamby RI, Tabrah F, Wisoff BG, et al. Coronary artery calcification: clinical implications and angiographic correlates. *Am Heart J.* 1974;87(5):565-570.

18. Bierner M, Fleck E, Dirschinger J, et al. Significance of coronary artery calcification: relationship to localization and severity of coronary artery stenosis. *Herz.* 1978;3(5):336-343.

19. Aldrich RF, Brensike JF, Battaglini JW, et al. Coronary calcifications in the detection of coronary artery disease and comparison with electrocardiographic exercise

testing. Results from the National Heart, Lung, and Blood Institute's type II coronary intervention study. *Circulation.* 1979;59(6):1113-1124.

20. Margolis JR, Chen JT, Kong Y, Peter RH, Behar VS, Kisslo JA. The diagnostic and prognostic significance of coronary artery calcification. A report of 800 cases. *Radiology.* 1980;137(3):609-616.

21. Hung J, Chaitman BR, Lam J, et al. Noninvasive diagnostic test choices for the evaluation of coronary artery disease in women: a multivariate comparison of cardiac fluoroscopy, exercise electrocardiography and exercise thallium myocardial perfusion scintigraphy. *J Am Coll Cardiol.* 1984;4(1):8-16.

22. Detrano R, Salcedo EE, Hobbs RE, et al. Cardiac cinefluoroscopy as an inexpensive aid in the diagnosis of coronary artery disease. *Am J Cardiol.* 1986;57(13):1041-1046.

23. Uretsky BF, Rifkin RD, Sharma SC, et al. Value of fluoroscopy in the detection of coronary stenosis: influence of age, sex, and number of vessels calcified on diagnostic efficacy. *Am Heart J.* 1988;115(2):323-333.

24. Ammann P, Brunner-La Rocca HP, Angehrn W, et al. Procedural complications following diagnostic coronary angiography are related to the operator's experience and the catheter size. *Catheter Cardio Inte.* 2003;59(1):13-18.

25. Cuddy E, Robertson S, Cross S, et al. Risks of coronary angiography. *Lancet.* 2005;366(9499):1825.

26. Sarma A, Heilbrun ME, Conner KE, et al. Radiation and chest CT scan examinations: what do we know? *Chest.* Sep 2012;142(3):750-760.

27. Mautner GC, Mautner SL, Froehlich J, et al. Coronary artery calcification: assessment with electron beam CT and histomorphometric correlation. *Radiology.* 1994;192(3):619-623.

28. Goldman LW. Principles of CT and CT technology. *J.Nucl Med. technology.* 2007;35(3):115-128; quiz 129-130.

29. Ledley RS, Wilson JB, Golab T, et al. The ACTA-scanner: the whole body computerized transaxial tomograph. *Comput Biol Med.* 1974;4(2):145-155.

30. Timins ME, Pinsk R, Sider L, Bear G. The functional significance of calcification of coronary arteries as detected on CT. *J Thorac Imag.* 1991;7(1):79-82.

31. O'Rourke RA, Brundage BH, Froelicher VF, et al. American College of Cardiology/American Heart Association Expert Consensus document on electron-beam computed tomography for the diagnosis and prognosis of coronary artery disease. *Circulation.* 2000;102(1):126-140.

32. Tanenbaum SR, Kondos GT, Veselik KE, et al. Detection of calcific deposits in coronary arteries by ultrafast computed tomography and correlation with angiography. *Am J Cardiol.* 1989;63(12):870-872.

33. Rumberger JA, Simons DB, Fitzpatrick LA, et al. Coronary artery calcium area by electron-beam computed tomography and coronary atherosclerotic plaque area. A histopathologic correlative study. *Circulation.* 1995;92(8):2157-2162.

34. Denzel C, Lell M, Maak M, et al. Carotid artery calcium: accuracy of a calcium score by computed tomography-an in vitro study with comparison to sonography and histology. *Eur J Vasc Endovasc.* 2004;28(2):214-220.

35. Hsiao EM, Rybicki FJ, Steigner M. CT Coronary Angiography: 256-Slice and 320-Detector Row Scanners. *Curr Cardiol Rep.* 2010;12(1):68-75.

36. Pickhardt PJ, Lawrence EM, Pooler BD, Bruce RJ. Diagnostic performance of multidetector computed tomography for suspected acute appendicitis. *Ann Intern Med.* 2011;154(12):789-796, W-291.

37. Sameshima T, Futami S, Morita Y, et al. Clinical usefulness of and problems with three-dimensional CT angiography for the evaluation of arteriosclerotic stenosis of

the carotid artery: comparison with conventional angiography, MRA, and ultrasound sonography. *Surg Neurol.* 1999;51(3):301-308; discussion 308-309.

38. Ota H, Takase K, Igarashi K, et al. MDCT compared with digital subtraction angiography for assessment of lower extremity arterial occlusive disease: importance of reviewing cross-sectional images. *AJR. Am J Roentgenol.* 2004;182(1):201-209.

39. Ghersin E, Litmanovich D, Dragu R, et al. 16-MDCT coronary angiography versus invasive coronary angiography in acute chest pain syndrome: a blinded prospective study. *AJR. Am J Roentgenol.* 2006;186(1):177-184.

40. Cademartiri F, La Grutta L, Malago R, et al. Prevalence of anatomical variants and coronary anomalies in 543 consecutive patients studied with 64-slice CT coronary angiography. *Eur Radiol.* 2008;18(4):781-791.

41. Budoff MJ, Dowe D, Jollis JG, et al. Diagnostic performance of 64-multidetector row coronary computed tomographic angiography for evaluation of coronary artery stenosis in individuals without known coronary artery disease: results from the prospective multicenter ACCURACY (Assessment by Coronary Computed Tomographic Angiography of Individuals Undergoing Invasive Coronary Angiography) trial. *J Am Coll Cardiol.* 2008;52(21):1724-1732.

42. Duarte R, Fernandez G, Castellon D, et al. Prospective Coronary CT Angiography 128-MDCT Versus Retrospective 64-MDCT: Improved Image Quality and Reduced Radiation Dose. *Heart Lung Circ.* 2011;20(2):119-125.

43. Chen BX, Ma FY, Wen ZY, et al. Diagnostic value of 128-slice CT coronary angiography in comparison with invasive coronary angiography. *Zhonghua Xin Xue Guan Bing Za Zhi.* 2008;36(3):223-228.

44. Mori S, Endo M, Nishizawa K, et al. Comparison of patient doses in 256-slice CT and 16-slice CT scanners. *Brit J Radiol.* 2006;79(937):56-61.

45. de Graaf FR, van Velzen JE, Witkowska AJ, et al. Diagnostic performance of 320-slice multidetector computed tomography coronary angiography in patients after coronary artery bypass grafting. *Eur Radiol.* 2011;21(11):2285-2296.

46. Honye J, Mahon DJ, Tobis JM. Intravascular ultrasound imaging. *Trends Cardiovasc Med.* 1991;1(7):305-311.

47. Mintz GS, Douek P, Pichard AD, et al. Target lesion calcification in coronary artery disease: an intravascular ultrasound study. *J Am Coll Cardiol.* 1992;20(5):1149-1155.

48. Mintz GS, Popma JJ, Pichard AD, et al. Patterns of Calcification in Coronary Artery Disease: A Statistical Analysis of Intravascular Ultrasound and Coronary Angiography in 1155 Lesions. *Circulation.*1995;91(7):1959-1965.

49. Ehara S, Kobayashi Y, Yoshiyama M, et al. Spotty calcification typifies the culprit plaque in patients with acute myocardial infarction: an intravascular ultrasound study. *Circulation.* 2004;110(22):3424-3429.

50. Karpiouk AB, Wang B, Emelianov SY. Development of a catheter for combined intravascular ultrasound and photoacoustic imaging. *Rev Sci Instrum.* 2010;81(1):014901.

51. Massoud TF, Gambhir SS. Molecular imaging in living subjects: seeing fundamental biological processes in a new light. *Genes Dev.* 2003;17(5):545-580.

52. Subramanian S, Jaffer FA, Tawakol A. Optical molecular imaging in atherosclerosis. *J Nucl Cardiol.* 2010;17(1):135-144.

53. Zaheer A, Murshed M, De Grand AM, et al. Optical imaging of hydroxyapatite in the calcified vasculature of transgenic animals. *Arterioscler Thromb Vasc Biol.* 2006;26(5):1132-1136.

54. Zaheer A, Lenkinski RE, Mahmood A, et al. In vivo near-infrared fluorescence imaging of osteoblastic activity. *Nat Biotechnol.* 2001;19(12):1148-1154.

55. Kozloff KM, Volakis LI, Marini JC, et al. Near-infrared fluorescent probe traces bisphosphonate delivery and retention in vivo. *J Bone Miner Res.* 2010;25(8):1748-1758.

56. Aikawa E, Nahrendorf M, Figueiredo JL, et al. Osteogenesis associates with inflammation in early-stage atherosclerosis evaluated by molecular imaging in vivo. *Circulation.* 2007;116(24):2841-2850.

57. Marcu L, Jo JA, Fang Q, et al. Detection of rupture-prone atherosclerotic plaques by time-resolved laser-induced fluorescence spectroscopy. *Atherosclerosis.* 2009;204(1):156-164.

58. Crean A, Dutka D, Coulden R. Cardiac imaging using nuclear medicine and positron emission tomography. *Radiol Clin N Am.* 2004;42(3):619-634,vii.

59. Sampson UK, Dorbala S, Limaye A, et al. Diagnostic Accuracy of Rubidium-82 Myocardial Perfusion Imaging With Hybrid Positron Emission Tomography/Computed Tomography in the Detection of Coronary Artery Disease. *J Am Coll Cardiol.* 2007;49(10):1052-1058.

60. Libby P, Ridker PM, Maseri A. Inflammation and Atherosclerosis. *Circulation.* 2002;105(9):1135-1143.

61. Wagner HN, Jr. PET is alive and well. *J Nucl Med.* 2007;48(4):495.

62. Rudd JH, Warburton EA, Fryer TD, et al. Imaging atherosclerotic plaque inflammation with F-18 fluorodeoxyglucose positron emission tomography. *Circulation.* 2002;105(23):2708-2711.

63. Rosenbaum D, Millon A, Fayad Z. Molecular Imaging in Atherosclerosis: FDG PET. *Curr Atheroscler. Rep.* 2012;14(5):429-437.

64. Rudd JH, Myers KS, Bansilal S, et al. Atherosclerosis inflammation imaging with F-18 FDG PET: carotid, iliac, and femoral uptake reproducibility, quantification methods, and recommendations. *J Nucl Med.* 2008;49(6):871-878.

65. Langer HF, Haubner R, Pichler BJ, et al. Radionuclide imaging: a molecular key to the atherosclerotic plaque. *J Am Coll Cardiol.* 2008;52(1):1-12.

66. Mitsos S, Katsanos K, Koletsis E, et al. Therapeutic angiogenesis for myocardial ischemia revisited: basic biological concepts and focus on latest clinical trials. *Angiogenesis.* 2012;15(1):1-22.

67. Fam NP, Verma S, Kutryk M, et al. Clinician Guide to Angiogenesis. *Circulation.* November 25, 2003;108(21):2613-2618.

68. Carmeliet P, Jain RK. Molecular mechanisms and clinical applications of angiogenesis. *Nature.* 2011;473(7347):298-307.

69. Willmann JK, Chen K, Wang H, et al. Monitoring of the Biological Response to Murine Hindlimb Ischemia With Cu-64 Labeled Vascular Endothelial Growth Factor-121 Positron Emission Tomography. *Circulation.* 2008;117(7):915-922.

70. Lu E, Wagner WR, Schellenberger U, et al. Targeted In Vivo Labeling of Receptors for Vascular Endothelial Growth Factor: Approach to Identification of Ischemic Tissue. *Circulation.* 2003;108(1):97-103.

71. Beer AJ, Haubner R, Goebel M, et al. Biodistribution and pharmacokinetics of the alphavbeta3-selective tracer F-18 galacto-RGD in cancer patients. *J Nucl Med.* 2005;46(8):1333-1341.

72. Laitinen I, Saraste A, Weidl E, et al. Evaluation of alphavbeta3 integrin-targeted positron emission tomography tracer F-18 galacto-RGD for imaging of vascular inflammation in atherosclerotic mice. *Circ Cardiovasc Imaging.* 2009;2(4):331-338.

73. Haukkala J, Laitinen I, Luoto P, et al. Ga-68 DOTA-RGD peptide: biodistribution and binding into atherosclerotic plaques in mice. *Eur J Nucl Med Mol Imaging.* 2009;36(12):2058-2067.

74. Beer AJ, Pelisek J, Heider P, et al. PET/CT Imaging of Integrin αvβ3 Expression in Human Carotid Atherosclerosis. *JACC Cardiovasc Imaging.* 2014;7(2):178-187.

75. Edwards D, Jones P, Haramis H, et al. Tc-99m NC100692--a tracer for imaging vitronectin receptors associated with angiogenesis: a preclinical investigation. *Nucl Med Biol.* 2008;35(3):365-375.

76. Dearling JL, Barnes JW, Panigrahy D, et al. Specific uptake of Tc-99m NC100692, an alphavbeta3-targeted imaging probe, in subcutaneous and orthotopic tumors. *Nucl Med Biol.* 2013;40(6):788-794.

77. Lees AM, Lees RS, Schoen FJ, et al. Imaging human atherosclerosis with Tc-99m labeled low density lipoproteins. *Arteriosclerosis.*1988;8(5):461-470.

78. Virgolini I, Rauscha F, Lupattelli G, et al. Autologous low-density lipoprotein labelling allows characterization of human atherosclerotic lesions in vivo as to presence of foam cells and endothelial coverage. *Eur J Nucl Med.* 1991;18(12):948-951.

79. Virgolini I, Angelberger P, O'Grady J, et al. Low density lipoprotein labelling characterizes experimentally induced atherosclerotic lesions in rabbits in vivo as to presence of foam cells and endothelial coverage. *Eur J Nucl Med.* 1991;18(12):944-947.

80. Tsimikas S, Palinski W, Halpern SE, et al. Radiolabeled MDA2, an oxidation-specific, monoclonal antibody, identifies native atherosclerotic lesions in vivo. *J Nucl Cardiol.*1999;6(1 Pt 1):41-53.

81. Shaw PX, Horkko S, Tsimikas S, et al. Human-derived anti-oxidized LDL autoantibody blocks uptake of oxidized LDL by macrophages and localizes to atherosclerotic lesions in vivo. *Arterioscler Thromb Vasc Biol.* 2001;21(8):1333-1339.

82. Hardoff R, Braegelmann F, Zanzonico P, et al. External imaging of atherosclerosis in rabbits using an I-123 labeled synthetic peptide fragment. *J. Clin. Pharmacol.* 1993;33(11):1039-1047.

83. Lu P, Zanzonico P, Lister-James J, et al. Biodistribution and autoradiographic localization of i-125-labeled synthetic peptide in aortic atherosclerosis in cholesterol-fed rabbits. *Am J Ther.* 1996;3(10):673-680.

84. Ohtsuki K, Hayase M, Akashi K, et al. Detection of monocyte chemoattractant protein-1 receptor expression in experimental atherosclerotic lesions: an autoradiographic study. *Circulation.* 2001;104(2):203-208.

85. Lee KH, Jung KH, Song SH, et al. Radiolabeled RGD uptake and alphav integrin expression is enhanced in ischemic murine hindlimbs. *J Nucl Med.* 2005;46(3):472-478.

86. Hua J, Dobrucki LW, Sadeghi MM, et al. Noninvasive imaging of angiogenesis with a 99mTc-labeled peptide targeted at alphavbeta3 integrin after murine hindlimb ischemia. *Circulation.* 2005;111(24):3255-3260.

87. Virgolini I, Muller C, Fitscha P, et al. Radiolabelling autologous monocytes with 111-indium-oxine for reinjection in patients with atherosclerosis. *Prog. Clin Biol Res.* 1990;355:271-280.

88. Lederman RJ, Raylman RR, Fisher SJ, et al. Detection of atherosclerosis using a novel positron-sensitive probe and 18-fluorodeoxyglucose (FDG). *Nucl Med Commun.* 2001;22(7):747-753.

89. Ben-Haim S, Kupzov E, Tamir A, et al. Evaluation of 18F-FDG uptake and arterial wall calcifications using F-18 FDG PET/CT. *J Nucl Med.* 2004;45(11):1816-1821.

90. Matter CM, Wyss MT, Meier P, et al. F-18 choline images murine atherosclerotic plaques ex vivo. *Arterioscler Thromb Vasc Biol.* 2006;26(3):584-589.

91. Kelly KA, Allport JR, Tsourkas A, et al. Detection of vascular adhesion molecule-1 expression using a novel multimodal nanoparticle. *Circ Res.* 2005;96(3):327-336.

92. Kolodgie FD, Petrov A, Virmani R, et al. Targeting of apoptotic macrophages and experimental atheroma with radiolabeled annexin V: a technique with potential for noninvasive imaging of vulnerable plaque. *Circulation.* 2003;108(25):3134-3139.

93. Kietselaer BL, Reutelingsperger CP, Heidendal GA, et al. Noninvasive detection of plaque instability with use of radiolabeled annexin A5 in patients with carotid-artery atherosclerosis. *N Engl J Med.* 2004;350(14):1472-1473.

94. Johnson LL, Schofield L, Donahay T, et al. Tc-99m annexin V imaging for in vivo detection of atherosclerotic lesions in porcine coronary arteries. *J Nucl Med.* 2005;46(7):1186-1193.

95. Isobe S, Tsimikas S, Zhou J, et al. Noninvasive imaging of atherosclerotic lesions in apolipoprotein E-deficient and low-density-lipoprotein receptor-deficient mice with annexin A5. *J Nucl Med.* 2006;47(9):1497-1505.

96. Schafers M, Riemann B, Kopka K, et al. Scintigraphic imaging of matrix metalloproteinase activity in the arterial wall in vivo. *Circulation.* 2004;109(21):2554-2559.

97. Minar E, Ehringer H, Dudczak R, et al. Indium-111-labeled platelet scintigraphy in carotid atherosclerosis. *Stroke.* 1989;20(1):27-33.

98. Moriwaki H, Matsumoto M, Handa N, et al. Functional and anatomic evaluation of carotid atherothrombosis. A combined study of indium 111 platelet scintigraphy and B-mode ultrasonography. *Arterioscler Thromb Vasc Biol.*1995;15(12):2234-2240.

99. Gawaz M, Konrad I, Hauser AI, et al. Non-invasive imaging of glycoprotein VI binding to injured arterial lesions. *Thromb Haemost.* 2005;93(5):910-913.

100. Mitchel J, Waters D, Lai T, et al. Identification of coronary thrombus with a IIb/IIIa platelet inhibitor radiopharmaceutical, Tc-99m DMP-444: A canine model. *Circulation.* 2000;101(14):1643-1646.

101. Cerqueira MD, Stratton JR, Vracko R, et al. Noninvasive arterial thrombus imaging with Tc-99m monoclonal antifibrin antibody. *Circulation.*1992;85(1):298-304.

102. Matter CM, Schuler PK, Alessi P, et al. Molecular imaging of atherosclerotic plaques using a human antibody against the extra-domain B of fibronectin. *Circ Res.* 2004;95(12):1225-1233.

103. Yagle KJ, Eary JF, Tait JF, et al. Evaluation of F-18 annexin V as a PET imaging agent in an animal model of apoptosis. *J Nucl Med.* 2005;46(4):658-666.

104. Li X, Link JM, Stekhova S, et al. Site-specific labeling of annexin V with F-18 for apoptosis imaging. *Bioconjugate Chem.* Aug 2008;19(8):1684-1688.

105. Thomas DM, Elferink LA. Functional analysis of the C2A domain of synaptotagmin 1: implications for calcium-regulated secretion. *J Neurosci.* 1998;18(10):3511-3520.

106. Zhao M, Zhu X, Ji S, et al. Tc-99m labeled C2A domain of synaptotagmin I as a target-specific molecular probe for noninvasive imaging of acute myocardial infarction. *J Nucl Med.* 2006;47(8):1367-1374.

107. Tavare R, Torres Martin De Rosales R, Blower PJ, et al. Efficient site-specific radiolabeling of a modified C2A domain of synaptotagmin I with [99mTc(CO)3]+: a new radiopharmaceutical for imaging cell death. *Bioconjugate Chem.* 2009;20(11):2071-2081.

108. Giersing BK, Rae MT, CarballidoBrea M, et al. Synthesis and Characterization of 111In−DTPA−N-TIMP-2: A Radiopharmaceutical for Imaging Matrix Metalloproteinase Expression. *Bioconjugate Chem.* 2001;12(6):964-971.

109. Woollard KJ, Geissmann F. Monocytes in atherosclerosis: subsets and functions. *Nat Rev Cardiol.* 2010;7(2):77-86.

110. Berliner JA, Navab M, Fogelman AM, et al. Atherosclerosis: basic mechanisms. Oxidation, inflammation, and genetics. *Circulation.* 1995;91(9):2488-2496.

111. Kircher MF, Grimm J, Swirski FK, et al. Noninvasive in vivo imaging of monocyte trafficking to atherosclerotic lesions. *Circulation.* 2008;117(3):388-395.

112. Derlin T, Richter U, Bannas P, et al. Feasibility of F-18 sodium fluoride PET/CT for imaging of atherosclerotic plaque. *J Nucl Med.* 2010;51(6):862-865.

113. Li Y, Berenji GR, Shaba WF, et al. Association of vascular fluoride uptake with vascular calcification and coronary artery disease. *Nucl Med Commun.* 2012;33(1):14-20.

114. Derlin T, Wisotzki C, Richter U, et al. In vivo imaging of mineral deposition in carotid plaque using F-18 sodium fluoride PET/CT: correlation with atherogenic risk factors. *J Nucl Med.* 2011;52(3):362-368.

115. Dweck MR, Chow MW, Joshi NV, et al. Coronary arterial F-18 sodium fluoride uptake: a novel marker of plaque biology. *J Am Coll Cardiol.* 2012;59(17):1539-1548.

116. Quirce R, Martinez-Rodriguez I, De Arcocha Torres M, et al. Contribution of 18F-sodium fluoride PET/CT to the study of the carotid atheroma calcification. *Revista espanola de medicina nuclear e imagen molecular.* Jan 2013;32(1):22-25.

117. Joshi NV, Vesey AT, Williams MC, et al. F-18 fluoride positron emission tomography for identification of ruptured and high-risk coronary atherosclerotic plaques: a prospective clinical trial. *The Lancet.* 2014;383(9918):705-713.

118. Blau M, Nagler W, Bender MA. Fluorine-18: a new isotope for bone scanning. *J. Nucl. Med.*1962;3:332-334.

119. Piert M, Zittel TT, Becker GA, et al. Assessment of porcine bone metabolism by dynamic. *J Nucl Med.* 2001;42(7):1091-1100.

120. Cherry SR. Multimodality in vivo imaging systems: twice the power or double the trouble? *Annual review of biomedical engineering.* 2006;8:35-62.

121. Kuhl DE, Hale J, Eaton WL. Transmission scanning: a useful adjunct to conventional emission scanning for accurately keying isotope deposition to radiographic anatomy. *Radiology.* 1966;87(2):278-284.

122. Fricke E, Fricke H, Weise R, et al. Attenuation correction of myocardial SPECT perfusion images with low-dose CT: evaluation of the method by comparison with perfusion PET. *J Nucl Med.* 2005;46(5):736-744.

123. Kinahan PE, Townsend DW, Beyer T, Sashin D. Attenuation correction for a combined 3D PET/CT scanner. *Med Phys* 1998;25(10):2046-2053.

124. Jarritt PH, Carson KJ, Hounsell AR, Visvikis D. The role of PET/CT scanning in radiotherapy planning. *Brit J Radiol.* 2006;79 Spec No 1:S27-35.

125. Shao Y, Cherry SR, Farahani K, et al. Development of a PET detector system compatible with MRI/NMR systems. *IEEE T Nucl Sci.* 1997;44(3):1167-1171.

126. Pichler BJ, Kolb A, Nagele T, Schlemmer HP. PET/MRI: paving the way for the next generation of clinical multimodality imaging applications. *J Nucl Med.* 2010;51(3):333-336.

127. Choi J-s, Park JC, Nah H, et al. A Hybrid Nanoparticle Probe for Dual-Modality Positron Emission Tomography and Magnetic Resonance Imaging. *Angew Chem Intern Edit.* 2008;47(33):6259-6262.

128. Nahrendorf M, Zhang H, Hembrador S, et al. Nanoparticle PET-CT imaging of macrophages in inflammatory atherosclerosis. *Circulation.* 12/24 2008;117(3):379-387.

129. Hwang do W, Ko HY, Kim SK, Kim D, Lee DS, Kim S. Development of a quadruple imaging modality by using nanoparticles. *Chemistry (Weinheim an der Bergstrasse, Germany).* 2009;15(37):9387-9393.

130. Torres Martin de Rosales R, Tavaré R, Glaria A, Varma G, Protti A, Blower PJ. Tc-99m Bisphosphonate-Iron Oxide Nanoparticle Conjugates for Dual-Modality Biomedical Imaging. *Bioconjugate Chem.* 2011/03/16 2011;22(3):455-465.

131. Cui X, Belo S, Kruger D, et al. Aluminium hydroxide stabilised MnFe2O4 and Fe3O4 nanoparticles as dual-modality contrasts agent for MRI and PET imaging. *Biomaterials.* Jul 2014;35(22):5840-5846.

132. Cai W, Chen K, Li ZB, Gambhir SS, Chen X. Dual-function probe for PET and near-infrared fluorescence imaging of tumor vasculature. *J Nucl Med.* 2007;48(11):1862-1870.

133. Russell RG, Watts NB, Ebetino FH, et al. Mechanisms of action of bisphosphonates: similarities and differences and their potential influence on clinical efficacy. *Osteoporosis Int.* 2008;19(6):733-759.

134. Lomashvili KA, Cobbs S, Hennigar RA, et al. Phosphate-induced vascular calcification: role of pyrophosphate and osteopontin. *J Am Soc Nephrol.* 2004;15(6):1392-1401.

135. Subramanian G, Mc Afee J, Blair R, et al. Technetium-99m-methylene diphosphate - a superior agent for skeletal imaging: comparison with other tecnetium complexes. *J Nucl Med.* 1975;16(8):744 - 755.

136. Love C, Din AS, Tomas MB, et al. Radionuclide bone imaging: an illustrative review. *Radiographics.* 2003;23(2):341-358.

137. Lantto T, Jarvi K, Toivio I, et al. The visualization of femoral vessels in delayed bone scans--a sign of arteriosclerosis? A comparison of Tc-99m MDP and Tc-99m DPD. *Eur J Nucl Med.*1989;15(5):265-268.

Chapter 3: Do radiolabeled bone seeking agents bind with minerals present in vascular calcification? An *in vitro* study.

3.1 Introduction

Although there have been significant advances in clinical *in vivo* imaging of vascular calcification, the earliest stages of calcification cannot be detected on a cellular and molecular level.[1] This is primarily due to the unavailability of suitable molecular imaging agents that detect early markers of calcification. Currently the gold standard for *in vivo* imaging of vascular calcification is electron beam computed tomography and multi-slice computed tomography.[2] However, these x-ray based imaging modalities depict the morphological changes in the anatomy depending on the changes in density of the organs. The early changes in the process of mineralisation are subtle and do not cause significant change in density to be detected by CT. This was demonstrated by Shroff *et al*. on patients with chronic kidney disease.[3] They demonstrated that molecular changes

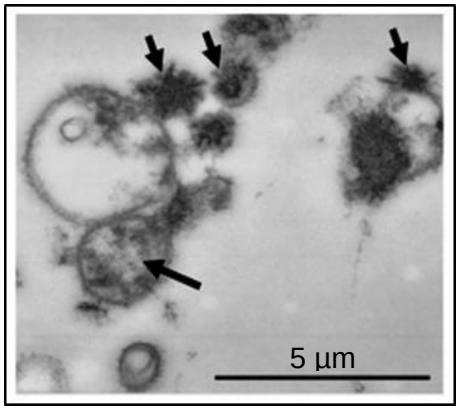

Figure 3.1: Transmission EM image of matrix vesicles (MV's) released into the extracellular matrix in response to cell death. These are the structures that form the nidus for calcification in the vessel wall. Kapustin et al. Circulation Research.2011; 109: e1-e12

that result in calcification begin as early as the pre-dialysis stages but remain clinically silent and cannot be diagnosed with CT. It has also been established that dialysis induces apoptosis and subsequent release of ABs and MVs which eventually results in overt calcification.[3]

MVs are membrane-bound vesicles produced by budding from chondrocytes, osteoblasts and odontoblasts. Chondrocytes are a unique cell type in articular cartilage tissue and are essential for cartilage formation and functionality.[4] Osteoblasts are specialised mesenchymal cells that are essential for bone resorption.[5] Odontoblasts are the cells responsible for the formation of dentine, the collagen-based mineralised tissue that forms the bulk of teeth.[6] MVs contain the necessary calcium-binding proteins and phosphatases for nucleation of hydroxyapatite and initiate calcification in bone formation and mineralising cartilage.[3] Ultrastructural study of young healthy arteries and calcified arteries obtained from patients with atherosclerosis and CKD shows the presence of hydroxyapatite minerals only in a subset of MVs of the calcified arteries but not in young healthy arteries.[4] MVs and ABs form a nidus for calcification.[7-9] ABs are released by dying VSMC's, promoting the release of MVs in the extracellular matrix (see Figure 3.1).

Calcium plays an important role in inducing apoptosis and in the formation and release of hydroxyapatite-laden matrix vesicles. *In vitro* treatment of VSMCs with high calcium conditions induces apoptotic cell death which results in release of more calcium.[7, 8] This leads to a vicious cycle of apoptosis, release of calcium, release of ABs and MVs resulting in overt calcification. High cytosolic calcium levels can change the intrinsic properties of VSMC-derived MVs and induce them to calcify. High calcium levels lead to annexin 6-phosphatidylserine nucleation complexes and enhanced matrix metalloproteinase-2 activity, which leads to elastin degradation and calcification. More importantly, exposure to high calcium levels will eventually deplete the endogenous

calcification inhibitor, MGP, from matrix vesicles, when vesicles contain preformed crystalline hydroxyapatite or become mineralisation competent, thereby promoting further calcification.[9]

The role of calcification in plaque rupture has been under debate; however in recent times a consensus has been developed that microcalcification is associated with plaque vulnerability, whereas homogeneous or sheet-like calcification macrocalcification favours plaque stabilisation.[10-14] MVs and ABs with nano-crystals of HA are potential targets to detect vascular calcification in its early stages. Small animal imaging (optical) with Pam78 (OsteoSense750/OS750, VisEn Medical Inc, Woburn), a fluorescent bisphosphonate conjugate, have been used to target the nano-crystals of hydroxyapatite for *in vivo* whole body imaging of vascular calcification.[15-17]

Radiolabeled bisphosphonates are clinically used as bone imaging agents and there are incidental findings of extra osseous uptake of the radiotracer associated with vascular calcification reported in the literature. However, the avenue has not been pursued clinically as a means of detecting vascular calcification, and novel radiolabeled bisphosphonates with higher binding potency and *in vivo* stability could be potential imaging agents to target the hydroxyapatite nano-crystals.

In this study we have performed *in vitro* binding experiments to evaluate the possibility of using novel radiolabeled bisphosphonate derivatives for imaging vascular calcification. *In vitro* studies provide a fast and cost-effective means to study the pharmaceutical interaction with the targets and generate data to support the hypothesis, and to provide ethical justification for *in vivo* studies.

3.2 Materials and Methods

3.2.1 Radiopharmaceuticals: Synthesis & Quality Control (QC)

^{18}F- NaF: ^{18}F-NaF was supplied by the PET Radiochemistry Laboratory at the St. Thomas' PET Centre. ^{18}F-fluoride was produced by irradiation of [^{18}O]-water (97 atom%, Isochem Ltd., Hook, UK) with 11 MeV protons from a CTI RDS 112 cyclotron (beam current 30 μA). The solution in [^{18}O]-water was diluted with sterile water (500 MBq, 5 mL) and used without further purification.

^{99m}Tc-MDP: ^{99m}Tc-MDP (1000 MBq in 100 μL), prepared by reconstitution of a Draximage kit with $^{99m}TcO_4^-$ eluted from a generator with physiological saline), was supplied by Guy's Hospital Radiopharmacy, Guy's and St Thomas' NHS Trust.

^{99m}Tc-DPA Ale ^{99m}Tc-DPA Ale was synthesised and characterised by a two-step chemical reaction described previously.[10] Firstly, $[^{99m}Tc(CO)_3(H_2O)_3]^+$ was prepared by injecting 1 ml of $^{99m}TcO_4^-$ (500 MBq) into tricarbonyl kit vial (Carbonyl labelling agent; Mallinckrodt Medical) and placing it in a heating block maintained at 90^{o}C. After 30 min of heating the kit was placed in the ice bath and neutralised by adding 120 μL of 1 M HCl into the vial. The pH of the solvent was measured using a pH paper (pH 6.5-7). QC was performed using TLC and **solvent system 1:** 1% HCl in methanol (MeOH) as the solvent. TLC analysis was carried out on glass-backed TLC silica gel 60 plates (Merck 1.15326.0001) with 1% HCl in methanol as the mobile phase. Radio-TLC chromatograms were analysed with a Mini-Scan TLC scanner (Bioscan) and Laura 4.0.2.75 (Lablogic) software.

In the second step, 50 μg of DPA Ale in 300 μL of 50 mM carbonate buffer (pH = 9, [NaCl] = 0.15 M) was mixed with 300 μL of an aqueous solution of $[^{99m}Tc(CO)_3(H_2O)_3]^+$ (250-300 MBq) in a glass vial with a rubber stopper and heated at 90 ºC for 30 min. The vial

was allowed to cool in an ice bath. The final compound was then analysed for radiochemical purity by radio-TLC using **solvent system 1.**

^{99m}Tc-N(DTCBP)$_2$: 800-1000 MBq $^{99m}TcO_4^-$ generator eluate (in 1 mL saline) was added to a lyophilised SDH kit vial (generous gift of Prof. Roberto Pasqualini, Cis Biointernational, IBA Group, Gif-sur-Yvette, France, as previously used for production of ^{99m}Tc-NOET) and incubated for 30 minutes at room temperature. The composition of the kit vial was as follows: SDH 5.0 mg; stannous dichloride dihydrate 0.10 mg; DPTA 5.0 mg; sodium dihydrogen phosphate monohydrate 0.6 mg; disodium phosphate heptahydrate 10.9 mg; under a dinitrogen atmosphere. Quality control was performed using TLC with solvent system 1. 500 µL of the resulting solution was then added to 500 µL of the of DTC-BP ligand (1 mg mL^{-1}) in carbonate buffer (pH 10). The vial was incubated at 60 °C for 30 minutes. QC was performed using TLC with solvent system 2. TLC analysis was performed on silica gel aluminium-backed TLC plates (Merck 1.16834.0001) using **solvent system 2:** Methanol + 1% of a 60% solution of HEDP (Sigma H6773). Silica gel plates were spotted with the sample on the origin and the spot was allowed to dry before development in the mobile phase. The chromatograms were analysed with Mini-Scan TLC and Laura 4.0.2.75 (Lablogic) software.

3.2.2 Binding measurements with minerals from human intimal plaques, medial plaques and equine (horse) bone

Rachel C. Murray of the Animal Health Trust provided us with the equine bone sample. Isolated minerals from human vessels with intimal calcifications medial calcifications were used. The minerals were left over from a previous study. The methods to release these biominerals from their organic matrix and connective tissues have been previously published.[18] Synthetic hydroxyapatite was purchased from Sigma-Aldrich. Binding study was performed with synthetic hydroxyapatite, powdered equine bone and powdered

minerals isolated from human intimal and medial plaques. A stock solution of 1 mg/mL of minerals was prepared by adding 100 mg of each of the minerals to 100 mL double distilled (dd) water in a 250 mL Duran borosilicate glass bottle. Suspensions of 0.5, 0.2, 0.1, 0.05 and 0.02 mg/mL of each sample were prepared in distilled water. 1 mL of the suspensions in triplicate (synthetic hydroxyapatite, powdered equine bone, medial and intimal arterial minerals) was placed in 1.5 mL eppendorf tubes alongside mineral-free controls. 20 µL of ^{99m}Tc-MDP, ^{99m}Tc-DPA Ale and ^{99m}Tc-N(DTCBP)$_2$ and ^{18}F-NaF (0.5-1 MBq) was added to each tube. The tubes were incubated for 5, 20 and 60 min in a shaker at 37 ºC and 550 RPM. The tubes were centrifuged at 13,200 RPM for 5 minutes. 50 µL of the supernatant from the vials were pipetted out and counts were measured in a gamma counter.

The percentage of the radioactivity bound to the mineral was calculated using the following equation:

$$\textbf{Binding}\ (\%) = \left[1 - \left(\frac{\textbf{cpm in sample aliquot}}{\textbf{cpm in standard aliquot}}\right)\right] \times 100$$

3.2.3 Tissue Culture

All chemicals and reagents used were purchased from Sigma Aldrich (Gillingham, UK). Human aortic vascular smooth muscle cells (VSMC) immortalised with SV40 large T antigen (VSMC-SV40) were used in the experiments. The cells were grown in culture medium (M199-Sigma Aldrich M2154), supplemented with 100 IU/mL penicillin, 100 mg/mL streptomycin and 4 mmol/L of L-glutamine. The flasks were placed in an incubator maintained at 37 ^{o}C with 5% CO_2. Cells were divided into new flasks when they reached 80% confluence.

3.2.4 *In vitro* model of calcification in VSMC: Media & Treatment

Human vascular smooth muscle cells immortalised with SV-40 large T-antigen (VSMC-SV40) were cultured in M199 medium supplemented with 20% FCS and antibiotics. VSMC were grown to 80% confluence and grown in Dulbecco's Modified Eagle's Salt Medium (DMEM) with 0.1% BSA. After starving the cells of serum for 24 h, the cells were washed in Earle's Balanced Salt Solution (EBSS) and treated with control (no Ca/Pi) or test media containing high calcium (Ca media; 2.0 and 3.0mM Ca) and high phosphate (Pi media; 1.5mM Pi).

3.2.5 Isolation of apoptotic bodies & matrix vesicles

Confluent VSMC were washed twice with EBSS and treated with a serum free media that contained 0.1% BSA in DMEM. After 24 h, the medium was pipetted out and a freshly prepared calcium phosphate-rich media with 0.1% BSA in DMEM was introduced to the cells. 24 h later the medium was pipetted out and spun at 2500 rpm for 5 min in a Sorvall RF7 centrifuge to remove the apoptotic bodies (AB) which form a pellet. The supernatant was collected to harvest the matrix vesicles (MV) by centrifugation at 45,000 rpm for 40 min at 4°C in a Beckman Ultracentrifuge (125647g). The cells left in the flask were scraped, re-suspended in EBSS and centrifuged (2000 rpm for 5 min) to obtain a pellet of cell debris. The MVs, ABs and the cell debris were collected in Eppendorf tubes and stored at -80^{o}C for further use.

3.2.6 Bicinchoninic acid (BCA) protein assay:

Micro-plate (BCA) protein assay was performed using a Protein Assay Kit (Bio-rad) to determine the protein concentrations in the apoptotic bodies. 8 serial dilutions of bovine serum albumin (BSA) standard (1.54 mg/mL) were prepared in 200 µL of PBS. The ABs obtained was resuspended in 300 µL of PBS. 5 µL of the BSA standards and the ABs

were transferred on to a 96 well plate and 25 µL of reagent A and 200 µL of reagent B was added. The plate was incubated in the dark for 5 minutes for the reaction to occur and then the absorbance of all samples was measured at 750 nm. A standard graph was obtained using the values and concentrations of the known BSA standard and the unknown concentrations were calculated.

3.2.7 ^{45}Ca assay

A previously established method by Hashimoto *et al*. was used to measure calcium deposition in the MVs and ABs.[19] A standard reaction medium or calcifying medium consisting 50 mM TES (*N*-tris(hydroxymethyl) methyl-2-amino-ethanesulfonic acid) at pH 7.65 (37 °C) with 2.2 mM $CaCl_2$ (50,000 cpm of ^{45}Ca), 1.6 mM KH_2PO_4, 1 mM ATP disodium salt, 1 mM $MgCl_2$, 85 mM NaCl, 15 mM KCl and 10 mM $NaHCO_3$ was prepared. The medium was then filtered with a 0.22 µm membrane (Millipore). MVs (10 µg of protein) and ABs (20 µg protein) isolated from control and calcified VSMC were added to 500 µL of calcifying medium and incubated in a water bath at 37 °C for 24 hrs. After the incubation period the samples were centrifuged at 13,200 rpm from 20 min in a microcentrifuge. The supernatant was pipetted out and collected into vials containing 4 mL of scintillation liquid (ScintiSafe™ Econo 2 cocktail, Fisher Scientific). The pellet obtained was washed with 250 µL cold calcifying medium, vortexed, centrifuged and the supernatant was collected into respective vials. The washing step was performed twice following which 250 µL of 0.1M HCl was added into it and allowed to incubate for 1 h at room temperature. To neutralise the sample, 250 µL of 0.1 M NaOH and 0.1% SDS were added into the vial. The samples were vortexed and pipetted into vials with scintillation liquid. Using a Beckman liquid scintillation counter the activity in the supernatant and the pellet was counted.

3.2.8 Binding study with ABs – *In vitro* and *in situ*:

In vitro: ABs were isolated from control VSMC's cultured in a serum free medium and VSMC's treated with elevated levels of Ca and Pi. Triplicates of 150 µg, 100 µg, and 50 µg, of protein equivalents were pipetted out and resuspended in eppendorf tubes containing 500 µL of PBS. The tubes were then incubated with the radiopharmaceuticals (50 µL) on a shaker maintained at 550 RPM and 37°C. After 60 minutes of incubation the Eppendorf tubes were centrifuged at 13,200 RPM for 5 min and 50 µL of the supernatant was pipetted out and counts were measured. Using the above mentioned equation the binding efficiencies were calculated.

In situ: Radiotracers (50 µL; 0.5-1 MBq) were added into T-75 flasks (n = 3) of VSMC cultured in a serum free medium and VSMC treated with elevated levels of Ca and Pi. After an incubation of 1 h the ABs were isolated by centrifuging the medium 13,200 RPM for 5 min. The pellet was transferred to eppendorf tubes, washed twice with PBS and then the tubes were scanned in a SPECT-CT scanner (Bisocan, NanoSPECT) or a PET-CT scanner (Bisocan, NanoPET).

3.3 Results

3.3.1 Radiolabeling and Quality control

The preparation of ^{99m}Tc-DPA Ale and ^{99m}Tc-N(DTCBP)$_2$ is schematically shown in Figure 3.2. For radiochemical purity analysis TLC (Figure 3.3, A-D) was performed with the intermediate as well as the final compound. For ^{99m}Tc-DPA Ale radio-TLC **solvent system 1** on silica plates was performed (intermediates: reduced hydrolysed technetium, Rf = 0; [^{99m}Tc(CO)$_3$(H$_2$O)$_3$]$^+$, Rf = 0.1-0.7; pertechnetate, Rf = 0.9; product, [^{99m}Tc-DPA Ale], Rf = 0]). Radiochemical purity of the final product was >99%. TLC with **solvent system 2** was used for the quality control of the intermediate (^{99m}Tc-N)$^+$ complex reduced

hydro lysed technetium, Rf = 0; required technetium nitride intermediate and pertechnetate, Rf = 0.9) as well as the final compound ^{99m}Tc-N(DTCBP)$_2$ (reduced hydrolysed technetium and ^{99m}Tc-N(DTCBP)$_2$, Rf = 0; required technetium nitride intermediate and pertechnetate, Rf = 0.9)

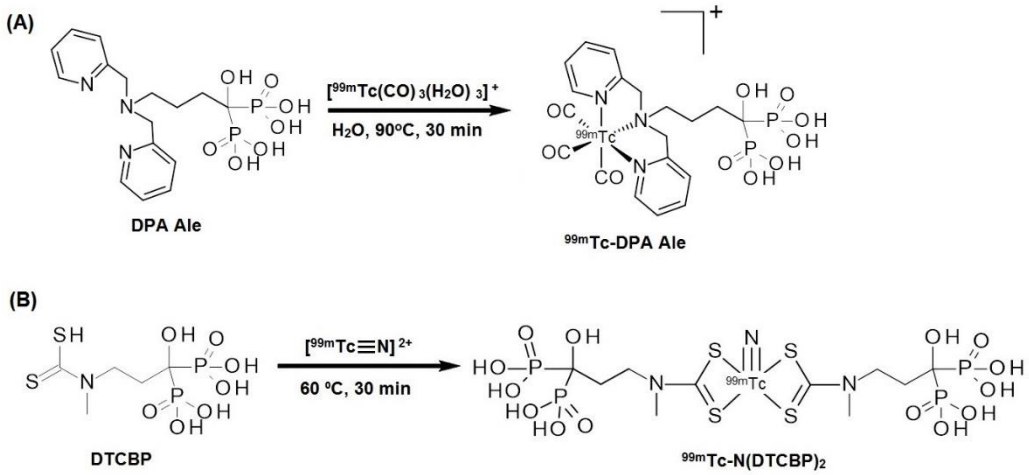

Figure 3.2: Synthesis of (A) ^{99m}Tc-DPA Ale and (B) ^{99m}Tc-N(DTCBP)$_2$

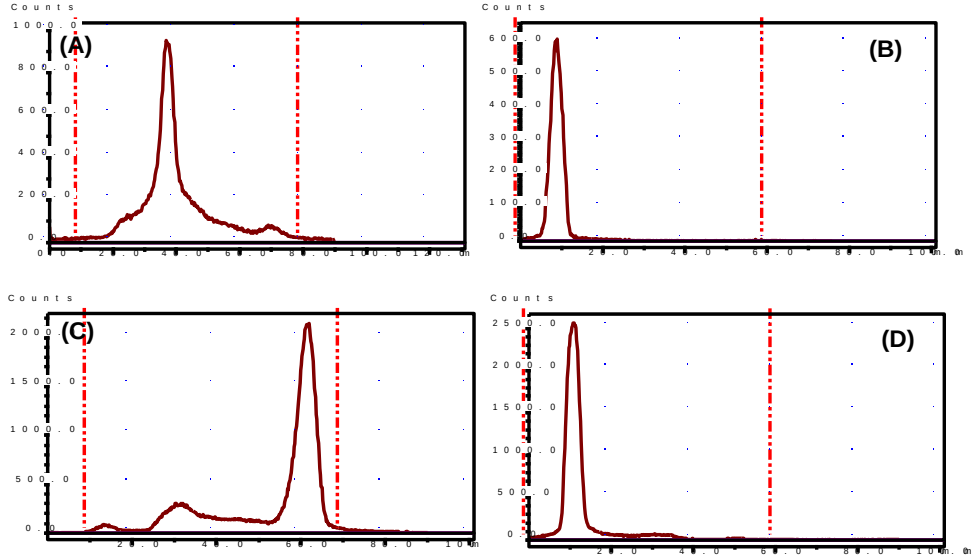

Figure 3.3: Radio-TLC chromatograms on silica gel coated glass plates of (A) [^{99m}Tc(CO)$_3$(H$_2$O)$_3$]$^+$ Rf = 0.1-0.7 and [^{99m}TcO$_4^-$] Rf = 0.9, solvent system 1; (B): [^{99m}Tc-DPA-Ale], Rf = 0], solvent system 1 (demonstrating the absence of pertechnetate and [^{99m}Tc(CO)$_3$(H$_2$O)$_3$]$^+$ at this stage); Radio-TLC chromatograms on silica gel coated glass-backed aluminium plates (C): ^{99m}TcN^{2+} intermediate and pertechnetate Rf = 0.9, solvent system 2 and (D): ^{99m}Tc-N(DTCBP)$_2$ Rf = 0, solvent system 2 (demonstrating the absence of both pertechnetate and ^{99m}TcN^{2+} intermediate in the final product).

3.3.2 Binding with synthetic HA

Binding studies were performed with different concentrations of synthetic HA for three time points: 5 min, 20 min and 60 min (See Figure 3.4 A-D). The radiotracers bound with the synthetic HA in a concentration-dependent manner. Highest radiotracer binding was observed with 0.5 mg/mL of synthetic HA and the binding percentage dropped with a drop in the concentration.

After 5 minutes of incubation with 0.5 mg/mL of synthetic HA the binding percentages were 93.1 ± 0.04%, 88.3 ± 1.1%, 87.3 ± 1.9% and 84.7 ± 1.7% for ^{99m}Tc-MDP, ^{18}F-NaF, ^{99m}Tc-DPA Ale and ^{99m}Tc-N(DTCBP)$_2$ respectively, whereas, with a concentration of 0.02 mg/mL the binding percentage after 5 min of incubation were 6.28 ± 2.7%, 26 ± 3.5%, 78.2 ± 2.6% and 20.7 ± 1.8%.

After 60 minutes of incubation the binding percentage measured were 91.9 ± 3.2%, 96.4 ± 1.1%, and 97.1 ± 1.7 and 94.6 ± 3.0% respectively with 0.5 mg/mL, and with 0.02 mg/mL concentration of synthetic HA, the binding percentage were 11.5 ± 1.2%, 35.35 ± 2.6%, 87.8 ± 2.7% and 34.5 ± 9.3%respectively.

In comparison to the other radiotracers used for the experiment, ^{99m}Tc-DPA Ale had the highest propensity to bind with synthetic HA both at low and high concentrations.

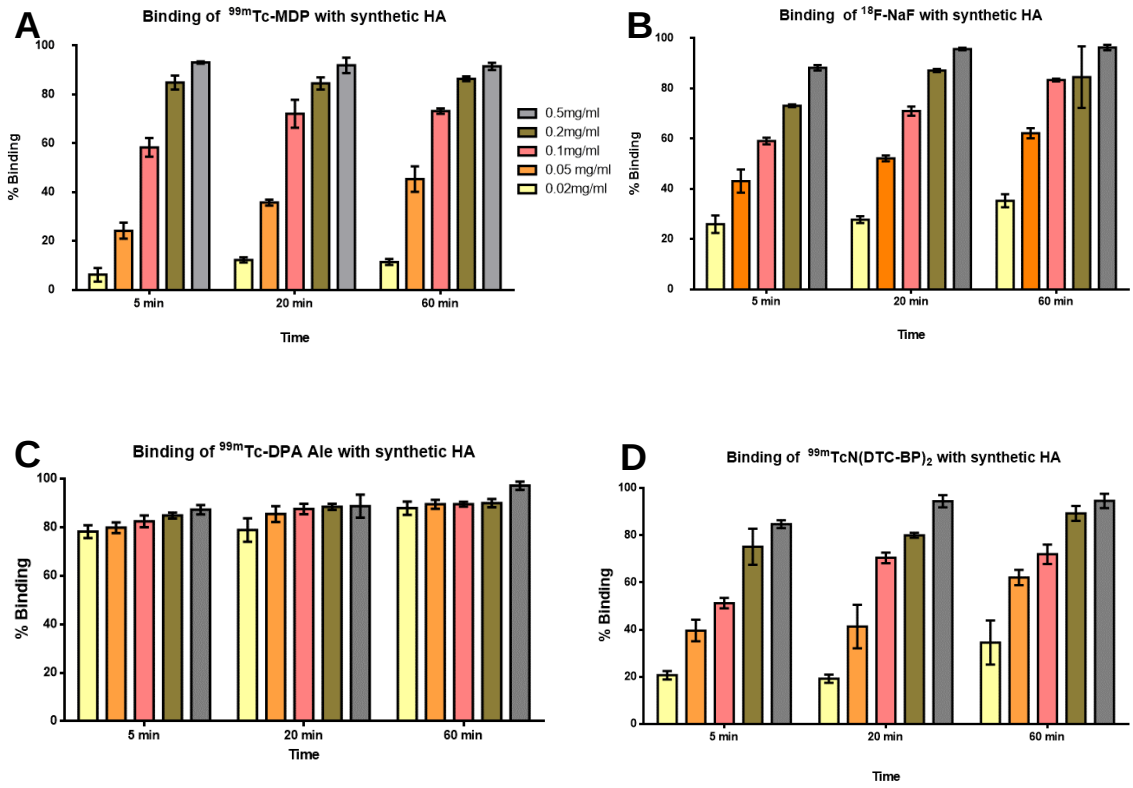

Figure 3.4: (A-D): Binding percentages (Mean ± SD, n=3) of the radiopharmaceuticals plotted against the concentration of synthetic hydroxyapatite.

3.3.3 Binding with powdered equine bone and minerals isolated from intimal and medial calcified plaques:

In vitro binding studies (Figure 3.5; A-C) were performed to evaluate the binding efficiencies of the radiopharmaceuticals ^{18}F-sodium fluoride, ^{99m}Tc- MDP, ^{99m}Tc-DPA Ale and ^{99m}Tc-N(DTCBP)$_2$] with minerals from intimal and medial calcification and bones. The results obtained were plotted as graphs with binding efficiencies (mean ± SD, n = 3) against the concentrations of minerals used. The concentrations of minerals used for the experiments were 0.5 mg/mL, 0.2 mg/mL, 0.1 mg/mL, 0.05 mg/mL and 0.02 mg/mL.

^{18}F-fluoride: After incubation for 60 min the binding percentages of ^{18}F-fluoride with 0.5 mg/mL of medial and intimal minerals and powdered equine bones were 83 ± 6%, 35 ± 8% and 63 ± 4% whereas the binding efficiency with 0.02 mg/mL of the same were 22 ± 10%, 16 ± 2% and 11 ± 3%.

^{99m}Tc-MDP: With 0.5 mg/mL of medial minerals, ^{99m}Tc-MDP had the highest binding percentage of 98 ± 1%. On the other hand the binding percentages with 0.5 mg/mL intimal mineral and crushed bone the binding efficiencies were 56 ± 5% and 90 ± 1%.

The binding percentages with 0.02 mg/mL of medial minerals, intimal minerals and powdered bone were 50 ± 11%, 6 ± 3% and 15 ± 2%.

^{99m}Tc-DPA Ale: In comparison to the other radiopharmaceuticals used in the experiment, ^{99m}Tc-DPA Ale showed higher binding percentages with the minerals in almost all concentrations. Binding percentage of 94 ± 1% was achieved with 0.5 mg/mL of medial minerals in 60 min incubation time. The binding percentages with similar concentration of medial mineral and powdered equine bone were 74 ± 3% and 88 ± 2%.

On the other hand the binding percentage with 0.02 mg/mL were measured to be 82 ± 6% (medial minerals), 52 ± 10% (intimal minerals) and 10 ± 8% (powdered bone) respectively.

^{9m}Tc-N(DTCBP)2: The binding percentage with 0.5 mg/mL of intimal minerals and powdered equine bone were 24 ± 7% and 51 ± 5% respectively.

The binding percentages of radiopharmaceuticals can be ranked as:

1. Powdered bone: ^{99m}Tc-DPA Ale ≈ ^{99m}Tc-N(DTCBP)$_2$ ≈ ^{18}F-NaF ≈ ^{99m}Tc-MDP
2. Medial minerals: ^{99m}Tc-DPA Ale > ^{99m}Tc-N(DTCBP)$_2$ > ^{18}F-NaF > ^{99m}Tc-MDP
3. Intimal minerals: ^{99m}Tc-DPA Ale >^{18}F-NaF > ^{99m}Tc-N(DTCBP)$_2$ > ^{99m}Tc-MDP

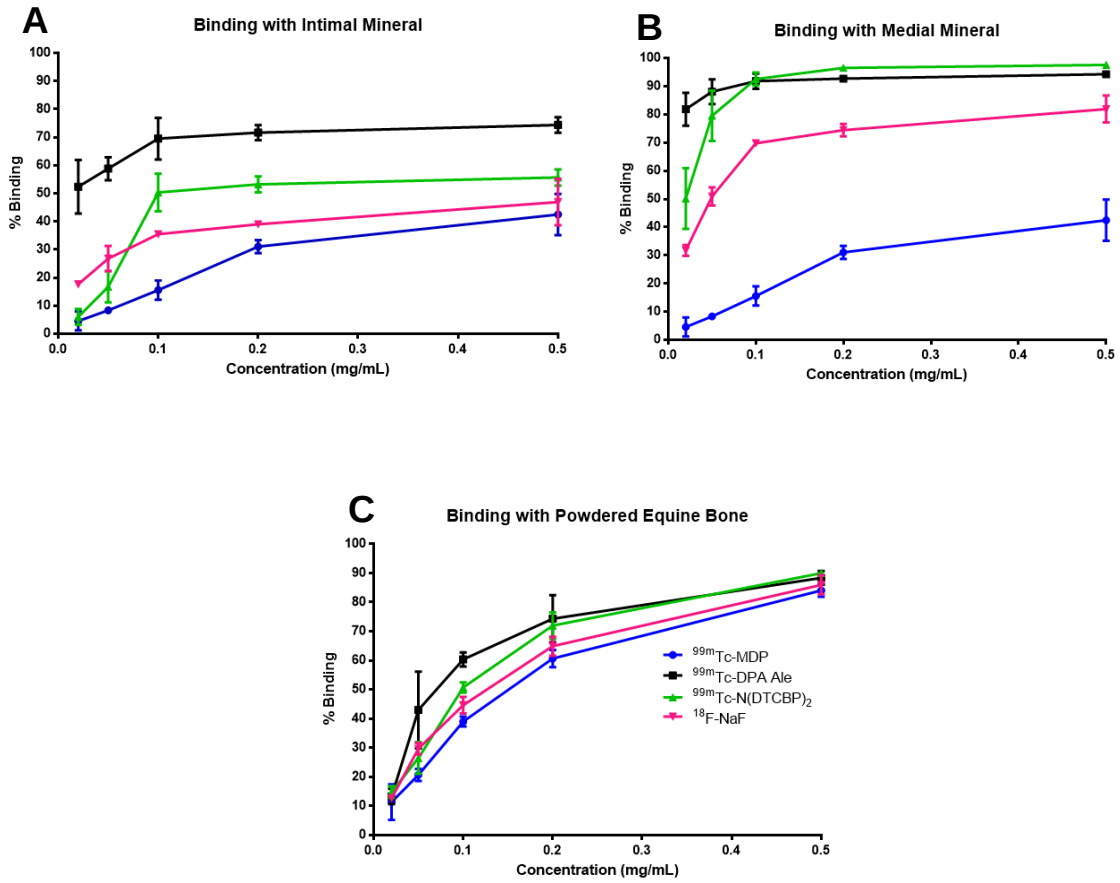

Figure 3.5: *In vitro* binding studies to evaluate the binding percentages of the radiopharmaceuticals ^{18}F-sodium fluoride (Pink), ^{99m}Tc-MDP (Blue), ^{99m}Tc-DPA-Ale (Black) and ^{99m}Tc-N(DTCBP)$_2$ (Green) with minerals isolated from (A) intimal and (B) medial calcified plaques and (C) powdered equine bone. The graphs represents binding percentages (mean ± SD, n = 3) against the concentrations of minerals used. The concentrations of minerals used for the experiments were 0.5 mg/mL, 0.2 mg/mL, 0.1 mg/mL, 0.05 mg/mL and 0.02 mg/mL. The binding percentages were calculated after an incubation periods of 60 minutes.

3.3.4 *In vitro* and *in situ* binding with ABs

In vitro binding experiments were performed with ABs isolated from VSMCs maintained in normal medium and medium with elevated levels of calcium and phosphate. BCA protein assay was employed to determine the protein concentrations. Protein equivalents of 0.15 mg, 0.10 mg and 0.05 mg were used for the binding experiments. Simultaneously, ^{45}Ca assay was performed using 5-10 µL (10 µg protein) of the isolated ABs. The latter assay confirmed that the ABs used in the experiments was calcified with more than 50% of the ^{45}Ca bound to the ABs within 24 hours of incubation.

Results (See Figure 3.6) show that ^{99m}Tc-N(DTCBP)$_2$ had the highest binding efficiency of >90% with protein weights of 0.15 mg/mL, 0.10 mg/mL and 0.05 mg/mL. ^{99m}Tc-DPA-Ale and ^{18}F-NaF had a binding percentage of 82 ± 2% and 81 ± 2% with 0.15 mg/mL, 81 ± 1% and 79 ± 3% with 0.10 mg/mL and 76 ± 3%, and 70±3% with 0.05 mg/mL of AB protein equivalent. Except for ^{18}F-NaF, the other radiopharmaceuticals showed 10-20% of binding with the control ABs. This may be due to non-specific protein binding properties of the ^{99m}Tc-labelled bisphosphonates.

The nano SPECT-CT scan (Figure 3.7) performed on the isolated ABs from the *in situ* binding study showed the uptake of radiotracers only in the ABs isolated from the calcified VSMCs. On the contrary there was no uptake of radiotracer in the ABs obtained from control VSMCs.

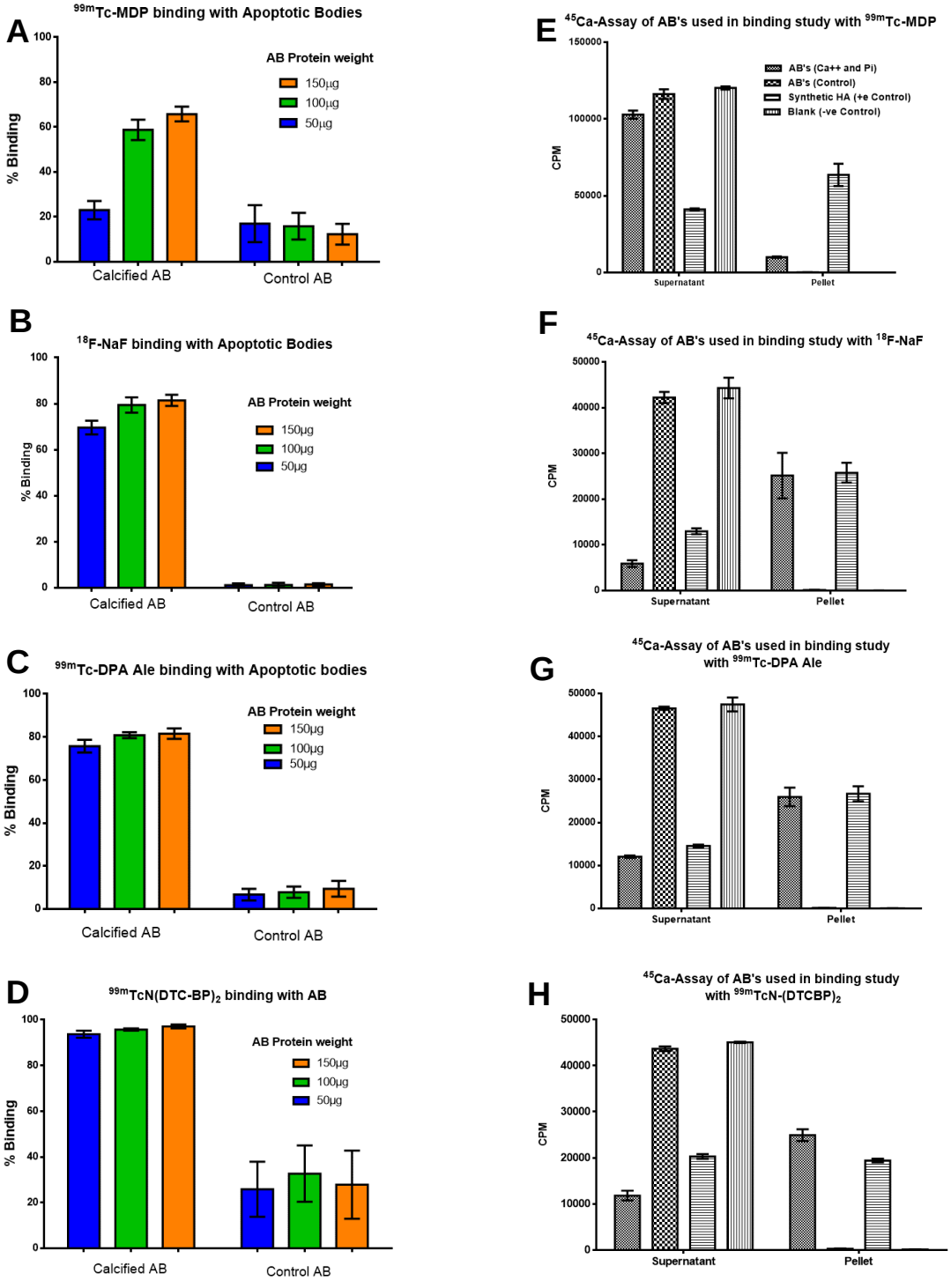

Figure 3.6: (A-D) Binding percentages of radiotracers (A) ^{99m}Tc-MDP, (B) ^{18}F-fluoride, (C) ^{99m}Tc-DPA-Ale and (D) ^{99m}Tc-N(DTCBP)$_2$ with isolated ABs from calcified and control VSMC. (E-H) ^{45}Ca-Assay of the ABs used for the *in vitro* binding study confirming that the ABs were calcified.

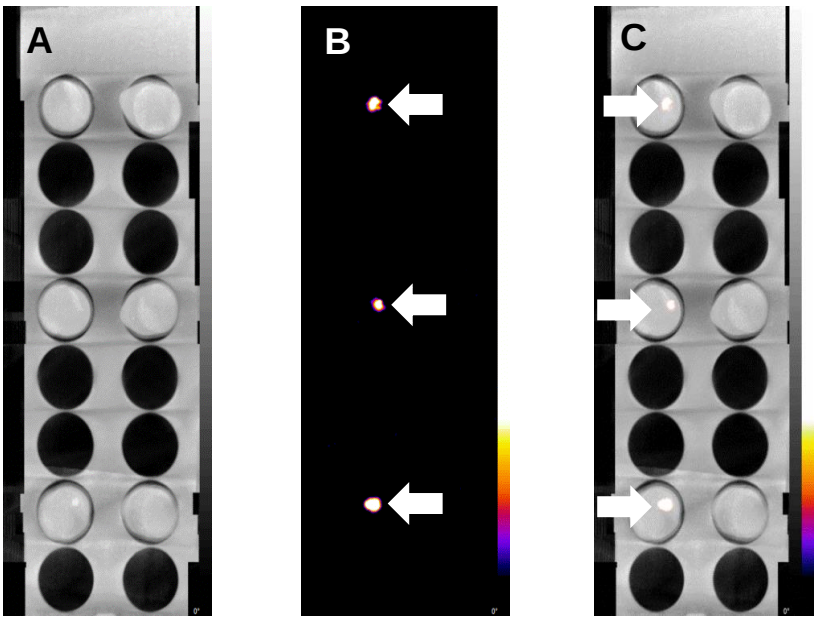

Figure 3.7: *In situ* studies were performed by adding radiotracers in flasks of VSMCs maintained in normal (control) and high Ca/Pi medium. The ABs from these cells were then isolated by centrifugation and collected in eppendorf tubes. The eppendorf tubes were scanned on a nano SPECT scanner. MIP images of the scanned tubes (A) CT, (B) SPECT and (C) SPECT-CT. The ABs were incubated with radiolabeled bone seeking agent (^{99m}Tc-DPA Ale). The arrows show the uptake of radiotracers only in the pallet of the tubes containing ABs isolated from VSMCs maintained in a high Ca/Pi medium.

3.4 Discussion

Vascular calcification is a clinically important risk predictor of cardiovascular disease.[20] Coronary artery calcium scoring with computed tomography is clinically used for risk classification and prediction of coronary heart disease events.[21, 22] It is a hallmark in patients with diabetes and chronic kidney disease, which is associated with higher prevalence of cardiovascular disease.[23] Recent findings suggest that microcalcification may play a crucial role in plaque rupture.[11] This has led to an emergent interest in developing different molecular imaging probes to target and visualise microcalcifications. Positron emission tomography (PET) imaging with the molecular probe ^{18}F-NaF in human subjects to target active microcalcification in atherosclerotic plaques has shown promising results.[24-27] Although, a sensitive imaging modality, the use of PET imaging is still restricted because of logistics and cost. ^{18}F has a half-life of 110 min and is a

cyclotron produced radioisotope. Therefore the use of ^{18}F-NaF requires an in-house medical cyclotron facility or a commercial supplier in the vicinity, which increases the cost of operations substantially. A SPECT alternative to ^{18}F-NaF would alleviate these disadvantages and enable a more accessible and convenient modality. Cardiovascular disease is more prevalent in developing countries,[28, 29] due to genetic susceptibility and other factors like diet and lifestyle.[29, 30] Especially, in this scenario a cost effective solution is a necessity.

A conjugate of bisphosphonate (pamidronate) and a NIR fluorophore IR Dye 78, Pam-78 has been used successfully for *in vivo* optical imaging of microcalcification in different mouse models.[1, 15, 17, 31, 32] Radiolabeled bisphosphonates can therefore be used to image microcalcifications in a more effective manner.

^{99m}Tc-MDP is a radiolabeled bisphosphonate clinically used as a bone imaging agent for more than four decades. However, it has some serious physiochemical limitations. The chemical structure and composition remains unknown and HPLC studies show that ^{99m}Tc-MDP exists as a mixture of small and long chain oligomer with varied chemical properties. The drawback of the older generation ^{99m}Tc-labelled bisphosphonates (^{99m}Tc-BPs) is that their design is ill-suited for the bifunctional role they are required to perform, which compromises it's *in vivo* stability. The bisphosphonate groups have to chelate the metal ion as well as bind with the HA target. The latter interaction is affected by the presence of the radiometal. This has led to a new generation of ^{99m}Tc-labelled bisphosphonates with known chemical structure and properties being developed. These novel ^{99m}Tc-BPs are based on a more logical drug design approach exploiting the concept of bifunctional radiopharmaceuticals. In this approach the carrier molecules (bisphosphonate) and radiometal chelating groups are separated within the molecule so that they can each function independently. This in turn enhances the *in vivo* stability and

the binding efficiency of the radiopharmaceutical.[33, 34] We have reported the radiolabelling of novel bisphosphonates ^{99m}Tc-DPA-Ale and ^{99m}Tc-N(DTCBP)$_2$ with a consistently high radiochemical yield of > 95%.[35]

In this study we characterise the biological applications of these novel radiolabeled bisphosphonates and compared them with the clinically established bone seeking agents. The binding studies show that at high mineral concentrations (0.5 mg/mL) all the radiopharmaceuticals bind avidly with synthetic HA and minerals from intimal and medial calcifications. On the other hand at low concentrations (0.02 mg/mL) of ^{99m}Tc-DPA-Ale exhibited the highest binding percentages of 52±10%, 82±6% and 81±5% with minerals isolated from intimal and medial plaques and synthetic hydroxyapatite respectively. The results corroborate previously published studies which confirmed that ^{99m}Tc-DPA Ale has a superior *in vitro* binding efficiency with synthetic HA as compared to ^{99m}Tc-MDP.[36]

3.5 Conclusions

Novel bisphosphonates DPA-Ale and DTCBP have been prepared and successfully radiolabeled with ^{99m}Tc, which consistently produced a high labelling yield. In comparison to clinically used radiolabeled bisphosphonate ^{99m}Tc-MDP, both ^{99m}Tc-DPA Ale and ^{99m}Tc-N(DTCBP)$_2$ demonstrated a high *in vitro* binding with minerals isolated from human intimal and medial plaques. The novel radiotracers also showed a high propensity of binding with mineral- laden ABs produced by calcified human VSMCs *in vitro* and *in situ*. These findings suggest that novel radiolabeled bisphosphonates with enhanced binding potency have the potential to image vascular calcification and preclinical imaging with these agents is warranted.

References

1. New SEP, Aikawa E. Molecular Imaging Insights Into Early Inflammatory Stages of Arterial and Aortic Valve Calcification. *Circ Res.* 2011;108(11):1381-1391.

2. Kucharczyk W, Henkelman RM. Visibility of calcium on MR and CT: can MR show calcium that CT cannot? *Am J Neuroradiol.* 1994;15(6):1145-1148.

3. Shroff RC, McNair R, Figg N, et al. Dialysis accelerates medial vascular calcification in part by triggering smooth muscle cell apoptosis. *Circulation.* 2008;118(17):1748-1757.

4. Lin Z, Willers C, Xu J, Zheng MH. The chondrocyte: biology and clinical application. *Tissue Eng.* 2006;12(7):1971-1984.

5. Caetano-Lopes J, Canhao H, Fonseca JE. Osteoblasts and bone formation. *Acta Reumatol Port.* 2007;32(2):103-110.

6. Arana-Chavez VE, Massa LF. Odontoblasts: the cells forming and maintaining dentine. *Int J Biochem Cell Biol .* 2004;36(8):1367-1373.

7. Kapustin AN, Davies JD, Reynolds JL, et al. Calcium regulates key components of vascular smooth muscle cell-derived matrix vesicles to enhance mineralization. *Circ Res.* 2011;109(1):e1-12.

8. Proudfoot D, Skepper JN, Hegyi L, et al. Apoptosis Regulates Human Vascular Calcification In Vitro: Evidence for Initiation of Vascular Calcification by Apoptotic Bodies. *Circ Res.* 2000;87(11):1055-1062.

9. Shanahan CM. Autophagy and matrix vesicles: new partners in vascular calcification. *Kidney Int.* 2013;83(6):984-986.

10. Pugliese G, Iacobini C, Blasetti Fantauzzi C, et al. The dark and bright side of atherosclerotic calcification. *Atherosclerosis.* 2015;238(2):220-230.

11. Wong KK, Thavornpattanapong P, Cheung SC, et al. Effect of calcification on the mechanical stability of plaque based on a three-dimensional carotid bifurcation model. *BMC Cardiovasc Disord.* 2012;12:7.

12. Kelly-Arnold A, Maldonado N, Laudier D, et al. Revised microcalcification hypothesis for fibrous cap rupture in human coronary arteries. *Proc Natl Acad Sci USA.* 2013;110(26):10741-10746.

13. Cilla M, Monterde D, Pena E, Martinez MA. Does microcalcification increase the risk of rupture? *Proc Inst Mech Eng. H J. Eng. Med.* 2013;227(5):588-599.

14. Bluestein D, Alemu Y, Avrahami I, et al. Influence of microcalcifications on vulnerable plaque mechanics using FSI modeling. *J Biomech.* 2008;41(5):1111-1118.

15. Zaheer A, Murshed M, De Grand AM, et al. Optical imaging of hydroxyapatite in the calcified vasculature of transgenic animals. *Arterioscler Thromb Vasc Biol.* 2006;26(5):1132-1136.

16. Zaheer A, Lenkinski RE, Mahmood A, et al. In vivo near-infrared fluorescence imaging of osteoblastic activity. *Nat Biotechnol.* 2001;19(12):1148-1154.

17. Aikawa E, Nahrendorf M, Figueiredo JL, et al. Osteogenesis associates with inflammation in early-stage atherosclerosis evaluated by molecular imaging in vivo. *Circulation.* 2007;116(24):2841-2850.

18. Reid DG, Shanahan CM, Duer MJ, et al. Lipids in biocalcification: contrasts and similarities between intimal and medial vascular calcification and bone by NMR. *J Lipid Res.* 2012;53(8):1569-1575.

19. Hashimoto S, Ochs RL, Rosen F, et al. Chondrocyte-derived apoptotic bodies and calcification of articular cartilage. *Proc Natl Acad Sci USA.* 1998;95(6):3094-3099.

20. Abedin M, Tintut Y, Demer LL. Vascular calcification: mechanisms and clinical ramifications. *Arterioscler Thromb Vasc Biol.* 2004;24(7):1161-1170.

21. Polonsky TS, McClelland RL, Jorgensen NW, et al. Coronary Artery Calcium Score and Risk Classification for Coronary Heart Disease Prediction. *JAMA.* 2010;303(16):1610-1616.

22. Bansal S, Blumenthal RS. Total coronary artery calcium score remains preferred metric to refine risk prediction in nearly all patients. *JACC. Cardiovasc Imaging.* 2008;1(1):70-72.

23. Goodman WG. Vascular calcification in chronic renal failure. *Lancet.* 2001;358(9288):1115-1116.

24. Dweck MR, Jenkins WS, Vesey AT, et al. ^{18}F- sodium fluoride uptake is a marker of active calcification and disease progression in patients with aortic stenosis. *Circ Cardiovasc Imaging.* 2014;7(2):371-378.

25. Tarkin JM, Joshi FR, Rudd JHF. PET imaging of inflammation in atherosclerosis. *Nat Rev Cardiol.* 2014;11(8):443-457.

26. Dweck MR, Chow MWL, Joshi NV, et al. Coronary Arterial ^{18}F- Sodium Fluoride Uptake: A Novel Marker of Plaque Biology. *J Am Coll Cardiol.* 2012;59(17):1539-1548.

27. Joshi NV, Vesey AT, Williams MC, et al. ^{18}F-fluoride positron emission tomography for identification of ruptured and high-risk coronary atherosclerotic plaques: a prospective clinical trial. *Lancet.* 2014;383(9918):705-713.

28. Celermajer DS, Chow CK, Marijon E, Anstey NM, Woo KS. Cardiovascular Disease in the Developing WorldPrevalences, Patterns, and the Potential of Early Disease Detection. *J Am Coll Cardiol.* 2012;60(14):1207-1216.

29. Reddy KS, Yusuf S. Emerging epidemic of cardiovascular disease in developing countries. *Circulation.* Feb 17 1998;97(6):596-601.

30. Winham SJ, de Andrade M, Miller VM. Genetics of cardiovascular disease: Importance of sex and ethnicity. *Atherosclerosis.* 2015(0).

31. Zaheer A, Lenkinski RE, Mahmood A, et al. In vivo near-infrared fluorescence imaging of osteoblastic activity. *Nat Biotech.* 2001;19(12):1148-1154.

32. Kozloff KM, Volakis LI, Marini JC, Caird MS. Near-infrared fluorescent probe traces bisphosphonate delivery and retention in vivo. *J Bone Miner. Res.* 2010;25(8):1748-1758.

33. Torres Martin de Rosales R, Finucane C, Mather SJ, et al. Bifunctional bisphosphonate complexes for the diagnosis and therapy of bone metastases. *Chemical Commun.* 2009(32):4847-4849.

34. Ogawa K, Saji H. Advances in drug design of radiometal-based imaging agents for bone disorders. *Int J Mol Imaging.* 2011:537687.

35. Bordoloi JK, Berry D, Khan IU, et al. Technetium-99m and rhenium-188 complexes with one and two pendant bisphosphonate groups for imaging arterial calcification. *Dalton Trans.* 2015(44): 4963–4975

36. Torres Martin de Rosales R, Tavaré R, Paul RL, et al. Synthesis of Cu-64(II) Bis(dithiocarbamatebisphosphonate) and Its Conjugation with Superparamagnetic Iron Oxide Nanoparticles: In Vivo Evaluation as Dual-Modality PET–MRI Agent. *Angew Chem Int Edit.* 2011;50(24):5509-5513.

Chapter 4: Refining animal models.

4.1 Introduction

Use of animals in research has always been a subject of debate. However, according to the Public Health Service, U.S. Department of Health and Human Services "virtually every medical achievement of the last century has depended directly or indirectly on animal research."[1] Animal models have contributed substantially to our understanding of disease pathogenesis, development of diagnostic techniques as well as testing and optimising of therapeutic procedures, whether pharmacological or interventional.[2, 3] It is indispensable for the translation of a pharmaceutical from bench to bedside.[4]

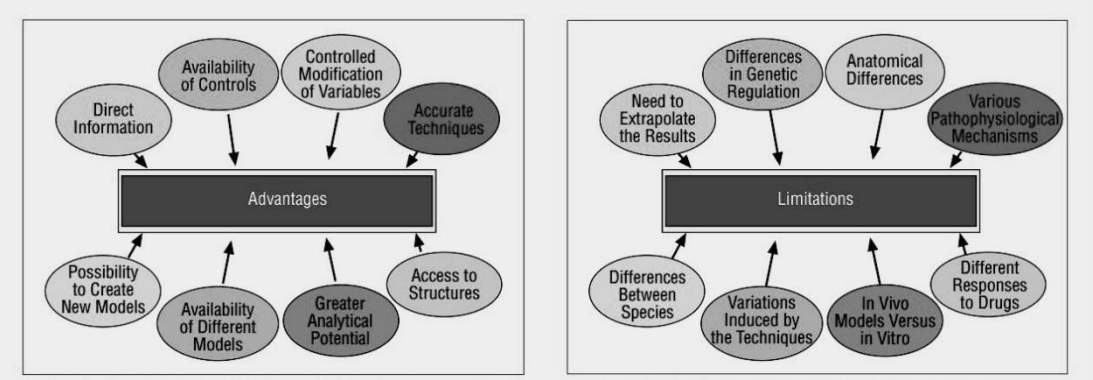

Figure 4.1: The advantages and limitations of using animal models. Chorro et al. Revista espanola de cardiologia. Jan 2009;62(1):69-84.

Animal models do make it possible to obtain direct information about specific events, offering good control over several variables while applying accurate and typically invasive procedures, which are difficult to employ in clinical studies. The limitation of using animal models is the difference in anatomic and genetic regulatory mechanism of diseases. Therefore animal models do not represent the clinical situations and cannot predict with certainty what will happen in the human counterpart; hence clinical trials are essential for translation.[5, 6] According to a study, only 11% of

pharmaceuticals that showed potential in animal models were successful in 'first in human clinical trials'.[7] However, a thorough animal study is a prerequisite for an investigational medicinal pharmaceutical to enter a phase 1 clinical trial. Rodents (mouse and rats) comprise more than 90% of the animals used in research. Over the years several murine knockout models and rat models of extraosseous calcification have been developed which have led to a better understanding of the pathogenesis of vascular calcification. Selected widely used mouse and rat models are summarised below.

4.2 Murine models of arterial calcification

4.2.1 MGP$^{-/-}$ mice

Luo *et al.* demonstrated spontaneous calcification of the aorta and cartilages in mice lacking matrix GLA protein. [8] Spontaneous calcification was observed in the elastic lamellae in the media of the aortic wall, coronary arteries and aortic valves without the presence of atherosclerosis in the MGP$^{-/-}$ mice. These mice showed phenotypic changes after two weeks and died within two months. Haemorrhage due to rupture of the aorta was reported as the cause of death.[8] Mutation in the genes encoding human MGP leads to Keutel Syndrome, an autosomal recessive disorder characterised by abnormal calcification of the cartilages, midfacial hypoplasia and peripheral pulmonary stenosis.[9, 10]

4.2.2 OPG$^{-/-}$ mice

An interesting mouse model for vascular calcification is the OPG null mouse that also develops osteoporosis.[11] Although this knock out model is not as severe as the MGP null model for vascular calcification it is of great mechanistic interest. This paradoxical model of calcification in the bone versus the vasculature describes a decrease in the total bone density that is therefore prone to fractures but an increase in medial calcification sites.[12] The role of OPG in the bone literature has been fairly well

characterised. OPG is a secreted factor that acts as a decoy of receptor activator of nuclear factor kappa-B ligand (RANKL) and therefore inhibits osteoclastic resorption of bone. The delicate balance in the opposing activity of osteoblasts and osteoclasts maintains healthy bone remodelling. However, with the lack of OPG, control over osteoclast differentiation is lost and bone mass is diminished. However, it is difficult to determine the mechanism leading to the inappropriate deposition of hydroxyapatite in the aorta upon loss of OPG. It is interesting to note that the arteries exhibiting calcification in the OPG knockout mice are sites of endogenous OPG expression, implying that OPG may have a role in protecting these arteries from pathological calcification.[12]

4.2.3 ApoE$^{-/-}$ mice

Apolipoprotein E (apoE) is a glycoprotein primarily synthesised in the liver and brain and is essential for the catabolism of triglyceride-rich lipoprotein constituents. Other tissues such as macrophages can also make apoE, which participates in the uptake and clearance of cholesterol-rich lipoprotein.[13] The ApoE$^{-/-}$ model was simultaneously reported by two groups (Meda *et al.* and Breslow *et al.*) in 1992 and since then has been a widely used animal model in cardiovascular research.[14-16] The model has played a crucial role in the understanding of the processes underlying the pathology of atherosclerosis such as inflammation, fibrinolysis, plaque remodelling and plaque vulnerability.[15] Vascular calcification occurs spontaneously in old apoE$^{-/-}$ mice.[17] Towler *et al.* demonstrated that high-fat, diabetogenic diet with low-density lipoprotein (LDL) results in arterial calcification in apoE$^{-/-}$ mice.[18] Recently, Schurgers *et al.* reported that vitamin K-antagonists (VKA) like warfarin can accelerate the process of calcification in ApoE$^{-/-}$ mice.[19]

4.2.4 DBA/2 mice

DBA/2 is a strain of inbred mouse developed at the Jackson Laboratories. Studies show that DBA/2 mice develop spontaneous calcified cardiovascular lesions when fed with a high fat diet.[20] Qiao *et al.* published a study comparing the pathophysiology of calcification in genetically distinct inbred and recombinant inbred strains of mice DBA/2J, SM/J, C57BL/6J, and C57BL/10ScSnA. Their findings revealed significant differences in arterial calcification among inbred strains and concluded that aortic calcification is partly determined by genetic factors.[21, 22] DBA/2 has been reported to be susceptible to aortic calcification. 100% of the animals developed calcification of the aorta when they were fed an atherogenic diet for 15 weeks.[22] It has also been reported that DBA/2 mice fed with a warfarin diet suffer calcification in both the medial layer of the aorta as well as in the heart in a dose- and time-dependent manner.[23]

4.3 Rat models of arterial calcification

Remnant kidney rat models are widely used in research related to chronic kidney failure. The model requires a two stage surgical procedure, a partial nephrectomy followed by a total nephrectomy to mimic progressive nephron loss. The remnant kidney rats are prone to medial calcification. When fed with a standard rodent diet for 10 weeks these rats develop calcification in the aortic arch.[24] Administration of 1,25$(OH)_2$ vitamin D_3 orally, subcutaneously or intraperitoneally to the remnant kidney rats results in massive calcifications of the entire aortic wall, involving both the thoracic and abdominal aorta.[24-26]

Price *et al.* were the first to report a rat model for vascular calcification that did not require a surgical intervention. They demonstrated that warfarin exposure of Sprague Dawley (SD) rats induces calcification in the elastic lamellae, heart valves and the arteries.[27] Findings in agreement with Price *et al*. were published by Howe *et al.* and they concluded that treatment of SD rats with warfarin caused extra-hepatic deficiency of vitamin K resulting in inhibition of γ-carboxylation of MGP.[28] Vitamin K_1

was supplemented along with warfarin to avoid lethal bleeding.[27] This leads to severe extraosseous calcification in the aorta and the kidneys. Price *et al.* later demonstrated that the process of warfarin-induced calcification can be accelerated by treating the rats with warfarin and vitamin D_3 simultaneously.[29]

The aim of the study is to develop a robust animal model of vascular calcification by making changes in previously established protocols, in order to reduce pain and stress imparted on the animal.

4.4 Materials and methods

4.4.1 Animal studies

All procedures were performed in accordance with licences and guidelines approved by the UK Home Office.

4.4.2 DBA/2J

Six DBA/2J (10 weeks old, female) mice were purchased from Harlan Laboratories, UK and maintained in a pathogen-free environment at the BSU in Denmark Hill Campus of KCL. After the acclimatisation period of 7 days the mice were divided into 2 groups, each comprising of three mice. One group was fed with normal diet whereas the other group was fed with a warfarin diet. Custom made rodent diet containing 3.0 mg/g of warfarin and 1.5 mg/g of vitamin K_1 was obtained from AB diets, Netherlands. Food and water was provided *ad libitum*. After 8 weeks of feeding the mice were culled, tissues dissected and fixed with 4% formaldehyde and snap-frozen in liquid nitrogen for histological and physiological studies. (Figure 4.2)

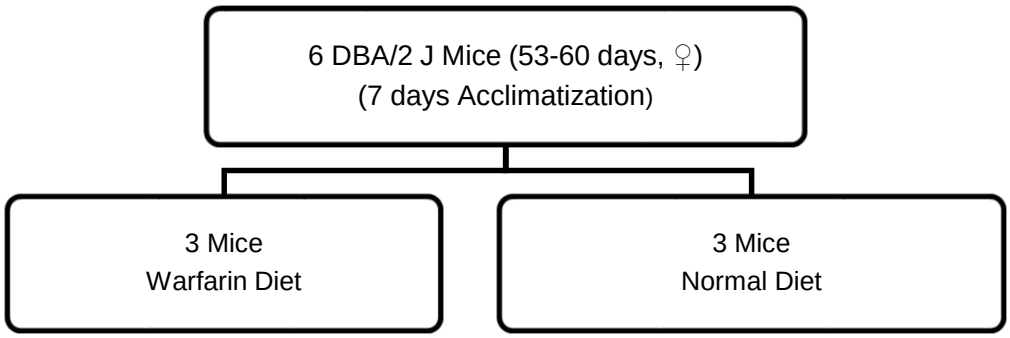

Figure 4.2: Flow diagram of the protocol used to induce calcification in DBA/2J mice.

4.4.3 DBA/2N Crl

Twenty female DBA2/N Crl mice were purchased from Charles River Laboratories and housed at the BSU in St. Thomas' campus of King's College, London. The mice were 57-63 days old on the day of arrival and were allowed to acclimatise. The mice were divided into two groups (9 mice each). One group received a warfarin diet whereas the other was kept on a normal rodent diet. Depending on the duration of the diet, the two groups were divided into three sub-groups, 6 weeks (3 mice), 7 weeks (3 mice) and 8 weeks (3 mice). Figure 4.3 illustrates the experimental protocol. At the end of the experiment the mice were sacrificed with CO_2 followed by neck dislocation and organs retained for histological and physiological studies.

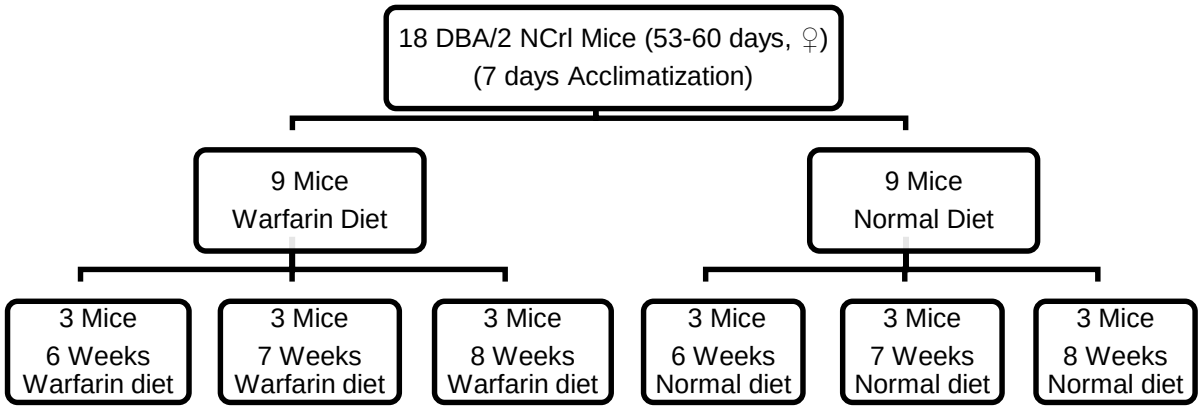

Figure 4.3: Flow diagram showing the protocol used to induce calcification in DBA/2NCrl mouse.

4.4.4 Sprague-Dawley (SD) rats

Sprague Dawley rats (n = 6; male; 21-27 days old) were purchased from Charles River Laboratories and housed at the BSU at Denmark Hill Campus. After an acclimatisation period of 7 days, the rats were divided into three groups comprising of two each. Figure 4.4 describes the protocol used in this study.

The first batch was maintained on a normal rodent diet, and these rats were used as a negative control for the experiment. The second batch of rats was fed with a diet containing warfarin (3 mg/g food) and vitamin K_1 (1.5 mg/g food) for 11 days. The rats were injected with 5 mg/kg/day (200,000 IU) subcutaneous injections of cholecalciferol (Sigma-47763) from day 7 to day 11 of the diet. The stock solution of cholecalciferol (vitamin D_3) for subcutaneous injection was prepared by dissolving 33 mg (1.32×10^6 IU) of cholecalciferol (Sigma- 47763) in 200 µL of absolute ethanol along with 1.4 mL of kollilphor (Sigma-C5135) in a foil-wrapped 50 ml tube with mixing (Stuart-roller mixer) for 15 minutes. Water (18.4 mL) containing 750 mg of dextrose

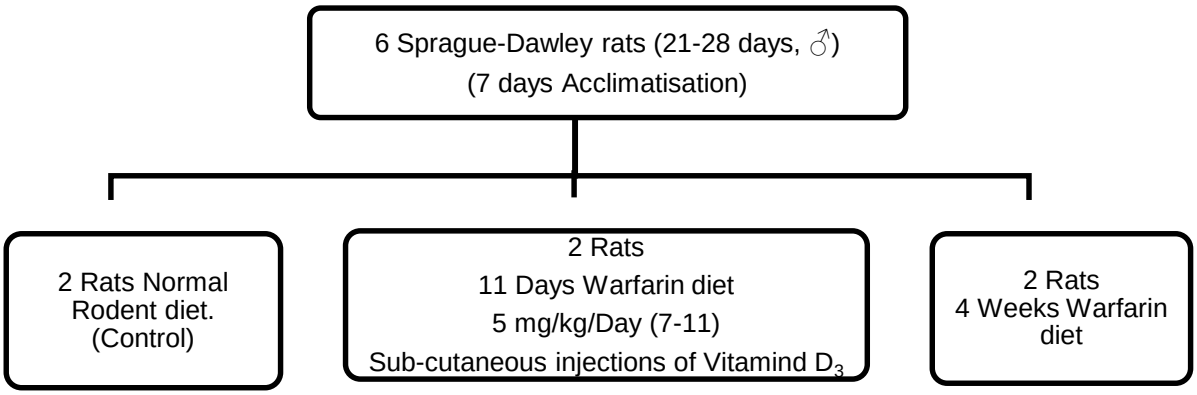

Figure 4.4: Flowchart describing the protocol used to induce calcification in SD rats.

(Sigma-D9434) was then added, and the final solution was mixed for an additional 15 minutes. The stock solution (1.32×10^6 IU) was then stored at 4°C and used for 3 days. Fresh vitamin D_3 solution was prepared for each 3-day injection. The third batch was maintained on a warfarin diet for 4 weeks, following which the animals were euthanised and organs were preserved.

4.4.5 *O*-cresolphthalein Complexone Assay

The tissues were decalcified with 1M HCl for 2 hours. The calcium content of HCl supernatant was determined colorimetrically by *o*-cresolphthalein complexone method (Calcium C-test Wako; Wako Pure Chemical Industries). After decalcification, the cells were washed three times with phosphate-buffered saline (PBS) and solubilised with 0.1N NaOH/0.1% sodium dodecyl sulfate (SDS). The protein content was measured with a BCA protein assay kit (Pierce). The calcium content of the cell layer was normalised to the protein content.

4.4.6 Histology

Specimens for histological analysis were fixed in 4% paraformaldehyde for 4 hours following which the tissues where transferred to 70% ethanol solution, embedded in paraffin, and cut into consecutive 5 µm sections. Von Kossa staining and alizarin red S staining was performed using standard procedures.

4.4.7 Histomorphometry

Paraffin embedded sections 5 µm thick, were cut from the thoracic aorta and abdominal aorta and cut using a microtome (Leica-RM2125RTF). Consecutive sections were stained alternately with Alizarin Red S (Sigma,UK). Images of stained sections were obtained using a Leica DM2000 LED microscope equipped with a Reitga Exi Fast1394 digital camera. Figure 4.5 describes the pre-processing steps involved prior to quantification. Quantitative analysis was performed using ImageJ histomorphometry software on at least six sections from each rat. The quantification was performed only on aorta samples of rats on warfarin and vitamin K_1 diet only.

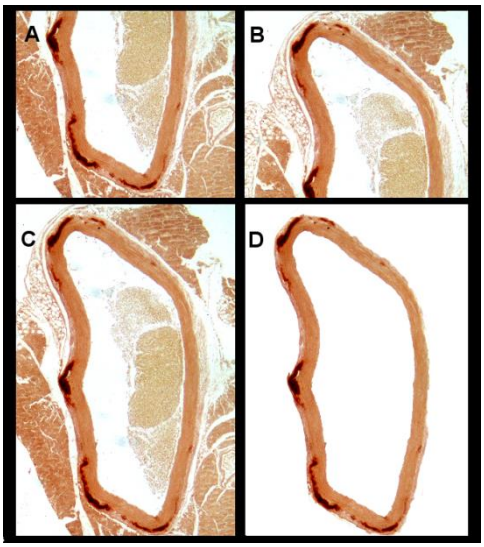

Figure 4.5: The pre-processing steps to obtain images of thoracic and abdominal rat aortas for histomorphometry. As the aorta sections are larger than the field of view of the camera, tiled images (A & B) of the aorta were obtained. (C) Using Image J stitching tool the tiled images were merged to obtain the whole aorta in a single image. (D) Using Adobe Photoshop CS6 quick selection tool, images of the unwanted tissues around the aorta were removed. Quantification was performed on these images by measuring the number of pixels in the stained region and the pixels in the aorta.

4.4.8 Statistical analysis

Data are expressed as the mean ± standard deviation (SD). Statistical analysis was performed using the GraphPad Prism 5.0 (GraphPad Software, Inc., USA).

4.5 Results

4.5.1 Warfarin feeding fails to induce calcification in DBA/2J

The DBA/2J mouse strain is known to be susceptible to vascular calcification. Previously published studies show that calcification can be induced in this strain of mouse by feeding them with a high fat diet for 15 weeks.[21] When fed with a diet containing warfarin (3 mg/g) and vitamin K_1 (1.5 mg/g) calcification can be induced in 6 weeks. However in our study DBA/2J mouse fed with warfarin and vitamin K_1 for 8 weeks did not show any significant changes in calcium load in the aortas (Figure 4.6). Paraffin embedded sections stained with von Kossa and alizarin red S (Figure 4.7; A-D) stain for calcification were negative for calcification.

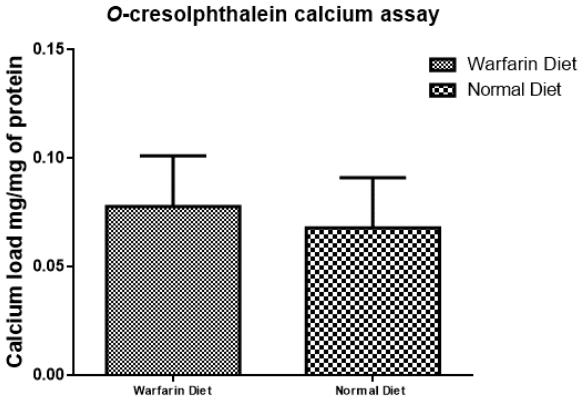

Figure 4.6 Measurement of the calcium load in the aorta of DBA/2J mouse (n=3) on a warfarin diet and control diet for 8 weeks.

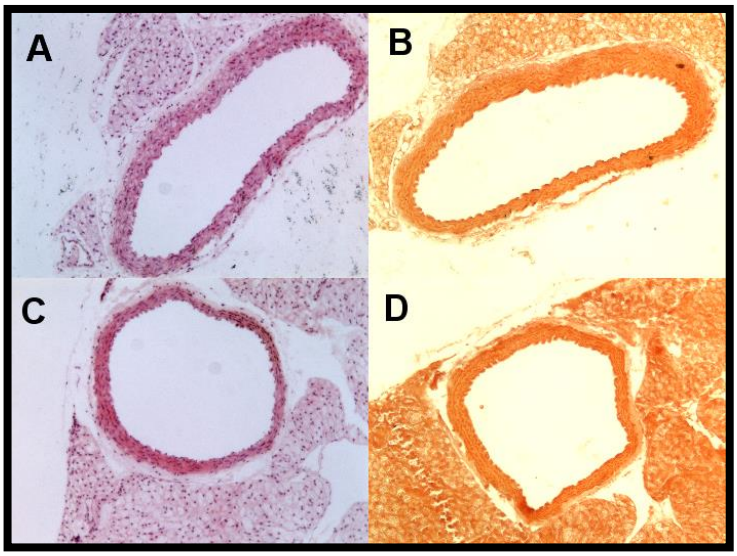

Figure 4.7: Paraffin embedded sections (5 μm) in von Kossa counter stained with H&E stain (A,C) andalizarin red S stain (B,D). Sections of aorta from a mouse on warfarin diet (A, B) and normal diet (C,D) were negative for the presence of calcification. (Magnification 10X)

4.5.2 Warfarin feeding induces calcification in DBA/2N Crl mouse

DBA/2 NCrl is a substrain of inbred DBA/2 mouse and is known to be prone to extraosseous calcification.[30] Calcification of the aorta was seen in all mice fed with a warfarin diet for 6, 7 and 8 weeks. Presence of calcification was demonstrated histologically by von Kossa and alizarin red staining (Figure 4.9), as well as colorimetrically with *O*-cresolphthalein assay (Figure 4.8). The extent and distribution of the arterial calcification varied between animals and were dependent on the duration of treatment. With an increase in the duration of warfarin treatment an increase in the extent of calcification was observed. The most heavily calcified aortas were from mice fed with the warfarin diet for 8 weeks with a calcium load of 1±0.32 mg/mg of protein, whereas the mice fed with a normal diet for the same duration had a calcium load of 0.32±0.04 mg/mg of protein. The calcium load in weeks 6 and 7 of warfarin feeding was 0.67±0.06 and 0.84±0.18 mg/mg of protein, respectively.

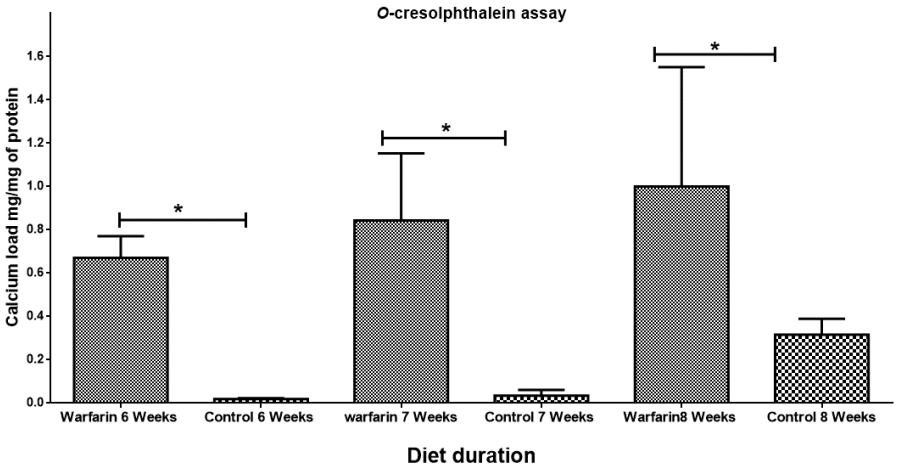

Figure 4.8: *O*-cresolphthalein assay measurements of the calcium load in the thoracic aorta of warfarin fed DBA/2 N mice at week 6, 7 and 8 (n=3). (* = $P < 0.05$)

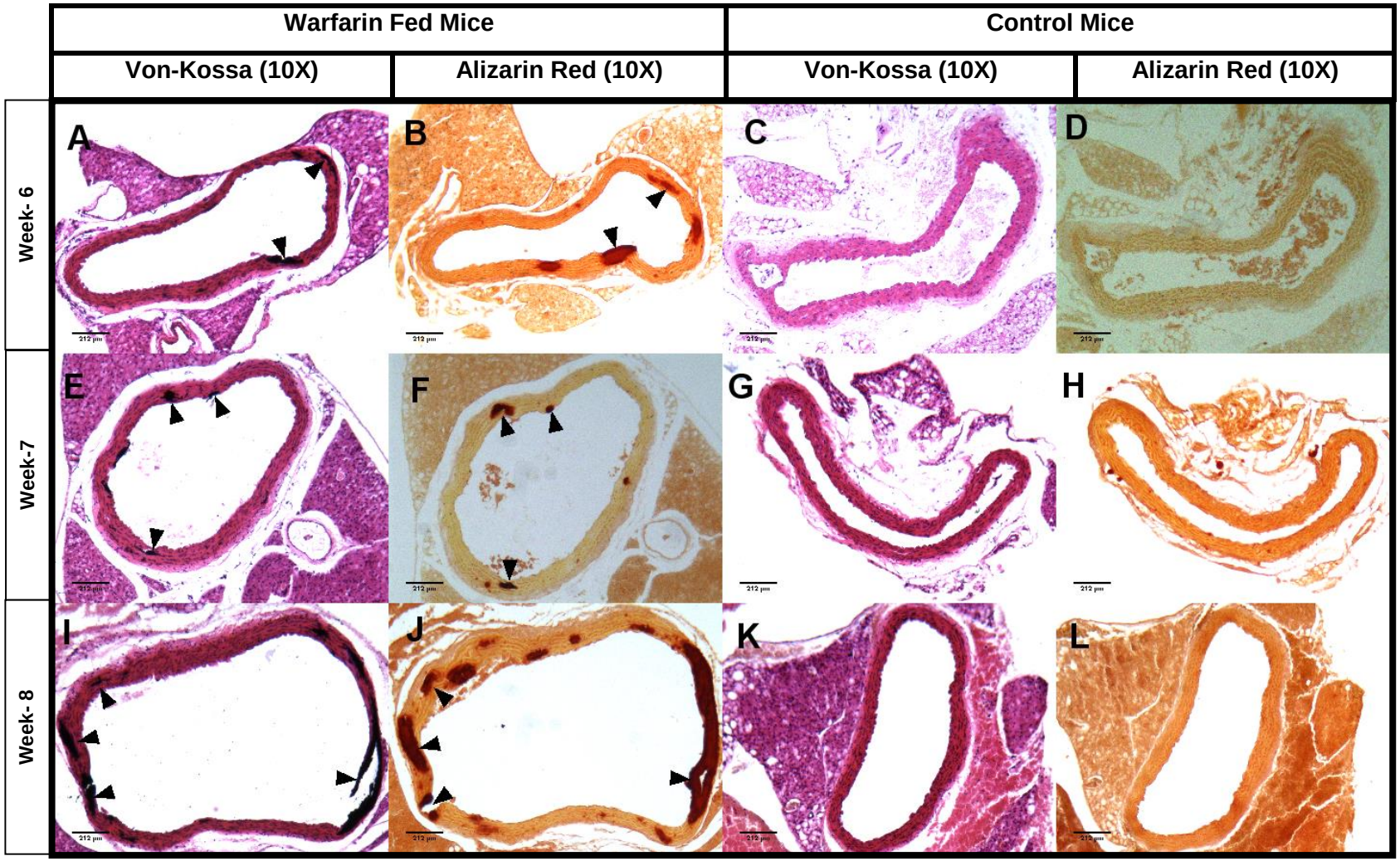

Figure 4.9: Aortic sections stanined with Von-Kossa counter stained with H&E stain (A,C,E,G,I & J), and alizarin red S stain (B,D,F,H,J&L). The black arrows in (A &B), (E & F), (I & J) show calcification in aorta of DBA/2NCrl mouse fed with warfarin diet for 6, 7 and 8 weeks respectively. Sections (C&D), (G&H) and (K&L) are aortas of DBA/2NCrl mouse on standard rodent diet for the same time point with no evidence of calcification. (Magnification 10X, Scale bar = 212 µm)

4.5.3 Warfarin feeding induces calcification in SD rats and vitamin D accelerates the process

In all of the rats fed with warfarin for 4 weeks, there was calcification along the abdominal aorta and thoracic aorta as demonstrated by von Kossa (Figure 4.11 A, C, E, G) and alizarin red-staining (Figure 4.11 B, D, F, H). Aortas of rats on a normal diet were not affected (Figure 4.10 B-E). Calcification was not observed in the whole aortic ring, rather it occurred in numerous centres of varying size in rats that received warfarin diet only for four weeks (Figure 4.11 A-H). The number of calcified centres and the extent of calcification in the thoracic aorta were less when compared with that seen in the abdominal aorta. The calcified areas in the thoracic aorta (Figure 4.11 C, D) were predominantly located near the adventitia whereas in the abdominal aorta (Figure 4.11 G, H) the calcification extended up to the lumen. The most heavily calcified vessel was usually the abdominal aorta and the extent of calcification gradually reduced towards the aortic arch. Calcification was absent in some aortic arch sections of rats treated with warfarin only. Histomorphometric analysis showed that the area of the aorta positively stained for calcification in the abdominal aorta was significantly higher than that in the thoracic aorta (Figure 4.13).

On the other hand, SD rats maintained on a warfarin diet for 11 days and injected with high doses of vitamin D_3 for 4 days (day 7-11) resulted in overt calcification both in the thoracic as well as the abdominal aorta (Figure 4.12 A-H). Unlike the rats treated with warfarin only, rats treated with warfarin and vitamin D_3 exhibited calcification in a concentric manner covering the whole aortic ring. Histomorphometric study demonstrated that both thoracic and abdominal aortas were equally affected. The percentages of area positively stained for calcification in the thoracic and the abdominal aorta were almost equal (Figure 4.13).

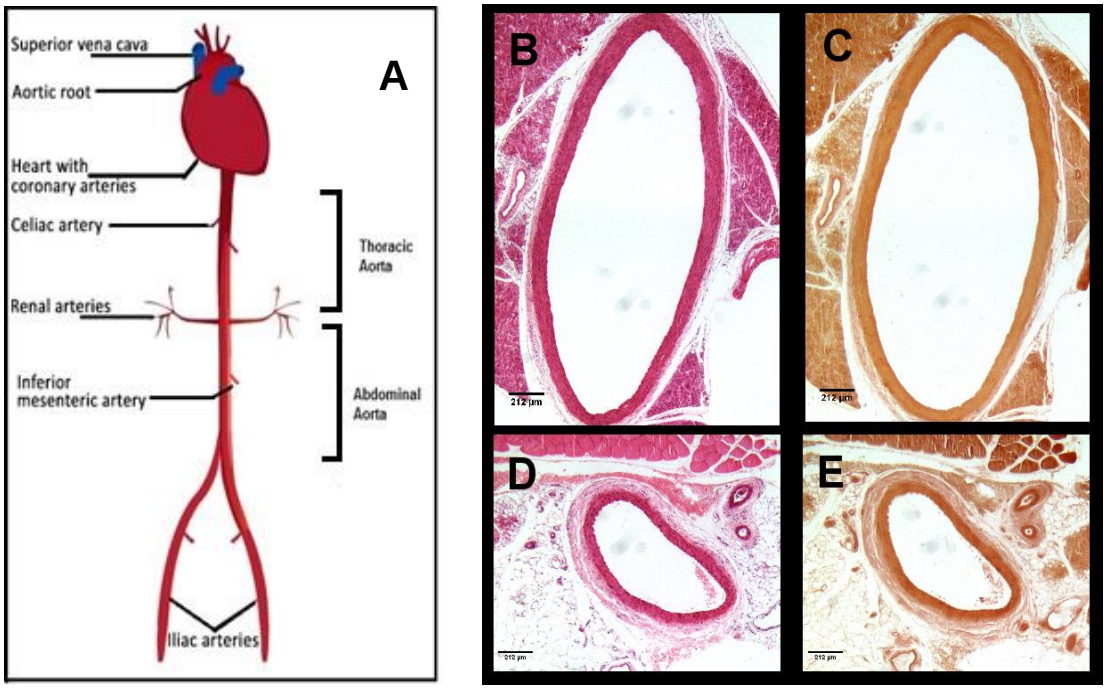

Figure 4.10: (A) Diagrammatic representation of the rat aorta showing the areas of the aorta used for sectioning and staining. The segment of t he between the aortic arch and the renal branch (thoracic aorta) and the renal branch and the iliac bifurcation (abdominal aorta) was removed at necropsy and fixed in 4% buffered formalin. Von-Kossa counter stained with Haematoxylin & Eosin stain and Alizarin red S stained sections of the (B & C) thoracic aorta and (D & E) abdominal aorta of SD rat on standard rodent diet for 28 days (4 weeks). (Magnification = 10X, Scale bar = 212 µm)

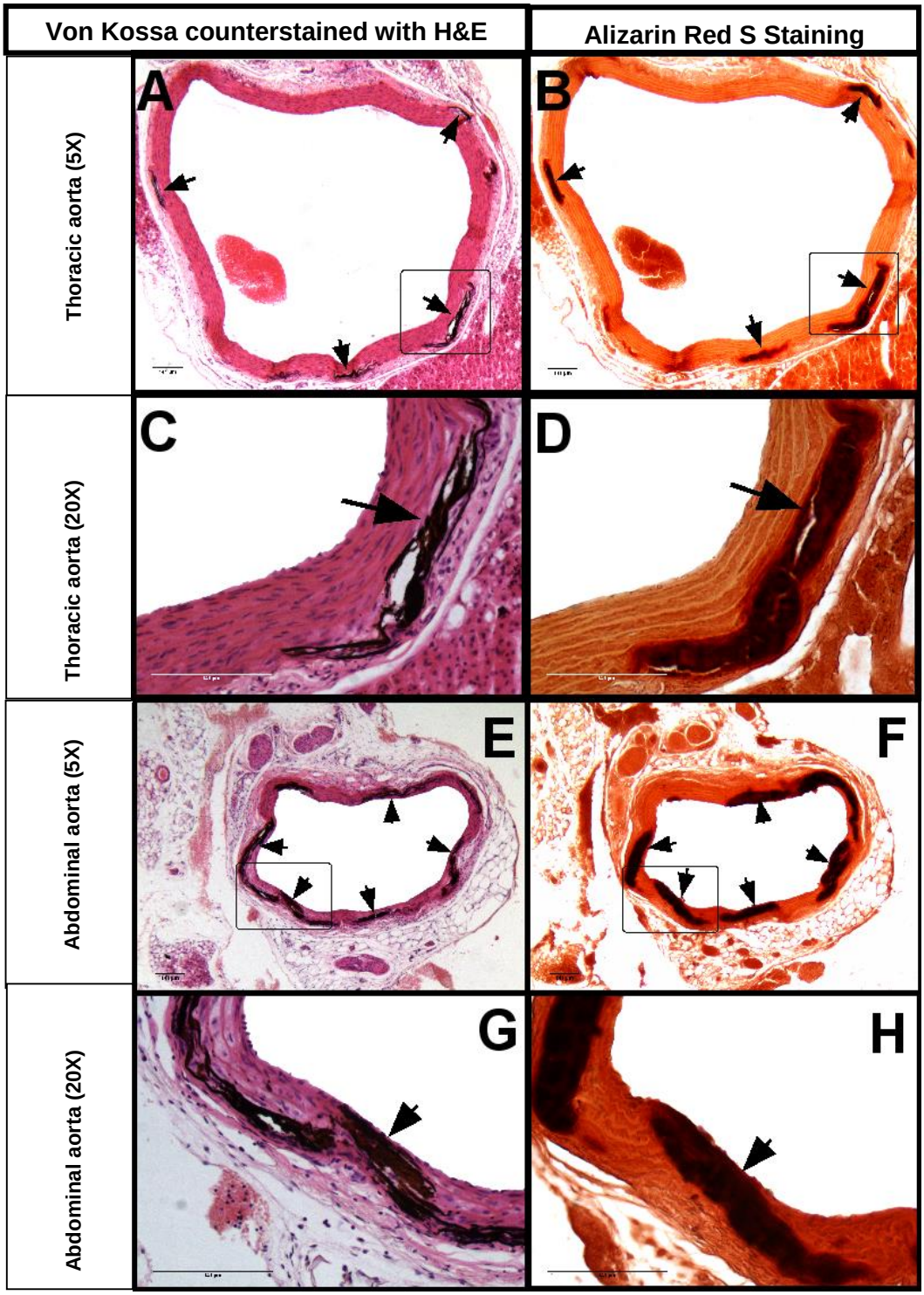

Figure 4.11: Effect of warfarin feeding on the thoracic (A-D) and abdominal (E-H) aorta of SD rats. Sections show the thoracic and abdominal aorta of rats fed with warfarin diet for 28 days (4 weeks). Consecutive longitudinal sections were stained with von Kossa counter stained with H&E stain and alizarin red S stain to detect areas of mineralization. A,B and E,F are sections of the thoracic and abdominal aorta stained for mineralization at 5X magnification; the arrows shows the calcified areas. (Scale bar = 212 µm)

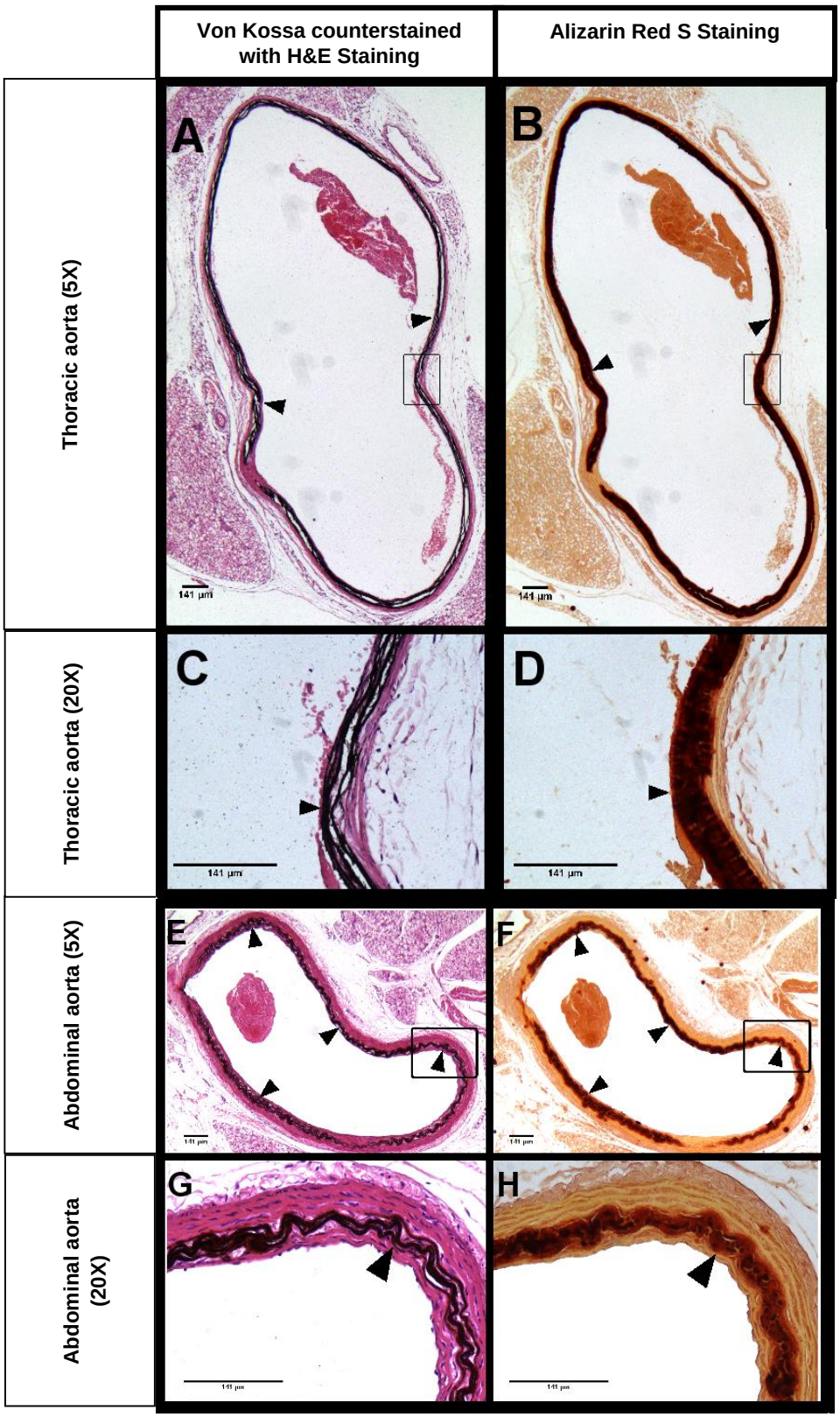

Figure 4.12: Circumferential calcification in the thoracic (A,B) and the abdominal (E,F) aorta of rat on warfarin diet for 11 days and receiving subcutaneous injections of 5 mg/kg/day of vitamin D3 from day 7 to day 11 of the diet. (C, D and G, H): Images of the aortas at higher magnification (20X). (Scale bar = 141 µm)

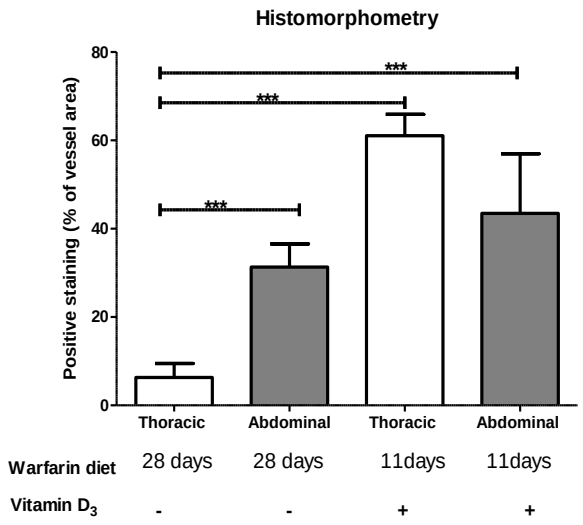

Figure 4.13: Histomorphometry of sections from the thoracic and abdominal aorta of rats treated with warfarin only (4 weeks) and warfarin with vitamin D3 administration stained with alizarin red. The values were calculated from 6 random sections. (*** = $P < 0.001$).

4.6 Discussion

The concept of 3R's replacement, refinement and reduction was first proposed and developed by Russel and Burch in 1959. The 3R's are now widely accepted internationally as the criteria for humane animal use in research. In these experiments we have tried to refine some previously published animal studies with minor changes to minimise the stress and pain imparted on the animals without changing the outcome.

We first explored replicating previously reported murine model[23] of vascular calcification. In our studies warfarin feeding of DBA/2J mice did not result in calcification of the arterial system, although previously published studies demonstrate that warfarin induces calcification in DBA/2J mice.[31, 32] Ectopic calcification in the DBA/2J mouse is attributed to allelic *Abcc6* mutation.[33] A likely explanation for the failure of calcification in DBA/2J could be the absence of a mutation of this gene in the mouse strain used in the experiment, however further studies are needed to confirm the exact reason of the failure. For the second experiment a substrain of the DBA/2 mouse, DBA/2 NCrl was used.

Feeding with the diet used in the previous experiment resulted in calcification of the aorta. The calcification was found to be dose-dependent and the calcium load in the aortas increased gradually with an increase in the duration of warfarin feeding.

In conjunction with the murine model, we modified the protocol of a previously published rat model by Price *et al*. They demonstrated that warfarin administration in SD rats' results in heavy calcification of the aorta. However, the protocol employed by Price *et al*.[29] required the administration of warfarin every 12 hours and vitamin K_1 every 24 hours either by gavage feeding or subcutaneous injections and the routine was followed up to 5 weeks. They also reported that the process can be accelerated by simultaneous administration of vitamin D_3. The vitamin D_3 administration calls for an additional dose every 24 hours. Administration by gavage or subcutaneous injection causes the animal distress. This is because it requires removing the animal from its cage, manually restraining it and inserting a small-diameter tube into the oesophagus for gavage feeding or injecting via subcutaneous route. Gavage feeding may damage the oesophagus or stomach due to accidental puncture. Inadvertent dosing into the lung while gavage feeding causes severe respiratory distress and as per guidelines the animal may have to be euthanised immediately.[34] Two or more subcutaneous injections per day over a period of 5 weeks would require the same injection sites to be used multiple times leading to inflammation and necrosis of the tissue.[35] In this study we report that vascular calcification can be induced in rodents by feeding them with a warfarin diet.

Warfarin is a coumarin derivative, and is clinically used as an anticoagulant therapeutic in patients with thromboembolic disorders like pulmonary embolism and deep vein thrombosis.[36] The anticoagulant effect of warfarin is produced by interfering with the cyclic interconversion of vitamin K_1 and its vitamin K_1 2,3 epoxide. Vitamin K_1 is a cofactor for the carboxylation of glutamate residues to γ-carboxyglutamates (Gla).[37] During the

carboxylation reaction vitamin K_1 is converted to vitamin K_1 2,3 epoxide. Interfering with the cyclic interconversion of vitamin K_1 thereby inhibits the carboxylation of glutamate residues to γ-carboxyglutamates (Gla). Proteins that contain a GLA domain include coagulation factors VII, IX, X, XIV and calcium inhibitors MGP and osteocalcin.[38-41] The deficiency of carboxylated MGP results in extraosseous calcification in the aorta.

Warfarin feeding of SD rats results in aortic calcification, which is in agreement with previously published studies by Price *et al*. and Howe *et al*.[27, 28] Calcification in the abdominal aorta of rats fed with a warfarin diet was severe in comparison to the thoracic aorta. Some sections of the thoracic aorta were negative for the presence of calcification suggesting that the abdominal aorta is more prone to calcification. Clinical studies published by Oyama *et al*. and Wong *et al*. on a cohort of 1763 and 1812 participants with early stage cardiovascular disease and hypertension concluded that prevalence of calcification in the abdominal aorta was higher than that in the thoracic aorta.[42, 43]

Vitamin D_3 administration in conjunction with warfarin treatment accelerates the process of calcification.[29] Vitamin D has pleiotropic activities in multiple organs and plays a crucial role in Ca^{2+} and bone homeostasis, immune system and the cardiovascular system.[44] Besides dietary sources vitamin D_3 can be generated through photolysis of 7-dehydrocholesterol in the skin in the presence of UV light.[45] It is known that a high dose of vitamin D_3 induces calcification in animals as well as humans.[46-48] In comparison to rats on with warfarin diet only for 28 days, the calcification in rats on warfarin diet for 11 days administered with vitamin D_3 injections demonstrated a higher degree of calcification. Rats on warfarin diet only demonstrated calcification in localised pockets whereas the calcification in those which received vitamin D_3 was circumferential. The severity of calcification in both the thoracic and the abdominal aorta was almost equal suggesting that the process of calcification is accelerated by vitamin D_3.

4.7 Conclusions

The major aim of this work was to characterize animal models of medial arterial for potential use in molecular imaging. In this study we have successfully demonstrated that calcification can be induced in the DBA/2 NCrl mouse strain and SD rats by feeding them a warfarin diet without going through the painstaking process of gavage feeding or injections. Warfarin in the form of diet reduces the distress and pain imparted in the animals substantially.

The rat model of calcification was considered for the *in vivo* studies as it presented with practical advantages over the murine model. The advantages are:

1. Validation and repeatability: The DBA/2 mice failed to calcify in one of our studies, raising concerns on the repeatability of the model.
2. The process of calcification in the rat model could be accelerated with the administration of vitamin D_3. This offered us with two models, one with extensive calcification and another progressive calcification which suited our requirements.

Reference

1. The importance of animals in biomedical and behavioral research-a statement from the Public Health Service. *Physiologist.* 1994;37(3):107.

2. Chorro FJ, Such-Belenguer L, Lopez-Merino V. Animal models of cardiovascular disease. *Rev Esp Cardiol.* 2009;62(1):69-84.

3. Zaragoza C, Gomez-Guerrero C, Martin-Ventura JL, et al. Animal models of cardiovascular diseases. *J Biomed Biotechnol.* 2011:497841.

4. Denayer T, Stöhr T, Van Roy M. Animal models in translational medicine: Validation and prediction. *New Horiz Transl Med.* 2014;2(1):5-11.

5. van der Worp HB, Howells DW, Sena ES, et al. Can Animal Models of Disease Reliably Inform Human Studies? *PLoS Med.* 2010;7(3):e1000245.

6. Martić-Kehl MI, Schibli R, Schubiger PA. Can animal data predict human outcome? Problems and pitfalls of translational animal research. *Eur J Nucl Med Mol Imaging.* 2012;39(9):1492-1496.

7. Kola I, Landis J. Can the pharmaceutical industry reduce attrition rates? *Nat Rev Drug Discov.* 2004;3(8):711-716.

8. Luo G, Ducy P, McKee MD, et al. Spontaneous calcification of arteries and cartilage in mice lacking matrix GLA protein. *Nature.* 1997;386(6620):78-81.

9. Keutel J, Jorgensen G, Gabriel P. A new autosomal-recessive hereditary syndrome. Multiple peripheral pulmonary stenosis, brachytelephalangia, inner-ear deafness, ossification or calcification of cartilages. *Deut Med Wochenschr.* 1971;96(43):1676-1681.

10. Munroe PB, Olgunturk RO, Fryns JP, et al. Mutations in the gene encoding the human matrix Gla protein cause Keutel syndrome. *Nat Genet.* 1999;21(1):142-144.

11. Simonet WS, Lacey DL, Dunstan CR, et al. Osteoprotegerin: A Novel Secreted Protein Involved in the Regulation of Bone Density. *Cell.* 1997;89(2):309-319.

12. Bucay N, Sarosi I, Dunstan CR, et al. osteoprotegerin-deficient mice develop early onset osteoporosis and arterial calcification. *Gene Dev.* 1998;12(9):1260-1268.

13. Boisvert WA, Spangenberg J, Curtiss LK. Treatment of severe hypercholesterolemia in apolipoprotein E-deficient mice by bone marrow transplantation. *J Clin Invest.* 1995;96(2):1118-1124.

14. Piedrahita JA, Zhang SH, Hagaman JR, Oliver PM, Maeda N. Generation of mice carrying a mutant apolipoprotein E gene inactivated by gene targeting in embryonic stem cells. *Proc Natl Acad Sci.* 1992;89(10):4471-4475.

15. Meir KS, Leitersdorf E. Atherosclerosis in the apolipoprotein-E-deficient mouse: a decade of progress. *Arterioscler Thromb Vasc Biol.* 2004;24(6):1006-1014.

16. Plump AS, Smith JD, Hayek T, et al. Severe hypercholesterolemia and atherosclerosis in apolipoprotein E-deficient mice created by homologous recombination in ES cells. *Cell.* 1992;71(2):343-353.

17. Bennett BJ, Scatena M, Kirk EA, et al. Osteoprotegerin Inactivation Accelerates Advanced Atherosclerotic Lesion Progression and Calcification in Older ApoE−/− Mice. *Arterioscler Thromb Vasc Biol.* 2006;26(9):2117-2124.

18. Towler DA, Bidder M, Latifi T, Coleman T, Semenkovich CF. Diet-induced Diabetes Activates an Osteogenic Gene Regulatory Program in the Aortas of Low Density Lipoprotein Receptor-deficient Mice. *J Biol Chem.* 1998;273(46):30427-30434.

19. Schurgers LJ, Joosen IA, Laufer EM, et al. Vitamin K-antagonists accelerate atherosclerotic calcification and induce a vulnerable plaque phenotype. *PloS one.* 2012;7(8):e43229.

20. Ball CR, Williams WL. Spontaneous and dietary-induced cardiovascular lesions in DBA mice. *Anat Rec.* 1965;152(2):199-209.

21. Qiao JH, Xie PZ, Fishbein MC, et al. Pathology of atheromatous lesions in inbred and genetically engineered mice. Genetic determination of arterial calcification. *Arterioscler Thromb Vasc Biol.* 1994;14(9):1480-1497.

22. Qiao J-H, Fishbein MC, Demer LL, Lusis AJ. Genetic Determination of Cartilaginous Metaplasia in Mouse Aorta. *Arterioscler Thromb Vasc Biol.* 1995 1995;15(12):2265-2272.

23. Kruger T, Oelenberg S, Kaesler N, et al. Warfarin induces cardiovascular damage in mice. *Arterioscler Thromb Vasc Biol.* 2013;33(11):2618-2624.

24. Koleganova N, Piecha G, Ritz E, Schmitt CP, Gross M-L. A calcimimetic (R-568), but not calcitriol, prevents vascular remodeling in uremia. *Kidney Int.* 2008;75(1):60-71.

25. Mizobuchi M, Finch JL, Martin DR, Slatopolsky E. Differential effects of vitamin D receptor activators on vascular calcification in uremic rats. *Kidney Int.* 2007;72(6):709-715.

26. Haffner D, Hocher B, Muller D, et al. Systemic cardiovascular disease in uremic rats induced by 1,25(OH)2D3. *J Hypertens.* 2005;23(5):1067-1075.

27. Price PA, Faus SA, Williamson MK. Warfarin Causes Rapid Calcification of the Elastic Lamellae in Rat Arteries and Heart Valves. *Arterioscler Thromb Vasc Biol.* 1998;18(9):1400-1407.

28. Howe AM, Webster WS. Warfarin exposure and calcification of the arterial system in the rat. *Int J Clin Exp Pathol.* 2000;81(1):51-56.

29. Price PA, Faus SA, Williamson MK. Warfarin-induced artery calcification is accelerated by growth and vitamin D. *Arterioscler Thromb Vasc Biol.* 2000;20(2):317-327.

30. Theuwissen E, Smit E, Vermeer C. The role of vitamin K in soft-tissue calcification. *Adv Nutr.* 2012;3(2):166-173.

31. Krüger T, Oelenberg S, Kaesler N, et al. Warfarin Induces Cardiovascular Damage in Mice. *Arterioscler Thromb Vasc Biol.* 2013;33(11):2618-2624.Bertola A, Mathews S, Ki SH, Wang H, Gao B. Mouse model of chronic and binge ethanol feeding (the NIAAA model). *Nat Protoc.* 2013;8(3):627-637.

32. Li Q, Guo H, Chou DW, Berndt A, Sundberg JP, Uitto J. Mouse models for pseudoxanthoma elasticum: genetic and dietary modulation of the ectopic mineralization phenotypes. *PloS one.* 2014;9(2):e89268.

33. Le Saux O, Martin L, Aherrahrou Z, Leftheriotis G, Varadi A, Brampton CN. The molecular and physiological roles of ABCC6: more than meets the eye. *Front Genet.* 2012;3:289.

34. Bertola A, Mathews S, Ki SH, Wang H, Gao B. Mouse model of chronic and binge ethanol feeding (the NIAAA model). *Nat Protocols.* 2013;8:627-637.

35. Diehl KH, Hull R, Morton D, et al. A good practice guide to the administration of substances and removal of blood, including routes and volumes. *J Appl Toxicol.* 2001;21(1):15-23.

36. Hirsh J, Fuster V, Ansell J, Halperin JL. American Heart Association/American College of Cardiology Foundation Guide to Warfarin Therapy. *Circulation.* 2003;107(12):1692-1711.

37. Fasco MJ, Hildebrandt EF, Suttie JW. Evidence that warfarin anticoagulant action involves two distinct reductase activities. *J Biol Chem.* 1982;257(19):11210-11212.

38. Persson E, Ostergaard A. Mg(2+) binding to the Gla domain of factor X influences the interaction with tissue factor. *J Thromb Haemost.* 2007;5(9):1977-1978.

39. Fenaille F, Groseil C, Ramon C, et al. Mass spectrometric characterization of N- and O-glycans of plasma-derived coagulation factor VII. *Glycoconjugate J.* 2008;25(9):827-842.

40. Blostein M, Cuerquis J, Landry S, Galipeau J. The carboxylation efficiency of the vitamin K-dependent clotting factors: studies with factor IX. *Haemophilia.* 2008;14(5):1063-1068.

41. Yao Y, Shahbazian A, Boström KI. Proline and gamma-carboxylated glutamate residues in matrix Gla protein are critical for binding of bone morphogenetic protein-4. *Circ Res.* 2008;102(9):1065-1074.

42. Oyama N, Gona P, Salton CJ, et al. Differential Impact of Age, Sex, and Hypertension on Aortic Atherosclerosis: The Framingham Heart Study. *Arterioscler Thromb Vasc Biol.* 2008;28(1):155-159.

43. Wong ND, Lopez VA, Allison M, et al. Abdominal Aortic Calcium and Multi-Site Atherosclerosis: The Multiethnic Study of Atherosclerosis. *Atherosclerosis.* 2011;214(2):436-441.

44. Verstuyf A, Carmeliet G, Bouillon R, Mathieu C. Vitamin D: a pleiotropic hormone. *Kidney Int.* 2010;78(2):140-145.

45. Jones G, Strugnell SA, DeLuca HF. Current understanding of the molecular actions of vitamin D. *Physiol Rev.* 1998;78(4):1193-1231.

46. Fleckenstein-Grun G, Thimm F, Frey M, Matyas S. Progression and regression by verapamil of vitamin D_3-induced calcific medial degeneration in coronary arteries of rats. *J Cardiovasc Pharm.* 1995;26(2):207-213.

47. Takeo S, Anan M, Fujioka K, et al. Functional changes of aorta with massive accumulation of calcium. *Atherosclerosis.* 1989;77(2-3):175-181.

48. Kerr DNS. Hypercalcemia and metastatic calcification. *Cardiovasc Res.*1997;36(3):293-297.

Chapter 5: In vivo imaging of vascular calcification with bone seeking agent: When to image?

5.1 Introduction

Drug discovery is a long and costly process. From the discovery of a compound to its approval and availability in the market takes an average of 12-15 years costing more than US $800 million.[1-3] Cutting the expenditure, shortening the length spent in research and development are the two greatest challenges in pharmaceutical industry today.[4] Molecular imaging with PET & SPECT can provide quantitative, and repetitive analytical information on molecules and biological processes in living organisms and is now widely used in field research and clinical drug development.[5-7] Small animal PET & SPECT scanning have been helpful in cutting the cost whilst accelerating the drug development process by providing valuable inputs in target identification and validation stages as well as synthesis and optimisation of drug candidates.[8-11] Pre-clinical imaging of animal models acts as a bridge between *in vitro* studies and those performed *in vivo*, in humans and is an indispensable part of pharmaceutical research.

5.1.1 Basic Principle of SPECT imaging

Single-photon emission computed tomography (SPECT) is a clinically established, sensitive nuclear imaging technique. It provides a three dimensional (3D) spatial distribution of single-photon emitting radiopharmaceutical/radiotracer within the body. A radiotracer is a pharmaceutical compound in which one or more atoms can be replaced by a radioisotope. It can be administered in trace amount, and hence used for *in vivo* imaging of biological processes without any pharmacological effects. The γ-rays emitted by the radiotracers are detected by the head of a gamma-camera, which comprises of a scintillation crystal, optically coupled to an array of photomultiplier tubes, which then converts the γ-rays into electric signals. The γ-rays

of the radiopharmaceuticals are emitted randomly; hence, multiple 2D images are acquired at different angles around the subject. Subsequently the images are reconstructed using reconstruction algorithms to generate cross-sectional images of the *in vivo* distribution of the injected molecules. The random emission of γ-rays calls for a geometric collimation to restrict the travelling direction of the emitted γ-rays from the body. It is accomplished by the use of lead collimators. Collimators are made of thousands of precisely aligned holes (channels). Different types of collimators are used in clinical set ups. Based on the energy of the radioisotope the collimators can be classified as low energy (~140 keV; ^{99m}Tc, ^{111}In etc.), medium energy (~250 keV; ^{67}Ga) and high energy (~364 keV; ^{131}I). The use of a lead collimator is considered as a 'necessary evil' as it reduces the detection efficiency and sensitivity of SPECT by absorbing the photons that travel in other directions than those specified by the aperture of the collimator. Modern SPECT systems can detect radiotracers within the whole-body, at nano to picomolar levels[12], the sensitivity required for *in vivo* tracking of radiolabeled drugs without inducing pharmacological effects or toxicity.

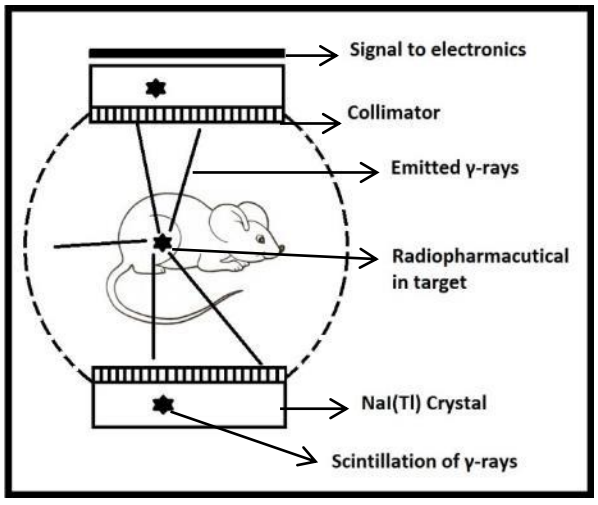

Figure 5.1 : Diagrammatic representation of a small animal SPECT scanner.

The energies of γ-ray emitting radionuclides used in SPECT imaging range approximately 30 to 300 keV. The half-lives of the SPECT radionuclides vary between hours to several days and are commercially available in the form of generators, or

cyclotron or reactor produced making them easy to transport and cheap. The radiometal technetium-99m (^{99m}Tc) is considered as the “work horse” in the field of conventional nuclear imaging. It is the most widely used SPECT radionuclide due to its favourable physical properties ($t_{1/2}$ = 6.03 h, Eγ = 140 keV) and its commercial availability in the form of ^{99}Mo/^{99m}Tc generator. Other routinely used γ-emitting radionuclides for SPECT imaging are gallium-67 (^{67}Ga), thallium-201 (^{201}Tl), indium-111 (^{111}In), iodine-123 (^{123}I) and iodine-131 (^{131}I).

Small animal SPECT scanners (Figure 5.1) have evolved from well-established clinical systems developed for human use, hence the fundamentals are same. However, the miniaturisation of the clinical SPECT system to image small animals poses its own challenges related to camera sensitivity, spatial resolution and image reconstruction and quantification. Recent advances in the SPECT instrumentation have successfully addressed those issues. A small animal SPECT scanner employs pinhole collimators allowing it to achieve millimetre or submillimetre spatial resolution.[13] Currently, multimodality approach or fusion imaging with CT or more recently MRI is employed to negate the drawbacks of SPECT system.

5.1.2 Basic Principle of PET Imaging

Positron emission tomography (PET) is a clinically established sensitive molecular imaging modality that records the distribution of imaging agents labelled with positron emitting radionuclides. Natural biological molecules as well as pharmaceuticals can be labelled with a positron-emitting radioisotope. One advantage of PET over SPECT is that it allows the use of isotopes of carbon, oxygen, and nitrogen, the three most common elements in living organism. Positron-emitting radioisotopes frequently used in clinical practice and research are carbon-11 (^{11}C), oxygen-15 (^{15}O), nitrogen-13 (^{13}N), and fluorine -18 (^{18}F), the latter used as a substitute for hydrogen. This allows the possibility of using active biological substances as radiotracers. Other positron emitting radionuclides include ^{14}O, ^{64}Cu, ^{62}Cu, ^{124}I, ^{76}Br, ^{82}Rb, and ^{68}Ga. Most of the

PET radioisotopes are produced in a cyclotron;[14] however some are available in the form of a generator (e.g., ^{68}Ga, ^{82}Rb).[15, 16] Unlike SPECT radiotracers, most of the positron-emitting isotopes used have relatively short half-lives (e.g., ^{18}F has t1/2 = 110 min). The short half-lives of the radioisotopes demands a fast and efficient chemical reaction to incorporate the isotope into the parent molecule and subsequently it is necessary to inject it to the patient quickly.

Proton-rich radioisotopes can decay via positron emission, in which a proton in the nucleus decays to a neutron, a positron and a neutrino. A positron traverses for a distance and annihilates to generate a pair of gamma rays that are ~180 degrees to each other with energy of 511 keV. The distance travelled by a positron is known as positron range. For the detection of the gamma rays PET scanners employ pairs of radiation detectors to measure the nearly simultaneous, coincident interaction of 511 keV photons. The detectors are normally arranged in geometric shapes that approximates a circle in 2D and a cylinder in 3D. The line that connects any two detectors in the PET scanner is called a line of response. One advantage of PET over SPECT is that allows better quantification of the distribution of the PET tracers *in vivo*. This is possible because the attenuation of the emitted radiation in PET can be corrected precisely. Reconstruction software makes corrections for dead time, and random coincidences, and scatter to reconstruct an image that depicts the localization and concentration of the positron-emitting radioisotope within a plane of the scanned organ. The main difference between SPECT and PET measurements is the use of lead collimators for the definition of the angle of incidence, compared with electronic collimation in the case of PET.

Small animal micro-PET scanners (Figure 5.2) have been developed, in the recent years with a spatial resolution of ~1-3 mm^3.[17-19] Development of small animal PET is particularly advantageous in drug development as it allows for an *in vivo* tool to study pharmacokinetics, pharmacodynamics, gene expression, cell tracking, protein-

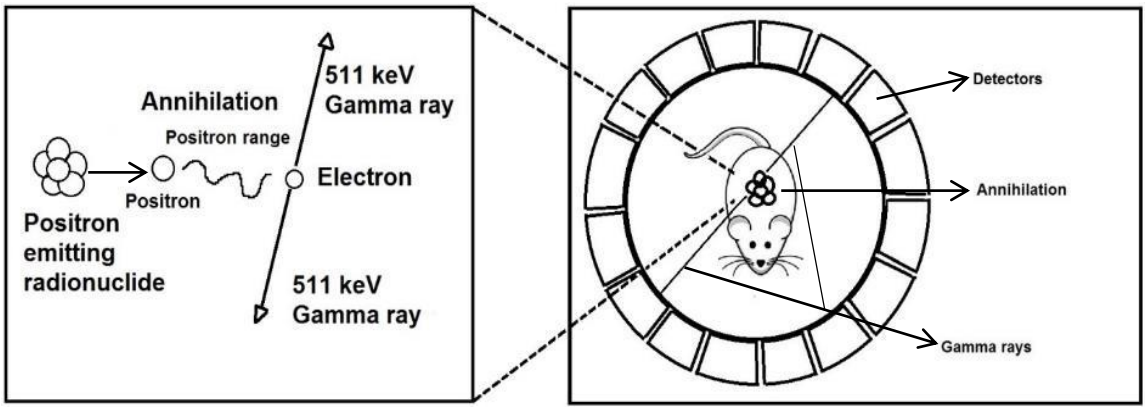

Figure 5.2: Diagrammatic illustration of a small animal PET scanner, co-incidence detection of positron and annihilation of a positron. A positron released from the radionuclide annihilates releasing two coincidence photons of 511 keV, which are detected by scintillation crystals. Coincidence detection of annihilated gamma rays along a line-of-response makes it possible to localize the source of the annihilation.

protein interaction and receptor-based imaging. The ability to perform translational research from a cell culture setting to preclinical animal models and further to clinical applications is one of the most unique and powerful features of PET technology.

The aim of these experiments is to answer two important questions:

1. Can bone seeking radiopharmaceuticals bind to sites with extra-osseous calcification?
2. What would be the ideal time point (post injection) to scan the animals?

5.2 Materials and methods

5.2.1 Maintenance of animal

All procedures were performed in accordance with licences and guidelines approved by the UK Home Office and were approved by a King's College ethics committee. The experiments in this section were carried out under the person project licence (PPL) 70/7097 (PPL holder Rene Botnar) and personal investigator licence (PIL) 70/23976 (PIL holder Jayanta Kumar Bordoloi). Sprague Dawley (SD) rats (n = 16; male; 21–27 days old) were purchased from Charles River Laboratories, UK. The animals were

housed at the BSU located at the St. Thomas' Hospital campus of King's College, London under a strict aseptic condition.

After an acclimatisation period of 7 days, the rats were divided two groups comprising 8 rats each. One group was fed with a diet containing warfarin (3 mg g^{-1} food) and vitamin K1 (1.5 mg g^{-1} food) for 11 days. The rats also received subcutaneous injections of cholecalciferol, 5 mg (200,000 IU) kg^{-1} per day for 4 days (from day 7 to day 11 of the diet). The other group was maintained in a normal rodent diet. All animals were maintained on a 12 hour light-dark cycling with access to environmental enrichment (tunnel). Food and water were provided *ad libitum*. For imaging the two groups of rats were further divided into 4 sub-groups of two rats each (as shown in Figure 5.1) to be scanned with the 4 below mentioned radiopharmaceuticals.

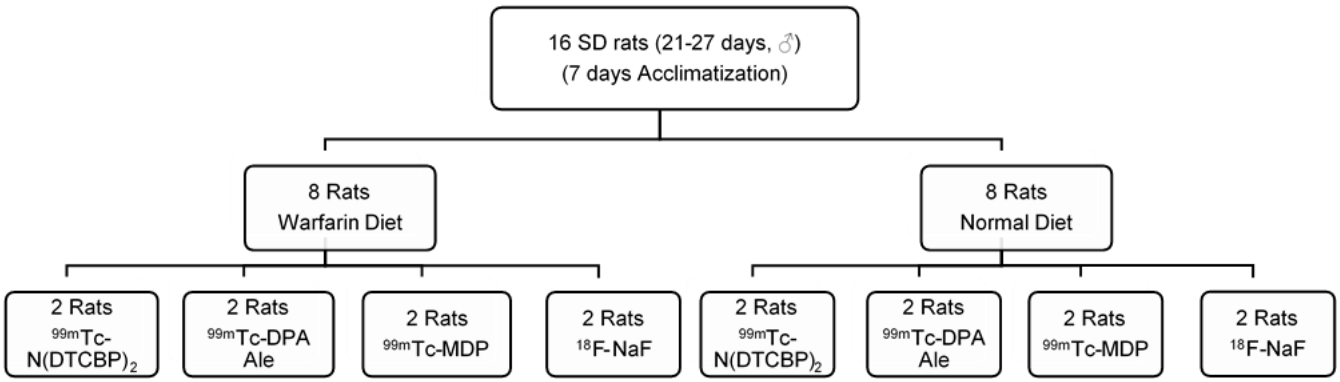

Figure 5.3: Scheme of the in vivo evaluation of bone seeking radiopharmaceuticals in SD rats.

5.2.2 Radiopharmaceuticals: radiolabelling and quality control

Four radiotracers were used in the study. They are clinically established bone seeking agents ^{99m}Tc-MDP and ^{18}F-NaF and novel radiotracers with pendant bisphosphonates groups ^{99m}Tc-DPA Ale and ^{99m}Tc-N(DTCBP)$_2$. The radiolabelling technique and quality control have been explained in detail in Chapter 4.

5.2.3 Image acquisition

5.2.3 (I) SPECT-CT imaging

The scans were performed on a BioScan nanoSPECT-CT®PLUS (Mediso, Hungary) machine using their proprietary acquisition software (Nucline 1.07). CT acquisition was performed at standard frame resolution (512×512 pixels), 55 kVp tube voltage, and 600 ms of exposure time and 360° projections. A total of two fields of views were scanned which required 24 minutes for completion. The SPECT scanner is equipped with 4 heads and multi pinhole general purpose (GP) collimator. Sequential SPECT images were acquired for each lasting for 30 minutes, for 4 h. This provided 7 sets of SPECT images starting from 30-60 minutes post-injection of the radiotracers to 210-240 minutes. At the end of the imaging experiments the animals were then euthanised and organs retained for biodistribution (gamma counting) and histological examinations.

5.2.3 (II) PET-CT acquisition

The PET-CT scans were performed on a BioScan nanoPET-CT®PLUS (Mediso, Hungary) scanner and their proprietary acquisition software (Nucline 1.07). The rats were injected on an injection table and then transferred to the scanner. The transfer of animal, scout image and positioning required 7 minutes. Dynamic PET scan was performed for a single volume of interest (VOI = 94.7mm) from 7 min to 240 min post IV administration of ^{18}F-NaF (8-10 MBq). Acquisition took place in 1–5 coincidence mode with coincidence window of 5 ns, 400–600 keV energy window. A CT scan was performed with the above mentioned parameters after the completion of the PET scan.

5.2.3 (III) Contrast enhanced CT

CT angiography was performed on one SD rat receiving warfarin diet for 11 days and vitamin D_3 injections from day 7 to 11. To obtain vascular contrast, the rat was injected with 0.8 mL of iodinated intravascular contrast agent eXIATM160XL (Binitio Biomedical Inc, Ottawa, Canada). CT acquisition consisted of 270 projections acquired with exposure time of 600 ms, x-ray voltage of 55 kVp, for a full 360° rotation.

5.2.3 (IV) Imaging protocol

1. The rats were transferred from the BSU to the pre-clinical lab and left to acclimatise for 30 minutes.
2. The rats were anaesthetised on the Vet tech rig, in the induction box (lined with Benchkote), O_2 flow rate of 1 l/min and isofluorane levels of 2.5-3.0%.
3. The rats were then transferred to the injection table on a paper tray. The rats were kept under anaesthesia on a mask maintained at 1 l/min O_2 and isofluorane level at 2.5 %.
4. The tail of the rat was heated with an infra-red heat lamp till the veins were prominent.
5. Radiotracer [200 µL; 8-10 MBq ^{18}F-NaF or 45-50 MBq of ^{99m}Tc-MDP, ^{99m}Tc-DPA Ale or ^{99m}Tc-N(DTCBP)$_2$] was injected via the tail vein with a 300 µL insulin syringe.
6. Rats were then transferred from the injection table to the scan bed (rat bed, lined with Benchkote) in the nanoSPECT-CT or nanoPET-CT.
7. A scout scan was performed to select the region of interest.
8. After completion of the scout scan, helical SPECT was started 7 min post injection with 45 sec/projection completing one study in 30 minutes. Sequential SPECT scan was performed for a maximum of 240 min (4 h) post injection. For

PET imaging, a dynamic scan was performed from 7 min to 240 min post injection. CT scan was performed after the completion of PET or SPECT study.

9. At the end of the study the rats were euthanised by Schedule 1 method (over dose of anaesthesia followed by neck dislocation).
10. The rats were then transferred on a tray to the dissection area.

5.2.4 *Ex-vivo* biodistribution study protocol

At the end of the experiment the animals were euthanised by a lethal dose of anaesthesia followed by neck dislocation. Multiple tissues samples were harvested, weighed and the activity measured in a gamma counter (LKB Wallac; 1282 Compugamma). The following were the steps involved:

1. The carcass was weighed.
2. The dead rat was transferred to the dissection area and placed on a lead lined dissection tray lined with Benchkote.
3. The tail was dissected and collected in a pre-weighed scintillation tube, and the carcass was weighed again.
4. The carcass was dissected and vital organs transferred to pre-weighed scintillation tubes.
5. Full vials with organs were weighed and recorded.
6. The activity in the organs was measured on a Wallac, Gamma Camera (10 sec/sample with a window levels of 110-155 for ^{99m}Tc and 175-220 for ^{18}F). The energy range of the gamma counter in 10-2000 keV which is divided algorithmically into 256 window levels. The selected energy levels of the gamma counter corresponds to the energy window of 120-160keV (^{99m}Tc) and 400-600 keV (^{18}F) respectively.
7. Tissue sample from the aorta, mesenteric artery, liver, kidney and lungs were fixed in 4% formaldehyde for histology. Samples of the same were snap-frozen in liquid nitrogen and stored at -80 ºC for biochemical assays.

5.2.5 Image reconstruction and analysis

SPECT: SPECT images were reconstructed in a 128 × 128 matrix using HiSPECT (ScivisGmbH), a reconstruction software package, and images were fused using proprietary Bioscan InVivoScope (IVS) software. All scans were 30 minutes long. **PET:** 3D expectation maximization (3D EM) PET reconstruction algorithm (Mediso Tera - Tomo TM) was applied to produce PET images. The reconstruction was performed using coincidence mode of 1:5, corrections for attenuation andscatter, dead time, decay, and randoms were applied. The number of iterations and subsets were 4 and 6, resulting in images with 0.4 mm voxel size and time frames of 6 × 30 min.

Target to background ratio (TBR) calculation: Using the 3D region of interest (ROI) tool provided with the analysis software (VivoQuant), volume of interest (VOI) were defined on the mesenteric arteries (target) and the thigh muscles (background). Transaxial sections were used to select the VOIs, however to ensure correct ROI placement reconstructed sagittal and coronal views were viewed too. Standard uptake value (SUV) was calculated using the equation: SUV = d/(ID/W), where 'd' is the measured activity in volume of interest, ID is decay corrected injected dose (MBq), and W is the weight of the rat (g). SUV_{max} of radiopharmaceuticals were calculated as the maximum pixel activity in region of interest. TBR_{max} was calculated as the mesenteric artery SUV_{max} normalized to muscle SUV_{max}.

5.2.6 Statistical analysis

If not mentioned otherwise, all the results are expressed as mean ± standard deviation. Statistical analyses were conducted using GraphPad Prism 5.0 statistical software (GraphPad Software, Inc., CA 92037 USA).

5.3 Results

5.3.1 Visual evaluation of SPECT-CT and PET-CT

CT: Visual inspection of the CT scans of treated SD rats (maintained on a warfarin diet and injected with toxic doses of vitamin D_3) revealed extensive calcification in the aorta extending from the aortic arch to the abdominal aorta (See Figure 5.4). Additionally an unexpected area of extraosseous calcification was also observed in the abdomen, located above the left kidney. On the other hand the scan of the corresponding controls, (rats maintained on a standard rodent diet) appeared to be normal with no evidence of extraosseous calcification. Histological sections stained with alizarin red S confirmed calcification in the aortas of the treated rats which was absent in the controls. (see Figure 5.15 A-D).

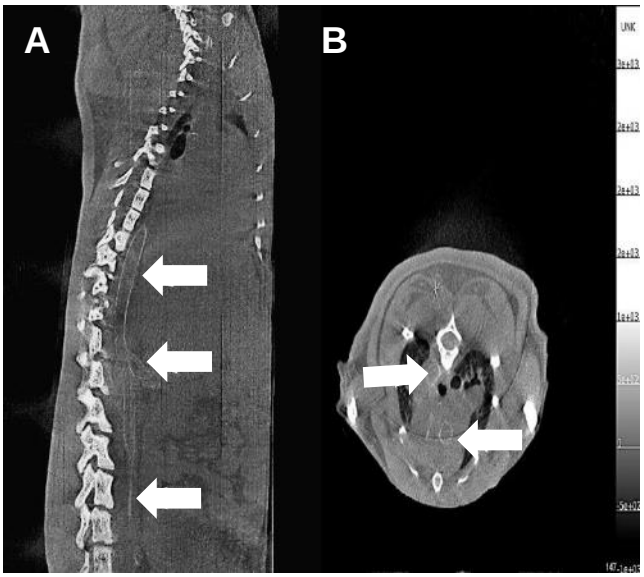

Figure 5.4: CT image of a SD rat fed with warfarin diet for 11 days and injected with vitamin D_3 (200,000 IU^{-1} kg^{-1} day^{-1}) from day 7-11. (A) Sagittal section; the arrow shows the calcified aorta in the (B) transversal section; arrows showing calcification in the ascending and descending aorta.

SPECT: Control rats injected with the ^{99m}Tc-labelled bisphosphonates (^{99m}Tc-MDP, ^{99m}Tc-DPAAle, ^{99m}Tc-N(DTCBP)$_2$) depicted a normal bone scan pattern with uptake primarily in the skeletal and the renal system (Figure 5.5 A-B). Compared to the images of the control rats obtained at 30-60 min there was a significant decrease in

the intensity of the radiotracers in the kidneys at 210-240 min, whereas the opposite was observed in the urinary bladder which indicates excretion of the tracer through the renal system.

Visual examination of the 30-60min SPECT-CT images of the treated rats revealed intense uptake of the ^{99m}Tc-labelled bisphosphonates in the kidneys (Figure 5.6, 5.7, and 5.8) which remains unchanged throughout the scan duration. Histological sections of the kidneys of these rats when stained with von Kossa (Figure 5.14 A) and alizarin red (Figure 5.14 B) disclosed the presence of calcification in the fine branches of the renal arteries.

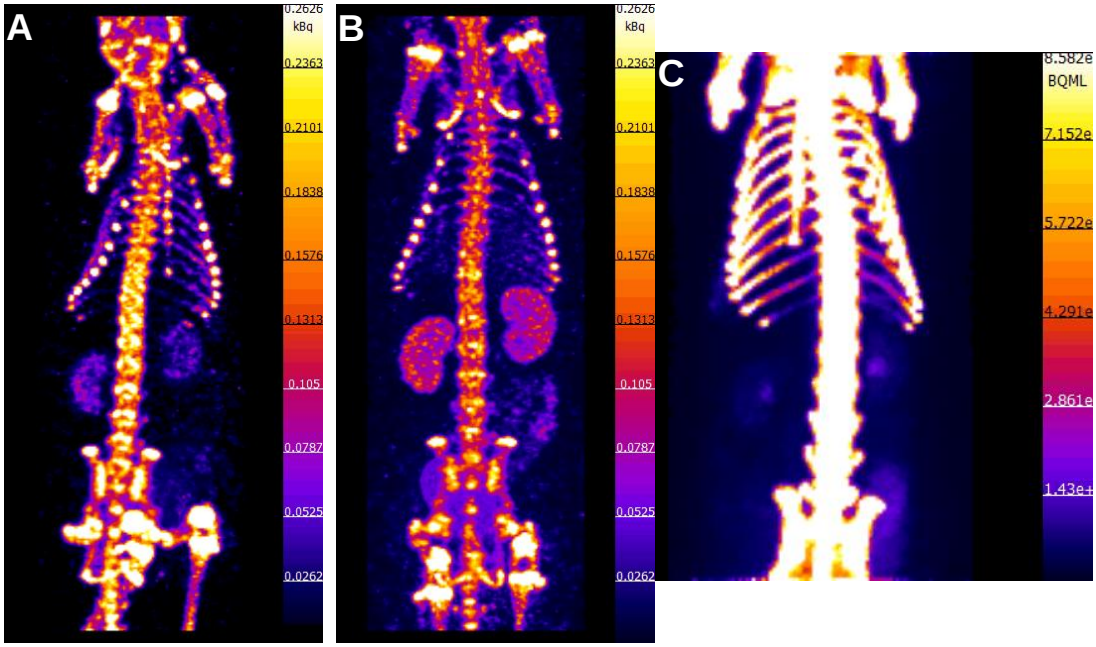

Figure 5.5: Maximum intensity progression of SPECT & PET scans of SD rats maintained on a control diet 210-240 min (4 h) after IV administration of (A) ^{99m}Tc-MDP, (B) ^{99m}Tc-DPA Ale and (C) ^{18}F-NaF. The intensity scales have been set low to visualise the areas of low uptake in the extraosseous tissues.

Corroborating the CT findings, ^{99m}Tc-labelled bisphosphonate accumulation in the unexpected calcified area above the left kidney was observed in the SPECT images (Figure 5.6, 5.7 and 5.8). Interestingly, despite CT (Figure 5.4) and histological confirmation of aortic (Figure 5.15 A,B) calcification, these areas did not show any visually noticeable uptake of the radiotracers in the SPECT study. There were no

notable changes between the images obtained at 30-60 min and 210-240 min post injection in the SPECT images of the treated rats. Rats (both control and treated) injected with ^{99m}Tc-N(DTCBP)$_2$ exhibited diffuse uptake in the liver at 30-60 min SPECT images (Figure 5.6 A-D) which gradually increased with time, suggesting some degree hepatobiliary excretion.

PET images: Visually ^{18}F-sodium fluoride PET scan (Figure 5.5 C) of the control rats appeared to be normal with uptake of the tracer primarily in the bones and the renal system. On the other hand the PET scan of the treated rats revealed high uptake of the probe in the unanticipated calcified region above left kidney (Figure 5.9 A-B), a similarity with the uptake pattern observed in the SPECT study with radiolabelled bisphosphonates.

However, there were startling differences between the uptake of ^{99m}Tc-labelled bisphosphonates and ^{18}F-NaF in the treated rats. Firstly, ^{18}F-NaF PET scan detected calcification in the abdominal aorta of the treated rats (Figure 5.9 C and D) which was missed in the ^{99m}Tc-labelled bisphosphonates. There was no visible uptake of ^{18}F-NaF and ^{99m}Tc-labelled bisphosphonates in the thoracic aorta, although there was CT (Figure 5.4A) and histological (Figure 5.15 A and C) evidence of calcification in the thoracic as well as abdominal aorta. Another striking difference was the absence of ^{18}F-NaF uptake in the kidneys of the treated rats (Figure 5.10 A; B). Intense uptake of ^{99m}Tc-labelled bisphosphonates was observed in the kidneys of the treated rats and histological sections of the kidneys of these rats confirmed the presence of calcification when stained with Von-Kossa and Alizarin red S (Figure 5.14 A-B). However, there were no noticeable difference in the uptake of ^{18}F-NaF in the kidneys of the control and treated rats. Appreciable reduction in the intensity of radiotracer uptake was observed in the 210-240 min (Figure 5.10 B) scan image in comparison to scan images of 30-60 min (Figure 5.10 A) post injection of ^{18}F-NaF.

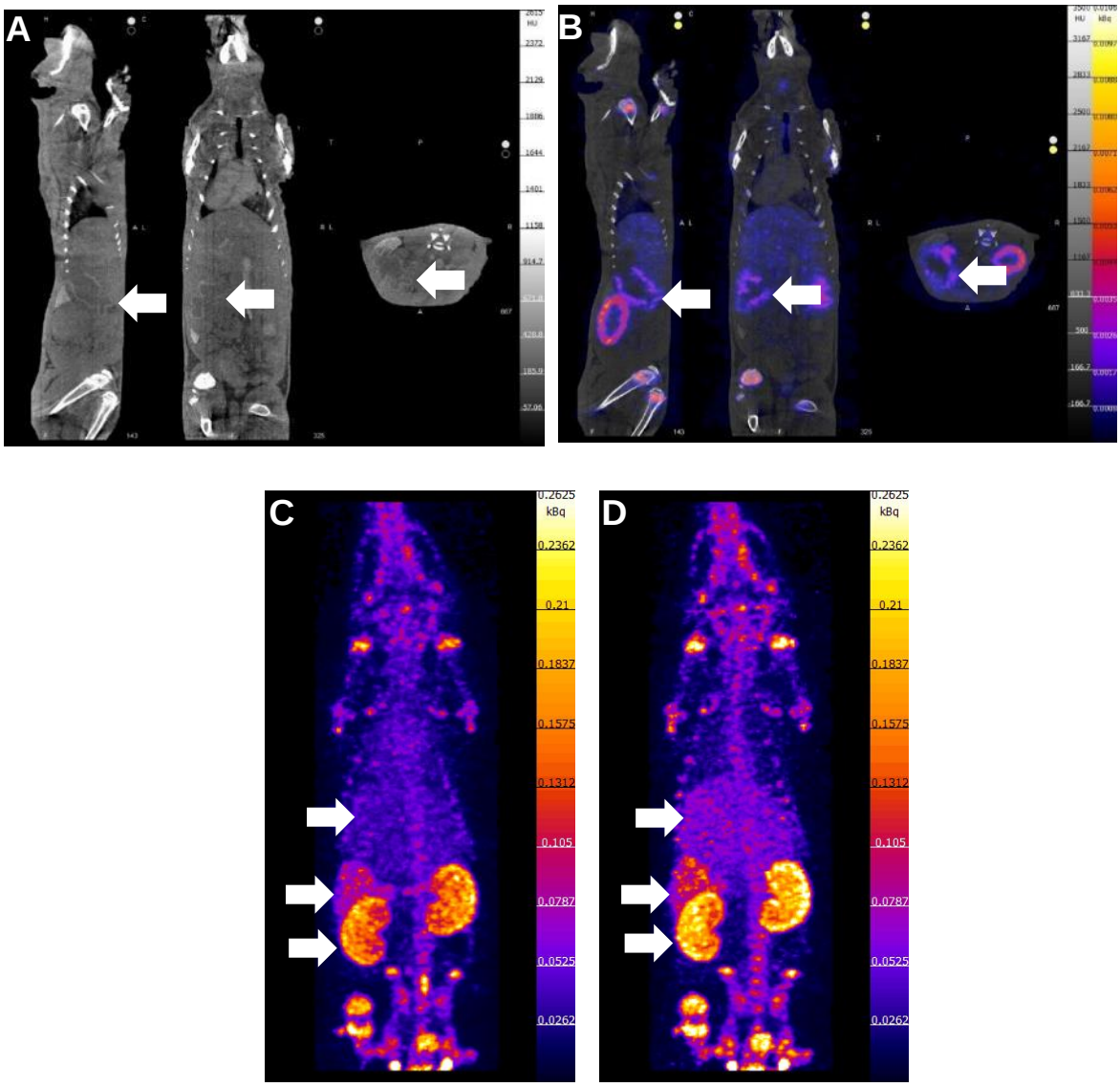

Figure 5.6: SPECT-CT scan images of calcified SD rats with ^{99m}Tc-N (DTCBP)$_2$. (A) Multi-view CT images showing extraosseous calcification above the left kidney. (B**)** Co-localised multi-view (Sagittal, Coronal and Transversal) images showing the uptake of the radiotracer in the calcified area above the left kidney. (C-D) Maximum intensity projections (MIP) of SPECT images at time points (C) 30-60 min, (D) 210-240 min respectively. The arrows show the uptake of the radiotracer in the liver, unexpected calcified region and kidneys.

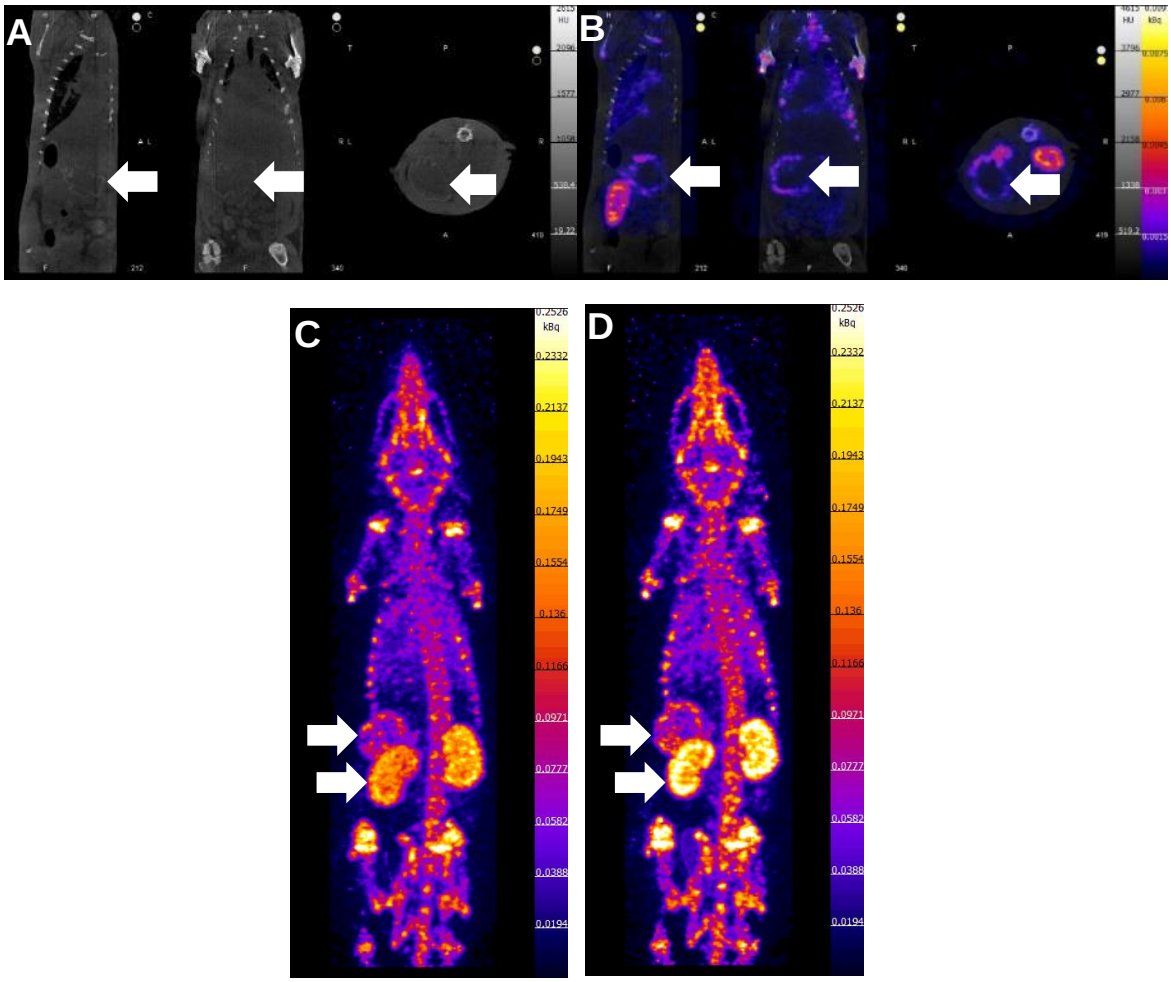

Figure 5.7: SPECT-CT scan images of calcified SD rats with ^{99m}Tc-DPA Ale. (A) Multi-view CT images showing extraosseous calcification in the mesenteric artery. (B) Multi-view (Sagittal, Coronal and Transversal) of fused images, the arrows show the uptake of the radiotracer in the calcified region above the left kidney. (C-D) Maximum intensity projections (MIP) of SPECT images at time point (C) 30-60 min, (D) 210-240 min respectively. The arrows show the uptake of the radiotracer in the mesenteric artery. Intense uptake of the radiotracer can also be seen in the kidneys.

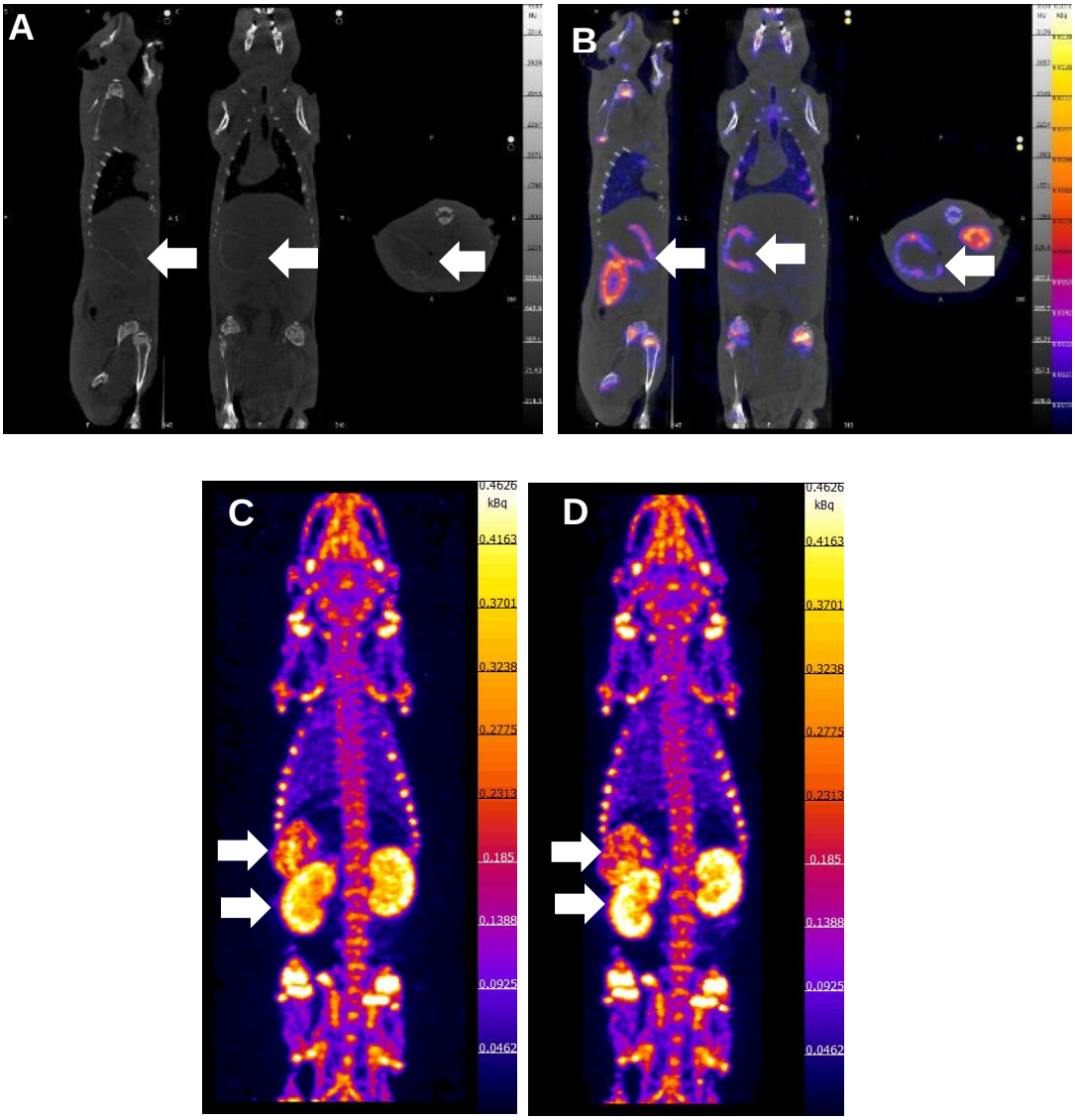

Figure 5.8: SPECT-CT scan images of calcified SD rats with ^{99m}Tc-MDP. (A) Multi-view CT images, the arrows show the extraosseous calcification above the left kidney. (B) Multi-view (Sagittal, Coronal and Transversal) fused images, the arrows show the uptake of the radiotracer in the calcified region above left kidney. (C-D) Maximum intensity projections (MIP) of SPECT images at time point (C) 30-60 min, (D) 210-240 min respectively. The arrows show the unexpected uptake of the radiotracer. Intense uptake of the radiotracer can also be seen in the kidneys.

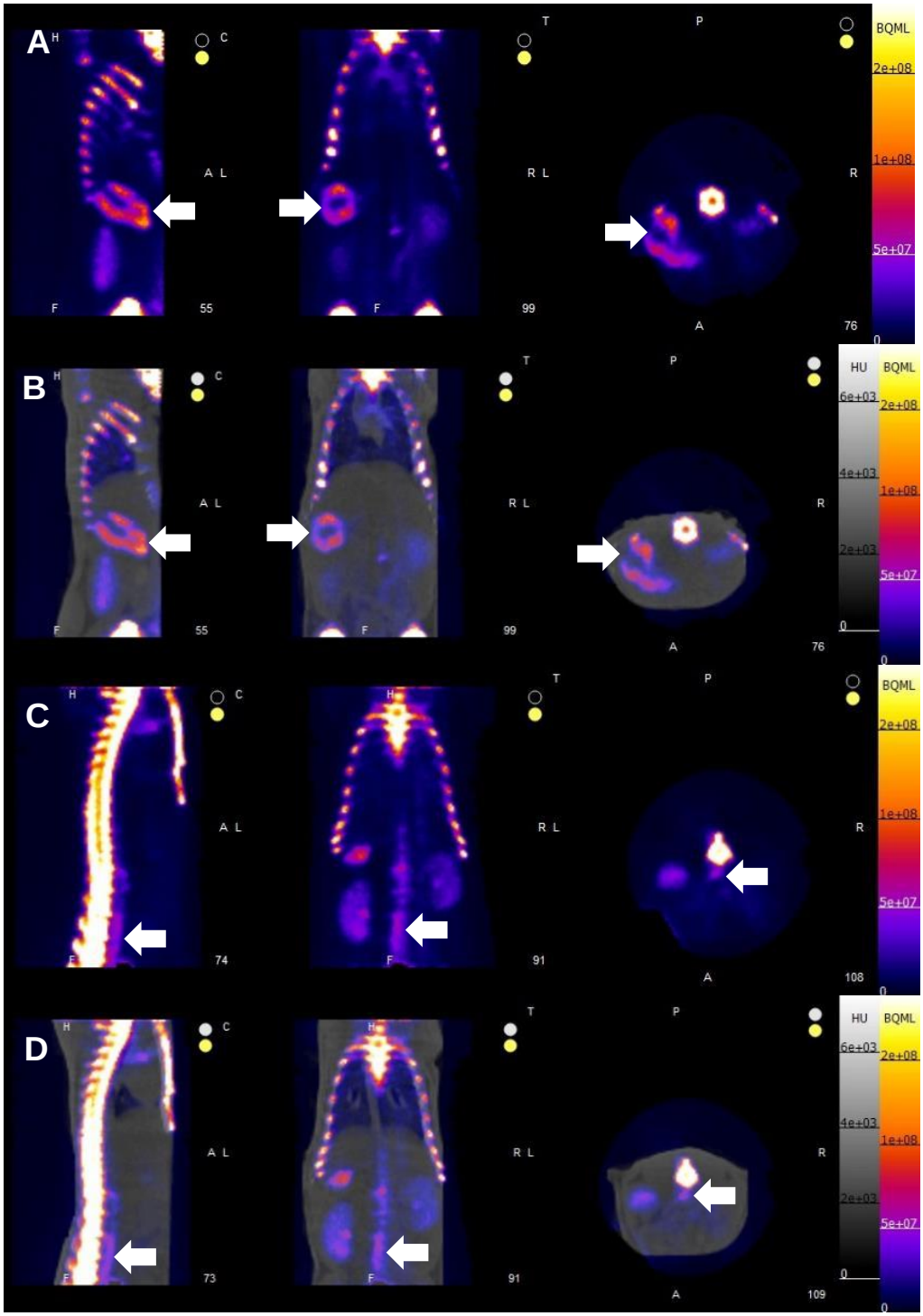

Figure 5.9 ^{18}F-NaF PET-CT scan SD rat fed with a warfarin diet for 11 days and injected with vitamin D_3 (200,000 IU $kg^{-1}day^{-1}$) from day 7-11. The Multiview layout consist of sagittal (left), coronal (middle) and transversal sections. (A) PET and (B) Fused PET-CT, the arrows show the unidentified calcified region above the left kidney. (C) PET and (D) PET-CT, the arrows show uptake in the abdominal aorta of the same rat.

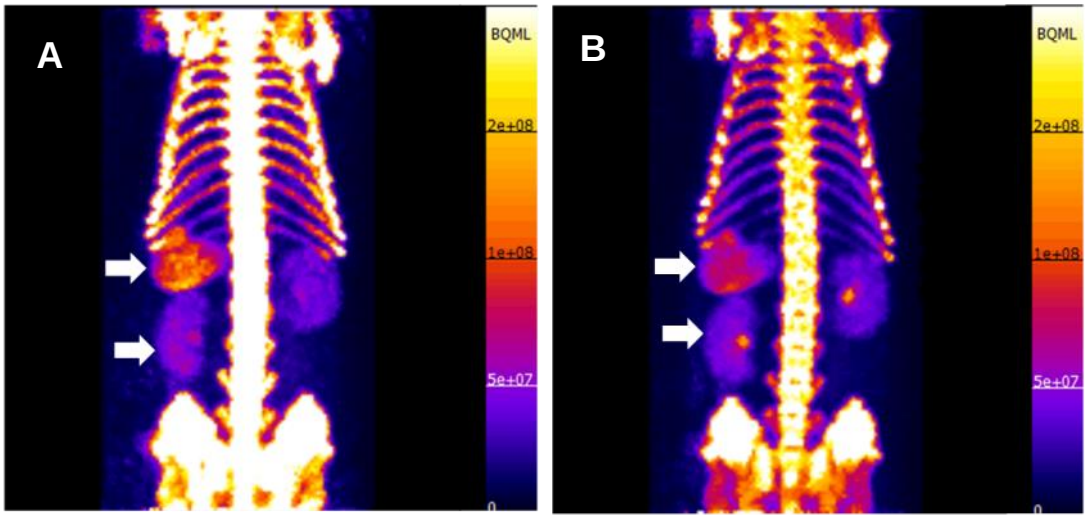

Figure 5.10: MIP of treated rats injected ^{18}F-NaF, scanned at (A) 30-60 min and (B) 210-240 min. The arrows show the uptake of the radiotracer in the kidneys and the unexpected calcified area above the left kidney.

5.3.2 Visual evaluation of contrast enhanced CT

One interesting finding of the SPECT-CT and PET-CT was the intense uptake of the radiotracer in a calcified area above the left kidney. Unenhanced CT images also confirmed that the area was heavily calcified, but was unable to delineate the exact branching from the aorta. Contrast enhanced CT was performed to visualise the exact anatomical structure *in vivo*. The contrast CT images (Figure 5.11 A-C) revealed that the calcified area was the superior mesenteric artery. Histological sections of the tissues collected from the rats confirmed the presence of calcification when stained with alizarin red staining. (Figure 5.11 D).

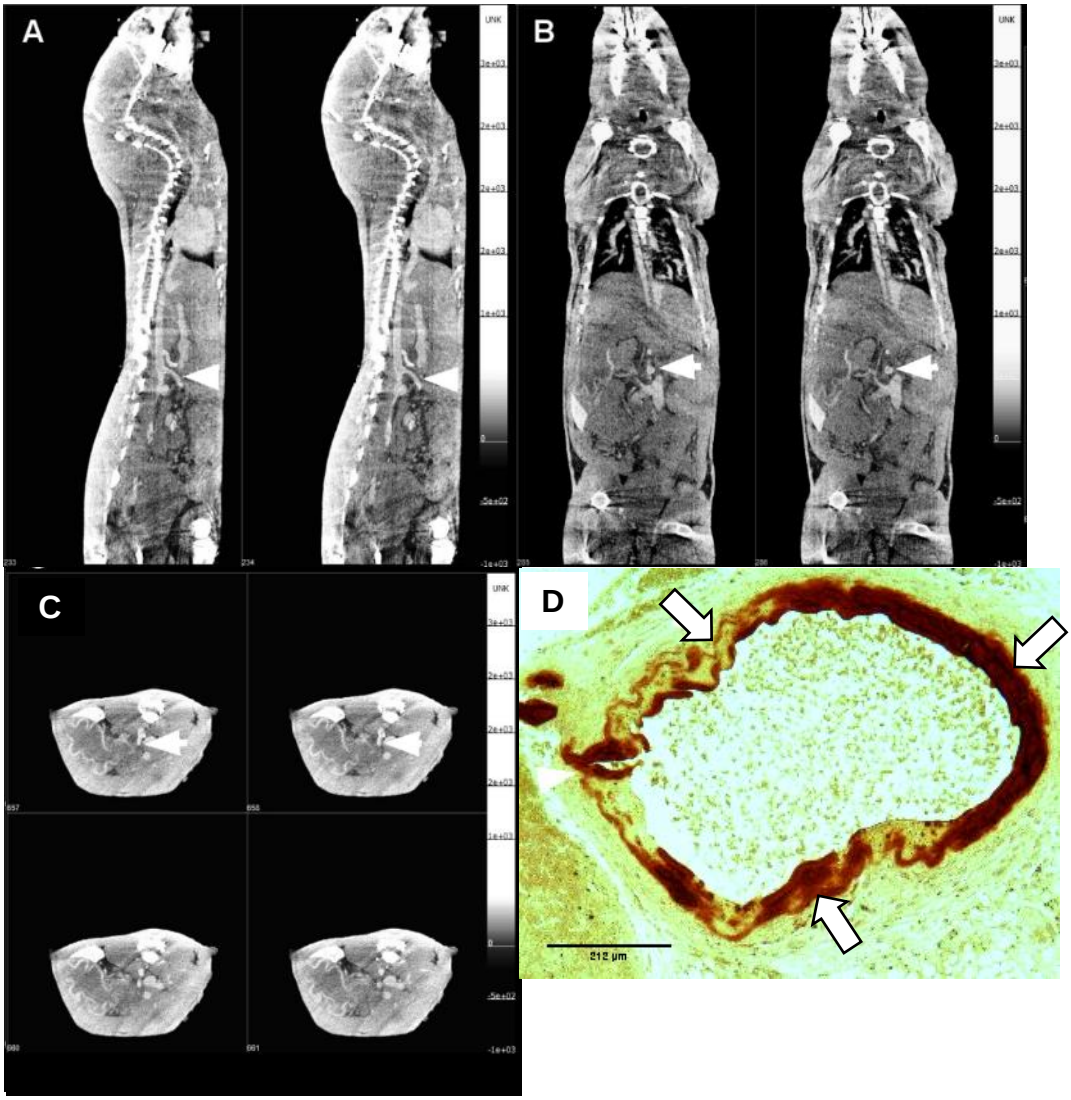

Figure 5.11: CT angiogram of a SD rat with vascular calcification (A) sagittal, (B) coronal and (C) transversal sections. The arrows shows that the unknown area of calcification above the left kidney braches from the superior mesenteric artery. (D) Histological sections of the superior mesenteric artery stained positively with alizarin red S confirming the presence of calcification. (Scale bar = 212 µm)

5.3.3 Target to background ratios

The target to background ratios (TBR_{max}) were measured as the ratio of the SUV_{max} of the mesenteric artery versus the muscles (Figure 5.12). The TBR_{max} at 30-60 min was 3.83±0.06, 2.44±0.01 and 1.76±0.01 for ^{99m}Tc-MDP, ^{99m}Tc-DPA Ale and ^{99m}Tc-N(DTCBP)$_2$ respectively. The TBR_{max} for each radiopharmaceuticals drops in the sequential images gradually with time. At the end of the study i.e. 210-240 min the TBR_{max} were 2.78±0.05, 1.79±0.02 and 1.45±0.01 for ^{99m}Tc-MDP, ^{99m}Tc-DPA Ale and ^{99m}Tc-N(DTCBP)$_2$ respectively. The highest TBR_{max} of ^{18}F-NaF in the calcified mesenteric artery was 6.10 measured in images obtained at the 30-60min post injection, whereas the lowest was 4.29 in the 210-240 min images.

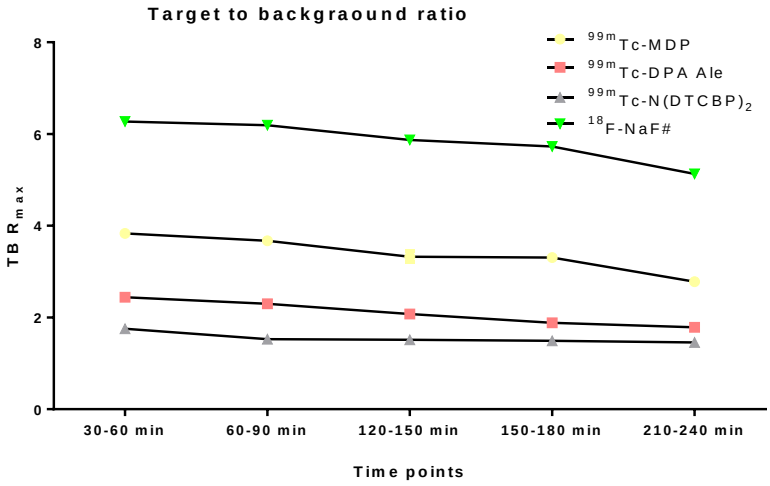

Figure 5.12: TBR_{max} of the treated rats at different time points after IV administration of the radiopharmaceuticals. (#; n=1)**.**

5.3.4 *Ex-vivo* biodistribution studies

Biodistribution studies were carried out on rats sacrificed after the scanning studies i.e. 4 hrs post IV administration of the radiopharmaceuticals. For comparison, biodistribution studies were performed on both treated and control rats. Data obtained from the studies have been summarised in table 5.1 (A-D). As expected the radiotracers mainly accumulated in the bones. The uptake in the femur (bone) of the rats with induced calcification, expressed as %ID/g, were 7.47±0.17, 20.60*(n=1), 7.65±1.00, and 16.57±0.22, for ^{99m}Tc-MDP, ^{18}F-NaF, ^{99m}Tc-N(DTCBP)$_2$ and ^{99m}Tc-DPA Ale respectively; whereas the uptake in the femur of the control rats were 7.39±0.63, 9.83±0.23, 6.18±1.49 and 6.36±1.50. The findings of the biodistribution studies are in agreement with the scan results and increased uptake is observed in the kidneys, lungs and the aorta of the treated rats. However, a comparison of the *ex-vivo* biodistributions of the control and treated rats reveal that an increased uptake of the radiopharmaceuticals was seen in all organs of the treated rats with muscles being the exception. The radiotracers showed fast and rapid renal clearance with >50% (data not shown) injected dose accumulated in the urinary bladder 4.66 h post injection.

Table 5.1: The results of %ID/g (Mean ±SD, n=2 except where specified) of (A) ^{99m}Tc-MDP, (B) ^{99m}Tc-DPA Ale, (C) ^{99m}Tc-N(DTCBP)$_2$ and (D) ^{18}F-NaF, respectively in the vital organs of rats with calcification induced by warfarin feeding and injecting high doses of vitamin D_3. The organs were harvested 280 min after the IV administration of the radiopharmaceuticals.

(Table 5.1 A)

^{99m}Tc-MDP

Organ	Treated#	Control
Heart	2.31±0.82	0.28±0.03
Lungs	6.91±0.59	0.16±0.02
Liver	0.30±0.06	0.04±0.03
Kidney	24.30±0.51	1.03±0.37
Femur	7.47±0.17	7.39±0.63
Aorta	1.99±0.75	0.08±0.03
Blood	0.20±0.02	0.07±0.01
Thyroid	3.80±3.06	0.29±0.02
Trachea	3.69±1.66	0.27±0.02
S. Intestine	1.03±0.58	0.03±0.03
L. Intestine	0.96±0.26	0.08±0.04
Spleen	1.29±0.86	0.14±0.01
Muscle	0.32±0.03	0.02±0.06

(Table 5.1 B)

^{99m}Tc-DPA Ale

Organ	Treated#	Control
Heart	3.30±0.82	0.05±0.02
Lungs	6.80±0.60	0.11±0.04
Liver	0.64±0.33	0.44±0.15
Kidney	16.36±10.04	2.67±3.2
Femur	16.57±0.23	6.18±1.49
Aorta	2.46±1.54	0.07±0.02
Blood	0.19±0.07	0.08±0.07
Thyroid	0.18±0.01	0.79±0.38
Trachea	3.73±2.04	1.39±0.5
S. Intestine	1.73±0.50	0.23±0.13
L. Intestine	2.09±1.44	0.28±0.09
Spleen	1.26±1.01	0.29±0.30
Muscle	0.37±0.07	0.03±0.01

(Table 5.1 C)

^{99m}Tc-N(DTCBP)$_2$

Organ	Treated#	Control
Heart	2.77±0.36	0.29±0.07
Lungs	4.037±1.12	0.41±0.04
Liver	5.85±2.22	4.14±1.08
Kidney	17.30±5.5	1.74±0.09
Femur	7.65±1.00	6.36±1.51
Aorta	4.24±0.77	0.16±0.09
Blood	1.24±0.63	0.06±0.03
Thyroid	2.04±0.12	0.22±0.07
Trachea	2.04±0.43	0.23±0.12
S. Intestine	1.45±0.05	1.56±0.62
L. Intestine	1.04±0.05	1.10±0.35
Spleen	3.35±0.27	0.36±0.16
Muscle	0.25±0.06	0.27±0.16

(Table 5.1 D)

^{18}F-NaF

Organ	Treated#(n=1)	Control
Heart	0.63	0.02±0.01
Lungs	0.62	0.02±0.01
Liver	0. 10	0.02±0.01
Kidney	0.51	0.04±0.01
Femur	20.59	9.83±0.23
Aorta	2.04	0.06±0.05
Blood	0.02	0.02±0.01
Thyroid	0.94	0.58±0.18
Trachea	3.23	0.39±0.22
S. Intestine	0.09	0.02±0.01
L. Intestine	0.05	0.21±0.04
Spleen	0.01	0.02±0.01
Muscle	0.03	0.03±0.01

5.3.5 Histology

Histological sections of the aorta (thoracic and abdominal), kidneys, and lungs were stained with von-Kossa (counter stained with H&E) and alizarin red to determine the presence of calcification. The treated rats were positively stained confirming the presence of extraosseous calcification, which was negative in the sections of the same organs obtained from the control rats.

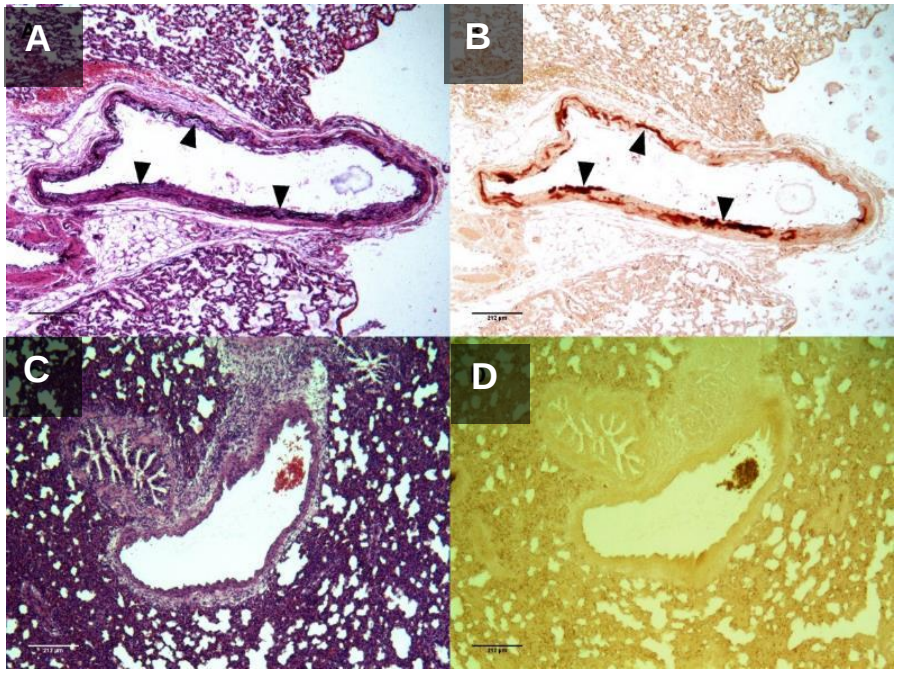

Figure 5.13: Histological evidence of calcification in the lungs shown with von Kossa (A,C) and alizarin red (B,D) staining. Von Kossa stain was counter stained with hematoxylin and eosin stain. The arrows shows the calcified blood vessels in the lungs. (Scale bar = 212 µm)

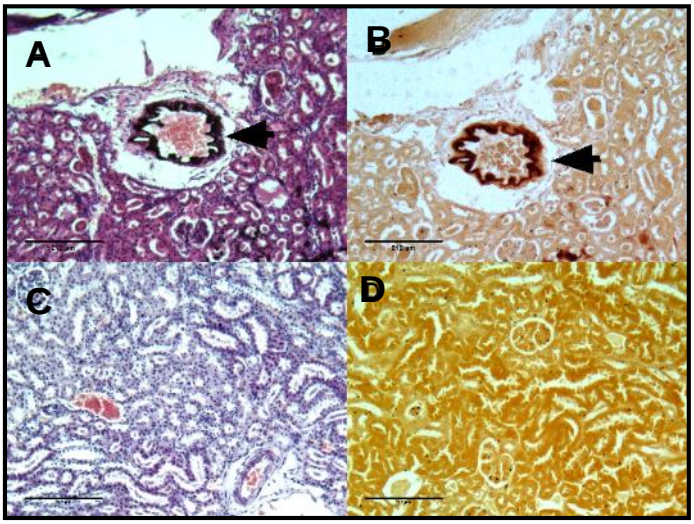

Figure 5.14: Calcification of renal blood vessels. Von Kossa (A, C) and alizarin red (B, D) staining of paraffin embedded section (5 µm thick) shows the calcification in the renal arteries of the treated rats. (Scale bar = 212 µm)

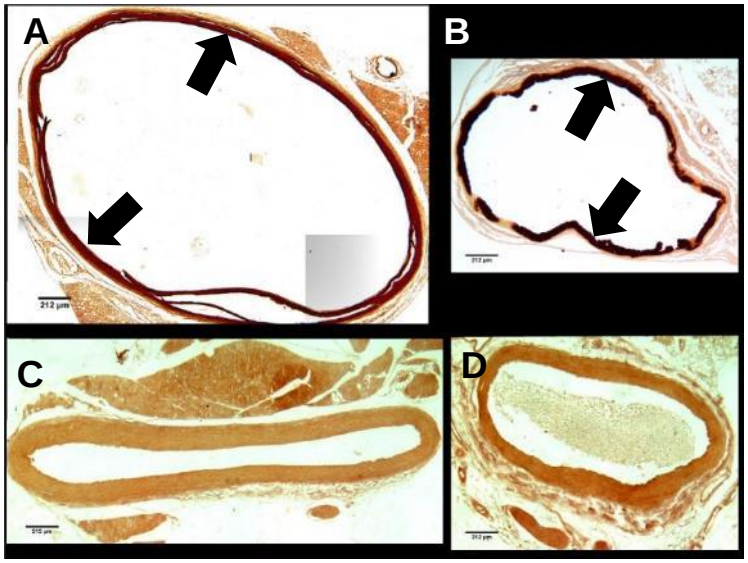

Figure 5.15: Positive alizarin red staining of paraffin embedded section (5 µm thick) obtained from the rat maintained on warfarin diet and injected with sub-cutaneous doses of vitamin D_3. Circumferential calcification pattern is seen in the (A) thoracic aorta and (B) abdominal aorta**.** Whereas the aortas; [(C) thoracic aorta and (D) abdominal aorta] of the control rats were normal. (Scale bar = 212 µm)

5.4 Discussions

We report the first comprehensive *in vivo* molecular imaging (SPECT-CT and PET-CT) study comparing rats with induced medial calcification and control rats with bone mineral seeking radiopharmaceutical. We report the use of:

1. Novel technetium complexes with two pendant bisphosphonate groups ^{99m}Tc-DPA Ale and ^{99m}Tc-N(DCTBP)$_2$
2. Clinically established bone seeking agents ^{99m}Tc-MDP and ^{18}F-NaF

This would also be the first study to compare CT findings with the findings of PET and SPECT scans with bone seeking agents in the detection of aortic calcification in animal models. For this pilot study we chose two animal per group in order to derive some statistical parameter like mean. Of the two treated rats in the ^{18}F-NaF group, one died during the induction of anaesthesia. Therefore, only one treated rat was scanned with ^{18}F-NaF.

Although SPECT and PET are very sensitive imaging modalities, they have the drawback of poor spatial resolution. Therefore, detection of aortic calcification and accurate localisation of the site of uptake in SPECT and PET images can be difficult. This is one of the reasons for choosing the rat model with extensive calcification over mouse models, as the increase in size of the animal and correspondingly larger organs provide bigger targets. The use of CT when using a hybrid PET-CT camera for image acquisition enables the exploitation of the superior spatial resolution of CT and thus improves the anatomic certainty of the site of extra-osseous radiotracer uptake. However, the drawback of CT is poor soft tissue contrast therefore the identification of the unexpected calcified area seen above the left kidney was difficult. A contrast enhanced study was performed on one rat which was helpful in delineating the fine branches of the aorta. It

revealed that the unexpected calcification to be the superior mesenteric artery and histology confirmed the same.

^{99m}Tc-MDP is a routinely used bone seeking radiopharmaceutical in the clinical set up. It has been used for more than four decades in the diagnosis of metabolic and metastatic bone diseases;[20-22] however it has some serious limitations. The structures of the active metal complexes are unknown and the compound is unstable. The instability arises because the bisphosphonate groups in these ligands serve the dual purpose of binding the metal ion (for which they are not well-suited) and for bone targeting (in which their affinity may be compromised by the bound radiometal). To achieve the improvements in *in vivo* stability and affinity for mineral deposits, two novel technetium complexes ^{99m}Tc-DPA Ale, ^{99m}Tc-N(DTCBP)$_2$ were developed. We adopted the strategy wherein the metal chelating site was separated from the bisphosphonate (bone targeting) site in a bifunctional molecule. This allows separate control/optimisation of metal chelation and bone targeting. The novel complexes demonstrated higher binding percentages with synthetic HA and HA from biological origin (chapter 3). However our findings show that these advantages were not translated to *in vivo* imaging of rat models with vascular calcification.

One interesting finding of this study was the differences in ^{99m}Tc-bisphosphonates and ^{18}F-NaF studies. With extensive calcification in the aorta, it was expected that the *in vivo* imaging with the bone seeking agents will also reflect the same. However, the radiolabelled bisphosphonates were not visualised in the aorta. On the other hand, the PET scan with ^{18}F-NaF enabled only visualisation of the abdominal aorta despite evidence of extensive calcification in the thoracic as well abdominal aorta both histologically as well as in CT images. However, the biodistribution study showed increased uptake of the tracer in the aorta. This might be because the whole aorta was used for the gamma counting instead of different segments. The uptake mechanism of

^{18}F-NaF resembles that of ^{99m}Tc-MDP, but they bind to different sites in the hydroxyapatite. The advantages of ^{18}F-NaF over ^{99m}Tc-bisphosphonates includes: smaller molecular size and weight and a negligible non-specific protein binding.[23, 24] The active diffusion of molecules from the capillary wall to the extravascular space is proportional to the molecular size; therefore, diffusion of small molecules of ^{18}F-NaF is expected to be more rapid than that of ^{99m}Tc-bisphosphonates. Comparison studies show that ^{18}F-NaF has a higher sensitivity and specificity in diagnosing metastatic bone diseases compared to ^{99m}Tc-MDP.[25-27]

There was no visible ^{18}F-NaF uptake in the kidneys of the treated rats. However, SPECT studies conducted with the ^{99m}Tc-bisphosphonates demonstrated intense uptake in the kidneys of the calcified rats, which was corroborated by *ex vivo* biodistribution results and further histological examinations of the kidneys revealed the presence of calcification in the renal vessels. These findings suggest that ^{99m}Tc-bisphosphonates and ^{18}F-NaF may be complimenting each other and binding to different processes or stages of calcification. Further study needs to be conducted to understand the reasons and implications of these differences.

Previously published studies show that SD rats treated with warfarin and toxic doses of vitamin D_3 suffer extensive calcification in the aorta, kidney, lungs, trachea, tongue and the liver.[28, 29] *In vivo* imaging and *ex vivo* biodistribution of the rat model presented with a unique opportunity to understand the effects of warfarin and toxic doses of vitamin D_3 in the whole body. The biodistribution findings suggest that the effects are severe and is not localised to the aorta, but the treatment has a global effect. This may explain why PET and SPECT imaging failed to detect increased tracer uptake in the aorta, whereas *ex vivo* organ counting did.

It was essential to find out the ideal time for imaging the rats with calcification, as there were no published data available. This would enable optimisation of the imaging

protocols for future studies. This in turn would also provide the added benefit of reducing the stress imparted on the animals, especially during longitudinal experiments, where the animal has to be revived and re-scanned at several time points. Rather than performing continuous dynamic imaging for hours, the animal can be injected and scanned once during the optimal scanning time. Another benefit of an optimized imaging protocol would be in minimising cost and increasing efficiency.

A limitation of the study was that, Patlak quantification of the dynamic PET study could not be performed. ^{18}F-NaF was administered on an injection table and following which the animal was transferred to scanner. Therefore an image derived input function (IDIF) could not be obtained. Invasive arterial sampling was not performed on warfarin fed rats as they are prone haemorrhage and bleeding. Therefore semi quantitative analysis techniques such as SUV and TBR were used.

In this study, we noted that the delayed images did not provide better target to background contrast during visual assessment. We performed continuous SPECT and PET images over 4 h. With the ^{99m}Tc-labelled bisphosphonates, visually there was no difference in the radiotracer intensity in the calcified areas at all the time points. The target to background ratios measured also showed a subtle change with time. However, in PET images with ^{18}F-NaF there was a visually noticeable loss in the intensity with passage of time. The TBR of the ^{18}F-NaF PET scan becomes more variable with delayed imaging, most probably because of the short half-life of ^{18}F resulting in decay of the tracer and the subsequent increase in image noise. Therefore, the possible benefits of delayed imaging are counterbalanced by the effects of image noise and more variable TB measurements.

5.5 Conclusions

In this study we performed sequential SPECT-CT and PET-CT imaging with novel and clinically established bone seeking agents. The study has shown that bone seeking SPECT and PET agents can detect the presence of extraosseous calcification. The optimum time for imaging was found to be 30-60min and delayed imaging did not offer any significant advantage. The tracer distribution showed that soft tissue calcification as a result of warfarin treatment was not limited to the main blood vessels but was global affecting many tissues.

Although, ^{99m}Tc-N(DTCBP)$_2$ showed high binding propensity with isolated minerals and ABs in both *in vitro* and *in situ* binding assays, the same was not replicated *in vivo.* Non-specific uptake of the radiopharmaceutical ^{99m}Tc-N(DTCBP)$_2$ was observed in the liver of both control and treated rats. Owing to this drawbacks we decided to drop radiopharmaceutical from the study.

References

1. DiMasi JA, Hansen RW, Grabowski HG. The price of innovation: new estimates of drug development costs. *J Health Econ.* 2003;22(2):151-185.

2. Adams CP, Brantner VV. Estimating the cost of new drug development: is it really 802 million dollars? *Health affair.* 2006;25(2):420-428.

3. Morgan S, Grootendorst P, Lexchin J, et al. The cost of drug development: a systematic review. *Health policy.* 2011;100(1):4-17.

4. Rawlins MD. Cutting the cost of drug development? *Nat Revi Drug Discov.* 2004;3(4):360-364.

5. Rudin M. Noninvasive structural, functional, and molecular imaging in drug development. *Curr Opin Chem Biol.* 2009;13(3):360-371.

6. Czernin J, Weber WA, Herschman HR. Molecular imaging in the development of cancer therapeutics. *Annu Revi Med.* 2006;57:99-118.

7. Gomes CM, Abrunhosa AJ, Ramos P, et al. Molecular imaging with SPECT as a tool for drug development. *Adv. Drug Deliver. Rev.* 2011;63(7):547-554.

8. Franc BL, Acton PD, Mari C, at al. Small-Animal SPECT and SPECT-CT: Important Tools for Preclinical Investigation. *J Nucl Med.* 2008;49(10):1651-1663.

9. Pomper MG. Can small animal imaging accelerate drug development? *J Cell Biochem.* 2002;39:211-220.

10. Pomper MG, Lee JS. Small animal imaging in drug development. *Current pharmaceutical design.* 2005;11(25):3247-3272.

11. Franc BL, Acton PD, Mari C, et al. Small-animal SPECT and SPECT-CT: important tools for preclinical investigation. *J Nucl Med.* 2008;49(10):1651-1663.

12. Meikle SR, Kench P, Kassiou M, et al. Small animal SPECT and its place in the matrix of molecular imaging technologies. *Phys Med Biol.* 2005;50(22):R45-61.

13. Funk T, Despres P, Barber WC, et al. A multipinhole small animal SPECT system with submillimeter spatial resolution. *Med Phys.* 2006;33(5):1259-1268.

14. Iribarren C, Sidney S, Sternfeld B, et al. Calcification of the aortic arch: risk factors and association with coronary heart disease, stroke, and peripheral vascular disease. *Jama.* 2000;283(21):2810-2815.

15. Rösch F. Past, present and future of Ge-68/Ga-68 generators. *Appl Radiat Isotopes.* 2013;76(0):24-30.

16. Saha GB, Go RT, MacIntyre WJ, et al. Use of the Sr-82/Rb-82 generator in clinical PET studies. *Int J Rad Appl Instrum. B.* 1990;17(8):763-768.

17. Visser EP, Disselhorst JA, Brom M, et al. Spatial resolution and sensitivity of the Inveon small-animal PET scanner. *J Nucl Med.* 2009;50(1):139-147.

18. Nagy K, Toth M, Major P, et al. Performance evaluation of the small-animal nanoScan PET/MRI system. *J Nucl Med.* 2013;54(10):1825-1832.

19. Prasad R, Ratib O, Zaidi H. NEMA NU-04-based performance characteristics of the LabPET-8 small animal PET scanner. *Phys Med Biol.* 2011;56(20):6649-6664.

20. Subramanian G, Mc Afee J, Blair R, et al. Technetium-99m-methylene diphosphate -a superior agent for skeletal imaging: comparison with other tecnetium complexes. *J Nucl Med.* 1975;16(8):744 - 755.

21. Subramanian G, McAfee JG, Blair RJ, at al. Technetium-99m-Methylene Diphosphonate - A Superior Agent for Skeletal Imaging: Comparison with other Technetium Complexes. *J Nucl Med.* 1975;16(8):744-755.

22. Love C, Din AS, Tomas MB, et al. Radionuclide bone imaging: an illustrative review. *Radiographics.* 2003;23(2):341-358.

23. Wong KK, Piert M. Dynamic bone imaging with Tc-99m labeled diphosphonates and F-18 NaF: mechanisms and applications. *J Nucl Med.* 2013;54(4):590-599.

24. Czernin J, Satyamurthy N, Schiepers C. Molecular mechanisms of bone F-18 NaF deposition. *J Nucl Med.* 2010;51(12):1826-1829.

25. Iagaru A, Young P, Mittra E, et al. Pilot prospective evaluation of 99mTc-MDP scintigraphy, F-18 NaF PET-CT, F-18 FDG PET-CT and whole-body MRI for detection of skeletal metastases. *Clin Nucl Med.* 2013;38(7):e290-296.

26. Iagaru A, Mittra E, Dick DW, Gambhir SS. Prospective evaluation of (99m)Tc MDP scintigraphy, F-18 NaF PET-CT, and F-18 FDG PET-CT for detection of skeletal metastases. *Mol Imaging Biol.* 2012;14(2):252-259.

27. Chakraborty D, Bhattacharya A, Mete UK, et al. Comparison of F-18 fluoride PET-CT and Tc-99m MDP bone scan in the detection of skeletal metastases in urinary bladder carcinoma. *Clin Nucl Med.* 2013;38(8):616-621.

28. Price PA, Faus SA, Williamson MK. Warfarin Causes Rapid Calcification of the Elastic Lamellae in Rat Arteries and Heart Valves. *Arterioscler Thromb Vasc Bio* 1998;18(9):1400-1407.

29. Price PA, Faus SA, Williamson MK. Warfarin-induced artery calcification is accelerated by growth and vitamin D. *Arterioscler Thromb Vasc Bio.* 2000;20(2):317-327.

Chapter 6: Longitudinal SPECT-CT and PET-CT imaging of rats with medial arterial calcification.

6.1 Introduction and aim

In vitro studies are the backbone for outlining biochemical interactions in basic biological and pharmaceutical research; however they have limitations. *In vitro* studies do not offer a true representation of the dynamics of complex biological processes in a living subject. *In vivo* studies compliment *in vitro* studies and provide a holistic view of the interactions of the biochemical under scrutiny. Molecular imaging of animal models is now an integral part of pharmaceutical research. It offers distinct advantages over conventional *in vitro* and cell culture research. Molecular imaging allows monitoring the temporal and the spatial biodistribution of a molecular probe and related biological processes in an intact organism. It also provides quantifiable data of biological phenomena keeping the physiology of the experimental subject intact. A further advantage of molecular imaging over *in vitro* and cell culture experimentation may be achieved by repetitive study of the same animal model, using identical or alternative biological imaging assays at different time points. This reveals a dynamic and more meaningful picture of the progressive changes in biological parameters under scrutiny, as well as possible temporal assessment of therapeutic responses, all in the same animal without recourse to its death. This yields better quality results from far fewer experimental animals.

In the previous experiments (chapter 5) we demonstrated that bone seeking pharmaceuticals can detect the presence of extraosseous calcification in rat models. The results were also used in optimising the imaging protocol for further studies. In continuation of the previous findings we plan to perform longitudinal study with rat model where extraosseous calcification is induced by warfarin feeding without the administration of vitamin D_3. In chapter 4 we have demonstrated that the rats fed with

warfarin diet show a slower progression mineralisation and the extent of mineralisation is significantly less than rats received vitamin D_3 injection along with a warfarin diet. This makes these rats suitable for a longitudinal imaging study.

The objectives of the experiments are to demonstrate that *in vivo* molecular imaging (SPECT-CT and PET-CT) with radiolabeled bone seeking probes can detect calcification in the early stages. The findings will also assist in comparing PET, SPECT and CT for detecting vascular calcification.

6.2 Materials and Methods

6.2.1 Experimental design maintenance of animals

All procedures were performed in accordance with licences and guidelines approved by the UK Home Office and were approved by a King's College ethics committee. The experiments in this section were carried out under the project licence (PPL) 70/7097 (PPL holder Rene Botnar) and personal investigator licence (PIL) 70/23976 (PIL holder Jayanta Kumar Bordoloi). The animals were housed at the BSU located at the St. Thomas' Hospital campus of King's College, London under a strict aseptic condition. All animals were maintained on a 12 hour light-dark cycling with access to environmental enrichment (tunnel). Food and water were provided *ad libitum*.

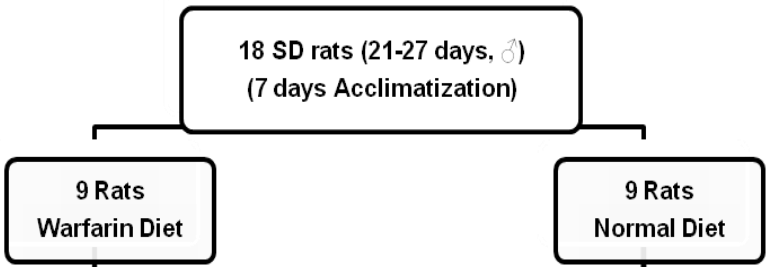

Figure 6.1: Flow chart showing the division of rats and diet modification of the SD rats used for longitudinal imaging.

Longitudinal study: Sprague Dawley (SD) rats (n = 18; male; 21–27 days old) were purchased from Charles River Laboratories, UK. After an acclimatisation period of 7 days, the rats were divided two groups comprising 9 rats each. One group was fed

with a diet containing warfarin (3 mg g^{-1} food). The other group was maintained in a normal rodent diet. For *in vivo* imaging studies, the two groups of rats were further divided into 3 sub-groups of two rats each (as shown in Figure 6.2) to be scanned with the 3 below mentioned radiopharmaceuticals. As this is a pilot study to demonstrate the feasibility of using radiolabeled bone seeking agent to detect vascular calcification, power analysis wasn't performed. The number of animals used in each group is kept at 3 to derive statistical parameters like mean and standard deviation. Observations of these studies may be used for statistical power evaluations for future studies.

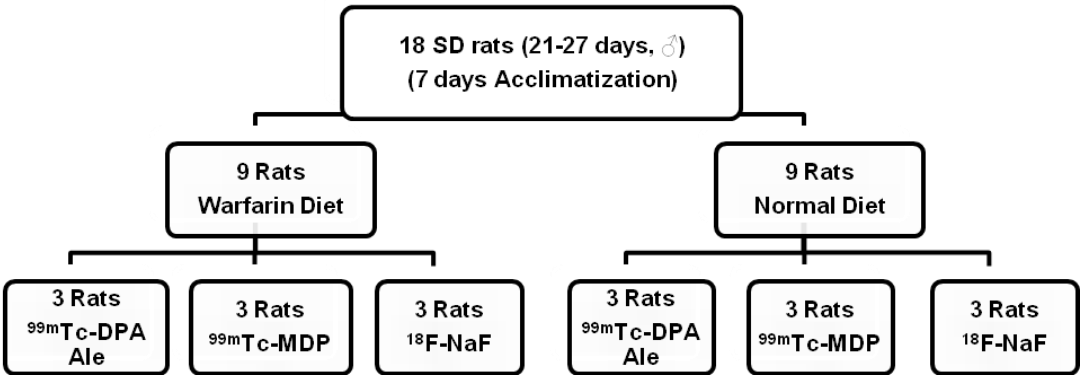

Figure 6.2: Flow chart showing the diet modification SD rats for the longitudinal imaging studies.

Dual radionuclide scan: Sprague Dawley (SD) rats (n = 12; male; 21–27 days old) were purchased from Charles River Laboratories, UK. As shown in figure 6.4, the rats were divided two groups comprising 6 rats each after an acclimatisation period of 7 days. One group was maintained on a diet containing warfarin (3 mg g^{-1} food), whereas the other was provided with a normal rodent diet.

6.2.3 Radiopharmaceuticals: radiolabelling and quality control

Three radiotracers were used in the study. They are clinically established bone seeking agents' ^{99m}Tc-MDP and ^{18}F-NaF and a novel radiotracer with pendant bisphosphonate group ^{99m}Tc-DPA Ale. The radiolabelling technique and quality control have been explained in detail in Chapter 3.

6.2.4 *In vivo* imaging - scanning protocol

Longitudinal imaging

As mentioned above, for the longitudinal study the rats were divided into two groups (Figure 6.1). One was maintained on warfarin diet whereas the other received normal rodent diet. SPECT-CT and PET-CT scans were performed on day 7, 14 and 28 (week 1, 2 and 4) of the diet.

Figure 6.3 depicts a brief illustration of the steps and the duration of the procedures used in the study.

1. The rats were transferred from the BSU to the pre-clinical lab and left to acclimatise (30 min).
2. The rats were anaesthetised on the Vet tech rig, in the induction box (lined with bench coat), O_2 flow rate of 1 l/min and isofluorane levels of 2.5-3.0%.
3. The rats were then transferred to the injection table on a paper tray. The rats were kept under anaesthesia on a mask maintained at 1 l/min O_2 and isofluorane level at 2.5%.
4. The tail of the rat was heated via an infra-red heat lamp till the veins were prominent.
5. Radiotracer (^{18}F-NaF = 5 MBq; ^{99m}Tc-MDP and ^{99m}Tc-DPA Ale = 50 MBq; volume = 200 µL) was injected via the tail vein with a 300 µL insulin syringe.
6. After IV injection of radiopharmaceuticals the rat was then transferred from the injection table to the scan bed (rat bed, lined with bench coat) in the nanoSPECT-CT or nanoPET-CT. The rat was kept under anaesthesia with the isofluorane levels maintained at 2-2.5%.
7. A scout scan was performed to select the region of interest, following which a helical CT scan was performed.

8. After completion of the CT scan, helical SPECT was started (30 min post injection) with 45 sec/projection completing one study in 30 minutes. For PET imaging, a dynamic scan was performed from 30 min (refer Figure 6.3).
9. At the end of the study the rats were revived and monitored for 30 min, following which they were transferred to the BSU and held in the isolated rat holding area for hot animals.
10. The procedure was repeated on day 14 and day 28 of warfarin diet. At the send of the study the rats were culled with schedule one technique (high dose of anaesthesia followed by neck dislocation) and organs were retained for histology and biodistribution. Details of the steps involved in dissection of the rats and gamma counting has been explained in chapter 5.

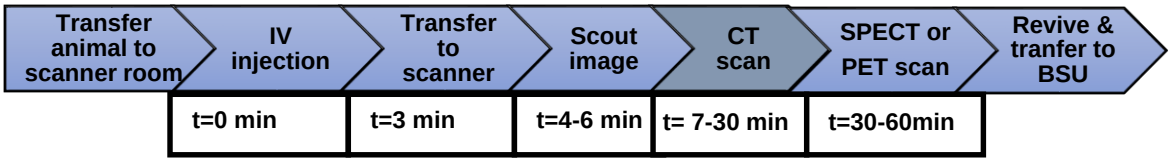

Figure 6.3: Steps involved in the longitudinal SPECT-CT and PET-CT imaging**.**

6.2.5 SPECT-CT acquisition

The scans were performed using a BioScan nanoSPECT-CT®PLUS (Mediso, Hungary) machine and their proprietary acquisition software (Nucline 1.07). CT first approach was followed in all the imaging studies. CT acquisition was performed at standard frame resolution (512×512 pixels), 55 kVp tube voltage, and 600 ms of exposure time and 360° projections. A total of two fields of view were scanned which required 24 minutes for completion. The SPECT scanner is equipped with 4 heads and multi pinhole general purpose (GP) collimator. SPECT images were acquired for the selected FOV, with 40 sec/projections and 45 projections in total and energy window settings of 15% for the centered window at 140 keV. At the end of the imaging experiment the rats were revived and kept under observation for 30 min before transferring them the BSU. For repetitive imaging study where in the rats were

recovered and held at the isolated holding facility in the BSU. The animals and holding facility was monitored for any radioactive spillage. Animal cages contaminated with radiotracers excreted by the animals were held (delay and decay), and released after the decay of the radioactivity. At the end of experiment (4 week of feeding and imaging) the animals were then euthanised and organs retained for biodistribution (gamma counting) and histological examinations.

6.2.6 PET-CT acquisition

The department is equipped with a BioScan nanoPET-CT®PLUS (Mediso, Hungary) scanner and their proprietary acquisition software (Nucline 1.07). A CT scan was performed with the above mentioned parameters. PET scan was performed for a single volume of interest (VOI) for 30 min (30 min to 60 min post IV administration of ^{18}F-NaF) binned with 400–600 keV energy window, 5 ns coincidence time and coincidence mode 1–5.

6.2.7 Dual radionuclide phantom study

A micro hollow sphere phantom (JRT Associates, USA) was used for dual radionuclide phantom study. The phantom is cylindrical with an inner diameter of 4cm equipped with four hollow microspheres. The volume of the empty cylinder is 408 cm^2. The spheres have a radius of ~ 5.95 mm, ~ 6.95mm, ~ 8.23mm and ~9.6 mm which holds a volume of ~ 31 µL, ~ 63 µL, ~ 125 µL, and ~ 250 µL respectively. The micro spheres were first filled with ^{18}F-NaF 1.5 MBq, 2.9 MBq, 4.83 MBq, and 7.75 MBq of ^{18}F-NaF. The outer cylinder was filled with water.

The phantom was placed on the nano PET-CT scanner, and a 30 min PET scan was acquired for a single bed position with the coincidence level set at 1-5, energy window 400-600 keV and coincidence time of 5 ns. This was followed by a helical CT scan acquired at standard frame resolution (512×512 pixels), 55 kVp tube voltage, and 600 ms of exposure time and 360◦ projections.

50 MBq of ^{99m}Tc-DPA Ale was injected into the cylinder and was shaken vigorously. SPECT-CT scan was done with the above mention parameter (section 6.2.6).

Dual-radionuclide scan

For dual radionuclide longitudinal study a total of 12 rats were used, 6 were kept on a warfarin diet whereas the other 6 were fed with a standard rodent diet. The scans were conducted on week 1 (day 7) and week 4 (day 28) since the introduction of the diet. After the completion of week 1 scan 3 rats each from the two diet regimes were sacrificed and organs were retained for histological evaluation. The same was repeated after finishing the week 4 scans.

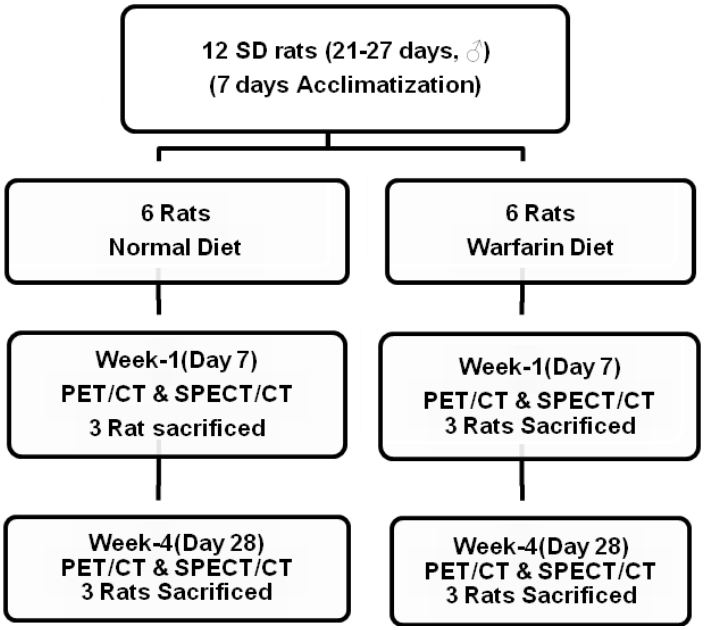

Figure 6.4: Flow chart showing the division of the SD rats, the details of the dual-isotope scan experiment.

The dosing and imaging protocol used for the dual radionuclide PET/SPECT scan has been described in figure 6.5. The rats were first placed under anaesthesia and injected with ~5 MBq (100 µl) of ^{18}F-NaF via the tail vein. The rats were then transferred to the nanoPET-CT scanner and a CT scan (55 kVp tube voltage, and 600 ms of exposure time and 360° projections) lasting for 24 minutes was initiated.

After completion of the CT scan (30 min post injection of PET tracer) a dynamic PET scan of the same FOV, was performed for 30 min.

After the completion of the PET scan, the rat was transferred to the nanoSPECT scanner and a blank SPECT study (multi-pinhole collimator, 40 sec/projection, 45 projections) was conducted which also lasted for 30 min, following which ~50 MBq (100 µl) of ^{99m}Tc-DPA Ale was injected and a CT scan followed by a SPECT scan was performed with the above mentioned parameters.

6.2.8 Image processing and quantification

All SPECT scans were reconstructed in a 256 × 256 matrix using HiSPECT (Scivis GmbH, Germany) software. The same reconstruction parameters were applied for all datasets: 35% Gaussian filtering, 9 iterations with a voxel size of 0.4 mm. The reconstruction algorithm calculate volumes from multiplexing overlapping multi-pinhole SPECT. The proprietary software suite VivoQuant™, Version 2.50 (Mediso, USA) automatically fused the SPECT with CT data sets and was used for quantifications and image analyses.

PET scans were reconstructed using Tera-Tomo (OSEM), iterative reconstruction algorithms provided by the nanoPET-CT vendor (Mediso Ltd). Reconstruction was performed with the detector coincidence mode set to 1:5. Corrections for decay, randoms, crystal dead time, detector normalization and attenuation were implemented. A total of 4 iterations and 6 subsets were applied. The PET and CT images were co-registered automatically. Images were reconstructed with a voxel size of 0.25×0.25×0.25 mm^3 for CT, and 0.4×0.4×0.4 mm^3 for PET.

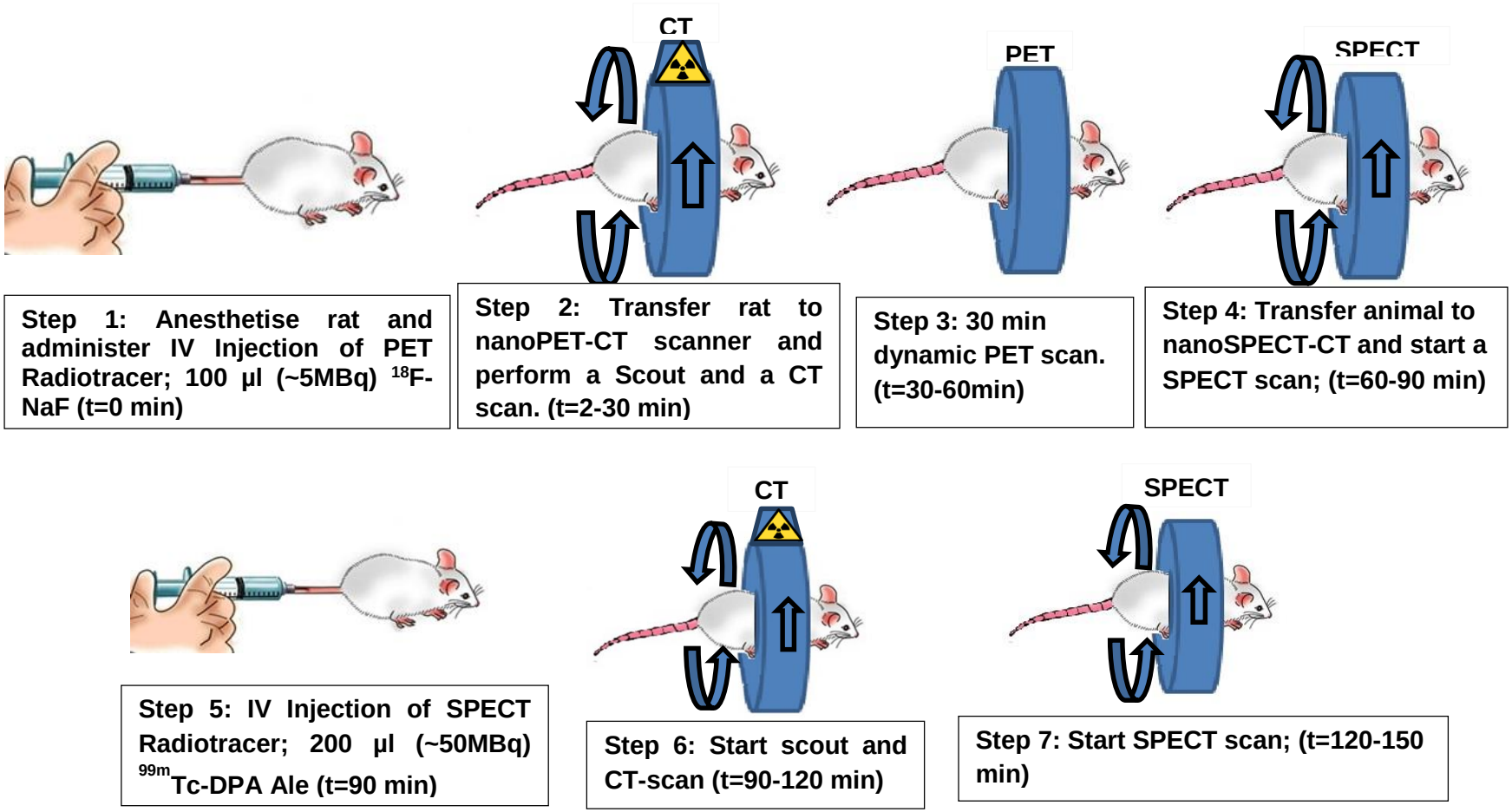

Figure 6.5: Diagrammatic illustration of the protocol used for dual tracer *in-vivo* imaging with PET and SPECT probes in rat model.

Image analysis was performed using pre-clinical image post processing software VivoQuant; (Version 2.5). Using 3D ROI tool feature of the software, cylindrical 3D ROI (volume = 9.9 mm^3) were manually delineated in the aorta and the spine (refer Figure 6.6). The SUV_{max} were calculated and used to determine the aorta to bone ratio. The analysis was performed on longitudinal ^{18}F-NaF scans of rats on a warfarin diet for week-1 and week-4.

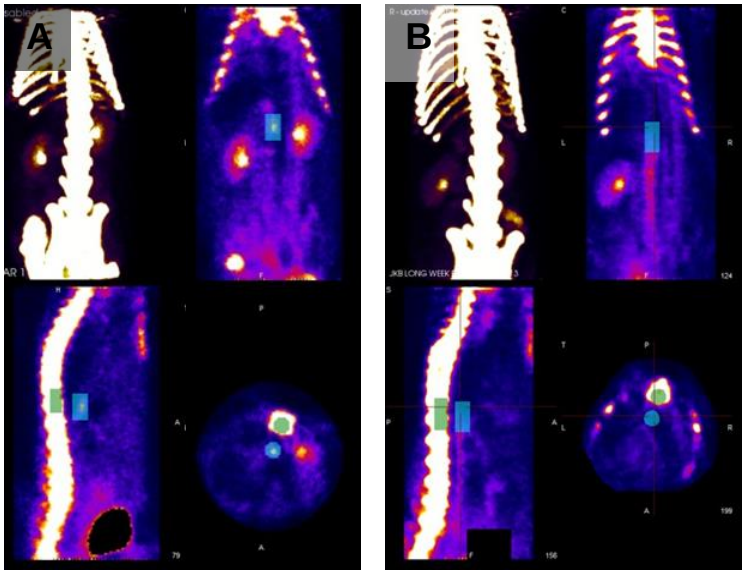

Figure 6.6: Example of image analysis. The analysis was performed on longitudinal scans of rats that were subjected to a warfarin diet. Cylindrical ROI was drawn around the aorta and the spine. Data from the ROI was used to calculate the SUVs within the defined ROI. Analysis was repeated on the same animal on (A) week-1 and (B) week-4. The ratio of the SUV_{max} of the aorta and the spine was calculated.

6.2.9 *Ex vivo* biodistribution studies

At the end of the experiments the animals were euthanised by a lethal dose of anaesthesia followed by neck dislocation. Multiple tissues samples were harvested, weighed and the activity measured in a gamma counter (LKB Wallac). Samples of tissues

originating from the aorta, kidney, lung and heart were preserved for histological examination.

6.2.10 Histology

Tissues were treated with 4% PFA in PBS for 24 hours and maintained at 4 degree Celsius following which the tissues were transferred to 70% ethanol. Paraffin embedding of the samples was performed using an automated embedding machine. Sections (5 µm) were cut on a microtome, and stained with von Kossa and alizarin red staining to detect the presence of calcification.

6.2.11 Histomorphometry

The steps involved in the histomorphometric analyses to determine has been described in detail in chapter 4 (Refining of animal model). A total of 8 randomly selected sections of the thoracic and abdominal aorta from the warfarin fed rats were stained with alizarin red. Using the previously described technique and software (ImageJ) the percentage of the aorta stained positively for the presence of calcification was determined. The software was also used to determine the distance of the pockets of calcifications in the aorta from the lumen. For sections with more than one calcified pocket, the area with the minimum distance from the lumen was selected.

6.2.12 Statistics

GraphPad Prism (version 5.0) was used for all statistical measurements and graphs. All data sets are represented as mean ± SD, except where mentioned. Unpaired *t*-tests were used to compare the continuous variables.

6.3 Results

6.3.1 Visual Inspection of longitudinal SPECT-CT scan

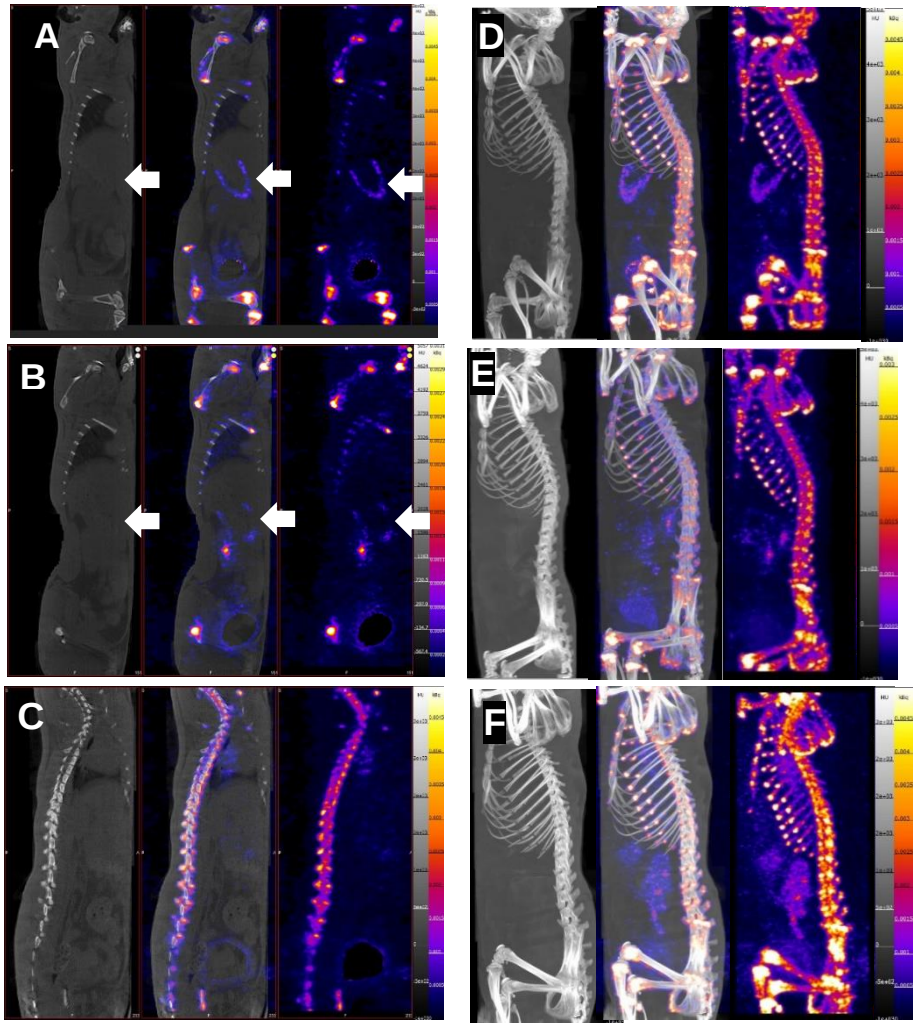

Figure 6.7: Multi-view (left-CT; center- SPECT-CT and right- SPECT) sagittal sections of a treated SD rat scanned 60 min after IV administration of ^{99m}Tc-MDP. Scans were performed on the same subject on (A) Week-1 (B) Week-2 and (C) Week-4 of treatment (warfarin feeding), the arrows show the area with extraosseous uptake in the abdomen (possibly mesenteric artery). The bladder has been removed from the image and the intensity of the images has been kept low, so that area with low uptake of the radiotracer is not missed. Other rats (n=2) in the group did not show any extraosseous uptake. (D-F) Corresponding MIP's for a 3D perspective (D) Week-1, uptake of ^{99m}Tc-MDP can be seen in the skeletal system, the urinary bladder has been removed. (E) On Week-2, ^{99m}Tc-MDP uptake can be seen in the skeletal system, the renal pelvis and urinary bladder (removed). Interestingly the intense uptake visualised in the abdomen on week-1 was faintly visualised. (F) Week-4 showed uptake in the skeletal and urinary system, the extraosseous uptake in the abdomen was absent.

^{99m}Tc-MDP: A total of 6 rats were scanned with ^{99m}Tc-MDP, of which 3 treated (warfarin diet) and the others with a normal rodent diet. On scans performed on week 1 (day-7) of the diet, the control rats depicted a normal scan pattern with uptake visible in the skeletal

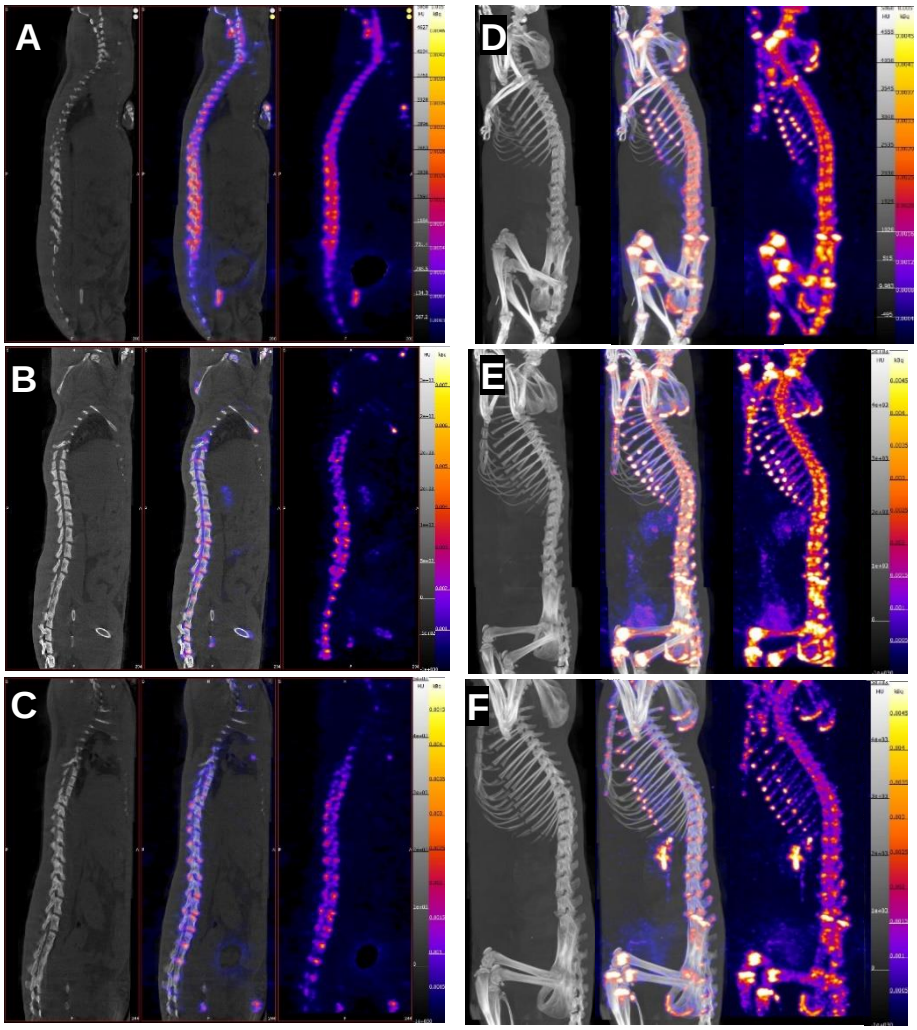

Figure 6.8: Multi-view (left-CT; centre- SPECT-CT and right- SPECT) sagittal sections of a control SD rat scanned 60 min after IV administration of ^{99m}Tc-MDP. Scans were performed on the same subject on (A) Week-1 (B) Week-2 and (C) Week-4. The bladder has been removed from the image. (D-F) Corresponding MIP's for a 3D perspective (D) Week-1, uptake of ^{99m}Tc-MDP can be seen in the skeletal system, the urinary bladder has been removed and there is no retention of ^{99m}Tc-MDP. (E) On Week-2, ^{99m}Tc-MDP uptake can be seen in the skeletal system, the renal pelvis and urinary bladder (removed). (F) Week-4 showed uptake in the skeletal and urinary system, the extraosseous uptake in the abdomen was absent. Uptake was seen in the kidneys.

and renal system (Figure 6.8 A; D). On week 1, extraosseous calcification was observed in the abdomen (possibly mesenteric artery) of one rat on warfarin diet (Figure 6.7 A; D). However, the other treated rats exhibited a normal scan pattern with no visible extraosseous uptake.

Scans performed on the same rat on week 2 and week 4 of the treatment didn't indicate any new area of extraosseous radiopharmaceutical uptake. Interestingly, the intensity of uptake in the previously visualised extraosseous calcification reduced in the week 2 scan (Figure 6.7 B; E), and in week 4 (Figure 6.7 C; F) there was no visible uptake in the abdomen. The control rats showed a normal scan pattern both in weeks 2 (Figure 6.8 B; E) and week 4 (Figure 6.8 C; F).

^{99m}Tc-DPA Ale: On week 1, the SPECT-CT study conducted on the warfarin fed rats did not reveal any visibly noticeable extraosseous uptake of the radiopharmaceutical (Figure 6.9 A). The results were identical to the scan images of the control rats with uptake visible in the skeletal and renal system (Figure 6.10 A). On week 2, uptake of the radiopharmaceutical was observed in two distinct areas of the upper and lower abdominal aorta of one warfarin fed rat (Figure 6.9 B), whereas the others had no extraosseous uptake of the tracer. The control rats revealed a normal scan pattern (Figure 6.9 B). The SPECT-CT performed on week 4 did not reveal any new area of extraosseous uptake of the radiotracer in the group of rat fed with the warfarin diet.

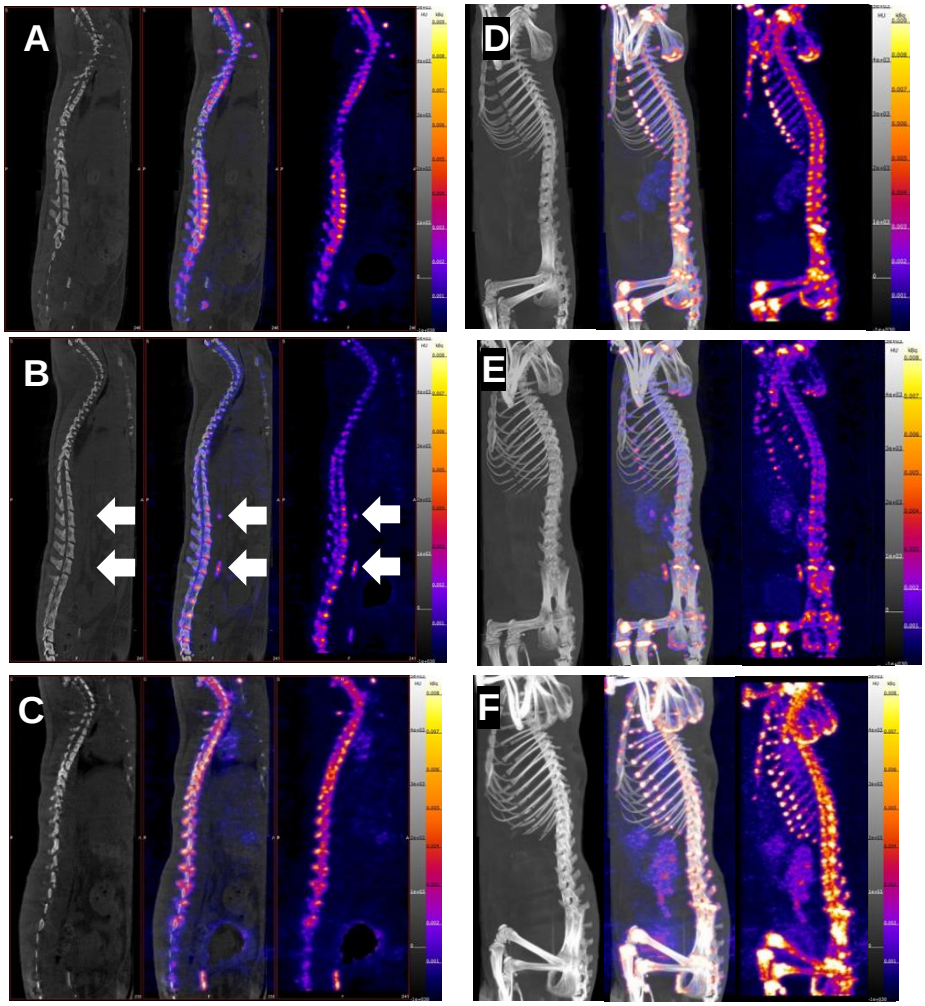

Figure 6.9: Multi-view (left-CT; center- SPECT-CT and right- SPECT) sagittal sections of a treated SD rat scanned 60 min after IV administration of ^{99m}Tc-DPA Ale. Scans were performed on the same subject on (A) week-1 (B) week-2 and (C) week-4 of treatment (warfarin feeding). The arrows show the area with extraosseous uptake in the abdominal aorta (B) on week-2. The bladder has been removed from the image. Other rats (n=2) in the group did not show any extraosseous uptake.(D-F) Corresponding MIP's for a 3D perspective (D) Week-1, uptake of ^{99m}Tc- DPA Ale can be seen in the skeletal system, the urinary bladder has been removed. (E) On Week-2, ^{99m}Tc- DPA Ale uptake can be seen in the skeletal system, the renal pelvis, and abdominal aorta. (F) Week-4 showed uptake in the skeletal and urinary system, the extraosseous uptake in the abdominal aorta was absent.

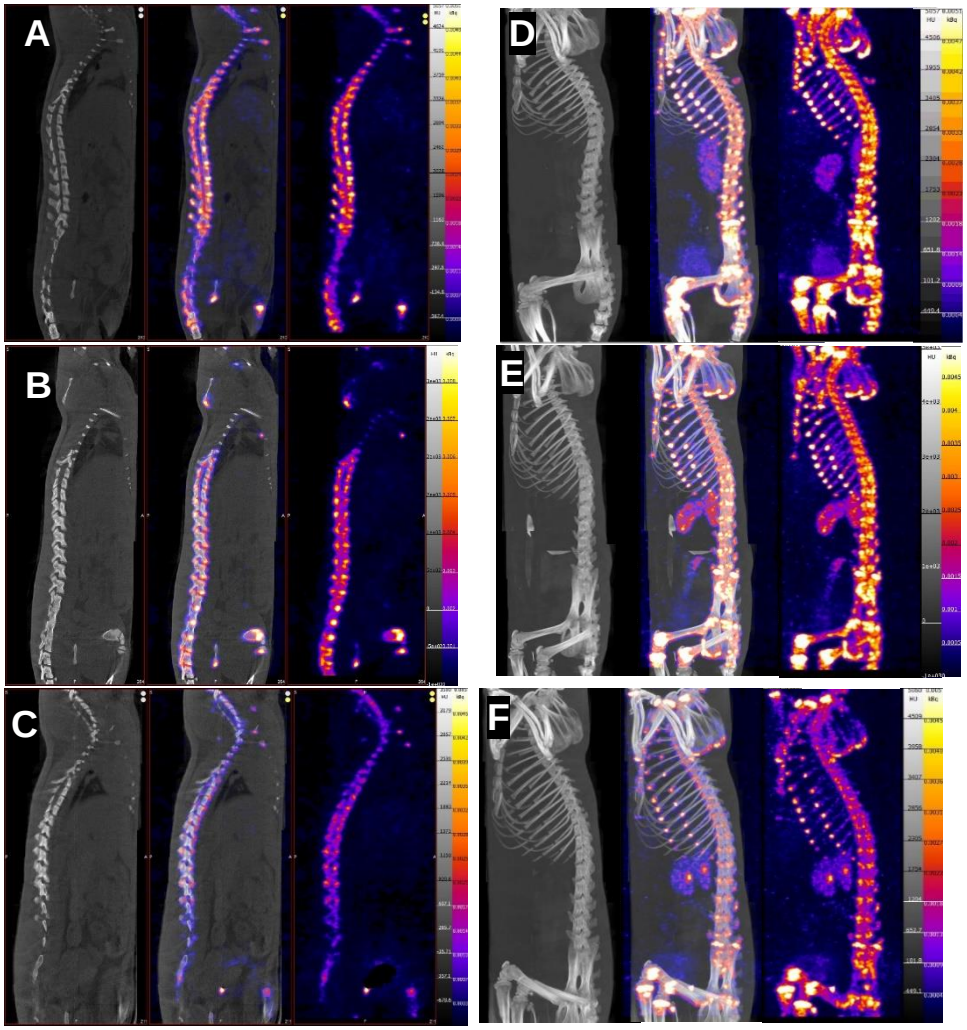

Figure 6.10: Multi-view (left-CT; center- SPECT-CT and right- SPECT) sagittal sections of a control SD rat scanned 60 min after IV administration of ^{99m}Tc-DPA Ale. Scans were performed on the same subject on (A) week-1 (B) week-2 and (C) week-4 of treatment (warfarin feeding). The urinary bladder has been removed from the image. The images depicted a normal bone scan pattern with uptake in the bones and the renal system (D-F) Corresponding MIP's for a 3D perspective.

^{18}F-NaF: The control rats scanned at the three time points i.e. weeks 1, 2 and 4 (Figure 6.11 A-F) were representative of a normal bone scan, with uptake visible in the skeletal system and the renal system. However, some activity was visible in the gut suggestive of some degree of hepatic clearance of the radiotracer in addition to the renal clearance.

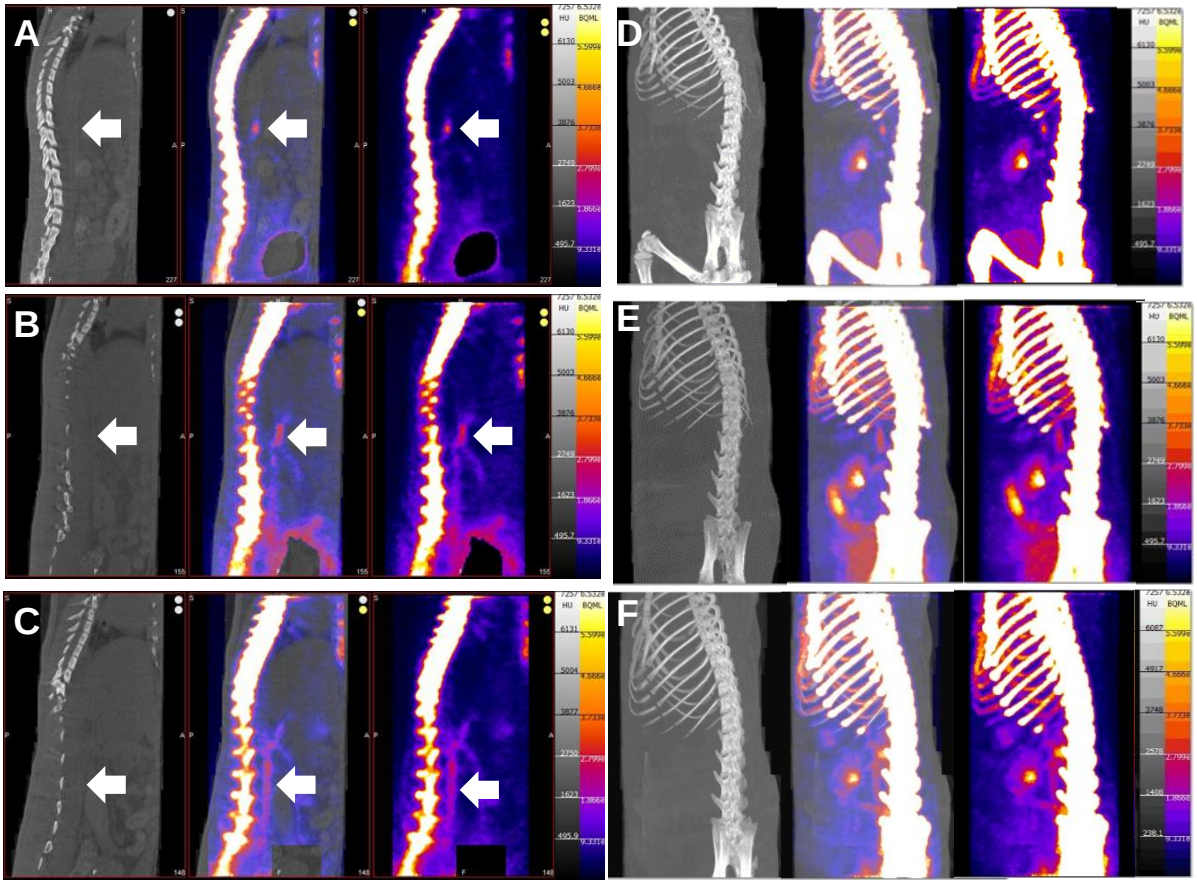

Figure 6.11: Longitudinal PET scans performed with the radiotracer ^{18}F-NaF of a treated rat (warfarin diet). Multi-view (left-CT; center- PET-CT and right- PET) sagittal sections of the week-1 (A) scan reveals intense uptake in the aorta show with an arrow. PET scan performed on week 2 (B) reveal uptake in the lower abdominal aorta shown with the second arrow. The same rat when scanned on week-4 (C) reveals radiotracer in the whole abdominal aorta and the as well as its branches. (D-F) Corresponding MIP of the scans. Besides bones and uptake of ^{18}F-NaF was also seen in the gut.

All rats that received warfarin diet and underwent PET scan with ^{18}F-NaF on week 1 had intense uptake of the tracer in the region of the aorta where the superior mesenteric aorta originates (See figure 6.11 A). On scans performed on the next time-point (week 2)

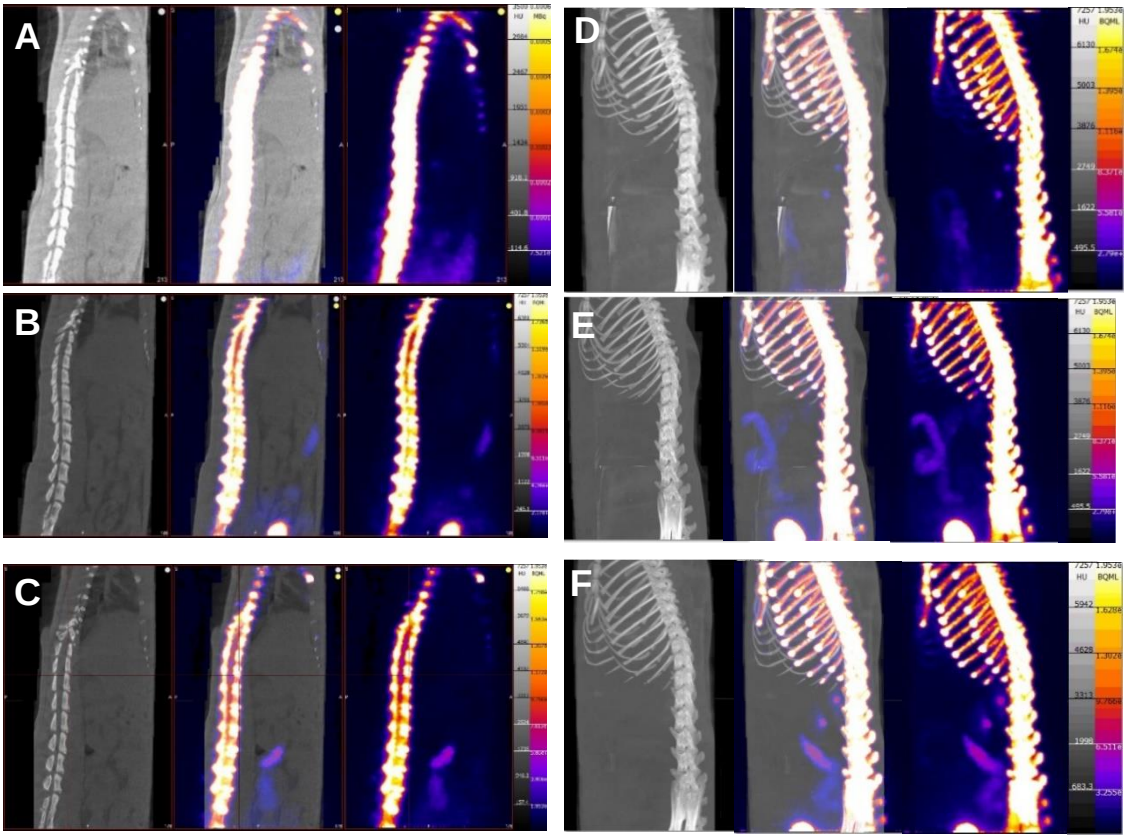

Figure 6.12: Longitudinal PET scans performed with the radiotracer ^{18}F-NaF of a control rat. Multi-view (left-CT; center- PET-CT and right- PET) of sagittal sections of the rat scanned on (A) week-1,(B) week 2, (C) week-4. The scans showed a normal scan pattern with uptake in the bones (skeletal system)and the renal system. (D-F) Corresponding MIPs of the scans.

uptake the progression of calcification was observed in parts of the abdominal aorta and the mesenteric artery (Figure 6.11B). ^{18}F-NaF PET scans performed on the same group of animals showed intense uptake in the whole of the abdominal aorta and the mesenteric artery (Figure 6.11C). Interestingly, the area of the aorta where calcification was visualised on week 1 (Figure 6.11 A) had no radiotracer uptake on the week 4 (Figure 6.11C) scan. The scan of the rats on normal diet depicted a normal bone scan, however radiotracer uptake in the gut was observed. The scan of the rats on normal rodent diet portrayed (Figure 6.12 A-E) a normal bone scan, with uptake in the bones and renal system.

6.3.2 Histomorphometry and distance measurements

Using ImageJ (Version 1.49) the extent of calcification in thoracic and abdominal aorta of the treated SD rats used in the longitudinal study was measured. The percentage of calcification in the thoracic aorta was found to be 3.52 ± 1.52 (n=8) whereas the abdominal aorta it measured to be 43.31 ± 4.35 (n=8). This shows that after 4 weeks of warfarin feeding both the thoracic and the abdominal aorta were calcified, however the damage to the abdominal aorta was significantly higher than the thoracic.

Visual inspection of the sections of the thoracic and abdominal aorta obtained from the treated rats (receiving warfarin diet for 4 weeks) revealed that the calcified areas in the thoracic aorta were deep seated where as those in the abdominal aorta were exposed to the lumen(See Figure 6.13 A-B). Using ImageJ, the distance of the calcified pockets from the lumen was measures (Figure 6.13 C).

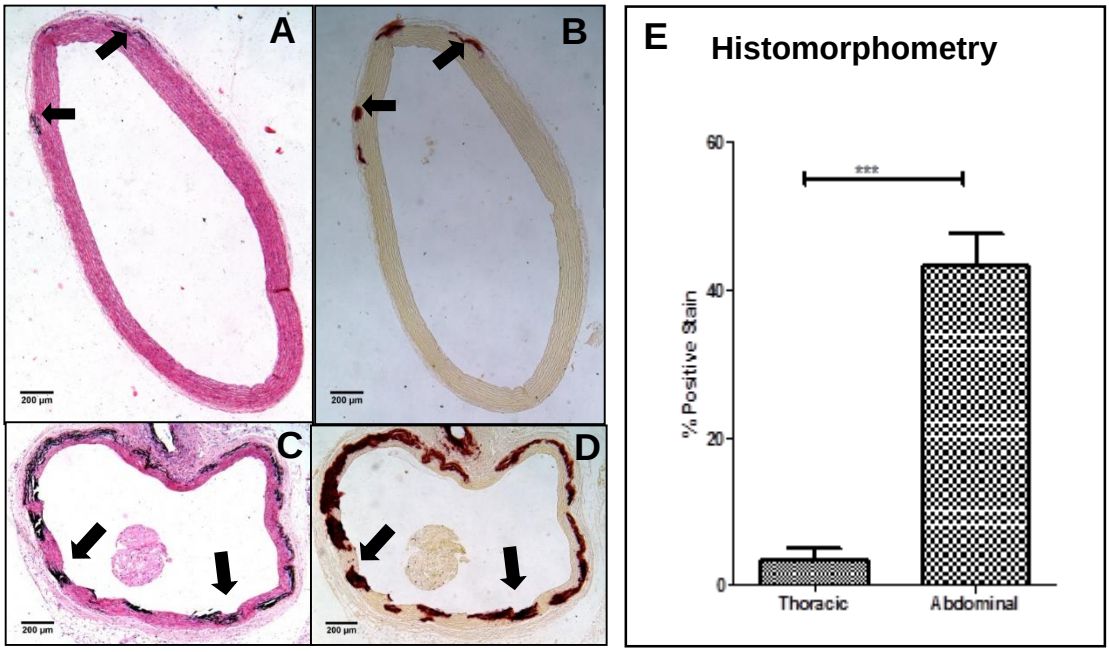

Figure 6.13 : Histological sections of the (A,B) thoracic and (C,D) abdominal aorta of a treated SD rat (warfarin fed for 4 weeks) with von Kossa (H&E counter stain) and alizarin red respectively. (Scale bar = 200 µm) (E) Histomorphometry analysis comparing the percentages of area positively stained for the presence ofcalcification. The percentage of calcification in the thoracic aorta was 3.52 ± 1.52 (n=8) and 43.31 ± 4.35 (n=8) in the abdominal aorta. (***=p<0.001)

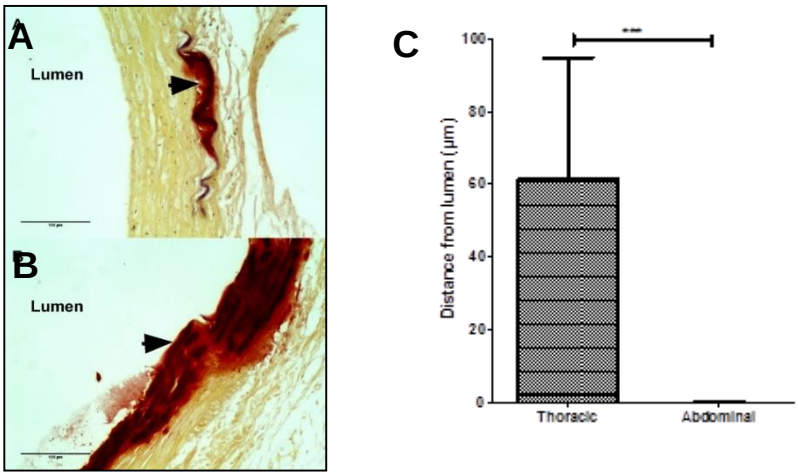

Figure 6.14: Histological sections of the (A) thoracic and (B) abdominal aorta of a treated SD rat (warfarin fed for 4 weeks) alizarin red. ImageJ was used to measure the distance of the calcified pockets from the lumen. In sections with multiple calcified regions, the one closest to the lumen was considered. As seen in fig 6.12 (A-D), the thoracic aorta has less calcification and calcified areas compared to the thoracic aorta, furthermore those pockets were deep seated in the tunica -media. On the other hand the abdominal aorta was heavily calcified with lesions exposed to the lumen.

6.3.3 Ex-vivo biodistribution studies

The biodistributions of ^{99m}Tc-MDP, ^{99m}Tc-DPA Ale, and ^{18}F-NaF in treated (SD rats on warfarin diet; 4 weeks) and normal SD rats are presented in Table 6.1. The samples were obtained from treated and control rats at the end of the longitudinal study. The radiotracers were injected 60 minutes before the animals were culled. The uptake of ^{18}F-NaF accumulated in the femur was substantially high both in the treated (10.68±5%) and control (14.32±4.27%) compared to 2.26±0.13% and 2.87±0.46% with ^{99m}Tc-DPA Ale and 1.77±0.40% and 2.49±0.47% with ^{99m}Tc-MDP for the treated and control rats respectively.

Increased uptake in the aortas, lungs and hearts of the treated rats compared to the controls was observed with all the radiopharmaceuticals.

Table 6.1: *Ex-vivo* biodistribution conducted on treated and control rat after the completion of the longitudinal study (mean±SD, n=3, %Id/g). The rats were culled 60 minutes after the injection of the radiotracers and the treated rats were on a warfarin diet for 4 weeks and the control rats were on a normal rodent diet for an equal duration.

Organ	^{18}F-NaF		^{99m}Tc-DPA Ale		^{99m}Tc-MDP	
	Treated	**Control**	**Treated**	**Control**	**Treated**	**Control**
Skin	0.08±0.01	0.22±0.18	0.08±0.07	0.04±0.01	0.08±0.02	0.05±0.03
Blood	0.13±0.02	0.17±0.09	0.07±0.05	0.06±0.02	0.07±0.03	0.06±0.05
Heart	0.50±0.24	0.13±0.07	0.36±0.16	0.05±0.01	0.28±0.02	0.04±0.03
Lung	0.60±0.07	0.17±0.09	0.43±0.23	0.09±0.01	0.27±0.04	0.06±0.05
Liver	0.14±0.01	0.18±0.06	0.35±0.19	0.33±0.05	0.03±0.01	0.03±0.02
Spleen	0.13±0.01	0.14±0.06	0.05±0.04	0.05±0.01	0.05±0.01	0.04±0.03
S. Intestine	0.24±0.06	0.38±0.18	0.23±0.13	0.14±0.03	0.07±0.02	0.06±0.04
L. Intestine	0.16±0.05	0.25±0.09	0.17±0.12	0.06±0.01	0.11±0.05	0.03±0.02
Stomach	0.21±0.12	0.17±0.11	0.32±0.28	0.11±0.03	0.16±0.01	0.05±0.03
Kidney	0.37±0.16	0.41±0.30	0.94±0.52	2.49±1.17	1.25±1.31	1.99±2.58
Muscle	0.14±0.02	0.12±0.06	0.06±0.04	0.02±0.01	0.03±0.01	0.04±0.03
Femur	10.68±5	14.32±4.27	2.26±0.13	2.87±0.46	1.77±0.40	2.49±0.47
Aorta	1.40±0.17	0.19±0.05	0.91±0.82	0.18±0.11	0.40±0.04	0.23±0.23
Mesenteric	0.13±0.05	0.08±0.03	0.07±0.03	0.02±0.02	0.13±0.025	0.03±0.02

6.3.4 Qualitative assessment of radionuclide phantom study

In order to see the feasibility of dual radionuclide in vivo imaging a phantom study was performed to see the effect of cross talk in the image quality. Reconstructed scan images of the phantom (A) PET-CT with the micro spheres filled with ^{18}F-NaF was compared the (B) reconstructed SPECT-CT scan of the phantom. The hot microspheres in the PET-CT appeared cold on the SPECT-CT images. Visual inspection of the reconstructed SPECT study clearly shows different noise textures between the spheres. The outline of the spheres with diameter of ~ 5.95 mm, ~ 6.95mm, and ~ 8.23mm were smooth without with

no noticeable noise on the image. However the largest sphere (~9.6 mm; 7.75 MBq) had noticeable noise with uneven edges.

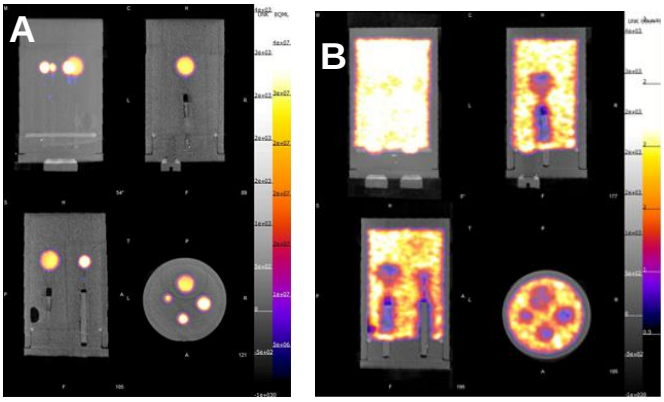

Figure 6.15: A multi-sphere phantom with ^{18}F-NaF in the spheres 7.75 MBq, 4.83 MBq, 2.9 MBq and 1.5 MBq respectively and the reconstructed PET image. (B) The reconstructed image of same multi-sphere with the tube with the above mentioned radioactivity and 50MBq of ^{99m}Tc-DPA Ale filled in the cylinder.

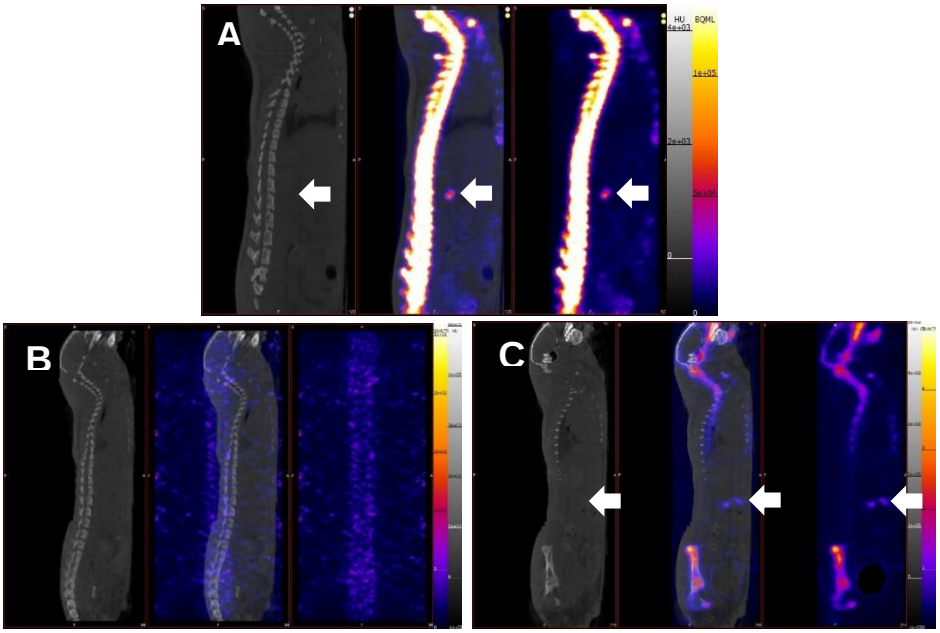

Figure 6.16: Multi-view (CT-left; SPECT-right; fused SPECT/CT-center) sagittal section of a SD rat on a warfarin diet for 1 week. (A) PET/CT scan conducted on week-1, the arrow shows the uptake of radiotracer in the aorta. (B) A blank SPECT/CT performed with ^{18}F-NaF and no SPECT agent. (C) SPECT/CT scan after administration of ^{99m}Tc-DPA Ale, the arrows show uptake in the mesenteric artery.

6.3.5 Dual-radionuclide longitudinal PET-CT and SPECT-CT scan

Dual radionuclide scans were performed as per the protocol mentioned in Fig 6.5. ^{18}F-NaF PET detected calcifications in 5 out of 6 treated rats on week 1, whereas ^{99m}TcDPA Ale SPECT detected calcification only in 1. All ^{18}F-NaF PET scans positive for calcification on week -1 had an area of intense uptake in the mid segment of the aorta (Figure 6.16 A), the region from which the superior mesenteric artery originates (parallel to L1-L2 vertebrae). No other area of extra osseous calcification was observed on the ^{18}F-NaF PET scans. 3 rats were revived and transferred to the BSU and the other 3 rats were culled and the organs were retained for histology.

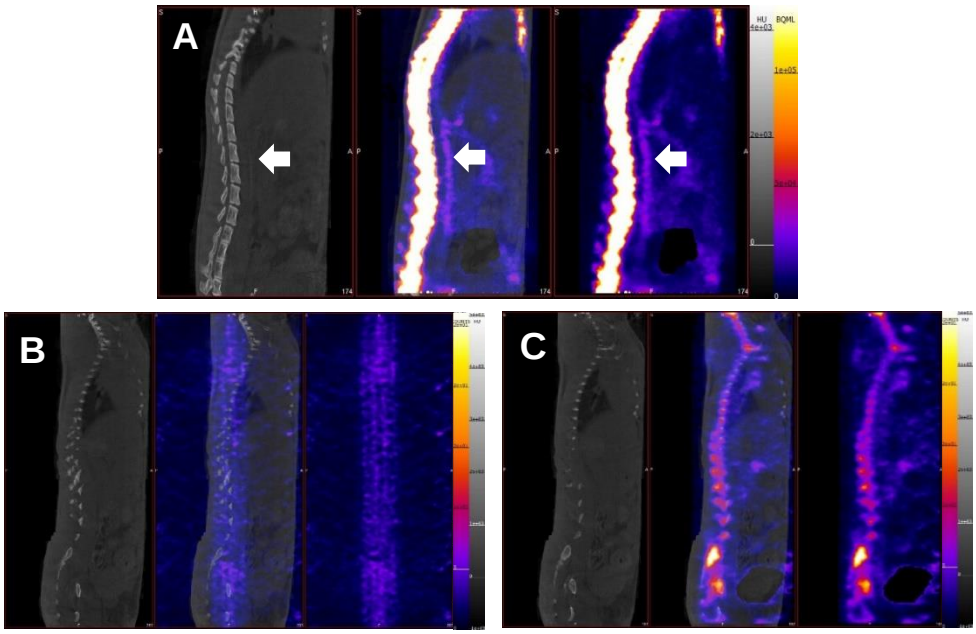

Figure 6.17 Multi-view (CT-left; SPECT-right; fused SPECT/CT-center) sagittal section of a SD rat on a warfarin diet for 4 week. (A) PET/CT scan conducted on week-1, the arrow shows the uptake of radiotracer in the aorta. (B) A blank SPECT/CT performed with ^{18}F-NaF and no SPECT agent. (C) SPECT/CT scan after administration of ^{99m}Tc-DPA Ale.

On week-4 scan PET scans (figure 6.17 A) with ^{18}F-NaF revealed calcification in all the 3 treated rats and SPECT with DPA Ale detected in 1. ^{18}F-NaF PET showed calcification the abdominal aorta and parts of the mesenteric artery, whereas ^{99m}Tc-DPA appeared to be a normal bone scan. The scans conducted on the control rats showed a normal scan

pattern both on week 1 and 4. No extraosseous uptake was seen in the PET or SPECT scans in the control mice. The uptake was primarily in the skeletal system and the renal system. Some uptake of the radiotracer was observed in the gut which is normal for both the radiotracers.

6.3.6 Histological examination of rat aorta

Histological examination of rat aorta (Week-1 of warfarin feeding)

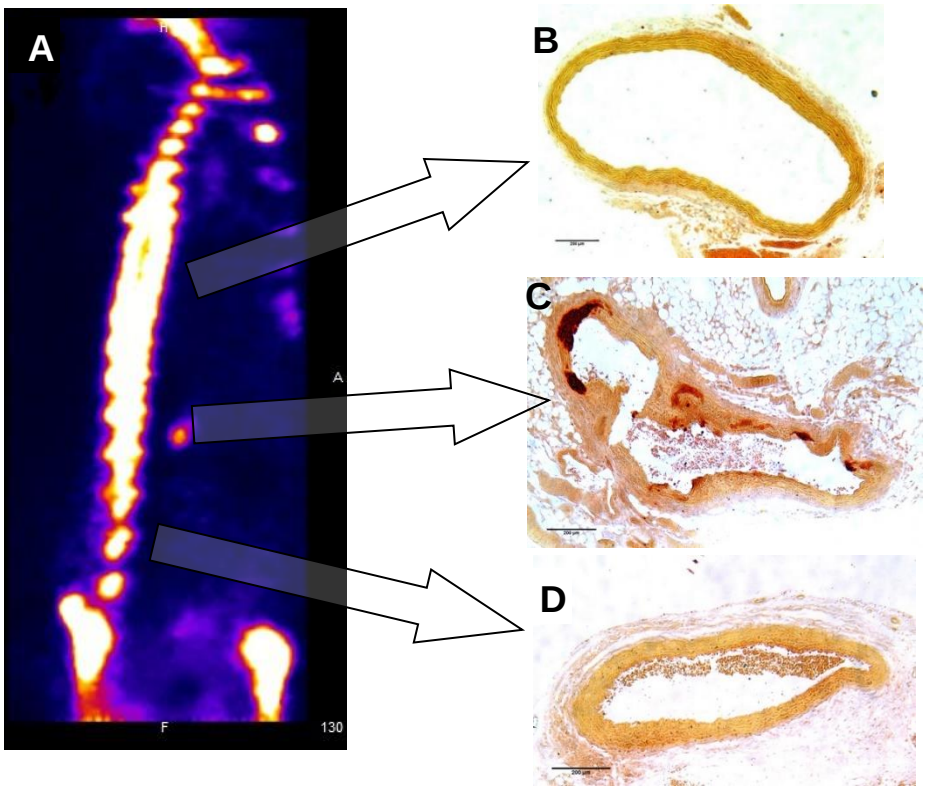

Figure 6.18: Sections of the aorta stained with alizarin red to detect the presence of calcifications. (A) Sagittal view of a SD rat receiving warfarin diet for 7 days and underwent an ^{18}F-NaF PET scan. The rat was culled and the aorta retained for histology. The arrows indicate the region of the aorta from which the sections were obtained. The sections from the thoracic (B) and abdominal (D) aorta were negative whereas the section from region of with ^{18}F-NaF uptake was positive for the presence of calcification. (Magnification 10X, Scale bar= 212 µm)

Histological examination of rat aorta (Week-4 of warfarin feeding)

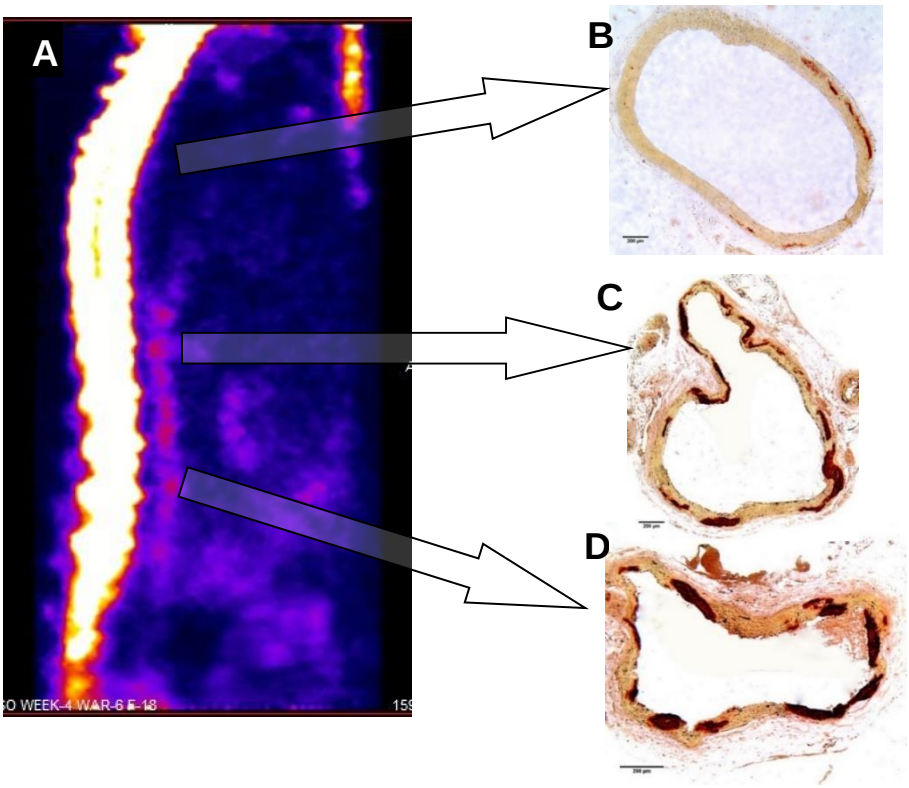

Figure 6.19: Sections of the aorta stained with alizarin red to detect the presence of calcifications. (A) Sagittal view of a SD rat 9^{18}F-NaF PET scan) receiving warfarin diet for 28 days (week-4). The rat was culled and the aorta retained for histology. The arrows indicate the region of the aorta from which the sections were obtained. The sections from the thoracic (B) and abdominal (C) region of the aorta with positive ^{18}F-NaF uptake on week 1 and (D) abdominal aorta were all positive for calcification. The section from the thoracic (B) aorta has less extent of calcifications which were located deep seated as compared to the other two sections. (Magnification 10X, Scale bar= 212 µm)

6.3.7 Aorta to bone ratio

The SUV_{max} of the aorta was normalised to the SUV_{max} of the bone (spine) to derive aorta to bone ratio. The aorta to bone ratios on week 1 was calculated to be 0.06 ± 0.01 (N=7) which was 58.5% higher than the ratio on week-4 which was 0.04 ± 0.01 (N=5).

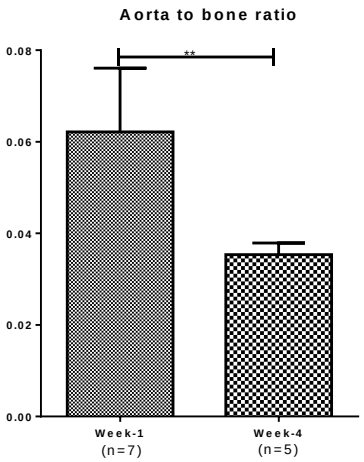

Figure 6.20: Aorta to bone calculated from the *in vivo* measurements at 60 min, after radiotracer injection in treated SD rats. ** $P < 0.01$.

6.4 Discussions

We report the first longitudinal PET-CT and SPECT-CT using rat model of arterial calcification to monitor the progression of disease. We also report the first dual-isotope, tri-modal (PET/SPECT-CT) longitudinal study using the small animal model (rat) to detect, monitor and compare the modalities.

^{18}F-NaF (PET) and ^{99m}Tc-bisphosphonates SPECT detects calcification earlier than CT

Our first important finding is that both ^{18}F-NaF and ^{99m}Tc-bisphosphonates detects calcification earlier than CT. Extraosseous uptake of ^{18}F-NaF (PET) as well as ^{99m}Tc-bisphosphonates (SPECT) were visualised in the aortas of the treated rats on scans performed on week 1 of warfarin diet. Whereas, CT scans of the same were negative for calcification. CT scans of the same rats conducted on week-4 were positive for aortic calcification.

Dual radionuclide longitudinal scans also corroborated the above mentioned finding of the longitudinal study. Interestingly, ^{18}F-NaF PET and SPECT scan with ^{99m}Tc-DPA Ale were positive for the presence of calcification on week 1, whereas aortic calcification was

visualised on CT scans performed on the 4th week of the diet modification. Von Kossa and alizarin red staining were performed on paraffin embedded sections of aortas obtained from warfarin fed rats scanned on week 1 and 4. Histomorphometric analysis of the sections show that the extent of calcification on week 1 is less than week 4. This finding indicates that warfarin feeding leads to a progressive vascular mineralisation and the extant ofvascular damage is proportional to the length of the treatment.

For clinical purposes CT is considered as the 'gold standard' *in vivo* imaging modality for detection and quantification of vascular calcification; however it has been demonstrated that it fails to detect early stages of calcification.[1-3] CT is an imaging modality that works on the principle of attenuation of x-rays and looks for structural changes in the anatomy. CT can detect the presence of macrocalcification; however it is an unreliable modality in detecting microcalcifications. A possible explanation for the failure of CT in detecting early stages of vascular calcification could be that the subtle changes involved in the early stages of mineralisation do not produce attenuation strong enough to cause a noticeable change in the scanned images. Furthermore, CT fails to provide any molecular information. Recent findings show evidence that microcalcification plays a detrimental role in plaque rupture.[4-6] This makes microcalcifications an important predictor as well as a target for the diagnostics of vulnerable plaques. Detecting vulnerable plaques has been a challenge for clinicians and molecular imaging with ^{18}F-NaF and ^{99m}Tc-bisphosphonates to target microcalcifications might open new doors in cardiovascular diagnostics.

^{99m}Tc-bisphosphonates compliments ^{18}F-NaF in detecting vascular calcification

Our findings from the previous chapters, and the findings of the longitudinal and dual radionuclide study indicate that both^{18}F-NaF and ^{99m}Tc-bisphosphonates complement each other in detecting calcification. These findings indicate that ^{18}F-NaF and ^{99m}Tc-bisphosphonates they bind to minerals at different stages of the process of calcification.

The distribution of both ^{18}F-NaF and ^{99m}Tc-bisphosphonates reflect blood flow in bone and osteoblastic activity. ^{99m}Tc-bisphosphonates binds to bone by physicochemical adsorption or chemisorption to the hydroxyapatite crystals of bone tissue. An increased deposition of ^{99m}Tc-bisphosphonates is observed in the epiphyseal growth plates and osteochondral junctions indicating it to be representation of osteoblastic activity.[7, 8] Autoradiographic studies show that ^{99m}Tc-MDP binds primarily at the mineralisation front of bone and at the osteocytic lacunae, but not near osteoclasts.[9] This makes it an unreliable agent in detecting diseases like multiple myeloma which is characterised by osteolytic bone lesions.[10] On the other hand, fluorides have anabolic properties and can enable increase in bone mass.[11] ^{18}F-NaF interacts with bone minerals in two steps; firstly it undergoes chemisorption which is followed by a direct incorporation into the bone matrix. Direct incorporation is possible because fluoride ions exchange with hydroxyl groups in the hydroxyapatite crystal (Ca_{10} $(PO_4)_6OH_2$) to form fluoroapatite ($Ca_{10}(PO_4)_6F_2$).[12]

The advantage of ^{18}F-NaF over ^{99m}TcMDP is that it has minimal non-specific binding to serum proteins, which allows rapid single-pass extraction and fast clearance from the soft tissues. This was evident in the *ex vivo* biodistribution study where ^{18}F-NaF had 5 fold high uptake in the bones as compared to the ^{99m}Tc-bisphosphonates (See Table 6.1). Although reports suggest that ^{18}F-NaF is superior imaging agent for bone imaging, but one has to take into account the imaging instrumentation into account too. Clinical PET scanners has the advantage of a higher sensitivity and image resolution over SPECT; these advantage do come into play when the radiopharmaceuticals are compared in the *in vivo* environment. The exact reason of our finding showing different binding of ^{99m}Tc-bisphosphonates and ^{18}F-NaF in different regions of calcification remains unanswered. A thorough study needs to be conducted to understand as to why these differences are observed and what could be its clinical implications.

Maturity in calcification effects radiopharmaceutical uptake

Another important finding of the longitudinal and dual isotope *in vivo* imaging study with the warfarin fed rats is that a negative relation of radiotracer uptake was observed with maturity in calcification. On week-1 scans of warfarin fed rats, uptake of ^{18}F-NaF was visualised in the region of the abdominal aorta where the superior mesenteric artery originates. Visually noticeable drop in intensity of radiotracer uptake was observed on week-4 scans. Aorta to bone ratios of the same region was calculated on week 1 and week 4 scans. The finding confirmed that maturity in calcification results in poor uptake of ^{18}F-NaF. Clinical studies have been published where in ^{18}F-NaF PET scanning have been utilised to detect calcifications in the carotid artery, coronary artery, aorta, identification of vulnerable atherosclerotic plaques and also soft tissue calcification associated with breast cancer.[2, 13-19] Dweck et al. also observed the absence of ^{18}F-NaF in certain patients with extensive coronary calcification evident on CT.[15] There are two possible explanations to this phenomenon. Firstly, early stage calcification comprises of thin, long nano sized hydroxyapatite crystals, offering a high surface area for the radiotracer to bind. The surface area of the hydroxyapatite may be one of the governing factors for the uptake of the radiopharmaceutical (^{18}F-NaF). As the process of calcification progresses, the hydroxyapatite nucleates to form macro sized calcification which results in a substantial loss surface area for the radiotracer to bind with. Secondly, ^{18}F-NaF provides quantitative estimates of bone metabolism.[20] Therefore, ^{18}F-NaF binding is an indicative of process of active biomineralisation. It is believed that once the macrocalcifications are formed the calcification process ceases therefore, those areas do not show any radiotracer uptake.

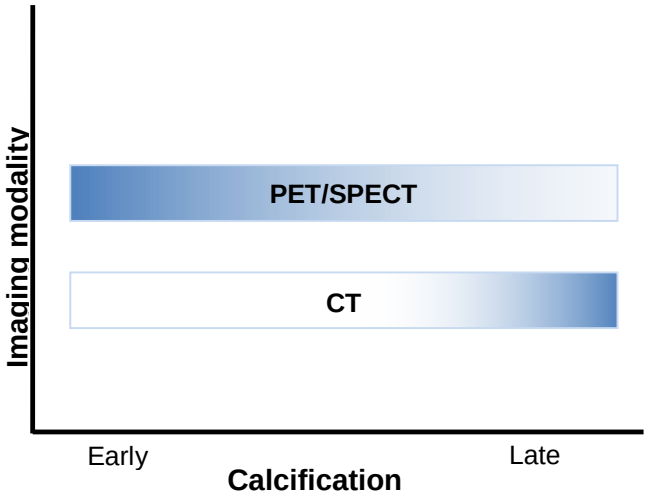

Figure 6.21: Our hypothesis on the detection vascular calcification based on the findings of the *in vivo* imaging studies. Both PET and SPECT detect early calcification, whereas CT fails to detect calcification the early stages. However, in the later stages of calcification the radiotracers may fail to detect calcification whereas CT can.

Availability of radiopharmaceutical a key factor

Von Kossa and alizarin red staining was performed on sections of the aortas obtained from treated rats that were scanned and sacrificed after week-1 and week-4 scans. Based on the ^{18}F-NaF PET scan findings the aorta was divided into three regions (thoracic, mid-abdominal and lower abdominal) see Figure 6.18. Sections from the thoracic and abdominal were negative for calcification with alizarin red whereas the section from the area of the aorta with positive uptake showed the presence of calcification. On week-4, the ^{18}F-NaF PET scan revealed uptake in the abdominal aorta only. However the sections from the aortas of those rats were positive for the presence of calcification in all the three regions. The findings indicate that warfarin feeding initiates aortic calcification in the aorta initiates in the region of the aorta where the superior mesenteric artery originates, and progresses towards the as well as abdominal aorta. These findings also suggest that the process of calcification in the aorta was active and progressive. The software ImageJ (version 1.49) was used to calculate the percentage of the section stained positive for calcification which showed that the extant of

calcification in the abdominal aorta significantly severe compared to the thoracic aorta. This finding is in agreement with reported in clinical studies that indicate abdominal aorta is more susceptible to calcification compared to the thoracic aorta.[21]

The exchange of a tracer between blood and tissue depends on three important parameters (I) blood flow, (II) surface area, and (III) the permeability of the capillary system.[22] ^{99m}Tc-bisphosphonates and ^{18}F-NaF undergo diffusion through the capillary wall into the extravascular space.[23, 24] Interestingly our findings show that ^{18}F-NaF uptake was observed only in the abdominal aorta, whereas there was no uptake of ^{18}F-NaF in the thoracic aorta. Sections of the aortas show that the calcified pockets in the abdominal aorta extended from the medial layer of the aorta to the intima and in some cases very close or exposed to the lumen whereas the calcified areas of the thoracic aorta were deep seated in the media adjacent to the outermost layer of the vessel wall, the adventitia. These findings suggest that:

(i) ^{18}F-NaF is directly taken up from the lumen and it may not be able to penetrate through the intimal layer therefore, isn't available for binding with the deep seated calcification located in the media.

(ii) The microvasculature (adventitial vasa vasorum) network has no role in the transport of the radiopharmaceutical.

Dual-radionuclide scan

A limitation of the longitudinal imaging study was that different set of animals were used for different radiopharmaceuticals which means variability within the animals cannot be ruled out. Ideally the same subject should be scanned with both PET and SPECT agents to rule out variability and yield a more meaningful data for comparison. To address this issue dual-radionuclide scanning was performed. However, simultaneous dual radionuclide PET and SPECT study has its challenges.

PET and SPECT dual tracer imaging has the potential in many research applications especially in situations where two or more radiopharmaceuticals are compared. However, it remains a challenge because of physical properties of the radiotracer and hardware limitations. The NanoSPECT-CT^{PLUS} (Mediso, Hungary) is optimised to for detection of gamma rays in energy range of 25keV to 354keV. For SPECT scans with ^{99m}Tc-bisphosphonates a low energy multi-pinhole collimator is utilised and the energy window maintained at 140 keV ± 15%. The low energy collimators are meant for absorption of scattered low energy gamma rays emitted by ^{99m}Tc. The presence of the PET tracer (^{18}F; 511keV) would lead to crosstalk as the high energy gamma rays can penetrate the SPECT collimator and the resulting down-scattered gamma rays fall within the SPECT energy window of 140keV±15%. On the other hand, the presence of ^{99m}Tc with ^{18}F results in the increase in the dead time due to an increased count rate. Studies have been reported that dual radionuclide PET and SPECT scans are feasible.[25,26, 27] Chapman et al. reported that in the presence of ^{18}F, a significant artifact was observed in the reconstructed SPECT images. Therefore, they employed the SPECT first protocol, where the animal is injected with the SPECT tracer and scanned followed by the PET.[27] On the other hand Yiping et al. suggested a SPECT followed by PET protocol. They reported that reconstructed SPECT images with no artifacts can be obtained with radioactivity ratio ≥5:1 (^{99m}Tc:^{18}F).

Our experience with NanoPET-CT^{PLUS} (Mediso, Hungary) indicates that scanning small animal scanning with radioactivity >10MBq results in substantial increase in dead time. We performed a simple experiment with a micro hollow sphere phantom (Figure 6.15) where the spheres were filled with ^{18}F-NaF and the cylinder was filled with ^{99m}Tc-bisphosphonate (left over from *in vivo* longitudinal imaging) and scanned. The microspheres of the phantom appeared as cold spots on reconstructed SPECT images

suggesting that the SPECT scanner with 15% window for discrimination of gamma rays emitted at 140 keV by ^{99m}Tc exclude the 511 keV emission stimulated by a PET tracer.

For *in vivo* imaging we followed the PET first protocol (see Figure 6.5) and used an activity ratio of 1:10 (^{18}F-NaF; [~5MBq]: ^{99m}Tc-DPA Ale; [~50MBq]). A blank SPECT scan was performed with ^{18}F-NaF only, which demonstrated that the SPECT scanner registered scattered photons that penetrated through the collimator and appeared like random background rather than an outline of the skeletal system. There was a gap of 90 minutes between ^{18}F-NaF and ^{99m}Tc-DPA Ale injections. The SPECT scan was performed 120 min after the PET tracer injection which allowed the activity to decay. These findings show that dual-radionuclide PET/SPECT study is feasible. However, the drawback of the study is that *ex vivo* biodistribution is not possible due to the cross contamination of the radioactivities. Further study

6.5 Conclusions

We report the first longitudinal PET-CT and SPECT-CT study of animal models with arterial calcification for detection and monitoring the progression of vascular calcification using bone seeking radiopharmaceuticals. We also report the first dual radionuclide tri-modality PET/SPECT-CT imaging with animal model. The findings show that dual radionuclide scanning is feasible, however have some limitations.

The studies have yielded some interesting results and have raised some intriguing questions. The findings prove that ^{18}F-NaF PET and SPECT with ^{99m}Tc-bisphosphonates detects calcification much earlier than CT. However, it was also observed that with maturity calcification the radiotracer uptake reduces. The study also shows that ^{99m}Tc-bisphosphonates and ^{18}F-NaF do not behave similarly, rather complement each other and may be binding to calcification at different stages. Histological examinations indicate that calcification close or exposed to the lumen is detected whereas the deep seated

active calcified area goes undetected. All these findings are promising and call for further studies and answering them will draw new understanding of the process of vascular calcification, and devising ways of detecting it early with more meaning clinical information to the physician.

References

1. Aikawa E, Nahrendorf M, Figueiredo JL, et al. Osteogenesis associates with inflammation in early-stage atherosclerosis evaluated by molecular imaging in vivo. *Circulation.* 2007;116(24):2841-2850.

2. Adamson PD, Vesey AT, Joshi NV, et al. Salt in the wound: 18F-fluoride positron emission tomography for identification of vulnerable coronary plaques. *Cardiovasc. Diagn. Ther.* 2015;5(2):150-155.

3. Aikawa E. Optical Molecular Imaging of Inflammation and Calcification in Atherosclerosis. *Curr. Cardiovasc. Imaging. Rep.* 2010;3(1):12-17.

4. Rambhia SH, Liang X, Xenos M, et al. Microcalcifications increase coronary vulnerable plaque rupture potential: a patient-based micro-CT fluid-structure interaction study. *Ann. Biomed. Eng.* 2012;40(7):1443-1454.

5. Vengrenyuk Y, Carlier S, Xanthos S, et al. A hypothesis for vulnerable plaque rupture due to stress-induced debonding around cellular microcalcifications in thin fibrous caps. *Proc. Natl. Acad. Sci. U.S.A.* 2006;103(40):14678-14683.

6. Kelly-Arnold A, Maldonado N, Laudier D, et al. Revised microcalcification hypothesis for fibrous cap rupture in human coronary arteries. *Proc. Natl. Acad. Sci. U.S.A.* 2013;110(26):10741-10746.

7. Christensen SB, Krogsgaard OW. Localization of Tc-99m MDP in epiphyseal growth plates of rats. *J. Nucl. Med.* 1981;22(3):237-245.

8. Guillet J, Guillet C, Blanquet P. [Radioisotopic study of bone growth and maturation. 160 cases]. *La semaine des hopitaux : organe fonde par l'Association d'enseignement medical des hopitaux de Paris.* Oct 21 1982;58(38):2199-2202.

9. Einhorn TA, Vigorita VJ, Aaron A. Localization of technetium-99m methylene diphosphonate in bone using microautoradiography. *J. Orthop. Res.* 1986;4(2):180-187.

10. Winterbottom AP, Shaw AS. Imaging patients with myeloma. *Clin. Radiol.* 2009;64(1):1-11.

11. Farley JR, Wergedal JE, Baylink DJ. Fluoride directly stimulates proliferation and alkaline phosphatase activity of bone-forming cells. *Science.* Oct 21 1983;222(4621):330-332.

12. Czernin J, Satyamurthy N, Schiepers C. Molecular mechanisms of bone 18F-NaF deposition. *J. Nucl. Med.* 2010;51(12):1826-1829.

13. Rudd JH, Warburton EA, Fryer TD, et al. Imaging atherosclerotic plaque inflammation with [18F]-fluorodeoxyglucose positron emission tomography. *Circulation.* Jun 11 2002;105(23):2708-2711.

14. Rudd JHF, Myers KS, Bansilal S, et al. Atherosclerosis Inflammation Imaging with 18F-FDG PET: Carotid, Iliac, and Femoral Uptake Reproducibility, Quantification Methods, and Recommendations. *J. Nucl. Med.* 2008;49(6):871-878.

15. Dweck MR, Chow MWL, Joshi NV, et al. Coronary Arterial 18F-Sodium Fluoride Uptake: A Novel Marker of Plaque Biology. *J. Am. Coll. Cardiol.* 2012;59(17):1539-1548.

16. Dweck MR, Jenkins WS, Vesey AT, et al. 18F-sodium fluoride uptake is a marker of active calcification and disease progression in patients with aortic stenosis. *Circ Cardiovasc Imaging* 2014;7(2):371-378.

17. Joshi NV, Vesey AT, Williams MC, et al. 18F-fluoride positron emission tomography for identification of ruptured and high-risk coronary atherosclerotic plaques: a prospective clinical trial. *Lancet.* Feb 22 2014;383(9918):705-713.

18. Wilson GH, 3rd, Gore JC, Yankeelov TE, et al. An Approach to Breast Cancer Diagnosis via PET Imaging of Microcalcifications Using 18F-NaF. *J. Nucl. Med.* 2014;55(7):1138-1143.

19. Beheshti M, Saboury B, Mehta NN, et al. Detection and global quantification of cardiovascular molecular calcification by fluoro18-fluoride positron emission tomography/computed tomography--a novel concept. *Hell J Nucl Med.* 2011;14(2):114-120.

20. Czernin J, Satyamurthy N, Schiepers C. Molecular Mechanisms of Bone (18)F-NaF Deposition. *J. Nucl. Med.* 2010;51(12):1826-1829.

21. Gu X, He Y, Li Z, et al. Relation Between the Incidence, Location, and Extent of Thoracic Aortic Atherosclerosis Detected by Transesophageal Echocardiography and the Extent of Coronary Artery Disease by Angiography. *Am. J. Cardiol.* 2011;107(2):175-178.

22. Renkin EM. *Transport of potassium-42 from blood to tissue in isolated mammalian skeletal muscles.* Vol 1971959.

23. Blau M, Nagler W, Bender MA. Fluorine-18: a new isotope for bone scanning. *J. Nucl. Med.* 1962;3:332-334.

24. Hughes SP, Davies DR, Bassingthwaighte JB, Knox FG, Kelly PJ. Bone extraction and blood clearance of diphosphonate in the dog. *Am.J.Physiol.* 1977;232(3):H341-347.

25. Tianyu M, Yiping S, Rutao Y, Manchiraju P. PET and SPECT dual-tracer imaging: correction of 511keV photon's down-scatter effect on SPECT. Paper presented at: Nuclear Science Symposium Conference Record, 2007. NSS '07. IEEE; Oct. 26 2007-Nov. 3 2007, 2007.

26. Yiping S, Rutao Y, Tianyu M, Manchiraju P. Initial studies of PET-SPECT dual-tracer imaging. Paper presented at: Nuclear Science Symposium Conference Record, 2007. NSS '07. IEEE; Oct. 26 2007-Nov. 3 2007, 2007.

27. Chapman SE, Diener JM, Sasser TA, et al. Dual tracer imaging of SPECT and PET probes in living mice using a sequential protocol. *Am J Nucl Med Mol Imaging.* 2012;2(4):405-414.

Chapter 7: Conclusions and future work

7.1 Conclusions

1. The major aim of the study was to investigate ^{99m}Tc-labelled novel bisphosphonate complexes as SPECT imaging agents for the *in vivo* detection of vascular calcification. The novel compounds are based on bifunctional ligands where in the metal chelating site is separated from the bisphosphonate, thereby improving the *in vivo* stability. The ligands dipicolyl-amine alendronate and dithiocarbamate-bisphosphonate were used in a kit-based approach to synthesise the novel complexes ^{99m}Tc-DPA Ale and ^{99m}TcN(DTC-BP)$_2$ with high (>95%) chemical purity and yield suitable for *in vivo* work.

2. The compounds were evaluated *in vitro* before proceeding to *in vivo* imaging. *In vitro* binding studies were conducted with synthetic hydroxyapatite, powdered equine bone and minerals isolated from calcified human intimal and medial calcification. The findings were compared to clinically established bone seeking tracers ^{99m}Tc-MDP (SPECT) and ^{18}F-NaF (PET). ^{99m}Tc-DPA Ale and ^{99m}TcN(DTC-BP)$_2$ demonstrated a high binding percentages with minerals isolated from calcified human intimal and medial calcification as well as synthetic hydroxyapatite.

3. Two rat models of vascular calcification were developed for the *in vivo* molecular imaging. The models were developed by making changes in pre-existing models, to reduce the pain threshold and meet the regulatory requirement of the Home Office (UK). The first model involved changing the diet regime of SD rats from a normal diet to warfarin diet [warfarin (3mg kg^{-1}) and vitamin K_1 (1.5 mg kg^{-1})] for 11 days and subcutaneous injections of vitamin D_3 (200,000 IU kg^{-1} day^{-1}) from day 7 to 11 of the diet. This resulted in acute and extensive vascular calcification in the

rats, and the model was suitable for the initial proof-of-principle and optimisation study. The second model was a milder model, where the development of calcification was slow. This was achieved by feeding the rats with warfarin diet only. The model was suitable for longitudinal studies. In addition to rat models, a mouse model was also replicated by feeding female DBA/2 NCrl with the warfarin diet.

4. The first set of *in vivo* imaging studies were conducted to optimise the imaging protocol as well as determine if these agents detect extraosseous calcification. Rat model with acute and extensive arterial calcification (warfarin diet with vitamin D_3 injections) was used in the study. Novel ^{99m}Tc-bisphosphonates as well as ^{99m}Tc-MDP and ^{18}F-NaF detected arterial calcifications. However, there were some noticeable differences between the SPECT and PET scans. The SPECT scans with ^{99m}Tc-DPA Ale, ^{99m}Tc-N(DTCBP)$_2$, and ^{99m}Tc-MDP uptake was visualised in the kidneys and mesenteric arteries and the kidneys and on ^{18}F-NaF PET scans, increased uptake was seen in the mesenteric artery and abdominal aorta. Histologically calcification was detected in the aorta (both abdominal and thoracic), mesenteric artery, kidneys and lungs of the treated rats. The optimum time for scanning was determined to be between 30-60min of IV administration of the radiopharmaceuticals.

5. Longitudinal imaging with warfarin fed rats (n=3) were performed on three time points (week 1, 2 and 4 of diet). SPECT and PET detected calcification earlier than CT. SPECT with ^{99m}Tc-DPA Ale and ^{99m}Tc-MDP detected calcification in 1 treated rat, whereas ^{18}F-NaF detected calcification in all 3 treated subjects. The scan findings also revealed that the maturity in calcification had a negative effect on the uptake of the radiotracers. Scans performed on control rats (SD rats on normal

diet) appeared to be normal with uptake primarily in the skeletal system and renal system, some gut activity was also visualised.

6. Phantom studies were conducted to determine the feasibility of dual isotope trimodality PET, SPECT and CT scans. An imaging protocol was generated from a phantom study which involved PET/CT followed SPECT/CT scans. Dual isotope longitudinal studies were performed with the radiopharmaceuticals ^{18}F-NaF and ^{99m}Tc-DPA Ale. Warfarin fed SD rats well as controls maintained on normal rodent diet were scanned on week 1 and 4. The findings show the uptake ^{18}F-NaF and ^{99m}Tc-DPA Ale in different calcified regions of the same animal, indicating that the tracers might bind to minerals at different stages of the process of biomineralisation.

   In summary, bone seeking tracers demonstrated potentially optimal properties for the imaging of vascular calcification. Although the novel tracers exhibited superior binding percentages with minerals *in vitro*, these advantages were not replicated *in vivo.* The findings do raise some intriguing questions, and answering them might reveal more insights about the complex process of vascular calcification and the means to image calcification *in vivo*. The initial success with the animal model does indicate the need to pursue the study in other animal models and if possible in human subjects too.

7.2 Future directions

1. **Increasing the cohort size:** A small number of animals were used in these studies, which may be inadequate to notice any statistically significant differences which results in the impression of similarity between the compared agents. The reasons for this are to cut the costs, pre-clinical *in vivo* especially PET/CT and

SPECT/CT are expensive which restricts the number of animals scanned. Repeating the experiments in a larger cohort of animals will yield a statistically meaningful result. This will also be helpful in determining whether our hypothesis from the initial study i.e. that bisphosphonates are superior imaging agents for calcification holds true.

2. ***Ex vivo* investigation of human samples:** The initial success with the pre-clinical *in vivo* SPECT and PET imaging study with both novel and clinically established bone seeking agents warrants for further investigation. Although the animal models should emulate the process of calcification in human, it is not an exact representation of the same. Therefore, *ex vivo* binding studies with calcified aortic samples from medial (calcified inferior epigastric artery, from adult patients undergoing renal transplant) and intimal calcification (calcified carotid arteries from patients undergoing carotid endarterectomy) will be helpful in answering the intriguing questions raised by the imaging study we conducted.

3. **Intimal vs medial calcification:** CT is considered as the 'gold standard' *in vivo* imaging modality in detection of vascular calcification.[1] However, differential diagnosis of intimal and medial calcification is not possible with CT.

   The etiology and pathophysiology of vascular calcification is not fully elucidated.[2, 3] However, the present understanding is that Mönckeberg's arteriosclerosis and atherosclerotic intimal calcifications are pathophysiologically different processes.[4, 5] The minerals in the medial plaques closely resembles bone whereas the minerals in intimal calcifications have cholesterol and cholesteryl acids associated with it.[3] Medial calcification also contains noncrystalline (or amorphous) calcium phosphate, whitlockite and crystalline Mg-substituted carbonate apatite $[(Mg,Ca)_{10}(PO_4,CO_3)_6(OH)_2]$.

These differences in the properties of the minerals can be exploited to detect intimal and medial calcifications. Radiolabelled bisphosphonates with varying lipophilicity can be developed. *In vitro* studies can be conducted with minerals isolated from intimal and medial plaques. Pre-clinical *in vivo* imaging can be conducted with murine models of atherosclerotic calcification and medial calcification for comparison.

4. **Vulnerable plaque imaging:** Myocardial infarction is the major cause of morbidity and mortality worldwide, despite all the advances in the field of medicine, surgery and diagnostics. Diagnosis of vulnerable plaques still remains the “Achilles heel” of medical diagnostics.

   The present understanding of the biology of atherosclerotic plaques indicates that microcalcifications influence the plaque rupture potential.[6-8] Therefore, microcalcifications could be a potential target for the detection of vulnerable plaques. Recently published clinical studies confirm that ^{18}F-NaF has the potential as a marker for *in vivo* diagnosis of vulnerable plaques.[9-11] A distinguishing feature of vulnerable plaques is the presence of a thin fibrous cap.[12] Fractures in the cap result in a change of the plaque geometry thereby initiating a series of reactions resulting in plaque rupture.[13]

   Our findings of the longitudinal studies indicate that the early stages of mineralisation (microcalcification) may go undetected if the calcifications are deep seated. Our findings showed that calcifications in the thoracic aortas with calcification in the media (in close proximity to the adventitia) weren’t detected by any of the radiopharmaceuticals used, including ^{18}F-NaF. This suggests that the vasa-vasorum doesn’t play a role in the transport of the radiotracers in the adventitia to the tunica media. However, in the abdominal aorta, where the

calcification sites were exposed to the lumen, calcification was visualised on ^{18}F-NaF scans. These findings indicate that ^{18}F-NaF uptake can be visualised only in mineralised areas exposed to the lumen. We believe that the same could be replicated in atherosclerotic plaques where ^{18}F-NaF will detect the calcified unstable plaques with fractures in the fibrous cap, whereas the stable plaques (with intact fibrous cap) should be negative due to the unavailability of the radiotracers. This is also consistent with the current data published were vulnerable plaques were detected post rupture rather than as a predictive model of rupture using F18.

Pre-clinical imaging study should be conducted on suitable animal models for vulnerable plaque. High fat diet fed ApoE$^{-/-}$ and LDL$^{-/-}$ mice has been the choice of animal models for the understanding of biology atherosclerosis, due to similarities to human plaque. However, these mouse strains rarely develop rupture-prone lesions. Several research groups have used rabbit models (New Zealand White) of atherosclerosis to image plaque vulnerability. The plaques can be induced by high-cholesterol diet and/or by surgery (balloon induced endothelial injury).[14] High-fat diet induced atherosclerotic plaques in rabbit models are better for nuclear imaging compared surgical models because the wound itself may create an artefact.

5. **Radiolabelled bisphosphonates for PET scanning:** ^{68}Ga-based radiopharmaceuticals have emerged as a prospective alternative to cyclotron dependent PET radiotracers. ^{68}Ga is attractive because of the several practical and economic advantages it offers.[15] Generator produced radionuclides eliminates the need of a costly cyclotron. ^{68}Ga can be eluted form a ^{68}Ge/^{68}Ga-generator, which is relatively cheap and allows for the easy availability of the isotope. The half-life of ^{68}Ge is 270.8 days; therefore the shelf life of the ^{68}Ge/^{68}Ga-generator is almost a yearlong which is an added benefit. The half-life of ^{68}Ga is 68 min, long enough for

the chemical manipulations.[16] Fellner et al. published the first in human study of ^{68}Ga labelled bisphosphonate (^{68}Ga-BPAMD) in patients with metastatic bone disease.[17, 18] Novel bisphosphonates labelled with ^{68}Ga could also be a prospective candidate for detection vascular calcification.

References

1. Kucharczyk W, Henkelman RM. Visibility of calcium on MR and CT: can MR show calcium that CT cannot? *AJNR Am J Neuroradiol.* 1994;15:1145-1148.

2. O'Neill WC, Lomashvili KA. Recent progress in the treatment of vascular calcification. *Kidney Int.* 2010;78:1232-1239.

3. Reid DG, Shanahan CM, Duer MJ, et al. Lipids in biocalcification: contrasts and similarities between intimal and medial vascular calcification and bone by NMR. *J. Lipid. Res.* 2012;53:1569-1575.

4. Proudfoot D, Shanahan CM. Biology of calcification in vascular cells: intima versus media. *Herz.* 2001;26:245-251.

5. O'Neill WC. Vascular calcification: not so crystal clear. *Kidney Int.* 2007;71:282-283.

6. Del Porto F, Proietta M, di Gioia C, et al. FGF-23 levels in patients with critical carotid artery stenosis. *Intern Emerg Med.* 2015:1-8.

7. Vengrenyuk Y, Carlier S, Xanthos S, et al. A hypothesis for vulnerable plaque rupture due to stress-induced debonding around cellular microcalcifications in thin fibrous caps. *Proc Natl Acad Sci.* 2006;103:14678-14683.

8. Rambhia SH, Liang X, Xenos M, et al. Microcalcifications increase coronary vulnerable plaque rupture potential: a patient-based micro-CT fluid-structure interaction study. *Ann Biomed Eng.* 2012;40:1443-1454.

9. Dweck MR, Chow MWL, Joshi NV, et al. Coronary Arterial ^{18}F-Sodium Fluoride Uptake: A Novel Marker of Plaque Biology. *J Am Coll Cardiol.* 2012;59:1539-1548.

10. Chen W, Dilsizian V. Targeted PET/CT imaging of vulnerable atherosclerotic plaques: microcalcification with sodium fluoride and inflammation with fluorodeoxyglucose. *Curr Cardiol Rep.* 2013;15:364.

11. Joshi NV, Vesey A, Newby DE, Dweck MR. Will 18F-sodium fluoride PET-CT imaging be the magic bullet for identifying vulnerable coronary atherosclerotic plaques? *Curr Cardiol Rep.* 2014;16:521.

12. Virmani R, Burke AP, Kolodgie FD, Farb A. Pathology of the thin-cap fibroatheroma: a type of vulnerable plaque. *J Interv Cardiol.* 2003;16:267-272.

13. Fischer A, Gutstein DE, Fayad ZA, Fuster V. Predicting plaque rupture: enhancing diagnosis and clinical decision-making in coronary artery disease. *Vasc. Med.* 2000;5:163-172.

14. Qi C, Deng L, Li D, et al. Identifying Vulnerable Atherosclerotic Plaque in Rabbits Using DMSA-USPIO Enhanced Magnetic Resonance Imaging to Investigate the Effect of Atorvastatin. *PloS one.* 2015;10:e0125677.

15. Velikyan I. Prospective of (68)Ga-Radiopharmaceutical Development. *Theranostics.* 2014;4:47-80.

16. Banerjee SR, Pomper MG. Clinical Applications of Gallium-68. *Appl.Rad.Isot.* 2013;0:2-13.

17. Fellner M, Baum RP, Kubicek V, et al. PET/CT imaging of osteoblastic bone metastases with ^{68}Ga-bisphosphonates: first human study. *Eur J Nucl Med Mol Imaging.* 2010;37:834.

18. Fellner M, Biesalski B, Bausbacher N, et al. 68Ga-BPAMD: PET-imaging of bone metastases with a generator based positron emitter. *Nucl. Med. Biol.* 2012;39:993-999.

Dalton Transactions

PAPER

View Article Online
View Journal | View Issue

Cite this: *Dalton Trans.*, 2015, **44**, 4963

Technetium-99m and rhenium-188 complexes with one and two pendant bisphosphonate groups for imaging arterial calcification†

Jayanta Kumar Bordoloi,[a,b] David Berry,[a] Irfan Ullah Khan,[a,c] Kavitha Sunassee,[a] Rafael Torres Martin de Rosales,[a] Catherine Shanahan[b] and Philip J. Blower*[a]

Received 25th September 2014,
Accepted 16th December 2014

DOI: 10.1039/c4dt02965h

www.rsc.org/dalton

The first ^{99m}Tc and ^{188}Re complexes containing two pendant bisphosphonate groups have been synthesised, based on the mononuclear M(v) nitride core with two dithiocarbamate ligands each with a pendant bisphosphonate. The structural identity of the ^{99}Tc and stable rhenium analogues as uncharged, mononuclear nitridobis(dithiocarbamate) complexes was determined by electrospray mass spectrometry. The ^{99m}Tc complex showed greater affinity for synthetic and biological hydroxyapatite, and greater stability in biological media, than the well-known but poorly-characterised and inhomogeneous bone imaging agent ^{99m}Tc-MDP. It gave excellent SPECT images of both bone calcification (mice and rats) and vascular calcification (rat model), but the improved stability and the availability of two pendant bisphosphonate groups conferred no dramatic advantage in imaging over the conventional ^{99m}Tc-MDP agent in which the bisphosphonate group is bound directly to Tc. The ^{188}Re complex also showed preferential uptake in bone. These tracers and the biological model of vascular calcification offer the opportunity to study the biological interpretation and clinical potential of radionuclide imaging of vascular calcification and to deliver radionuclide therapy to bone metastases.

Introduction

Techetium-99m (^{99m}Tc) complexes of MDP (methylene diphosphonate, **1**, Fig. 1) and related 1,1-bisphosphonates such as HDP (hydroxymethylene diphosphonate) have been used successfully for decades in the clinic for acquiring planar and SPECT images of osteoblastic processes associated with bone tumours and metastases.[1–3] Another 1,1-bisphosphonate analogue, HEDP (**2**) has found use in palliative treatment of bone metastases with the beta-emitting rhenium isotopes rhenium-186 (^{186}Re) and rhenium-188 (^{188}Re).[4–7] Despite the proven value of these complexes in imaging and therapy, both the technetium and rhenium complexes have limitations. The structures of the active metal complexes are unknown, and certainly not homogenous.[8] Despite their periodic relationship, the technetium and rhenium complexes are not chemically analogous (for example, the technetium complexes are biologically effective at no-carrier-added concentrations whereas the rhenium complexes are ineffective without carrier non-radioactive rhenium,[9] suggesting that they are polymeric). The complexes show poor *in vivo* stability; while this is not a major problem over the short time scales of imaging with ^{99m}Tc (typically 3 h) it is detrimental to therapeutic use of $^{186/188}$Re, as a high proportion of the rhenium is rapidly converted to perrhenate,[10] which does not bind to bone and is taken up in thyroid or excreted renally. The instability arises because the bisphosphonate groups in these ligands serve the dual purpose of binding the metal ion (for which they are not well-suited) and for bone targeting (in which their affinity may be compromised by the bound radiometal).

In addition to the need for improved *in vivo* stability and therapeutic efficacy of bone-targeting rhenium complexes, new applications are emerging for imaging calcification (or decalcification) processes that place more stringent demands on imaging agents than conventional imaging of osteoblastic bone metastases. For example, imaging osteolytic lesions characteristic of multiple myeloma has very poor sensitivity with conventional ^{99m}Tc-bisphosphonate complexes,[11] and imaging soft tissue calcification associated with cardiovascular diseases such as atherosclerosis and arterial calcification may require complexes with improved imaging characteristics because the lesions are small and mineral content and mineralisation/demineralisation rates may be low.

[a]*King's College London, Division of Imaging Sciences and Biomedical Engineering, St Thomas' Hospital, London SE1 7EH, UK. E-mail: Philip.Blower@kcl.ac.uk*
[b]*King's College London, Cardiovascular Division, James Black Centre, London SE5 9NU, UK*
[c]*Institute of Nuclear Medicine and Oncology (INMOL), New Campus Road, Lahore 54600, Pakistan*

†Electronic supplementary information (ESI) available. See DOI: 10.1039/c4dt02965h

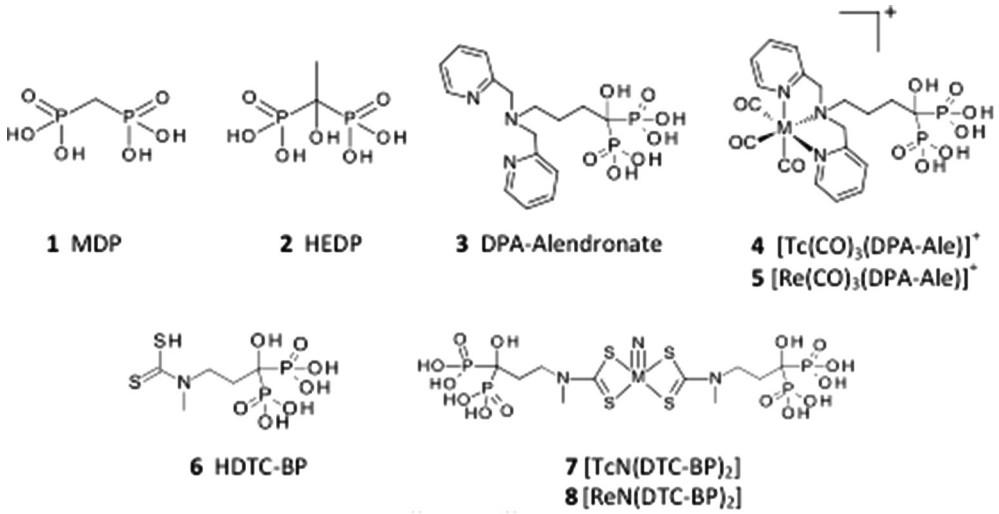

Fig. 1 Bone targeting bisphosphonate derivatives and their ^{99m}Tc and ^{188}Re complexes with ^{99m}Tc and ^{188}Re.

To achieve the required improvements in *in vivo* stability and affinity for mineral deposits, we adopted the strategy of separating the metal chelating site from the bisphosphonate (bone targeting) site in a bifunctional molecule. This allows separate control/optimisation of metal chelation and bone targeting, exemplified by the ligand DPA-Alendronate (**3**) and its ^{99m}Tc[12] and ^{188}Re[13] complexes (**4**) using the readily-synthesised tricarbonyl $[M(CO)_3]^+$ cores. [^{188}Re]-**5** showed higher bone uptake and more prolonged bone retention of ^{188}Re *in vivo* and higher biological stability compared with ^{188}Re-HEDP (^{188}Re-**2**) over a 24 hour period.[13] The results indicate that [^{188}Re]-**5** has potential as an improved palliative agent for bone metastases, but remains non-ideal due to modest uptake in non-target organs such as the liver, attributed to the increased lipophilicity of the complex.

In this paper we extend the concept of bifunctional ligands for bone targeting, by synthesising complexes with increased mineral affinity by the inclusion of two pendant bisphosphonate groups in the molecule, and evaluating them in the challenging setting of an animal model of arterial calcification. The pentavalent technetium/rhenium nitrido bis(dithiocarbamate) core was identified as potentially meeting the requirements of retaining a structurally discrete, well-characterised and stable Tc/Re core with the expectation that the Tc and Re complexes will share similar biological behaviour. Precursors containing the $[M{\equiv}N]^{2+}$ core (M = ^{99m}Tc or ^{188}Re) are readily synthesised[14] and react with dithiocarbamates to give symmetrical $MN(DTC)_2$ complexes.[15–17] Despite the simplicity of the structures and syntheses, $MN(DTC)_2$ complexes have found only limited use in radiopharmaceuticals, amongst which ^{99m}Tc-NOET for myocardial perfusion imaging has been most prominent.[17,18] Here we have used the ligand DTC-BP (**6**), previously used to form a copper-64 complex,[19] in a kit-based approach to synthesise the novel bis(bisphosphonate) complex ^{99m}TcN(DTC-BP)$_2$ ([^{99m}Tc]-**7**) and its rhenium analogues **8** and [^{188}Re]-**8**, and compared their biological behaviour with that of the mono(bisphosphonate) derivative [^{99m}Tc]-**4** and the conventional bone-imaging agent ^{99m}Tc-**1**.

Experimental

Equipment and consumables

TLC analyses were carried out using silica gel on aluminium-backed TLC plates (Merck 1.16834.0001) cut to 100 mm × 25 mm, using four mobile phase systems. Solvent system 1: ethanol–chloroform–toluene–0.5 M ammonium acetate (6/3/3/1);[16] solvent system 2: methanol + 1% of a 60% solution of HEDP (Sigma H6773); solvent system 3: methanol–10% Ammonium Acetate (1/1) containing 15 mM EDTA; solvent system 4: 1% HCl in methanol. The spots were allowed to dry before development in the mobile phase. Paper chromatography was carried out using Whatman 3MM paper or Whatman P81 paper and 0.9% saline as mobile phase. Radio-TLC chromatograms were analysed with a Mini-Scan TLC scanner (Bioscan) with FC3600 detector and γ-detector probe and Laura 4.0.2.75 (Lablogic) software. HPLC analyses were carried out on an Agilent 1200 series HPLC with degasser (G1322A), quaternary pump (G1311A), UV detector (G1314B) and manual injector (Rheodyne 7725i). The column used was an Agilent Zorbax Eclipse analytical XDB-C18 column (150 mm × 4.6 mm, 5 μm) unless otherwise indicated. Gamma counting of ^{99m}Tc and ^{188}Re samples was done using a 1282 Compugamma Gamma Counter (LKB Wallac) with Ultroterm software, counting for 10 seconds using a 110–155 KeV window. Higher activities were measured with a CRC-25R (Capintec) dose calibrator. Freeze drying of samples was done using an Edwards freeze dryer connected to an Edwards RV8 vacuum pump. Mass spectra were acquired on an Agilent 6520 Accurate-Mass Q-TOF LC/MS with electrospray ionisation coupled to an Agilent 1200 HPLC system with degasser, quaternary pump and autosampler (G1329A), using Agilent Masshunter

workstation acquisition software, B.02.1 (B2116). Data were analysed using Agilent Masshunter Qualitative software B.03.01 (Build 3.1.346.14 service pack 3). Sample shaking and centrifugation were done on a Grant PHMT shaker and an Eppendorf centrifuge 5424 microcentrifuge, respectively. ^{99m}Tc-**1** (^{99m}Tc-MDP, prepared by reconstitution of a Draximage kit with [^{99m}Tc]-pertechnetate eluted from a generator with physiological saline), was supplied by Guy's Hospital Radiopharmacy, Guy's and St Thomas' NHS trust. [^{188}Re]-perrhenate was eluted with physiological saline from a generator purchased from ITG (Isotope Technologies, Garching GmbH) and, where necessary, concentrated using a previously described procedure.[20,21] *S*-Methyl-*N*-methyl-dithiocarbazate (DTCZ) was synthesised as previously described.[22]

Radiolabelling and quality control of [^{99m}Tc]-4

[^{99m}Tc-**4**] was synthesised and characterised according to procedures described previously.[12,23] 50 μg of DPA-ale in 300 μL of 50 mM carbonate buffer (pH 9) containing 0.15 M NaCl was mixed with 300 μL of an aqueous solution of [^{99m}Tc]-$[Tc(CO)_3(H_2O)_3]^+$ (250–300 MBq) in a glass vial with a rubber stopper and heated at 90 °C for 30 min. The product was purified by passing it through a Sep-Pak C-18 Plus Light cartridge (Waters, WAT-23501) activated with absolute ethanol. [^{99m}Tc]-**4** trapped by the column was eluted with 500 μL of 1 : 1 ethanol–water. The ethanol was then evaporated under a stream of nitrogen and the remaining solution diluted with 250 μL of saline for injection. The intermediates and product were analysed by radio-TLC using solvent system 4 on silica plates (intermediates: reduced hydrolysed technetium, R_f = 0; $[Tc(CO)_3(H_2O)_3]^+$, R_f = 0.1–0.7; pertechnetate, R_f = 0.9; product, [^{99m}Tc-**4**], R_f = 0). Radiochemical purity of the final product was >99%.

Synthesis and mass spectrometry of [TcN(DTC-BP)$_2$] (7)

K[^{99}TcO$_4$] (Amersham International plc, UK; 0.6 mg, 20 μL of a 30 mg mL^{-1} solution) was added to a vial containing 3.6 mg succinic dihydrazide (SDH) and 1.3 mg 1,2-diaminopropanetetraacetic acid (DPTA) in 500 μL physiological saline, followed by 500 μL of a 10 mg mL^{-1} solution of $SnCl_2$ in 0.05 N HCl. The solution immediately turned yellow/orange and a precipitate formed. After 35 minutes the solution was centrifuged and 50 μL of the supernatant was added to 1.3 mg HDTC-BP (**6**), synthesised as described previously,[19] in 400 μL of pH 10 carbonate buffer. The solution was heated at 60 °C for 30 minutes before cooling to room temperature and analysing by mass spectrometry using the LC-MS system without a column. The mobile phase was 15 mM ammonium bicarbonate, adjusted to pH 9.4 with 30% NH_4OH solution. The flow rate was 0.5 mL min^{-1} and a splitter was fitted (10% LC flow to mass spectrometer, 90% flow to waste). The mass spectrometer was run in negative ion mode with a gas temperature of 325 °C, an N_2 gas flow of 5 L min^{-1} and a nebuliser pressure of 20 psi. The capillary voltage was 3500 V and the fragmentor voltages were 175 V and 250 V. The injection volume for each sample was between 0.1 and 1 μL.

Synthesis and mass spectrometry of [ReN(DTC-BP)$_2$] (8)

$[ReNCl_2(PPh_3)_2]$[24] was reacted with 1,3,5-triaza-7-phosphaadamantane (PTA) to produce the water-soluble complex $[ReNCl_2(PTA)_3]$ according to an established method.[25] This complex (8.9 mg, 1.12×10^{-5} mol) was dissolved in 1 mL water to give a cloudy brown solution which was then added to **6** (8 mg, 2.46×10^{-5} mol, 2.2 eq.) and shaken at 800 rpm at room temperature for 80 min. The solution was then freeze dried. The freeze dried material was reconstituted to 1 mg mL^{-1} in water for mass spectrometry analysis, giving a clear yellow solution. This was analysed by mass spectrometry as described above for [^{99}Tc]-**7** but with fragmentor voltage set at 125 V or 325 V.

Radiolabelling of [^{99m}Tc]-7

Method 1 (arrived at after extensive optimisation to ensure reliable quantitative radiochemical yield): To a vial containing SDH (2.5 mg) and DPTA (1 mg) in 500 μL saline was added 695 MBq $^{99m}TcO_4^-$ generator eluate (120 μL), followed by 50 μL of a 10 mg mL^{-1} solution of $SnCl_2$ in 0.05 N HCl. The mixture was shaken at room temperature for 1 h. Quality control was performed using TLC with solvent system 1 (pertechnetate, R_f = 0.5; reduced hydrolysed technetium, R_f = 0; required technetium nitride intermediate, R_f = 0–0.3) and solvent system 2 (reduced hydrolysed technetium, R_f = 0; required technetium nitride intermediate and pertechnetate, R_f = 0.9). 300 μL of this solution was then added to a vial containing 0.5 mg **6** in 200 μL carbonate buffer, to give a total of 280 MBq in 500 μL. The solution was heated at 60 °C for 30 minutes, followed by quality control by TLC using solvent system 2 ([^{99m}Tc]-**7**, R_f = 0). For *in vivo* administration 200 μL of the solution was added to 80 μL 0.1 N HCl, to give 101 MBq of ^{99m}Tc-**7** in 280 μL with a final pH of 6.6–7.

Method 2 (developed after optimising the synthesis *via* method 1): 623 MBq $^{99m}TcO_4^-$ generator eluate (in 1 mL saline) was added to a lyophilised SDH kit vial (generous gift of Prof. Roberto Pasqualini, Cis Biointernational, IBA Group, Gif-sur-Yvette, France, as previously used for production of ^{99m}Tc-NOET)[17,18] and incubated for 30 minutes at room temperature. The composition of the kit vial was as follows: SDH 5.0 mg; stannous dichloride dihydrate 0.10 mg; DPTA 5.0 mg; sodium dihydrogen phosphate monohydrate 0.6 mg; disodium phosphate heptahydrate 10.9 mg; under a dinitrogen atmosphere. Quality control was performed using TLC with solvent system 1. 300 μL of the resulting solution was then added to 300 μL of the of DTC-BP ligand (1 mg mL^{-1}) in carbonate buffer (pH 10). The vial was incubated at 60 °C for 30 minutes. QC was performed using TLC with solvent system 2.

Radiolabelling of [^{188}Re]-8

Kit vials were prepared as follows: 1.5 mg DTCZ was placed in a nitrogen-purged vial followed by 2.8 mg mL^{-1} $SnCl_2{\cdot}2H_2O$ dissolved in 0.5 mL of 20% glacial acetic acid and 28 mg sodium oxalate. The vial was capped with a rubber stopper, sonicated and purged with nitrogen for 10 min. To a kit vial

thus prepared, 500 MBq $^{188}ReO_4^-$ in 0.5 mL generator eluate was added. The vial was vortex-mixed, heated at 80 °C for 2–3 min and allowed to cool to room temperature for 15 min. TLC was performed using solvent system 1 above. This intermediate solution as also analysed by radioHPLC using an Agilent HPLC with an Eclipse XDB-C18 column (4.6 × 150 mm) and a guard column eluted with 95% water, 5% methanol each with 0.1% trifluoracetic acid, at a flow rate of 1 mL min^{-1}. In this system perrhenate (5% of eluted activity) eluted at <2 min, while the rhenium nitride intermediates (95% of eluted activity) eluted as a series of isomeric species at 10–13 min. 50 μL of this solution of ^{188}Re-nitride intermediate was then added to 71.4 μg DTC-BP in 100 μL carbonate buffer (0.5 M, pH 9.0), to give a total of 25 MBq in 150 μL. The solution was gently vortexed and heated at 80 °C for 30 min, followed by quality control by TLC using solvent system 3 (perrhenate, R_f = 0.8–0.9; [^{188}Re]-**8**, R_f = 0).

Log *P* measurement

The lipophilicity of each ^{99m}Tc and ^{188}Re radiotracer, with a radiochemical purity of at least 95%, was determined by partitioning the complex between 1-octanol and water. 50 μl (~1–2 MBq) of the radiotracer was added to a 1.5 mL Eppendorf tube (n = 9) containing 500 μL 1-octanol and 495 μL of distilled water and vortexed at room temperature for 15 minutes and then centrifuged at 1200 RPM for 5 minutes. A 0.2 mL aliquot of each phase was pipetted out and counted in a gamma-counter. The partition coefficient was calculated as log P = log((cpm in octanol − cpm background)/(cpm in water − cpm background)).

Synthetic and biological mineral binding studies

Preparation of mineral salts and buffer solutions: 1 mg of each bone mineral analogue (hydroxyapatite, β-tricalcium phosphate, calcium phosphate dibasic, calcium oxalate, calcium carbonate or calcium pyrophosphate, all purchased from Sigma-Aldrich) was added to a 1.5 mL plastic microcentrifuge tube in duplicate. 1 mL TRIS-HCl buffer (50 mM, pH 6.8) was added to each tube followed by 10 μL of either ^{99m}Tc-**7** (prepared by method 1) or 10 μL of the $^{99m}TcN^{2+}$ intermediate (method 1, as a control). 10 μL of either tracer were also added to control tubes containing 1 mL TRIS-HCl with no mineral salts. All tubes were then shaken at 900 rpm for 1 h then centrifuged at 10 000 rpm for 5 min. 10 μL of supernatant was removed from each tube (including the controls) and added to 1 mL TRIS-HCl buffer (50 mM, pH 6.8) in triplicate. Percentage binding of radioactivity to the mineral salts was calculated as $(1 - cpm_{sample}/cpm_{control}) \times 100\%$.

Similar studies were performed with mineral samples of biological origin, including powdered equine bone and human minerals isolated from vascular intimal and medial calcified plaques obtained from surgical procedure with appropriate ethical approval. The methods to release these biominerals from their organic matrix and connective tissues have been previously published.[26,27] Suspensions of 0.5 mg mL^{-1} of each sample were prepared in distilled water. 1 mL of the suspensions in triplicate (synthetic hydroxyapatite, powdered equine bone, medial and intimal arterial minerals) was placed in 1.5 mL Eppendorf tubes in triplicate alongside mineral-free controls. 20 μL of ^{99m}Tc-**1**, [^{99m}Tc]-**4** and [^{99m}Tc]-**7** (0.5–1 MBq) was added to each tube. The tubes were incubated for 60 min in a shaker at 37 °C and 550 RPM. The tubes were centrifuged at 13 200 RPM for 5 minutes. 50 μL of the supernatant from the vials were pipetted out and counts were measured in a gamma counter. The binding percentage was calculated as above.

Hydroxyapatite binding in the presence of serum and serum protein binding

To microcentrifuge tubes containing 2 mg mL^{-1} hydroxyapatite in TRIS-HCl buffer (50 mM, pH 6.8) or human serum (Sigma) were added 10 μL of either [^{99m}Tc]-**7** or ^{99m}Tc-**1**. Identical controls without mineral were prepared similarly. All tubes were prepared in triplicate. All samples were then incubated with shaking at 1400 rpm at 37 °C. At intervals of up to 23 h all tubes were centrifuged at 10 000 rpm for 5 minutes. 5 μL supernatant was removed from each tube and counted in a gamma counter. Hydroxyapatite % binding was calculated as described above. Binding to serum proteins in the serum-containing samples was assessed as follows: 70 μL ethanol was added to 50 μL aliquots of the supernatant after centrifugation of each serum incubation. The tubes were centrifuged at 10 000 rpm for 5 minutes and the supernatant was removed. The pellets were washed with another 70 μL ethanol, centrifuged again and the supernatant was decanted and added to the supernatant from the initial precipitation. The pellets and supernatant were then counted separately in a gamma counter. Percentage serum protein binding was calculated as $100\% \times cpm_{pellet}/(cpm_{pellet} + cpm_{supernatant})$. Control samples of [^{99m}Tc]-**7** in buffer were also subjected to ethanol precipitation to ascertain whether or not the addition of ethanol caused the complex to precipitate.

Animal studies

All procedures were performed in accordance with licences and guidelines approved by the UK Home Office and were approved by a King's College ethics committee. Normal female BALB mice, 9 weeks old, were used for preliminary comparative biodistribution studies with ^{99m}Tc-**1**, [^{99m}Tc]-**7** and [^{188}Re]-**8**. For imaging of arterial calcification, Sprague Dawley rats (n = 6; male; 21–27 days old) were purchased from Charles River Laboratories. After an acclimatisation period of 7 days, 6 rats were fed with a diet containing warfarin (3 mg g^{-1} food) and vitamin K1 (1.5 mg g^{-1} food) for 11 days. The rats were given 200 000 IU kg^{-1} per day subcutaneous injections of cholecalciferol (Sigma-47763) from day 7 to day 11 of the diet. It has been reported that warfarin treatment in the form of diet, oral administration (gavage) or subcutaneous injections induces vascular calcification[27,28] and the process is accelerated by vitamin D_3 (cholecalciferol). All animals were maintained on a 12 hour light-dark cycling with access to environmental enrichment (tunnel). Food and water were provided *ad libitum*.

SPECT/CT scanning and biodistribution: Mice (n = 1) under Isoflurane anaesthesia were injected with 40 MBq of either [^{99m}Tc]-**1** or [^{99m}Tc]-**7** in ~100 μL *via* a tail vein. SPECT-CT scans were acquired at intervals up to 338 min using a Nano-SPECT-CT scanner (Bioscan, USA) with SPECT acquisition time 1800 s, obtained in 24 projections using a 4-head scanner with 4 × 9 (2 mm) pinhole collimators in helical scanning mode and CT images with a 45 kVP X-ray source, 500 ms exposure time in 180° projections over 9 min. Images were reconstructed in a 128 × 128 matrix using HiSPECT (SciVisGmbH), a reconstruction software package, and images were fused using proprietary Bioscan InVivoScope (IVS) software. All scans were 30 minutes long. Kinetic studies (% uptake) were carried out by calculating the radioactivity in local regions of interest (ROIs) relative to the radioactivity in the whole body ROI. ROI data were calculated for both a knee joint and a single vertebra. The mice were sacrificed with an overdose of anaesthesia at the end of scanning and the organs and tissues were harvested, weighed and counted in a gamma counter. Uptake was reported as standard uptake values (SUVs). Rats under Isoflurane anaesthesia were injected with 40–50 MBq (100 μL) of the radiotracers *via* a tail vein with ^{99m}Tc-**1**, [^{99m}Tc]-**4** or [^{99m}Tc]-**7** (n = 2 in each case). CT images were acquired with a 55 kVP X-ray source, 100 ms exposure time in 360° projections over 24 min. SPECT imaging was performed with above mentioned parameters at intervals of 30 min up to 240 min. After 4 hours of SPECT-CT scanning the rats were culled by an overdose of anaesthesia. Vital organs were harvested, weighed and counted with a gamma counter, along with standards prepared from a sample of the injected material. The percent of injected dose per gram of tissue (% ID g^{-1}) was calculated. Biodistribution of [^{188}Re]-**8** was determined similarly (n = 3) after injection of 8.5 MBq (50 μL) of the radiopharmaceutical. Mice were killed at 24 h post-injection and organs harvested as described above, weighed and counted in a gamma counter.

Results

Chemical syntheses and characterisation

[TcN(DTC-BP)$_2$] (7). The beta-emitting isotope ^{99}Tc has a long half-life (200 000 years) and hence, unlike the gamma-emitter ^{99m}Tc, a low enough specific activity to be handled in quantities sufficient to perform conventional spectrometry. Compound **8** was synthesised by a scaled-up version of the no-carrier-added method used with ^{99m}Tc (see below), starting from potassium pertechnetate and reducing it with stannous chloride in the presence of succinic dihydrazide as a nitride source and propane-1,2-diamine tetraacetic acid as an intermediate chelator of the technetium complex and possibly of tin. Like the rhenium analogue (see below for details), the clear yellow solution resisted isolation of the product in pure form by virtue of its intractable solubility and chromatography properties, and was therefore characterised by electrospray mass spectrometry (again, like the rhenium analogue discussed below). Negative ion mass spectra of the yellow ^{99}Tc solution show that at 250 V the only technetium-containing ions detected were those derived from the expected molecule **7** *i.e.* $(M - H)^-$ (m/z = 759.8003) and sodium adducts $(M - 2H + Na)^-$ (781.7815) and $(M - 3H + 2Na)^-$ (803.7624). At 175 V the doubly charged $(M - 2H)^{2-}$ species was also present. No ions containing Tc in a form other than this (*e.g.* with oxo-ligand rather than nitride, or with a ligand-to-metal ratio other than 2 : 1, or oligomeric species) were detected. A full list of ions can be found in Table S2 of the ESI†, along with raw spectra.

[ReN(DTC-BP)$_2$] (8). Synthesis of **8** (Fig. 2) was achieved in three steps. The well-known Re(v) nitride precursor [$ReNCl_2(PPh_3)_2$] was synthesised according to an established method[24] and was then reacted with 1,3,5-triaza-7-phosphaadamantane (PTA) to make the water-soluble [$ReNCl_2(PTA)_3$] according to an established method.[25] The aqueous solubility of [$ReNCl_2(PTA)_3$] enabled its reaction with the dithiocarbamate-bisphosphonate conjugate **5** which is soluble only in water; the resulting clear yellow aqueous solution was typical in appearance to previously reported [$ReN(dtc)_2$] complexes but because of the extreme water solubility of the product, its extreme insolubility in non-aqueous solvents, and its strong adherence to all of the wide variety of chromatographic stationary phases tested (including reverse-phase silica-based HPLC media) it remained resistant to isolation in pure form. Therefore the crude clear yellow aqueous solution was analysed by electrospray mass spectroscopy (in negative mode due to the expected negative charge), as the only analytical approach by which the complex could be characterised without interference from other components of the mixture. Because of the irreversible adsorption to all chromatographic media, the LC-MS system was used without a column. The sample was analysed at two different cone voltages. At 325 V the only ion species showing the characteristic $^{185/187}$Re isotope pattern were the negatively charged ions corresponding to the expected molecule **8** ionising by loss of H^+ or $2H^+$, and variants with H^+ replaced by Na^+. In the case of the dominant ^{187}Re isotope these were $(M - H)^-$ complex (m/z = 847.8721) and related sodium adducts $(M - 2H + Na)^-$ (869.8517) and $(M - 3H + 2Na)^-$ (891.8341), and doubly charged relatives $(M - 2H)^{2-}$ (m/z = 423.4129) and related sodium adducts $(M - 3H + Na)^{2-}$ (434.4033) and $(M - 4H + 2Na)^{2-}$ (445.3949). The mass spectrum also showed another ^{187}Re species with m/z 765.8919 (together with its ^{185}Re partner), corresponding to a fragmentation involving loss of $P(OH)_3$ and ionisation by loss of H^+. No ions of higher molecular weight that would indicate oligomeric species, or with ratios of ligand-to-rhenium nitride other than 2 : 1, or indeed rhenium species not containing the nitride ligand, were detected in the mass spectrum at 325 V. At 125 V, the main species identified were again the doubly charged $(M - 2H)^{2-}$ derived from **8** and related sodium adducts $(M - 3H + Na)^{2-}$ and $(M - 4H + 2Na)^{2-}$. However, also present at 125 V were peaks derived from [$ReN(DTC\text{-}BP)_2(PTA)$] with $(M - H)^-$ and $(M - 2H)^{2-}$ and related sodium adducts. There was also a set of peaks relating to $ReN(DTC\text{-}BP)_3$ $(M - H)$. The absence of these peaks from the 325 V spectrum of the same sample

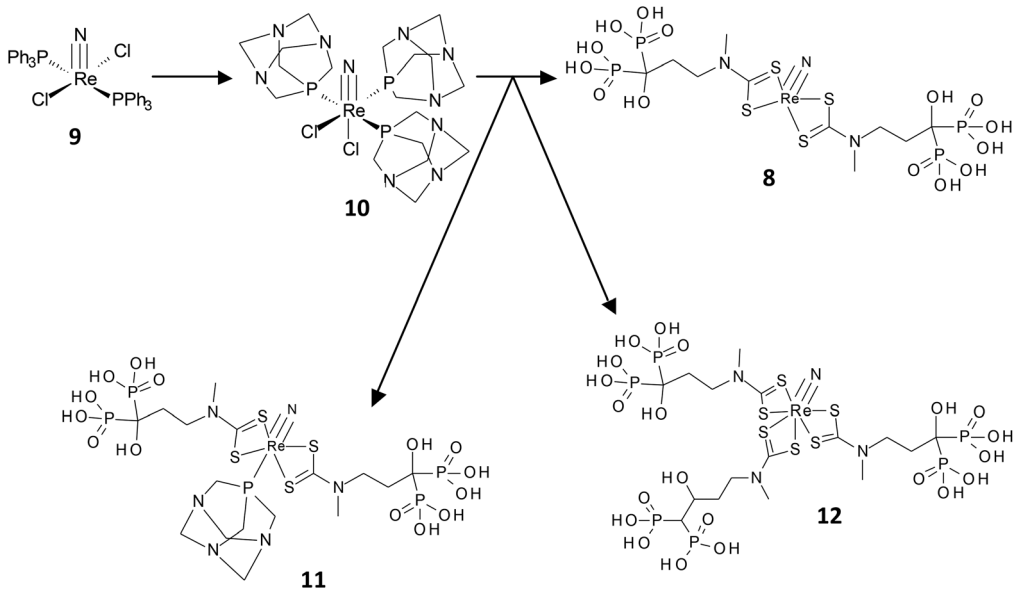

Fig. 2 Intermediates and products (the latter as identified by detection of corresponding molecular ions in electrospray mass spectrometry) in the synthesis of rhenium nitride complexes.

suggests that they appear of greater significance under the milder ionisation conditions because the major species derived from **8** itself are less efficiently ionised at this low voltage. A full list of ions can be found in Table S1 of the ESI† along with the raw spectra.

Radiolabelling and quality control of [^{99m}Tc]-7

The radiolabelling method was developed from the established two-step methods used for radiolabelling the lipophilic ^{99m}TcN(DTC)$_2$ complexes such as ^{99m}Tc-NOET.[15–17] The general method was to make the pentavalent $^{99m}TcN^{2+}$ intermediate (presumably with PDTA as ancillary ligands) from pertechnetate by stannous reduction in the presence of succinic dihydrazide as the nitride source in the first step before adding this solution to the dithiocarbamate (in this case **5**) in the second step. As expected from the adsorption and solubility behaviour of **8** (above), analysis of radiochemical purity of [^{99m}Tc]-7 using reverse phase HPLC proved to be unsuccessful, leading to retention of all radioactivity on all columns evaluated (whether reverse- or normal-phase) even after prolonged washing with various solvents. The nitride intermediate and the starting pertechnetate were, on the other hand, eluted successfully from HPLC columns and migrated in suitable TLC conditions, as expected. Two solvent systems were adopted for quality control using silica gel TLC. Solvent system 1 could distinguish between $^{99m}TcO_4^-$ and the $^{99m}TcN^{2+}$ intermediate (Fig. 3A and B respectively). Solvent system 2 could distinguish between the $^{99m}TcN^{2+}$ intermediate and [^{99m}Tc-7] (Fig. 3C and D respectively); all three species could be distinguished using these two systems. Thus, the main evidence for the formation of the required [^{99m}Tc]-7 is the presence of a radioactive species with R_f = 0 under conditions of both TLC methods 1 and 2; no such species appeared at earlier stages of the synthesis. These TLC methods were used to optimise the kit-based process for synthesising [^{99m}Tc]-7, before finally arriving at the conditions described in the Experimental section. Octanol–water solvent extraction confirm that [^{99m}Tc]-7 is highly hydrophilic ($\log P = -2.76 \pm 0.08$), and its increased lipophilicity compared to ^{99m}Tc-**1** and [^{99m}Tc]-**4** ($\log P = -2.40 \pm 0.16$ and 2.05 ± 0.03 respectively; see ESI†) is consistent with the presence of two pendant bisphosphonate groups.

Radiolabelling and quality control of [^{188}Re]-8

The approach to ^{188}Re radiolabelling was similar to that used for ^{99m}Tc labelling. First a labelled rhenium–nitrido intermediate was prepared using stannous chloride to reduce rhenium from Re(VII) to Re(V) and DTCZ as a source of the nitride group, as previously described.[29] TLC and HPLC showed that at this stage 95% of perrhenate had been converted to the intermediate. This intermediate was then treated with the dithiocarbamate ligand to produce [^{188}Re]-**8**, which was used both to confirm the equivalence of the radioactive species by TLC with the cold complex characterised by mass spectrometry, and for preliminary biodistribution studies. The final TLC showed that no perrhenate or intermediate remained in the product. As in the case of [^{99m}Tc]-7, no HPLC or TLC conditions could be found in which the product could be eluted from the stationary phase.

In vitro bone mineral binding studies

To determine the propensity of the complexes to bind to hydroxyapatite (HA) and other calcium phosphates, as a crude *in vitro* assessment of bone targeting potential and to confirm the availability of bisphosphonate groups for mineral binding, [^{99m}Tc]-7 was mixed with a suspension of hydroxyapatite and allowed to partition between solid and solution phase.

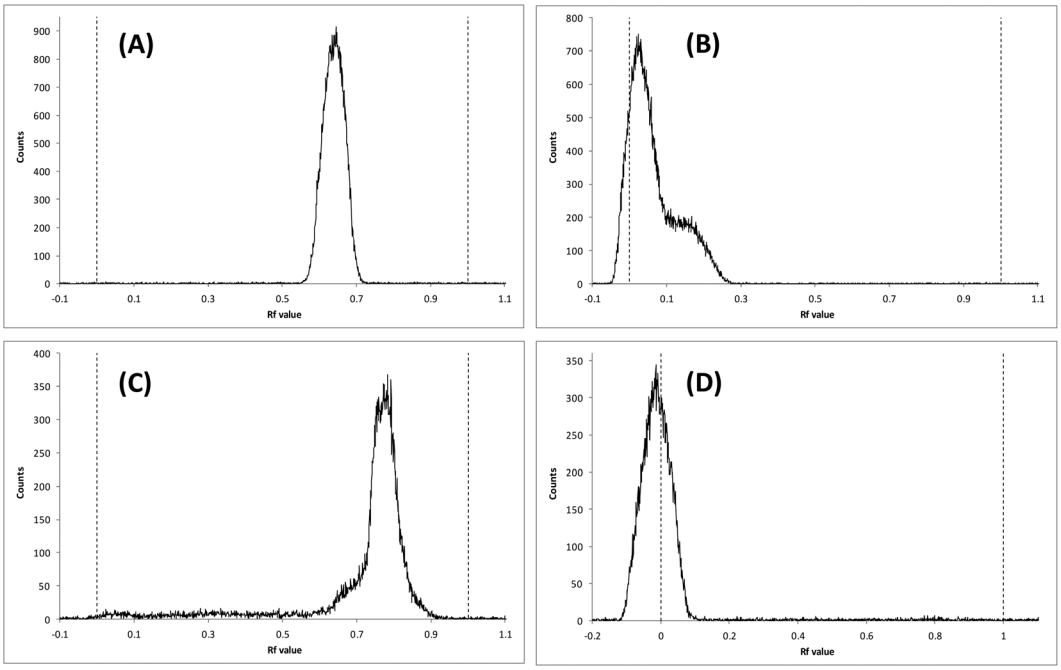

Fig. 3 Radio-TLC chromatograms on silica gel coated aluminium plates of (A) $^{99m}TcO_4^-$, solvent system 1; (B) $^{99m}TcN^{2+}$ intermediate, solvent system 1, (demonstrating the absence of pertechnetate at this stage); (C) $^{99m}TcN^{2+}$ intermediate, solvent system 2 and (D) ^{99m}Tc-**7**, solvent system 2 (demonstrating the absence of both pertechnetate and the Tc-nitride intermediate in the final product).

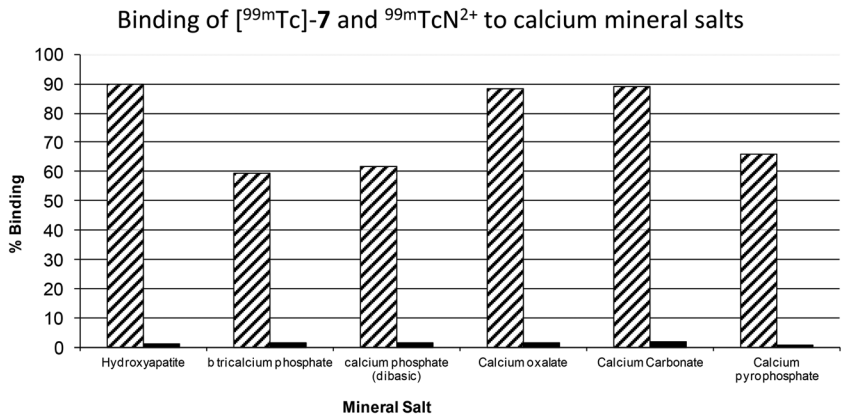

Fig. 4 Graph showing results of bone mineral binding studies of [^{99m}Tc]-**7** (hatched bars) and $^{99m}TcN^{2+}$ intermediate (black bars).

Binding of [^{99m}Tc]-7 was high for each mineral salt with values ranging between 59% for β-tricalcium phosphate up to 90% for hydroxyapatite as shown in Fig. 4. "Non-specific" binding of radioactivity of the $^{99m}TcN^{2+}$ intermediate to mineral salts was very low with all values ≤1.6%. This encouraging result prompted comparison of [^{99m}Tc]-7 with the other ^{99m}Tc-bisphosphonate complexes, ^{99m}Tc-**1** and [^{99m}Tc]-**4**, in their affinity for synthetic and biologically-derived calcium phosphates.

Each of these ^{99m}Tc-complexes was incubated with 0.5 mg mL^{-1} of synthetic HA, equine bone and isolated minerals from human intimal and medial atherosclerotic plaque samples. The results are shown in Fig. 5. The percentages of ^{99m}Tc-**1**, [^{99m}Tc]-**4** and [^{99m}Tc]-7 bound to synthetic HA were 88.5 ± 0.9%, 92.4 ± 0.7% and 94.5 ± 3.05% respectively. A similar range and ranking was observed with powdered bone and with mineral from medial calcified plaques. However with the minerals isolated from intimal plaques the % binding was significantly lower (possibly because these minerals contain a lipid component) and the MDP complex had a markedly reduced tendency to bind compared to the pendant bisphosphonate complexes.

Binding to hydroxyapatite and proteins in serum

^{99m}Tc-**1** and [^{99m}Tc]-7 were incubated in serum (and a non-phosphate buffer, as a control) with and without hydroxyapatite

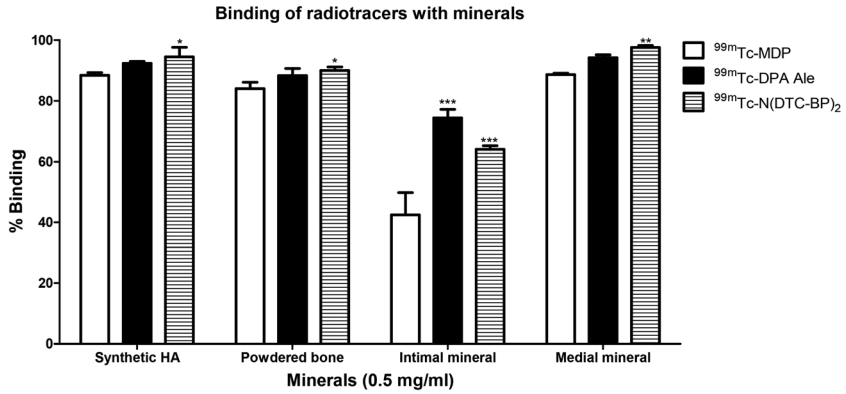

Fig. 5 Graph showing the % binding (mean ± SD) of ^{99m}Tc-**1**, [^{99m}Tc]-**4** and [^{99m}Tc]-**7** with synthetic hydroxyapatite, powdered equine bone and minerals from intimal and medial plaques. *significant a $p > 0.05$, **significant at $p > 0.001$ and ***significant at $p > 0.0001$.

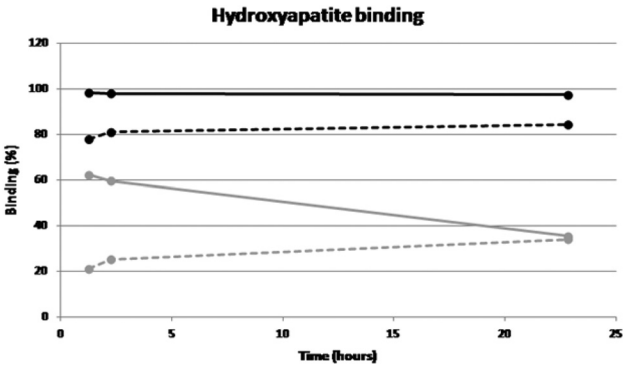

Fig. 6 Graph showing binding of [^{99m}Tc]-**7** to hydroxyapatite in buffer (black solid line) and in serum (black dotted line); ^{99m}Tc-MDP in buffer (grey solid line) and in serum (grey dotted line).

over a period of 23 h in order to determine whether a biological milieu interferes with mineral binding, and to compare their binding to serum proteins. [^{99m}Tc]-**7** binds well (>90%) to hydroxyapatite in buffer and only slightly less well (>80%) in serum, and the binding is largely retained during the 23 h. ^{99m}Tc-**1** on the other hand binds less well in buffer (>60%) in qualitative agreement with Fig. 6 despite the changed conditions, and the binding is severely diminished (>30%) by the presence of serum; moreover the fraction bound in buffer diminishes with time (to *ca.* 35% by 23 h), whereas there is no corresponding loss of binding with time in serum. Possibly this behaviour is associated with vulnerability of ^{99m}Tc-**1** to gradual oxidation to pertechnetate, against which serum may offer some protection, and to which [^{99m}Tc]-**7** is less sensitive because of the more appropriately designed chelator used. Both complexes display a high level of binding to proteins

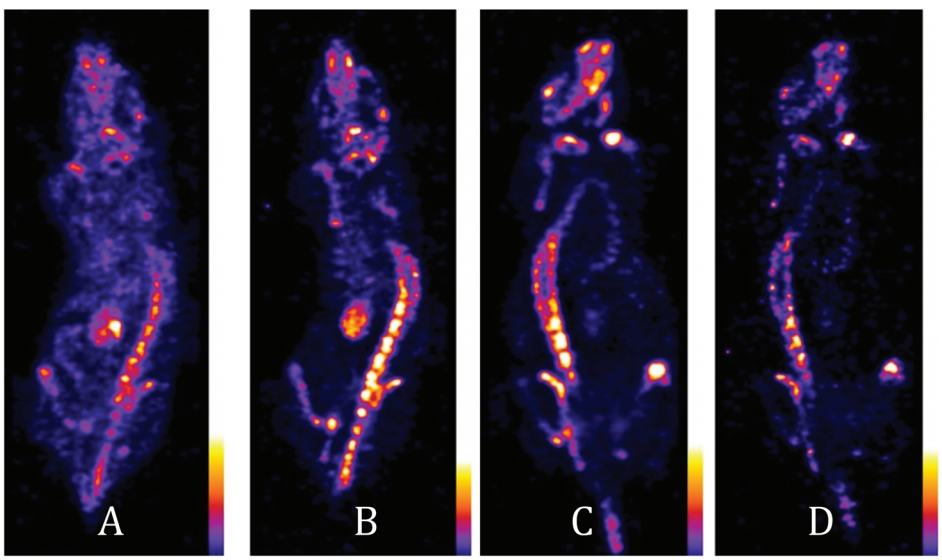

Fig. 7 SPECT images (coronal sections) of a mouse injected with [^{99m}Tc]-**7** at 54 min (A) and 365 min (B), and of a mouse injected with ^{99m}Tc-**1** after 104 min (C) and 368 min (D), post injection. The bladders have been digitally removed from the field of view for the sake of clarity. All scans show high uptake in bone and especially joints. A and B show transit and retention of activity by kidney, whereas in C and D the renal excretion process is essentially complete and the kidneys are not evident.

(70–80% in the case of [^{99m}Tc]-**7**, 60–70% in the case of ^{99m}Tc-**1**), with a much faster loss of protein binding over time in the case of ^{99m}Tc-**1**, possibly again because of gradual oxidation to pertechnetate.

Biodistribution and imaging

The biodistribution of the new tracer [^{99m}Tc]-**7** was compared with that of the conventional bone imaging agent ^{99m}Tc-**1** in normal mice. Both tracers (Fig. 7) show qualitatively similar biodistribution, with high uptake in bone and especially the joints, no marked uptake in any other tissue except kidney and bladder but a marked difference in the rate at which the tracer accumulates and clears through the renal pathway. The biodistribution of ^{99m}Tc-**1** reached a steady state by 100 min, with renal excretion essentially complete and no further uptake in or clearance from bone and joints. [^{99m}Tc]-**7** on the other hand was still visibly being excreted through kidney at this time, while Fig. 8 shows that activity continued to migrate from blood and soft tissues to bone and joints until at least 6 h. Although the SUV of [^{99m}Tc]-**7** in bones and joints was lower than that of ^{99m}Tc-**1** at 1 h, by 2 h the SUVs were similar and by 6 h the SUV of [^{99m}Tc]-**7** was significantly higher than that of ^{99m}Tc-**1**. The bladder (removed from the image for clarity of display) contained 61% of the radioactivity from 104 minutes onwards for ^{99m}Tc-**1** compared with 24% at 54 minutes for [^{99m}Tc]-**7**, rising to 28% at 365 minutes post injection.

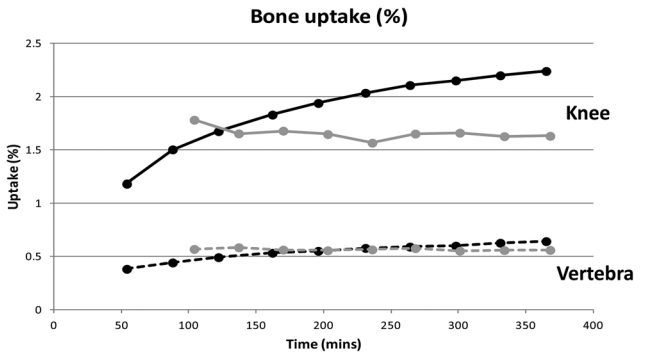

Fig. 8 Graph showing uptake in knee joint (solid lines) and single vertebra (broken lines) over 6 h. ^{99m}Tc-**7** is represented by black lines, ^{99m}Tc-**1** is represented by grey lines.

Biodistribution data at 6 h post injection are shown in Fig. 9. SUVs are higher in bone and joint for [^{99m}Tc]-**7** compared with ^{99m}Tc-**1** but non-specific binding in most soft tissues is higher for [^{99m}Tc]-**7** particularly in the kidneys because of slower excretion and slower binding to bone, and minor uptake in trachea, spleen and liver. Also of note from Fig. 8 is that [^{99m}Tc]-**7** displays a higher ratio of uptake in joint to mature bone than ^{99m}Tc-**1**.

The new rhenium-188 radiopharmaceutical [^{188}Re]-**8**, like [^{99m}Tc]-**7**, shows high specificity for bone and joints in preliminary biodistribution studies in mice (see ESI†). Radioactivity concentration in bone and joints is high at 24 h (a much later time point than in the evaluation of its ^{99m}Tc analogue) and higher than in kidney and other tissues.

The ability of the tracers to detect vascular calcification was compared in a rat model in which arterial calcification was induced by administration of warfarin and vitamin K in the diet and vitamin D subcutaneously. The resulting arterial calcification in the aorta and mesenteric arteries was confirmed by histological staining (see ESI†). SPECT-CT scans (Fig. 10 and ESI†) were then performed with novel agents [^{99m}Tc]-**7** and [^{99m}Tc]-**4** and the conventional agent ^{99m}Tc-**1**. As well as in bones and joints, intense uptake of all the radiotracers was most strikingly seen in the calcified mesenteric artery within 30 min of the injection. This manifests as a hollow sphere of activity, in the abdominal region below the liver that does not correspond to any major solid organs and is not visible in scans of normal rats. *Ex vivo* biodistribution demonstrates significantly increased uptake (%ID g^{-1}) in most tissues (including bones) compared to normal rats; of the tissues that could be dissected and weighed (which do not include the mesenteric arteries), the increase is particularly marked for all three tracers in the aorta, heart and lungs (Fig. 11) although uptake in these organs is still too small to be clearly evident on the scans at the thresholds used in Fig. 10. While these data demonstrate the ability of the new tracers to detect vascular

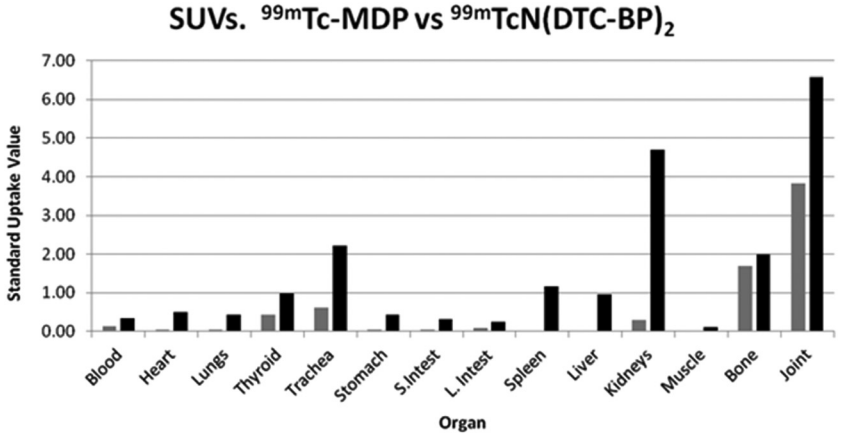

Fig. 9 Standard Uptake Values (SUVs) for ^{99m}Tc-**1** (grey bars) and [^{99m}Tc]-**7** (black bars) in mice at 6 h post injection.

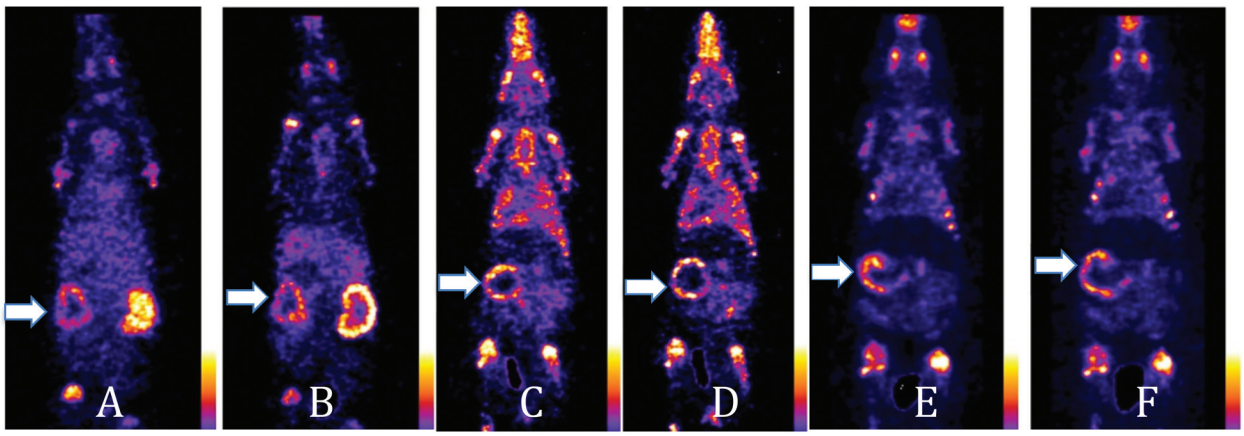

Fig. 10 A, B: Coronal sections of a rat scanned 30 min and 4 h, respectively after i.v. injection of [^{99m}Tc]-**7**. C, D: Coronal sections of a rat scanned at 30 min and 4 h, respectively, after i.v. injection of [^{99m}Tc]-**4**. E, F: Coronal sections of a rat scanned at 30 min and 4 h, respectively, after i.v. injection of ^{99m}Tc-**1**. Arrows show the uptake of the radiotracers in the calcified mesenteric arteries.

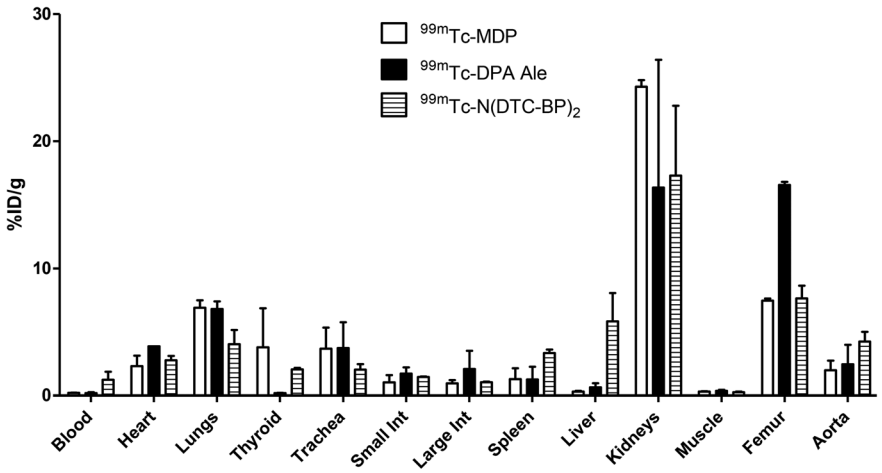

Fig. 11 Biodistribution (%ID g^{-1}, mean ± SD) in rats 4 h after injection of tracers ^{99m}Tc-**1**, [^{99m}Tc]-**4** and [^{99m}Tc]-**7** (n = 2).

calcification, at the present stage of analysis they do not demonstrate any dramatic advantage in sensitivity of the new tracers with pendant bisphosphonate groups compared to the conventional heterogeneous tracer ^{99m}Tc-**1** in this application.

Discussion

We have described a simple synthesis and radiolabelling of the first technetium and rhenium complexes with two pendant bisphosphonate groups, building on the early development of complexes in which bisphosphonate groups are bound directly to the radiometal (and which have become established radiopharmaceuticals for imaging and palliative therapy of bone disease[2]) and the later development of complexes containing a pendant bisphosphonate group.[12,13] We reasoned that this sequence of developments in design should yield radiopharmaceuticals with improved homogeneity, *in vivo* stability and targeting of biomineral deposits. To produce a well-defined complex with two pendant bisphosphonate groups we chose to use the well-known technetium/rhenium(v) nitridobisdithiocarbamate core, in conjunction with a dithiocarbamate–bisphosphonate conjugate ligand, **6**, which we previously showed to coordinate to copper(II) *via* its dithiocarbamate group to form a complex with two pendant bisphosphonate groups.[19]

The synthesis of the ^{99}Tc and ^{99m}Tc complexes is based on the established formation of a M(v) nitride complex using succinic dihydrazide as a source of nitrogen to form the nitride.[17,18] To establish a robust, kit-based synthesis with sufficiently high yield (>95%) to avoid the need for a purification step, it was necessary to optimise the composition of the kit and in particular to ensure that the concentrations and molar ratios of the intermediate chelator DPTA and the final ligand **6** were appropriately balanced: too little DPTA leads to inadequate stabilisation of the metal nitride intermediate,

while too much causes competition with the dithiocarbamate ligand in the second step. This optimisation led to methods 1 and 2 each of which provides a simple route to the ^{99m}Tc complex. The ^{99}Tc analogue was also synthesised, using the same reagents, to generate sufficiently high concentrations for analysis by mass spectrometry. The route to the rhenium complex was based on conventional rhenium nitride starting materials, adapted for compatibility with an aqueous synthesis because **6** is only soluble in water.

The characterisation of the product complexes posed major problems because the solubility and adsorption properties of both **7** and **8** precluded purification by recrystallisation or chromatography. The bisphosphonate complexes are all extremely hydrophilic (see log *P* data, ESI†) and adherent to various stationary phases. As a result, only negative ion electrospray mass spectrometric data are available to confirm the identity of the products. The mass spectra, however, confirm several key aspects relating to the structure and homogeneity of both **7** and **8**. The ions observed are consistent with the presence of a mononuclear nitrido complex with two dithiocarbamate–bisphosphonate ligands, with the metal in oxidation state five. This is consistent with the body of literature on technetium and rhenium nitride bis(dithiocarbamate) complexes.[14] These data cannot, however confirm that ligand is coordinated through the dithiocarbamate group rather than the bisphosphonate group; but comparison with literature on technetium and rhenium with coordinated bisphosphonates would suggest such complexes are inhomogenous and polymeric,[8,9] and there is no evidence of such behaviour in the mass spectra of **7** and **8**. Moreover, dithiocarbamates are well known to form transition metal complexes with high affinity, whereas bisphosphonates and pyrophosphates are have been used because of their relative instability, as intermediate chelators to make metastable Tc intermediates in which the bisphosphonates are ultimately displaced by more powerful ligands (*e.g.* during protein radiolabelling at thiol groups of reduced antibodies[30]). The mass spectra are also unable to distinguish possible isomers due to the different relative orientations of the ligands (*e.g. syn-* and *anti-* disposition of the methyl groups of the two ligands); however, this is unlikely to be problematic because the metal coordination sphere in this class of complexes is well-known to be highly fluxional. The equivalence of carrier free (radiolabelled, characterised only by virtue of its R_f value of zero on TLC) and carrier added ($^{185/187}$Re and ^{99}Tc, identified by mass spectrometry and R_f value of zero on TLC) is demonstrated only by sharing R_f values of zero in various TLC conditions and failure to elute from various HPLC columns. This is weak evidence because many species such as reduced hydrolysed Tc share this property. However, although differences in structure and speciation of radioactivity are often observed in technetium complexes at the tracer and macroscopic levels, these typically involve oligomerisation at the higher concentration but not at the lower; since the high concentration solutions here have been shown by mass spectrometry to contain only mononuclear complexes, there is no reason to doubt that the tracer level complexes are also mononuclear.

Both the new pendant tracers [^{99m}Tc]-**4** and [^{99m}Tc]-**7** show improved binding both to synthetic calcium-based minerals and to hydroxyapatite-like minerals isolated from human calcified tissue, and improved stability in buffer and serum compared to ^{99m}Tc-**1**, as indeed they were designed to do. This advantage is conferred by the design of the metal coordinating ligands to match the known preferences of the metal core, rather than relying on the relatively poor chelating ability of the bisphosphonate group. This translates into improved stability in buffer and blood serum, and *in vivo*, which in turn leads to higher uptake in bone and calcified soft tissues than ^{99m}Tc-**1**. However, this potential advantage is set against disadvantage of the greater time taken to achieve the best target-to-background ratio *in vivo*. Thus, the advantages in practical use are likely to arise in situations where prolonged action are important, that is, therapeutic applications of the longer lived isotopes ^{188}Re (17 h) and ^{186}Re (90 h) rather than imaging applications of the short lived ^{99m}Tc (6 h). These advantages will be manifested if the biodistribution and kinetics of the Tc and Re analogues prove to be the same, as they have done in the case of [^{99m}Tc]-**4** and [^{188}Re]-**5**;[12,13] preliminary *in vivo* biodistribution studies suggest that this is also the case for [^{188}Re]-**8** (see ESI†). [^{188}Re]-**8** shows the expected and desired specificity for bone and joints and low retention in kidney, at 24 h, giving a qualitative indication of prolonged *in vivo* stability. Although quantitative comparison with other rhenium-188 bone targeting radiopharmaceuticals has not been part of this study, the data suggest that [^{188}Re]-**8** will have advantages over ^{188}Re-HEDP and warrants further evaluation as a radiopharmaceutical for radionuclide therapy of bone metastases. Thus both [^{188}Re]-**5** and [^{188}Re]-**7** are likely to offer improvements in radionuclide therapy compared to the conventional agents $^{188/186}$Re-HEDP.

^{31}P NMR and X-ray powder diffraction studies of calcified plaques from animals and humans show that the minerals present in vascular calcification closely resemble hydroxyapatite.[31] Radiolabelled bisphosphonates bind avidly with hydroxyapatite; hence they have the potential to be used as agents for imaging of vascular calcification. This prediction presupposes that the mechanism of uptake in calcified tissue and bone is through direct binding to mineral – but it could also be related to cellular transport mechanisms involving osteoclast/osteoblast-like cells involved in the calcification process, as has been implicated in the mechanism of action of bisphosphonate drugs used to treat bone disorders.[32] Nevertheless it is consistent with the observation that the tracers described here bind to the pathological mineral samples tested, and the *in vivo* results show that the tracers indeed target not only bone but also vascular soft tissue calcification. There have been previous reports of extra-osseous uptake of ^{99m}Tc-**1** linked with atherosclerosis and vascular calcification. For example DeLong *et al.* reported the visualisation of calcified femoral arteries in delayed images of patients undergoing bone scans.[33] The clinical value of imaging vascular calcification has, however, yet to be fully explored.

Conclusion

The new technetium and rhenium complexes with two pendant bisphosphonate groups have been synthesised by simple methods amenable to kit-based radiolabelling. The presence of one and two pendant bisphosphonate groups confers advantages over conventional bisphosphonate complexes in which the bisphosphonate group is involved in technetium or rhenium chelation, in terms of *in vivo* stability and affinity for hydroxyapatite of synthetic and biological origin. These advantages are likely to be significant in therapeutic applications involving the longer half-life isotopes ^{186}Re and ^{188}Re. All three classes of ^{99m}Tc complex described here are capable of imaging vascular soft tissue calcification as well as bone disease. The tracers and biological models described here prove a means to study the diagnostic meaning and value of imaging of vascular calcification, leading to clinical applications; however, the present data do not indicate that the advantages in stability and mineral affinity displayed by the new complexes translate into practical advantages in imaging compared to conventional ^{99m}Tc-bisphosphonate tracers such as ^{99m}Tc-**1**. Finally, [^{188}Re]-**8** deserves further biological evaluation as a radiopharmaceutical for palliative treatment of bone metastases because of its high *in vivo* stability, selective uptake in bone and joints, and low retention in kidney at 24 h.

Acknowledgements

This research was supported by the Centre of Excellence in Medical Engineering funded by the Wellcome Trust and EPSRC under grant number WT088641/Z/09/Z, the Kings College London and UCL Comprehensive Cancer Imaging Centre funded by the CRUK and EPSRC in association with the MRC and DoH (England), the British Heart Foundation centre of Research Excellence at King's College London and the National Institute for Health Research (NIHR) Biomedical Research Centre at Guy's and St Thomas' NHS Foundation Trust and King's College London. The views expressed are those of the authors and not necessarily those of the NHS, the NIHR or the Department of Health. Imaging equipment used was purchased through an equipment grant from Wellcome Trust. A postdoctoral placement at King's for IUK was funded by the Higher Education Commission (HEC), Islamabad, Pakistan. We thank Rachel C. Murray of the Animal Health Trust for providing us with the equine bone sample.

References

1 G. Subramanian, J. G. McAfee, R. J. Blair, F. A. Kallfelz and F. D. Thomas, *J. Nucl. Med.*, 1975, **16**, 744–755.
2 S. Zhang, G. Gangal and H. Uludağ, *Chem. Soc. Rev.*, 2007, **36**, 507–531.
3 V. J. Lewington, *J. Nucl. Med.*, 2005, **46**, 38S–47S.
4 J. M. de Klerk, A. D. van het Schip, B. A. Zonnenberg, A. van Dijk, J. M. Quirijnen, G. H. Blijham and P. P. van Rijk, *J. Nucl. Med.*, 1996, **37**, 244–249.
5 B. T. Hsieh, J. F. Hsieh, S. C. Tsai, W. Y. Lin, S. J. Wang and G. Ting, *Nucl. Med. Biol.*, 1999, **26**, 973–976.
6 K. Liepe, J. Kropp, R. Runge and J. Kotzerke, *Br. J. Cancer*, 2003, **89**, 625–629.
7 M. C. Graham, H. I. Scher, G.-B. Liu, S. D.-J. Yeh, T. Curley, F. Daghighian, S. J. Goldsmith and S. M. Larson, *Clin. Cancer Res.*, 1999, **5**, 1307–1318.
8 A. Handeland, M. W. Lindegaard and D. E. Heggli, *Eur. J. Nucl. Med.*, 1989, **15**, 609–611.
9 S. J. Wang, W. Y. Lin, M. N. Chen, C. S. Chi, J. T. Chen, W. L. Ho, B. T. Hsieh, L. H. Shen, Z. T. Tsai, G. Ting, S. Mirzadeh and F. F. Knapp Jr., *J. Nucl. Med.*, 1998, **39**, 1752–1757.
10 J. M. H. de Klerk, A. van Dijk, A. D. van het Schip, B. A. Zonnenberg and P. P. van Rijk, *J. Nucl. Med.*, 1992, **33**, 646–651.
11 A. P. Winterbottom and A. S. Shaw, *Clin. Radiol.*, 2009, **64**, 1–11.
12 R. T. M. de Rosales, C. Finucane, S. J. Mather and P. J. Blower, *Chem. Commun.*, 2009, 4847–4849.
13 R. Torres Martin de Rosales, C. Finucane, J. Foster, S. J. Mather and P. J. Blower, *Bioconjugate Chem.*, 2010, **21**, 811–815.
14 D. J. Berry, R. Torres Martin de Rosales, P. Charoenphun and P. J. Blower, *Mini Rev. Med. Chem.*, 2012, **12**, 1174–1183.
15 M. A. Stalteri, S. J. Parrott, V. A. Griffiths, J. R. Dilworth and S. J. Mather, *Nucl. Med. Commun.*, 1997, **18**, 870–877.
16 F. Demaimay, L. Dazord, A. Roucoux, N. Noiret, H. Patin and A. Moisan, *Nucl. Med. Biol.*, 1997, **24**, 701–705.
17 R. Pasqualini, A. Duatti, E. Bellande, V. Comazzi, V. Brucato, D. Hoffschir, D. Fagret and M. Comet, *J. Nucl. Med.*, 1994, **35**, 334–341.
18 R. Pasqualini and A. Duatti, *J. Chem. Soc., Chem. Commun.*, 1992, 1354–1355.
19 R. Torres Martin de Rosales, R. Tavaré, R. L. Paul, M. Jauregui-Osoro, A. Protti, A. Glaria, G. Varma, I. Szanda and P. J. Blower, *Angew. Chem., Int. Ed.*, 2011, **50**, 5509–5513.
20 J. Singh, K. Reghebi, C. R. Lazarus, S. E. M. Clarke, A. P. Callahan, F. F. Knapp Jr. and P. J. Blower, *Nucl. Med. Commun.*, 1993, **14**, 197–203.
21 P. J. Blower, *Nucl. Med. Commun.*, 1993, **14**, 995–997.
22 M. Abkar Ali, S. E. Livingstone and D. J. Phillips, *Inorg. Chim. Acta*, 1972, **6**, 11–16.
23 R. Torres Martin de Rosales, R. Tavaré, A. Glaria, G. Varma, A. Protti and P. J. Blower, *Bioconjugate Chem.*, 2011, **22**, 455–465.
24 J. Chatt and G. A. Rowe, *J. Chem. Soc.*, 1962, 4019–4033.
25 A. Marchi, E. Marchesi, L. Marvelli, P. Bergamini, V. Bertolasi and V. Ferretti, *Eur. J. Inorg. Chem.*, 2008, **2008**, 2670–2679.
26 D. G. Reid, C. M. Shanahan, M. J. Duer, L. G. Arroyo, M. Schoppet, R. A. Brooks and R. C. Murray, *J. Lipid Res.*, 2012, **53**, 1569–1575.

27 P. A. Price, S. A. Faus and M. K. Williamson, *Arterioscler. Thromb. Vasc. Biol.*, 2000, **20**, 317–327.
28 L. J. Schurgers, H. M. H. Spronk, B. A. M. Soute, P. M. Schiffers, J. G. R. DeMey and C. Vermeer, *Blood*, 2007, **109**, 2823–2831.
29 A. Boschi, C. Bolzati, L. Uccelli and A. Duatti, *Nucl. Med. Biol.*, 2003, **30**, 381–387.
30 S. J. Mather and D. Ellison, *J. Nucl. Med.*, 1990, **31**, 692–697.
31 W. Guo, J. D. Morrisett, M. E. DeBakey, G. M. Lawrie and J. A. Hamilton, *Arterioscler. Thromb. Vasc. Biol.*, 2000, **20**, 1630–1636.
32 R. G. G. Russell, *Bone*, 2007, **40**, S21–S25.
33 E. B. Silberstein and S. DeLong, *Clin. Nucl. Med.*, 1985, **10**, 738–739.